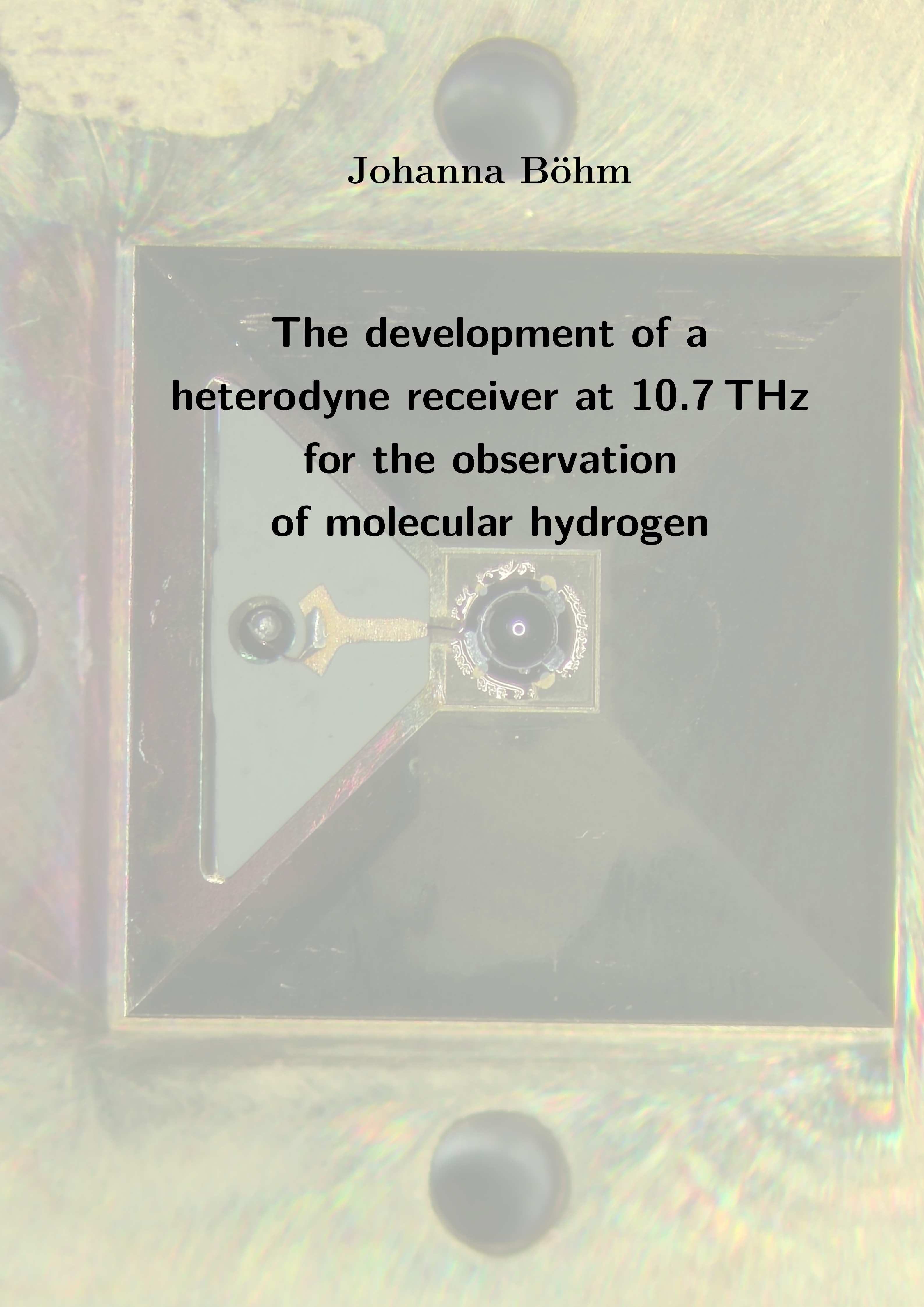

Johanna Böhm

The development of a heterodyne receiver at 10.7 THz for the observation of molecular hydrogen

The development of a heterodyne receiver at 10.7 THz for the observation of molecular hydrogen

Inaugural - Dissertation

zur

Erlangung des Doktorgrades

der Mathematisch-Naturwissenschaftlichen Fakultät

der Universität zu Köln

vorgelegt von

Johanna Böhm

aus Schleswig

Köln, 2023

Berichterstatter:	Prof. Dr. Jürgen Stutzki
(Gutachter)	Prof. Dr. Lucas Labadie

Tag der mündlichen Prüfung: 31.05.2023

Abstract

The focus of this thesis is the development of a superconducting hot electron bolometer (HEB) mixer intended for the operation as a heterodyne receiver for the observation of the electric quadrupole transition of molecular hydrogen in space at 10.7 THz.

The developed detector is based on a quasi-optical receiver concept using a lens to couple the RF-signal to an antenna. The mixing element is a phonon-cooled niobium nitride microbridge that is integrated in the center of the antenna. The detector consists of a copper tellurium detector block containing the IF-board and IF-connector and the HEB-device glued to the flat backside of the silicon lens. The HEB-device is a circular RF-chip based on a 9 µm thick silicon carrier membrane with the RF-circuit structures and integrated HEB-element on its upper side.

For the development of the RF-circuits the dielectric properties of the carrier substrate that consists of high resistivity float zone silicon (HRFZ Si) have been determined since the data available is insufficient for this high frequency range at cryogenic temperatures. The dielectric properties were investigated by means of transmission measurements of different plane parallel silicon samples with two Fourier Transform Spectrometers (FTS) within a frequency range from 4 THz to 18 THz for temperatures between 5 K to 300 K. The measured refractive index increases less than 0.002 with frequency within a frequency interval of 12 THz. From 300 K to 5 K it is reduced by 0.83 % in average. The absorption coefficient of HRFZ Si roughly decreases by 35 % from 300 K to 5 K. The determined permittivity of the carrier substrate at cryogenic operating temperatures of the receiver is 11.4(±0.1).

In total 20 different designs of RF-circuits have been developed and fabricated on one wafer by E-beam and UV-lithography technology in the in-house microfabrication facility. The RF-circuits are based on three different broadband antennas and variations of a narrow-band antenna. One narrow-band and one broadband RF-circuit address an operating frequency around 4.7 THz instead of 10.7 THz to enable a comparison with the UpGreat receiver which has been developed in our research group. The broadband antennas are a self-complementary logarithmic, a logarithmic and an Archimedean spiral antenna. The narrow-band antenna is a double-slot antenna of a full effective wavelength in length that is attached to an RF-filter. To investigate the influence of the lens on the antenna beam of the 10.7 THz double-slot antennas a software has been developed and evaluated that is based on a spectral ray tracing technique because the available commercial CST software is not suitable for that task within the present resources and time constraints.

According to numerical calculations the double-slot antenna out of the investigated antennas reaches the highest overall coupling efficiency. The predicted Gaussian coupling efficiency without considering losses within the gold layers is 49 % for the designed 4.7 THz double-slot antenna when being mounted at the backside of the silicon lens without an anti-reflection coating. From all broadband antennas the Archimedean spiral antenna that typically is used for distinct lower frequencies below 1 THz, is predicted to obtain the highest overall power coupling to a Gaussian beam of about 39.4 %. Applying an anti-reflection layer on the lens these Gaussian coupling efficiencies are expected to increase to about 64% and 57% for the double-slot antenna and for the Archimedean spiral antenna, respectively.

In total five different RF-circuits have successfully been assembled in the detector block and used as an external power detector of an FTS to determine their spectral response within an interval from 3 THz to 12 THz. They are based on three narrow-band designs for 10.7 THz, one narrow-band design for 4.7 THz and a broadband circuit based on the Archimedean spiral antenna. The detectors with the double-slot antennas exhibit a distinct polarization-dependent sensitivity that is maximal at the dedicated polarization direction of the DS-antenna and vanishes for the polarization direction perpendicular to it. All assembled 10.7 THz narrow-band detectors show a response peak slightly below the intended operating frequency with deviations of the center frequencies less than 4 % to 8 %. The measured curves of the RF-response around the operating frequency agree well with the predicted curves of the coupling efficiency between the HEB-element and the antenna. The detector with the Archimedean spiral antenna shows a significant direct response over the entire frequency range from 3 THz to 12 THz. To our knowledge the Archimedean spiral antenna as well as the double-slot antenna till now so far are the only antennas designed for 10.7 THz that have been realized and verified as direct HEB power detectors. The measurement results confirm that these HEB-devices are suitable candidates for future heterodyne measurements. The local oscillator (LO) source that is needed to operate the detectors in heterodyne mode is a Quantum Cascade Laser developed by the Quantum Optoelectronics Group of the IQE, ETH Zurich, and has not yet been completed at the end of this work.

Zusammenfassung

Gegenstand dieser Arbeit ist die Entwicklung eines supraleitenden Hot Electron Bolometer (HEB) Mischers, welcher als Heterodyne-Empfänger für die Beobachtung des elektrischen Quadrupol-Übergangs von molekularem Wasserstoff im Weltall bei 10.7 THz eingesetzt werden soll.

Der entwickelte Detektor basiert auf einem quasi-optischen Konzept, bei dem das HF-Signal mit Hilfe einer Silizium Linse in eine Antenne mit integriertem Mischelement eingekoppelt wird. Das Mischelement besteht aus einer Phononen-gekühlten Niobnitrid Mikrobrücke im Zentrum der Antenna. Der Detektor setzt sich aus einem Kupfer Tellurium Gehäuse und darin enthaltener ZF-Platine, ZF-Anschlüssen und dem HEB-Bauteil zusammen, welches an die flache Rückseite einer Silizium Linse geklebt ist. Das HEB-Bauteil ist eine kreisrunde HF-Platine, welche aus einer 9 µm dicken Trägermembran aus Silizium besteht auf deren Oberseite die Hochfrequenzschaltkreise aus Gold mit darin integriertem Mischelement aufgebracht wurden.

Aufgrund der unzureichenden Datenlage zu den dielektrischen Eigenschaften des zugrunde liegenden Trägersubstrates der RF-chips bei der gewünschten Betriebsfrequenz und kryogenen Betriebstemperaturen wurden Untersuchungen von hoch reinem Silizium (High Resistivity Float Zone Silicon) vorgenommen. Anhand von unterschiedlichen plan-parallelen Silizium-Scherben wurde mit Hilfe von Transmissionsmessungen mit zwei Fourier Transform Spektrometern der frequenzabhängige, als auch temperaturabhängige Brechungsindex der unterschiedlichen Proben über einen Frequenzbereich von 4 THz bis 18 THz für Temperaturen zwischen 5 K und 300 K ausgewertet. Die Messergebnisse zeigen, dass der Brechungsindex innerhalb eines Frequenzintervalls von 12 THz weniger als 0.002 mit der Frequenz ansteigt und von 300 K auf 5 K durchschnittlich um 0.83 % sinkt. Die Permittivität des Trägermaterials bei der Betriebstemperatur des Empfängers wurde anhand der Messergebnisse auf 11.4($\pm$0.1) geschätzt.

Insgesamt wurden 20 unterschiedliche Entwürfe von Hochfrequenzschaltkreisen aus einem gemeinsamen Wafer mit Hilfe von Elektronenstrahl und UV Lithographie im hausinternen Mikrofabrikationslabor hergestellt. Die Hochfrequenzschaltkreise basieren auf drei unterschiedlichen Breitband-Antennen und Variationen einer schmalbandigen Antenne. Neben den Entwürfen für 10.7 THz wurde jeweils ein schmalbandiger und ein breitbandiger Hochfrequenzschaltkreis für eine Betriebsfrequenz von 4.7 THz entworfen um einen späteren Vergleich mit dem UpGreat Empfänger zu ermöglichen, welcher in unserer Forschungsgruppe entwickelt wurde. Als Breitbandantennen wurden eine selbstkomplementäre logarithmische, eine logarithmische und eine Archimedische Spiralantenne

verwendet. Die schmalbandige Antenne besteht aus einer Doppelschlitz-Antenne mit der Länge einer effektiven Wellenlänge, an welche ein Hochfrequenzfilter angeschlossen ist. Um den Einfluss der Linse auf die Hauptkeule der 10.7 THz Doppelschlitz-Antennen zu untersuchen wurde eine Software entwickelt und evaluiert, welche auf einer Technik mit spektraler Strahlungsverfolgung (spectral ray tracing) basiert. Die verfügbare kommerzielle CST Software ist mit den vorhandenen Rechenressourcen und aus Zeitgründen für diese Aufgabe nicht geeignet.

Numerischen Berechnungen zu Folge erlangt die Doppelschlitz-Antenne von allen untersuchten Antennen die insgesamt höchste Kopplungseffizienz mit einem Gauss-Strahl. Die vorhergesagte Gaussian coupling Effizienz ohne Berücksichtigung von Verlusten in den Leiterschichten aus Gold beträgt für die 4.7 THz Doppelschlitz-Antenne 49%, wenn die Antenne auf die Rückseite der Silizium Linse platziert wird und die Linse keine Antireflektionsbeschichtung hat. Von allen Breitband-Antennen erreicht die Archimedische Spiralantenne, welche üblicherweise Anwendung bei deutlich niedrigeren Frequenzen unter einem Terahertz findet, die höchste insgesamte Leistungsankopplung an einen Gauss-Strahl von um die 39.4%. Es wird erwartet, dass die Gaussian coupling Effizienzen bei Auftragung einer Antireflektionsbeschichtung auf der Linsenoberfläche auf um die 64% für die Doppelschlitz-Antenne und 57% für die Archimedische Spiralantenna angehoben werden kann.

Insgesamt wurden fünf unterschiedliche Hochfrequenzschaltkreise erfolgreich in einen Detektorblock eingebaut und als externer Leistungsdetektor eines Fourier Transform Spektrometers verwendet um ihre spektrale Empfindlichkeit in einem Frequenzintervall von 3 THz bis 12 THz zu messen. Die Hochfrequenzschaltkreise basieren auf drei schmalbandigen Entwürfen für 10.7 THz, einem schmalbandigen Schaltkreis für 4.7 THz und einem breitbandigen Entwurf mit einer Archimedischen Spiralantenne.

Alle Detektoren mit schmalbandigen Antennen weisen eine klar polarisationsabhängige Empfindlichkeit auf, deren Maximum in der zugehörigen Polariaztionsrichtung der Antennen liegt und welche für die Polarisationsrichtung senkrecht dazu auf Null abfällt.

Für alle drei schmalbandigen 10.7 THz Detektoren wurde ein Maximum um die 10 THz in der spektralen Empfindlichkeitskurve gemessen, welches weniger als 4 % bis 8 % von der vorhergesehenen Betriebsfrequenz entfernt liegt. Der gemessenen frequenzabhängige Verlauf der Empfindlichkeitskurven um die Betriebsfrequenz deckt sich mit den Vorhersagen für die Kopplungseffizienz zwischen HEB-Element und Antenne. Das Detektormodul mit der Archimedischen Spiralantenne weist ein Antwortsignal über den kompletten Frequenzbereich von 3 THz bis 12 THz auf. Nach unserem Kenntnisstand sind die Archimedische Spiralantenna als auch die Doppelschlitz-Antennen für 10.7 THz die bisher einzigen

Antennen, welche bislang für 10.7 THz entworfen und als direkter HEB-Leistungsdetektor realisiert und verifiziert wurden. Die Messergebnisse weisen sie als geeignete Kandidaten für kommende Heterodyne-Messungen aus. Der vorhergesehene Lokaloszillator, welcher für den Betrieb der Detektoren als Heterodyne-Empfänger notwendig ist, ist ein Quantum Cascade Laser, welcher von der Quantum Optoelectronics Group im IQE, ETH Zürich entwickelt wird und bei Abschluss dieser Arbeit noch nicht fertig gestellt wurde.

Contents

List of Figures

Acronyms

AR	Axial ratio
ar	anti-reflection
Au	Gold
CPW	Coplanar waveguide
DC	Direct current
DS	Double-slot / Double-slot antenna
FFT	Fast Fourier Transformation
FTS	Fourier Transform Spectrometer
GO	Geometrical Optics
HEB	Hot electron bolometer
HRFZ Si	High resistivity float zone silicon
IF	Intermediate frequency
LHP	Left-handed polarized
NbN	Niobium Nitride
PEC	Perfect Electrical Conductor
RF	High frequency
RHP	Right-handed polarized
SEM	Scanning electron microscope
Si	Silicon
SiO_2	Silicon Dioxide (quartz)
SRT	Spectral domain Ray Tracing
TDS	Time-domain Spectrometer

1. Introduction

1.1. Astronomical observations of molecular hydrogen in space

Molecular hydrogen is the most abundant molecule in the universe[168]. It exists as two spin isomers which differ in the spin states of their nuclei[75]. In its para-form the two protons have anti-parallel spins (see Fig. 1.1). For ortho-hydrogen the spins of both protons are parallel to each other. Since there is only forbidden radiative transitions[1] between both spin states[75], they can be considered as independent states as long as no catalytic acting compounds are present. A conversion between the para and ortho form, however, can be strongly hastened by collisions with appropriate collision partners like dust grains. The actual para-ortho ratio of H_2 in comparison to its expected thermal equilibrium ratio therefore can provide important information about the physical parameters of its environment.

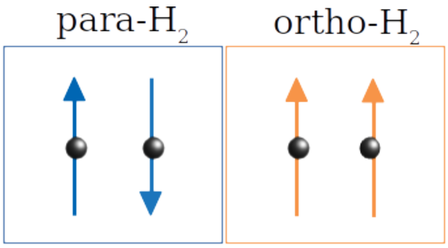

Figure 1.1.: Spin isomers of molecular hydrogen. The spins of both protons are antiparallel for the para-H_2 and parallel for the ortho-H_2.

Being a homonuclear[2] and diatomic molecule molecular hydrogen neither exhibits permanent nor vibrational induced electrical dipole moments due to its symmetry, but only provides the weak emission features of electric quadrupole transitions ($\Delta J = \pm 2$)[168] owing to small spontaneous emission Einstein coefficients[145][3] [4]. Basically, molecular hydro-

---

[1] The radiative orho-para transition rate in the ground vibrational level (J:1→ 0), for instance, is approximately $6.20(62) \times 10^{-14}\,\mathrm{y}^{-1}$ [129]

[2] composed of only one element

[3] Difference to the respective next multipole depends on α^2 (fine-structure constant)

[4] The magnitude of the Einstein coefficients for the first pure rotational transmission lines, for instance, lies between $10^{-11}\,\mathrm{s}^{-1}$ to $10^{-7}\,\mathrm{s}^{-1}$ [145].

gen exhibits three different spectroscopic transitions for astrophysical observations[177]. Besides the pure rotational transitions in the mid-IR, that is the ro-vibrational transitions in the near-IR and elecronic bands in the UV.

Molecular hydrogen is an important target for observations since it plays a key role in many astrophysical contexts[69, 164, 33, 75, 107, 177, 165, 124, 105, 43, 120, 59] which are too manifold to mention them all in detail at this point. As a major cooling agent in astrophysical media whose physical conditions correspond to those of warm molecular gas [161, 75, 177], and as an initiator of chemistry of interstellar gas by its formation on dust grains [86], it plays for instance a key role in understanding the processes that regulate star formation and the evolution of galaxies [51].

The lowest rotational transmission line at around 10.7 THz, which is the operational frequency of the designed receiver of this work, especially is important for the investigation of warm clouds since the directly observable coldest H_2-gas[141] in the nearby Universe, is only possible by the 28 µm transition line of the para-form H_2. So far, most information in this field has been obtained from tracer measurements or absorption lines in other emission spectra. At cloud-temperatures below 50 K H_2 is expected to be predominately in its ground state with a para-spin state configuration, where the para-ortho rate in thermodynamical equilibrium is reached due to the interactions of the molecules with the cold interstellar dust. A common and highly abundant molecule in the interstellar clouds to probe the cold H_2 gas is CO whose lowest transition frequency occurs around 115 GHz. This main tracer of molecular clouds, according to hydrodynamical and magnetohydrodynamical simulations, is formed with a significant delay with respect to the formation of H_2 [29, 158] with the consequence that CO is expected not to be a good tracer for instance in the initial phases of molecular clouds evolution. Theoretical and observational studies suggest that a significant part of molecular hydrogen around 30 % to 70 % is not traced by CO[72, 130, 104, 158] at all. Furthermore, the conversion into abundance of H_2 from observation data of CO is dependent on many aspects (e.g. metallicitiy, density) which are subject of ongoing debates [65, 18], but most of the time is expected to not perfectly map the H_2-gas. As a consequence, tracer measurements with CO seldom are able to reflect the complex reality of the object of observation what emphasizes the importance of direct observations of H_2, especially at colder temperatures by the 28 µm quadrupole line of the transition from J:2→ 0 (510 K above the ground state J=0) of the para-hydrogen. The 28 µm quadrupole-transition line, moreover, is an indicator for collapse phases in early star formation[70] if the spectral line-resolution is high enough to provide details about the velocity structure. In emission it is further observable in Photon-dominated regions (PDRs) and shocked regions[19, 21].

The direct observation of molecular hydrogen is challenging for several reasons. First of all, its electronic transitions occur in the ultraviolet that is opaque to the Earth's atmosphere. Even so a space-based observation of the Lyman-Werner bands (11.2 to 13.6 eV) in absorption as done by the Far Ultraviolet Spectroscopic Explorer (FUSE) is possible it requires a bright background source (like an O or B star) to observe these absorption bands. Since it can be expected that most of the gas in the ISM does not have a bright UV background source the potential targets being observable are limited. In addition, it is expected that in many cases cold cloud structures of H_2 would not have be seen at all during observations as a large fraction may be located in cool, shielded regions [33] where the excitation in the IR is too low and the UV pumping lines suffer too much extinction to be detectable through emission lines.

The second challenge to observe molecular hydrogen is given by the fact that many of the ro-vibrational and rotational emission lines are considerably weak based on their electric quadrupole origin and can only be observed due to the high abundance of H_2. The direct observation of these lines, subsequently, requires high sensitivity measurements. In many cases the IR-lines, additionally, lie on top of a strong dust continuum emission and only can be disentangled from the bright background by high spectral resolution[115].

Moreover, in the mid-IR, the almost opaque Earth's atmosphere makes an Earth-based detection of most of the pure rotational lines unfeasible. Observations of few emissions-lines in the mid-IR from ground are limited to high flux compact H_2 emission sources "with fluxes typically larger than 1 Jy"[177].

An adequate observation in particular of the 28 µm spectral line, however, either asks for space-based missions (such as ISO, Spitzer and JWST in the mid-IR range) or platforms located at a very high altitude of the Earth's atmosphere at least from the stratosphere provided by airplane or balloon-based telescopes (like SOFIA or ESBO). The study of dynamics moreover requires a resolving power greater than $R = \frac{\lambda}{\Delta\lambda} = 10^6$ (thermal line width ≈ 0.1 km/s) A short overview of existing and retired observatories and therein operated instruments for the mid to far-IR regime from 3 µm to 30 µm is summarized in table 1.1. As can be seen there is an ongoing effort to investigate the rotational transitions of molecular hydrogen in the mid-IR. The recently launched MIRI instrument on the James Webb Space Telescope (JWST) has been designed to cover a frequency range that allows the observation of the lowest rotational emission line at 28.2 µm with a high spatial resolution around about $\approx 0.1''$ and a medium spectral resolution around about 3000.[5]. From Table 1.1 it is clear that even the highest spectral resolution, as offered by the EXES instrument still is an order of magnitude lower than what is required for the

---

[5] To the current state (Dez.22) the spectral observational range is possible from 4.9 µm to 27.9 µm[41]

targeted H_2 observations At the current state of technology receivers with higher grating-based resolving power at 10.7 THz are difficult to be suitably implemented in satellite or balloon-based missions due to opto-mechanical limitations, reasons of mechanical and thermal stabilities and of weight. The only option open to achieve the required very high resolution for kinematic observations of the 28 µm spectral line is then a heterodyne detection technique as is proposed here. NbN HEB mixers have shown[16] to be able to reach a sensitivity of 5 times the quantum limit ($\frac{h\nu}{k_B}$), which should be adequate. A 10.7 THz HEB mixer, combined with a QCL local oscillator can be made small, light weight and with a low enough power consumption for a balloon or a satellite mission. Such a receiver is a necessary supplement to the JWST that after 2022 is the only platform for 28 µm observations. The development of the heterodyne mixer that is the focus of this work was originally intended to fly on the Stratospheric Observatory for Infrared Astronomy (SOFIA) whose operational time was recently shortened to the end of September of 2022. Test-measurements of the receiver are ongoing and can unfortunately not be finalized during this work as long as the local oscillator that is mandatory for heterodyne detection is still under development by IQE, ETH Zurich. Although an operation of the receiver on the SOFIA observatory is not possible anymore, a mission on a balloon-borne telescope (such as the European Stratospheric Balloon Observatory (ESBO) or the Super-pressure Balloon-borne Imaging Telescope (SuperBIT)) is still conceivable.

observatory/instrument	wavelength [µm]	power resolution $R = \frac{\lambda}{\Delta\lambda}$
ground-based		
VLT/CRIRES	1-5	20,000-100,000
VLT/ISAAC	1-5	1000-10,000
VLT/VISIR	5-24	350-25,000
IRTF/SpeX	0.7-5.3	50-2500
IRTF/iSHELL	1.06 - 5.3	80,000
IRTF/MIRSI/MOC	2-20	100-200
IRTF/TEXES	5-25	15,000-100,000
airborne		
SOFIA/EXES (end mid 2022)	4.5-28.3	10,000-100,000
space-based		
IRAS (end 1983)	12-100	low
ISO (end 1998):		
ISO/ISOCAM	2.5-17	40
ISO/ISOPHOT	2.5-12	62-134
	3-120	broadband filter
ISO/SWS	2.5-45	1000-35,000
Spitzer(SIRTF) (end 2020):		
Spitzer/IRS	5.3 - 38	90-600
Spitzer/MIPS	24,70,160	bandwidth 5,19,35µm
JWST/MIRI	4.6 -28.6	100-3000

Table 1.1.: Summary of existing and past observatories with instruments suitable for observations in the mid-IR to the far-IR regime (3 µm to 30 µm respectively 100 THz to 10 THz).

1.2. Receivers for the observation of THz signals

The focus of this work is the development of a heterodyne receiver at 10.7 THz whose mixing element consists of a Hot Electron Bolometer (HEB). This section gives a brief overview about the chosen HEB-based approach in the context of existing technology for heterodyne receivers in the THz range that are used for astrophysical observations.

Two fundamental categories of detection may be distinguished. The first one is the *direct* detection where only the power or number of photons is detected. The second category encompass the *heterodyne* detection where the phase and amplitude information of the incoming signal is preserved. Two prominent examples for direct detectors in the THz regime are Kinetic Inductance Detectors (KIDs) and Transition Edge Sensors (TES) both based on a superconducting element. The spectral resolution of such devices is determined by the limits of realizable optical spectroscopic methods like filters and gratings which typically enables a moderate to medium resolution. The available instruments for observations around 28 µm (EXES, TEXES, MIRI) use filters and gratings which enable to only reach a resolution up to 10^5 so far (see Tab.1.1).

In a heterodyne detector the sky signal is combined with a much stronger local oscillator signal. The detector has a highly non-linear characteristic and the beat frequency that is the result of this combination of the two signals on this detector contains both, the amplitude and the phase information of the sky signal at a frequency that is orders of magnitude lower. A resolution of 10^6 is easily achievable in that case. Consequently, to enable the very high frequency resolution about 10^6 that is required for the receiver to be developed, a heterodyne detection approach is chosen.

Common mixing devices in the THz range are Schottky-barrier diodes (a metal-semiconductor junction), Superconductor Isolator Superconductor (SIS) tunnel junctions and Hot Electron Bolometers (HEBs). Schottky diodes are semiconductor devices that are generally cooled to 77K for best mixer performance, but that have nevertheless a sensitivity generally considerably less than that of superconducting detectors[108]. An SIS tunnel junction consists of two superconductors cooled below their critical temperature which are separated by a thin insulator. Currently, the SIS mixers are the most sensitive heterodyne mixers from 0.3–1.2 THz [108] and can easily reach an IF-bandwidth of about 12 GHz or more. The maximum THz frequency at which SIS junctions can be used as mixing elements, however, is determined by the sum of the frequencies determined by the superconducting energy gap of their junction electrode materials. Above this sum gap frequency the SIS junction cannot be used as a sensitive mixing element. For niobium (Nb), that is the most commonly used material, the maximum frequency is about two times the gap frequency $\frac{2\Delta}{h} \approx 0.7\,\text{THz} = 1.4\,\text{THz}$, if both electrodes are made of this material. There is an ongoing attempt to further push this upper frequency limit by using other suitable junction materials, but present high gap-voltage SIS-junctions are still far away from enabling a 10 THz mixer.

An HEB is a superconducting microbridge consisting of a thin layer of a superconducting material that is placed on a carrier substrate and is attached at both of its ends to generally normal conducting contact pads. Contrary to SIS mixers, for a HEB mixer it is the lower frequency limit that is determined by the superconducting gap of its material. This gap is a function of several parameters like the temperature, thickness and contact conditions of the superconducting film. In the mixing mechanism of HEBs the Local Oscillator signal creates a distribution of so called "hot electrons" in the superconducting film that are the result of the breaking of Cooper pairs. The temperature of this hot electron distribution is modulated by the beat between the local oscillator signal and the sky signal. This temperature modulation, generates the intermediate frequency (IF) signal when the HEB is biased , by a combination of DC current and LO radiation, at the critical temperature of the bridge. The hot electrons release their energy by scattering, which is transported out of the system e.g. as phonons in the substrate, and can reassemble to Cooper pairs. The elastic electron-electron scattering time sets the general, ultimate upper frequency limit for a HEB mixer. It basically is the time the electrons need to share their energy with other electrons to have an uniform electron gas in the superconducting film and thereby pinpoints where the real RF-resistance ceased to be frequency-independent. This upper limit is expected to be around about 10^{-15} s which equals a frequency around about 160 THz[136, 117, 64]. The superconducting material Niobiumnidride (NbN) that is used for this work has been proven to respond to near-infrared to submillimeter radiation (64 THz) with an intrinsic response time for a NbN film smaller than 50 ps [71, 54]. The IF-bandwidth of a superconducting HEB mixer is determined by the thermal response time that is dependent on the film material parameters, the material of the underlying wafer material or the length of the bolometer film. Most common material combinations are Niobiumnitride (NbN) films on silicon (3-5 GHz bandwidth [17, 182]) or on GaN (7 GHz bandwidth[101]) or MgB_2 on Al_2O_3(11 GHz bandwidth [126]). There is an ongoing research on suitable material combinations and methods to increase the IF bandwidth for example by applying additional films on top of the superconducting film (0.1-14 GHz bandwidth [96]). Currently, the HEB bridges are proven to be the best option for heterodyne mixers at higher THz frequencies. A receiver based on a HEB mixing element, consequently, is the best choice to fulfill the requirements profile elucidated in the above section.

1.3. The development of a 10.7 THz mixer

At the beginning of the development of a heterodyne receiver several steps need to be regarded. First, a receiver concept for the whole RF-design needs to be chosen (e.g. How to couple in the signal? What is the mixing element?). Secondly, RF circuits needs to be designed according to the formalism provided by microwave-engineering and refined by means of numerical FEM solvers provided for instance by CST studio suite[66]. Modular parts of the detector unit including IF-parts and housing need to be purchased or designed and fabricated and an assembly concept needs to be found. A stable and continuous wave, maybe even a phase-locked local oscillator (LO) at the operating frequency is required to produce the reference signal needed for the heterodyne measurements. Necessary components for a test-setup to characterize the assembled detector needs to be found, designed, fabricated and put together.

Based on additional challenges related to the high operational frequency the work necessary to enable the development of a 10.7 THz heterodyne receiver implied the development of additional software tools and the investigation of different material properties for cryogenic and vacuum applications at the operating frequency. Consequently, the main work of this thesis can be divided up into four sections.

- The first part outlined in the chapter “RF design” introduces the chosen mixer concept and contains the designs of the high-frequency circuits to embed the mixing element. It implies narrow-band and broadband antenna designs and addresses the problem that the calculation basis based on quasi static electro-engineering formalism becomes insufficient to predict the performance of the RF circuits and uses an alternative formalism for setting up the high-frequency circuits parts of the RF-designs with narrow-band antennas.

- The second section of this work introduced in chapter “Optics” describes a software that has been developed to calculate the influence of the lens of the lens-antenna on the beam-pattern at 10.7 THz which due to restrictions in the computational resources is not possible with the available commercial software CST[66]. The new software is based on a spectral ray tracing method and can be executed in parallelization.

- The third part arises from the still scant knowledge about material properties in this specific frequency range of operation and encompasses the search of suitable materials for the measurement setup and assembly of the receiver as well as the measurement of the to this time unknown dielectric constant of high-resistivity silicon at cryogenic temperatures in the operating frequency range of the receiver. The knowledge of the dielectric constant of silicon is crucial as it has a strong effect on the RF-designs. To determine the dielectric permittivity as a function of temperature an own test-setup with a Fouriertransform Spectometer has been build-up and an additional measurement performed by Philipp Warzanowsky in the Second Institute of Physics has been evaluated. The results are discussed and compared with different theoretical models.

- The fourth main part follows after a short description of the fabrication method of the device and the lay out of the mixerblock. It comprises the measurements and evaluation of several HEB-devices. First of all, a detailed DC-characterization of various fabricated HEB-devices have been done to allow a pre-selection of suitable candidates for the assembly into the detector unit. In total five different HEB-devices, which have been mounted in the detector blocks, were investigated regarding their frequency-dependent direct response to a THz broadband source. The response spectra were obtained by using the HEB-mixer as external power detector of a Fourier transform spectrometer. Optical elements of the setup have been chosen based on the research of suitable materials for the high frequency regime in the third part of this work. All investigated HEB-devices, one broadband device, one narrow-band device for 4.7 THz and three narrow-band devices for 10.7 THz, showed a spectral response which is compared with predictions. Good conformity with the predictions as well as deviations are discussed. A detailed investigation of potential sources of error is carried out. According to their measured spectral response all three narrow-band 10.7 THz HEB-devices and the broadband HEB-device are suitable candidates for heterodyne test-measurements. The intended LO-source for the generation of the reference signal for the heterodyne measurements at 10.7 THz is a Quantum Cascade Laser (QCL) developed at the IQE, ETH Zurich. Since at the end of my dissertation time the development of the local oscillator has not been finished yet, no heterodyne measurements could be carried out. The potential LO source for 4.7 THz from the at this time ceased upGREAT mission is on its way back to our research group, by sea-fare, and soon will be accessible to perform heterodyne measurements with the HEB-devices that are suitable for 4.7 THz. This remains a future task.

The overall structure of this thesis is as follows. First the theory needed for the characterization of the bolometer mixer is presented. In the subsequent chapter all RF-parts of the mixer are introduced including the elements of the quasi-optical receiver concept, and several narrow-band and broadband RF-circuits for 10.7 THz and 4.7 THz. The RF-circuits are compared with each other. Chapter 4 introduces the software developed to calculate the influence of the lens on the antenna beam. Chapter 5 summarizes the investigation and results about the frequency-dependent and temperature dependent dielectric permittivity of very pure silicon and other materials needed for the detector or the measurement setup. The subsequent chapter describes the fabrication and assembly of the detector unit. The fabrication of and needed process development for the RF-chips has been done by Dr.Karl Jacobs. The design of the IF-chips, the housing and assembly of the detector is the work of Michael Schultz. The IF-design of the passage between the IF-chip and the RF-chip with regards to their embedding into the copper housing has been done by Dr. Netty (C.E.) Honingh. Chapter 7 presents the measurement results of various fabricated HEB-devices and the final chapter gives short conclusion and outlook.

2. Bolometric detectors

2.1. Bolometers

The detection mechanism of bolometers in general is based on the heating of an absorbing material caused by incoming radiation at the frequency regime of interest. Changes in the temperature of the absorber are measured by means of a temperature sensitive resistor. The resistor either is a separate element thermally linked with the absorber (composite bolometer), or the absorbing material itself (integrated bolometer). The temperature dependence of the resistor can be defined by its temperature coefficient α

$$\alpha = \frac{1}{R\left(T_{\mathrm{Abs}}\right)} \frac{\mathrm{d}R\left(T_{\mathrm{A}bs}\right)}{\mathrm{d}T_{\mathrm{A}bs}} \quad [1/\mathrm{K}], \tag{2.1}$$

where $R(T_{\mathrm{A}bs})$ and $T_{\mathrm{A}bs}$ are the temperature-dependent resistance and the temperature of the resistor, respectively. The temperature of the absorber and the resistor are the same. The general bolometer structure, depicted in Figure 2.1, consists of an absorber that is

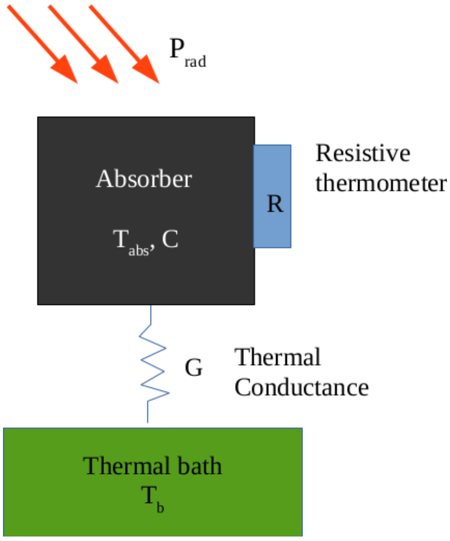

Figure 2.1.: Schematic of a bolometer

thermally coupled with a thermal bath $T_{\mathrm{b}} \leq T_{\mathrm{A}bs}$. Incident radiation yields an increase of the absorber temperature. Via the thermal interface the absorbed radiation power P_{abs} is transmitted to the thermal bath. After switching off the incident radiation the bolometer needs some time to return in its initial state with $T_{\mathrm{b}} = T_{\mathrm{A}bs}$. The characteristic time for this process is given by the heat capacity C of the absorber and the thermal conductance G

$$\tau = \frac{C}{G}\ [\mathrm{s}]. \tag{2.2}$$

In case that the bolometer itself is used as a temperature-dependent resistor and is biased with a constant current I, its voltage responsivity S (change in voltage drop per watt of absorbed signal power) to a time varying radiant input power can be written as[140]

$$S = \frac{I \cdot R \cdot \alpha}{G - I^2 \frac{dR}{dT}\left(1 + i\omega_S \tau_{eff}\right)}\ [\mathrm{V/W}], \tag{2.3}$$

where ω_S is the angular frequency of the time varying part of the radiant input power and dR/dT is the gradient of the resistance of the bolometer with temperature. The thermal time constant is[140]

$$\tau_{eff} = \frac{C}{G - I^2 dR/dT}, \tag{2.4}$$

and defines the maximum in frequency at which the receiver power can be modulated. It determines the frequency bandwidth by

$$f_{IF} = (2\pi\tau_{eff})^{-1}. \tag{2.5}$$

For a high responsivity and a small thermal time constant a large resistance gradient as well as a small heat capacity is required. This is basically done by reducing the volume of the bolometer and by optimizing the detector material properties to get a sharp transition of the resistance with temperature. The thermal time constant can be further reduced by increasing the thermal conductivity to the bath. Superconductors around the temperature of their phase transition from superconducting to normal conducting have a favorable high resistance gradient and therefore are suitable as power detectors. An overview of superconducting hot electron bolometers and their cooling mechanism is given in the following sections.

2.2. Superconducting hot electron bolometers

A superconducting hot electron bolometer consists of a superconducting thin film on a dielectric substrate, that is in contact with two metal pads that typically are normal conducting. Since the film is only several nm thick, a few µm wide and a few hundreds of nm long (see Fig. 2.2), it is also called a microbridge in the context of this work. The contact between the contact pads and the microbridge layer typically is improved by applying an additional adhesion layer (see Fig. 2.2(c)).

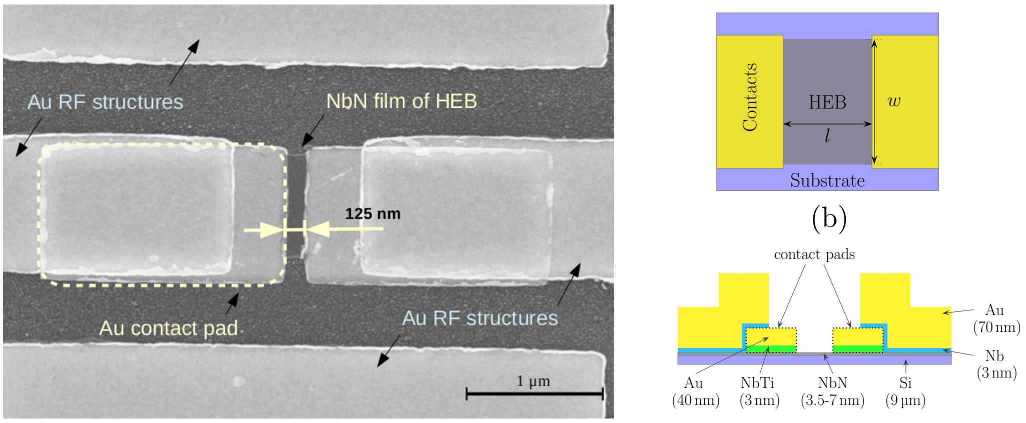

(a) (b) (c)

Figure 2.2.: (a) SEM image of a fabricated HEB microbridge with a length of 125 nm integrated into an RF-circuit. The dark colored areas are parts of the silicon membrane which are not covered by the NbN film in the center or by the gold structures. Sketch of an HEB microbridge: (b) Top view, (c) Cross section with typical dimensions and additional adhesion layers that are used used for the HEBs of this work

One way to model the HEB is to separate it into co-existing thermal subsystems [131, 150], namely Cooper pairs, quasiparticle which are electrons from broken Cooper pairs, phonons in the film, and phonons in the substrate as depicted in Fig. 2.3. Each of the subsystems can be described by distribution functions with an individual effective temperature. The subsystems can interact with each other via electron-phonon scattering and phonon-phonon scattering. The substrate can be thought as a thermal reservoir. The interaction time between electrons and phonons in the thin film is a function of temperature and increases for cryogenic temperatures due to a decrease in the phonon-density. At temperatures of a few degree of Kelvin the phonon-system and the electron-system consequently are only weakly coupled. Under these conditions, power that is fed into the electron system yields an increase in the effective temperature of the electron system that is higher than the temperature of the phonon system. These electrons that are driven out of thermal equilibrium and can be described by a Fermi function with an effective elevated temperature[150] are called “Hot electrons”, where this term was initially introduced for this effect in semiconductors[142]. Similar to the general description of a bolometer, the performance of the HEB is determined by the heat capacity and the thermal conductivity, which are the electron heat capacity, c_e, and the electron-phonon thermal conductivity, respectively. Coupling power into the HEB yields a change in the distribution function of the hot electrons that causes a measurable variation of the resistance of the microbridge.

2.2.1. Phonon-cooled HEB mixer

Depending on the dominant cooling mechanism of the hot electrons in the microbridge superconducting HEB mixers are classified as diffusion-cooled or the phonon-cooled. In the latter case the mixers release the thermal energy of their hot electrons via electron-phonon collisions in the thin superconducting film. The energy of the film phonons is relaxed via the phonons in the substrate. For a diffusion-cooled HEB bridge the relevant path for the heat relaxation is via out-diffusion of the electrons into the contact pads. This mechanism is dominant if the length l_{HEB} (see Fig. 2.2(b)) of the microbridge is short in comparison to the thermal diffusion length, $L_{th} = \sqrt{D \cdot \tau_e}$, where D is the diffusion constant of the material and τ_e is the electron cooling time [136]. The cooling via out diffusion is dominant if the out-diffusions time $\tau_{dif} = \frac{l_{HEB}^2}{D}$ is significantly shorter than the time a hot electron needs to release its energy via the phonons to the temperature bath (τ_Θ). The length of the HEB should therefore be short in comparison to the thermal diffusion length L_{th}. A commonly used diffusion-cooled HEB material is Niob (Nb) on silicon, with a diffusion constant of around $1\,\mathrm{cm}^2/\mathrm{s}$ for a $10\,\mathrm{nm}$ thick Nb film and an electron-phonon inelastic scattering time around $\tau_{ep} = 1\,\mathrm{ns}$[136] at $4.2\,\mathrm{K}$. Since those bolometers based on Nb are extremely sensitive to damage by ESD, they require an extremely careful handling and operation that is not compatible with an astronomical receiver[166].

For the chosen material combination Niobium Nitride (NbN) on very pure silicon the according heat relaxation process is dominated by phonon cooling. The electron relaxation time in NbN is more than an order of magnitude smaller[150] than of Nb with a diffusion constant about $0.35\,\mathrm{cm}^2/\mathrm{s}$ to $0.47\,\mathrm{cm}^2/\mathrm{s}$ for films with a thickness between $5.5\,\mathrm{nm}$ and $7\,\mathrm{nm}$, respectively [157]. The phonon cooling requires ultrathin films ($< 10\,\mathrm{nm}$) that have to be described in the dirty limit, and a good acoustic coupling of phonons of the film with the substrate phonons [74]. An even better acoustic coupling is present between thin NbN films and GaN (membrane) substrates [102, 101] , but the development of that technology is outside of the scope of this work.

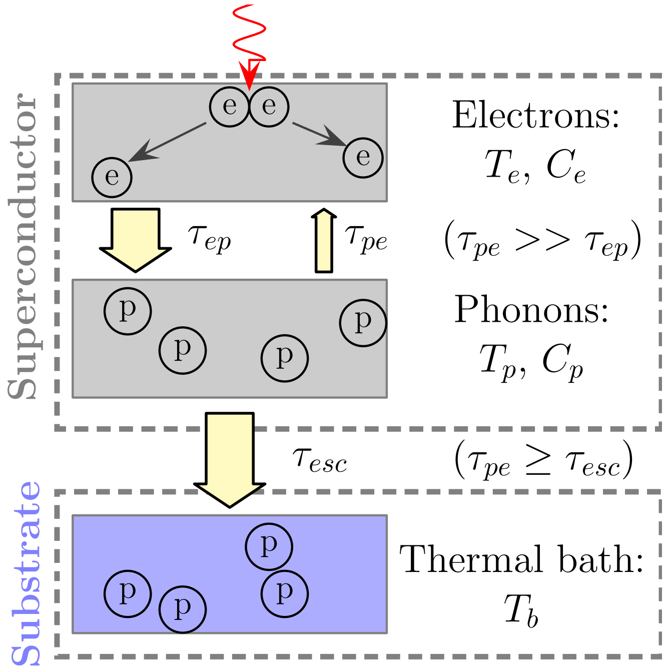

Figure 2.3.: Thermalization scheme of the 2-T model and energy transfer channels.

The thermal coupling scheme of a phonon-cooled HEB, where the diffusion cooling of electrons through the contact pads can be neglected, is depicted in Fig. 2.3. The interaction within the system can be described by time constants that refer to the time which a component needs to exchange its thermal energy with another component. τ_{ep} and τ_{ep} are the exchange times of thermal energy from electrons to phonons and from phonons to electrons, respectively. The escape time τ_{esc} is the time a phonon in the film needs to escape into the substrate. To enable the energy relaxation of the electrons via the substrate presenting the thermal bath the thermal energy transfer towards the thermal bath needs to be much faster than the transfer towards the upper subsystems. In equilibrium the phonon-electron relaxation time is given by[150]

$$\tau_{pe} = \tau_{ep} \frac{c_p}{c_e}, \tag{2.6}$$

where c_p and c_e are the specific heat capacity of the phonons and the electrons, respectively. The escape time of the phonons into the substrate is proportional to the thickness,

d, of the superconducting film and defined by

$$\tau_{esc} = \frac{4d}{\beta \cdot u}, \tag{2.7}$$

where u is the speed of sound and β is the acoustic phonon transmission coefficient. For NbN the speed of sound is about 4.7 km/s, the estimated electron-phonon interaction time in NbN films is 12 ps[71] and and the escape time determined for a 5 nm thick NbN film on Si is about 25.9 ps[157].

In the simplified approach where c_e is much larger than c_p in the low temperature limit the electron temperature relaxation time τ_Θ is given by[149]

$$\tau_\Theta = \tau_{ep} + \tau_{esc}\frac{c_e}{c_p}. \tag{2.8}$$

To obtain a larger bandwidth this overall thermal relaxation time constant needs to be minimized (see Eq. (2.5)). From Eq. 2.7 it is obvious that the reduction of the film thickness results into a shorter phonon escape time and a faster overall thermal relaxation. The film, however cannot be made arbitrarily thin since this leads to a large amount of defects.

2.3. DC characterization of HEBs

The HEB element, is a superconducting microbridge (S) which is connected on both ends with normal metal (N) contacts. Its DC properties thus mainly corresponds to the properties of a superconductor, namely the intrinsic critical temperature T_c of the superconducting material, and the critical current density J_c.

Below its critical temperature the superconductor enters the superconducting phase. This means that the DC resistance steeply drops to zero below T_c as schematically sketched in Figure 2.4 (a). In this superconducting state the resulting potential difference at the ends of a superconducting wire would be zero. This DC current however cannot take arbitrarily magnitude as is sketched in Fig. 2.4 (b). Increasing the DC current above a certain value which is called the critical current I_c causes a sudden change of the IV curve in form of a measurable voltage as it induces the phase transition of the wire into the normal state. After passing this phase transition the current is a linear function of the voltage. Reducing the current again the material reverts to the superconducting state at a current value I_h which is smaller than I_c. This is because of the power dissipation raising the temperature of the superconductor above its critical temperature. Only when

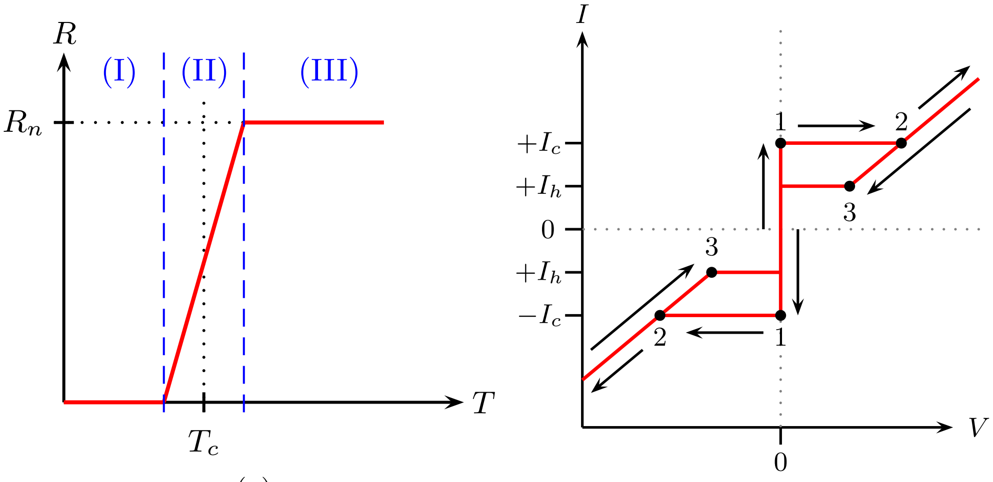

(a)

(b)

Figure 2.4.: Schematic RT and IV curve of a superconducting bridge. The DC resistance R_n of a superconductor in its normal state (III) drops down to zero below a critical temperature T_c in the superconducting state (I) after a phase transition (II). Above a critical current I_c the superconducting state (1) breaks down and the superconductor switchs over to the normal conducting state (2). Reducing the bias current again ((2)→(3)) the IV curve is a hysteresis where the superconducting state occurs at a current value I_h smaller than I_c.

the dissipation power and thus the DC current through the wire is sufficiently small the superconductor can jump back to its superconducting state. The critical current as well as I_h strongly depend on the operating temperature of the superconductor (see Fig. 7.22 in Chapter 7 . If the operating temperature approaches the critical temperature T_c the hysteresis-behavior of the IV curve vanishes. For the DC-characterization of an actual HEB-device from its IV-curve measured at 4.2 K the critical current refers to the maximum DC-current value close to the bias voltage around zero from which a sudden voltage jump to a point with higher bias voltage and lower bias current can be observed. Due to series resistance contributed by normal-conducting lines the I_c usually does not occur at exactly zero bias voltage as can be seen from the measurement results in Chapter 7.

The development of former HEB receivers in the Institute of Physics I clearly showed that each single mixing element needs to be characterized separately, since even if two HEB microbridges are from the same batch their electromagnetic properties deviate from each other. For each superconducting bridge there needs to be a RT-measurement to determine the critical temperature, the temperature width ΔT_c of the phase transition and the resistance R_{max}, which is the maximum value for the resistance in the normal state just before the transition into the superconducting state (see picture 2.4). R_{max} is needed to match the RF circuit to the HEB bridge. Where the normal resistance equals the RF impedance [95]. The smaller the width ΔT_c of the phase transition the higher the sensitivity of the bolometer. [140] An IV measurement of the HEB bridge in the superconducting state yields the critical current and including the bridge dimensions the critical current density.

According to Shcherbatenko et al. [153], Vercruyssen et al. [176], and Boogaard et al. [11] there is evidence that a further intrinsic property of the NSN device can be stemmed from the RT curves. They report about a contact resistance in NSN devices occurring as an effect of the transition of the current from the normal conducting into the superconducting phase. An investigation concerning this resistance was carried out by Shcherbatenko et al. [153] based on six HEB elements. Their results point to a charge-conversion process at the NS interfaces as the most likely source for the measured resistance. Given this interpretation the charge-conversion allows to estimate the coherence length of the superconducting bridge.

2.4. Detection principle

2.4.1. Direct detection

An HEB, being a bolometer, can be used for the direct detection of the incoming radiation. To that effect the superconducting bridge is operated at its critical temperature, carrying a small DC bias current. At this bias point the voltage responsivity (Eq. (2.3)) is at its maximum. Operating it as a power detector it integrates over the incoming spectral radiation power. To gain frequency-dependent information about the RF direct response of the HEB-devices of this work, they are used as direct power detectors of a Fourier Transform Spectrometer (see Chap. 7.2). To limit the spectrum of the incoming radiation a heat IR-filter is used to shield the devices from radiation above the desired measurement bandwidth.

2.4.2. Heterodyne detection

A heterodyne mixer, converts the RF-signal to be observed down to a few GHz by means of a reference signal that is called the local oscillator (LO). The signal that is converted to lower frequencies and thus is called intermediate frequency (IF) signal then can be amplified with low noise amplifiers and processed with well-established spectrometers. The reference signal with high output power of several µW is at a fixed frequency (ideally phase-locked) very close (about 1 GHz shift) to the operating frequency of the receiver. Reference signal and RF-signal typically are combined by a beam-splitter and simultaneously forwarded through the antenna to the mixing element, in this case the HEB. In contrast to classical mixers (like Schottky diodes or SIS junctions) where the LO signal and the RF signal are multiplied by a highly non linear IV-characteristic, the HEB is a power detector mixer. The sum of the RF and the reference voltage signals is effectively being squared in the power detector, such that the overall dissipated power in the mixer with resistance R is given by

$$P = \frac{1}{R}\left(V_{RF} \cdot \cos(\omega_{RF} \cdot t) + V_{LO} \cdot \cos(\omega_{LO} \cdot t)\right)^2 , \tag{2.9}$$

where the index RF and LO of the voltage amplitudes V and the angular frequencies, ω, refer to the RF signal to be observed and the LO reference signal, respectively. The equation can be rearranged by means of trigonometric identities to

$$P = \frac{1}{R}\left(\frac{V_{RF}^2 + V_{LO}^2}{2} + \frac{V_{LO}^2 \cos(2\omega_{LO} t)}{2} + \frac{V_{RF}^2 \cos(2\omega_{RF} t)}{2}\right) \tag{2.10}$$

$$+ \frac{1}{R}\left(V_{LO} V_{RF}\left[\cos([\omega_{LO} - \omega_{RF}]\, t) - \cos([\omega_{LO} + \omega_{RF}]\, t)\right]\right) \tag{2.11}$$

For the HEB the thermal time constant (Eq. (2.4)) is of the order of a few 10^{th} of pico seconds. Accordingly, the temperature of the electron gas cannot change with the high frequencies, and the power in the high frequency signals causes only an increase in the average temperature of the bolometer. The frequency-varying part of the equation is given by the difference in the angular frequencies $\pm(\omega_{LO} - \omega_{RF})$. The generated IF voltage signal thus is proportional to

$$V_{IF} \propto V_{LO} V_{RF}\left(\cos(|\omega_{LO} - \omega_{RF}|\, t)\right), \tag{2.12}$$

where $\omega_{LO} - \omega_{RF}$ is called the lower sideband, and $\omega_{LO} + \omega_{RF}$ is the upper side band of the mixer.

2.5. Mixer characteristics

Although for this work no performance characteristics could be measured as the LO source is still in the development process, for completeness, some basic parameters are briefly introduced in the following. It is important to distinguish between both terms, the receiver and the mixer. The term receiver includes all parts, like amplifier and other electronic components of the receiver system. Speaking about the mixer means the actual detector module.

The sensitivity of a receiver is determined by the noise of its different components and on the fundamental quantum noise limit. The output power of receiver system for an input signal with power P_{in} is determined by the gain G_i and the input noise P_i of the individual component by

$$P_{rec} = P_{in} \cdot G_1 G_2 \cdots G_n + P_1 G_2 \cdots G_n \tag{2.13}$$

The first gain component $G_1 = G_{mix}$ in case of the HEB-receiver is the mixer conversion gain that consists of the overall antenna efficiency times the HEB conversion efficiency. The mixer performance is characterized by G_{mix} through the output IF power P_{IF} by

$$G_{mix} = \frac{P_{IF}}{P_{in}}. \tag{2.14}$$

The gain components with higher index relate to the back-end electronic components after the signal passes the HEB-mixer.

The equivalent noise temperature of the receiver is given by

$$T_{rec} = T_1 + \frac{T_2}{G_1} + \frac{T_3}{G_1 G_2} + \cdots + \frac{T_n}{G_1 G_2 \cdots G_n}, \tag{2.15}$$

where T_i is the equivalent noise temperature in the noise power in a bandwidth B

$$T_i = \frac{P_i}{k_B B}, \tag{2.16}$$

with the the Boltzmann constant k_B. The equivalent noise temperature $T_1 = T_{mix}$ refers to the mixer noise temperature, and T2 to that of the first (cryogenic) amplifier.

The sources of noise in a HEB mixer are Johnson noise, T_J, fluctuation noise T_{FL}, and quantum noise, T_Q[94]. The Johnson noise (thermal noise) is generated by the thermal movement of the electrons in the HEB. The fluctuation noise is based on fluctuations in the electron temperature due to random energy exchange with the reservoir. The quantum noise is an unavoidable contribution which appears for mixers due to vacuum fluctuations in the input signal [1] and is the fundamental lower limit of the noise which is also present should all other noise contributions vanish. It is given by $T_Q = \frac{h\nu}{k_B}$. A typical mixer noise temperature that could be obtained with the NbN HEB mixers of the UpGreat receiver for 4.7 THz is about 430 K with a conversion gain of -5.9 dB[17].

---

[1] fluctuation-dissipation theorem

3. RF design

The following chapter deals with the different RF-circuit designs and their implementation into the underlying RF-receiver concept. It is organized as follows:

1. First, the choice of the underlying RF concept is explained in context to alternative implementations.
2. Secondly, a short overview of the RF-components used for the RF-circuits is given.
3. The restricting boundary conditions for the impedance match at the bolometer-antenna interface are outlined.
4. The last block engages with the actual THz receiver designs, including the lens and the RF-chip. In total, five variations of a narrow-band circuit design for 10.7 THz, one narrow-band circuit RF-design for 4.7 THz as well as four versions of different broadband spiral antennas for 10.7 THz and 4.7 THz are presented, respectively. In the conclusion at the end of the chapter the broadband RF-designs and the 4.7 THz narrow-band design are compared with each other.

At this point, it should be noted that this chapter presents broadband as well as narrow-band antenna designs for 4.7 THz and 10.7 THz although the focus of this work is the design of a receiver for a narrow transition line at 10.7 THz, where a large broadband capacity for the antenna is not necessitated for most observational purposes. A receiver supporting high directivity to increase the receiver gain advices the use of antennas providing particularly high directivity as can be found among resonant, narrow-band antennas. The design of such antennas at very high frequencies, however, is a delicate matter due to several reasons which are addressed in more detail in the according design chapter. Among others this includes that the standard design rules and calculation basis for the antennas from the GHz range lose their validity at higher frequencies. Consequently, scaling of functioning design concepts fails and needs to be replaced by other approaches. At the same time, the numerically calculation due to the high operating frequency and simultaneously comparatively large objects is extremely costly in terms of time and computational resources. Secondly, the limitations and tolerances due to fabrication constraints in the dimensions of the RF-structure and HEB mixing elements as well as in the uncertainties in the materials properties make it very difficult to conceive a design which is tolerant against a multitude of parameters which can affect the performance of the antenna. The prediction of the performance of such narrow-band heterodyne receivers therefore remains to a certain extent uncertain. Another important aspect which needs to be considered is that the LO source required for a 10.7 THz heterodyne receiver likewise first needs to be designed and manufactured as no such QCL LO does exist to date. It is uncertain if the development of the receiver and the development of the LO can be finalized to the same time. The 4.7 THz designs further enable a comparison of the quasi-optical receiver scheme chosen for this work with the waveguide receiver scheme of the upGREAT receiver[17] developed in our research group . Based on the above considerations, the RF-design does not only include narrow-band circuits but also circuits with broadband spiral antennas around 10.7 THz and around 4.7 THz where a LO source is already available.

3.1. RF-receiver concept

3.1.1. Why an antenna?

Thinking of a mixer layout intended for very weak signal detection it is particularly important to reduce and avoid sources of losses and noises. Given that at 10.7 THz we have no superconducting material for circuits available, the Au conduction lines should be as short as possible and planar printed circuit boards on chips should be composed of as few elements as possible. A well-known problem occurs when using planar antennas. Due to imperfections in the interface an additional parasitic resistance of the antenna contacts to the HEB bridge is added to the system. Thus a legitimate question is if an antenna is actually necessary and can be omitted to directly eliminate this source of loss. Indeed, there is one HEB mixer from [54] with an open structure layout where an extended hemispherical lens directly focuses the signal on the HEB bridge without an additional antenna. This HEB mixer is for frequencies in the range of 20 to 40 THz and uses a NbN bridge of 30 × 20 µm with 5 nm thickness and a critical transition temperature of 9.4 K. The optimal absorbed LO power at a LO frequency of 10.6 µm in [54] is estimated to about 16 µW. The numbers for the critical temperature and the thickness of the bridge are in good agreement with numbers which are provided by the in-house fabricated NbN

---

[0] The receiver has been developed to observe one of the most important cooling lines of the interstellar medium, a fine structure transition line of atomic oxygen [OI] at the rest frequency of 4.745 THz [17]

HEB mixers of the institute for 4.7 THz [16]. Following the diffraction limited ratio of the bridge dimensions given in [54], the bridge dimensions for the center wavelength λ_0 is about $3 \cdot \lambda_0 \times 2 \cdot \lambda_0$. For the wavelength of interest of this thesis this corresponds to a surface size of about $90 \times 60\,\mu\text{m}^2$. Assuming that the optimal LO power absorbed by the HEB is linearly proportional to the volume of the HEB bridge this leads to a LO power of about $3 \times 3 \times 16\,\mu\text{W} = 144\,\mu\text{W}$ required for the mixing element excluding any loss accounts based on the beam path and optical elements in the setup. The only Quantum Cascade laser (QCL) development so far that covers an operating wavelength about 28 µm reports on a peak output power of 0.1 mW [128] and thus is not sufficient for the operation of an HEB mixer without integrated antenna structures. Even when going close to the diffraction limit by choosing a bridge size of $60 \times 35\,\mu\text{m}^2$ the LO power needed for the HEB bridge still is about 56 µW. A rough estimation of all losses just before the lens of an open structure mixer is about $1 - 2$ dB. This corresponds to an output power of $70.5 - 88.8\,\mu\text{W}$ of the LO. Considering additional losses due to the lens of at least 1 dB, the power requirement needed to operate the mixer cannot be obtained just as in the previous assessment before. To conclude, there is strong evidence that the state-of-the-art QCLs of the current status of research are not sufficient yet for the operation of NbN HEB mixers without integrated antennas at the desired operating frequency.

3.1.2. Quasi-optical approach: Integrated lens-antenna

In the mid- to far-IR range there are two common methods to couple the THz radiation into the receiver. The first relies on a waveguide horn while the second uses a lens directly attached to or in the close vicinity of a planar antenna. In the waveguide horn approach the RF-circuit is deposited on a thin membrane that is placed in a hollow metallic waveguide of rectangular cross section which ends into the horn (schematically illustrated in Fig.3.1(b)). As the membrane itself can operate as a dielectric waveguide it needs to be considerably thinner than the operating wavelength to prevent not tolerable signal-losses due to coupling into substrate modes. Mode coupling is possible as soon as the phase velocity of a substrate mode becomes larger than that of the deposited transmission line which is indicated by dropping below a critical frequency f_c that is dependent on the membrane thickness and the individual substrate mode. Figure 3.1 depicts the critical frequencies of the first TM and TE modes to be expected for the transmission lines used in this work [1] that has been estimated based on the formalism provided by [31]. According

---

[1] coplanar waveguides on a silicon substrate

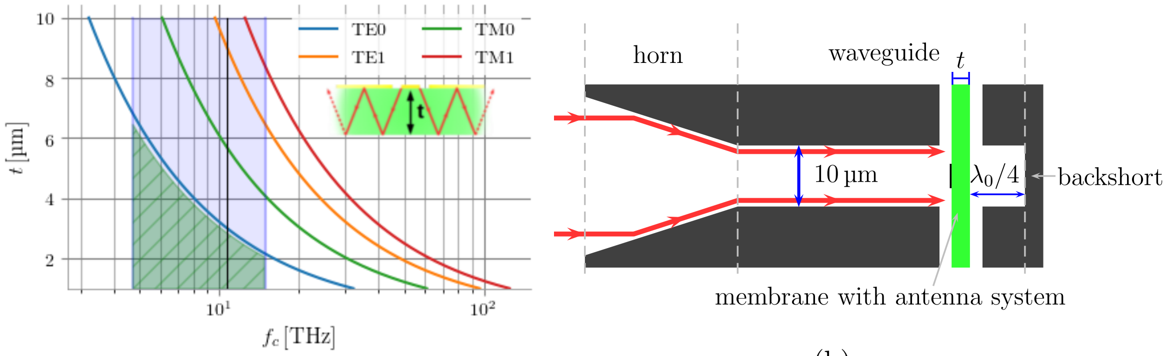

(a)

(b)

Figure 3.1.: (a) Critical frequencies f_c for the coupling of the Coplanar Waveguide mode with different TE and TM substrate modes in dependence of the thickness, t, of a silicon substrate. (b) Schematic of a waveguide-horn approach of a receiver.

to these results a silicon membrane used in the intended frequency range of this work (highlighted area in Fig.3.1) preferably needs to be thinner than 2 µm to avoid mode coupling. There is the real risk that such a thin RF chip easily breaks[2] and/or provides too little thermal conduction to ensure a sufficient cooling capacity which is mandatory for the mixing process. Membranes of the required size further are questionable to procure as not belonging to the standard provided by common companies and the expense factor for a suitable horn which needs to be an one-off production due to the non-standard frequency is considerably high. Based on these facts the quasi-optical approach using an integrated lens antenna as sketched in Fig.3.2 is the concept of choice for the 10.7 THz receiver. Attaching the membrane with the planar antenna directly to the backside of a lens avoids the problem of power loss from coupling into waveguide modes and provides mechanical stability as well as a good thermal coupling of the RF-chip to the heat bath. A lens further presents a suitable socket for the broadband-antenna test-structures of this work whose bandwidth exceeds that bandwidth of 2:1 which typically is realizable with a waveguide-horn approach[3]. A drawback of the lens-concept is the power loss suffered from reflections at the vacuum-lens interface which can get significant for lenses with a high dielectric constant. In case of using silicon as lens material up to 30 % of the incoming power can be reflected back in the worst case of normal incidence. This is

---

[2] Such a thin membrane suffers an enormous deflection when being cooled down in the waveguide and would need to be place on a super smoothed rest in the hollow waveguide with a roughness distinctly smaller than the membrane-thickness

[3] Restricting factors are the backshort that is only optimal for one frequency and the limits in the dimensions of the hollow waveguide to suppress unwanted power coupling into higher order modes

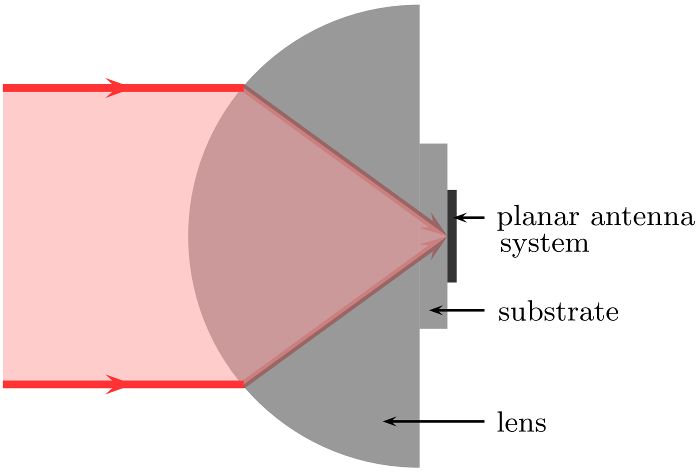

Figure 3.2.: Schematic of a quasi-optical receiver: The planar antenna system is deposited on a substrate which is directly attached to the backside of a lens.

tantamount with an increase of the noise temperature of about 30 % and would yield a respective higher integration time and thus less observation efficiency. To counter this effect a common method is to apply an anti-reflection (ar) layer on the lens surface. The optimal refractive index, n_{ar}, and thickness, t_{ar}, for a single-layer film for minimized reflection at perpendicular incidence of radiation is[91]

$$n_{ar} = \sqrt{n_{lens} \cdot n_{surround}} \tag{3.1}$$

and

$$t_{ar} = \frac{(2m+1) \cdot \lambda}{4 \cdot n_{ar}} \qquad , m = 0, 1, 2 \cdots , \tag{3.2}$$

respectively. Although the thickness of the layer theoretically can be any odd number of a quarter wavelength, one quarter wavelength is the convention with the goal to minimize potential power dissipation in the film. Based on its concept of enhancing the transmission by destructive interference the matching layer only works well within a bandwidth of roughly 10 %[87], which is fine for most of astronomical observations and sufficient for the narrow-band antenna designs of this work heading for a single operational frequency. For an expected refractive index of silicon about $n = 3.37$ at operating temperatures (see chapter 5) in vacuum the ideal respective index for an ar-film according to Eq.(3.1) is around about 1.836. Common used materials like SiO, Alumina-loaded epoxy, Zinc selenide (ZnSe) $(n = 2.257@21.7\,\mu\mathrm{m}[137])$, low-density polyethylene (LDPE), Mylar (a

BO-PET) or Kapton (a Polyimide) become to absorptive in the required frequency range or are difficult to apply [91] (see also Sec. 5.3). A suitable, albeit not ideal, material that successfully has been used [91, 87] as coating material for optics up to a few Terahertz is Parylene C, that belongs to a family of thermoplastic polymers made from para-xylylene. Its negligible outgassing behavior, only little transmissivity for moisture and little permeability for gases[163, 162] render it a popular coating material for optics with a high refractive index. However, there is only little information about its refractive index in the transition between mid to far-IR at room temperature and no details about n can be found at cryogenic temperatures. From two graphs from literature one may read off a real dielectric constant for Parylene C of about $\epsilon_r = 2.56$[110] at 10 THz which equals n=1.60 and a refractive index of about 1.56-1.63 [77] between 10 THz and 11 THz for an unspecified type of Parylene. Furthermore strong absorption bands has been reported at around 3.29 µm, 6.89 µm and 9.57 µm[77] and can be seen in Fouriertransform-IR spectra [103, 172] up to 22 µm. Upon request at some commercial companies, which offer coating with Parylene, the required, estimated film thickness between 4.3 µm to 4.6 µm was too thin for the round lens surface geometry to enbale a uniform *ar*-layer. Due to the imponderable factors of thickness tolerances and uncertainties of the refractive index a coating of the lenses is at first renounced with the consequence that the interference with the back-reflected power will cause a ripple pattern in the beam pattern[55]. However, ongoing development on vacuum deposition techniques and material research may lead to a practicable *ar* coating in the future. Moreover, for the present project, with a fractional bandwidth of only a few percent, a thick Parylene coating (m>0 in Eq. (3.2)) might suffice for the commissioned receiver.

3.2. Introduction of the RF-circuit elements

All different RF-circuits designed for this work are premised on planar antennas which are placed on a dielectric substrate (see Appx. B.2) and which are briefly introduced in the following sections. Fundamental antenna parameters needed for the description of the performance of antennas are not further discussed at this point. The definitions used in this work comply with the international standards, basically those of the International Electrotechnical Comission (IEC) and the IEEE Standard Definitions of Terms for Antennas [143]. A brief overview of the definitions of these parameters is given in the Appx. B.2. More detailed insight can be found in [4], [143] and [160].

3.2.1. Coplanar Waveguides at high frequencies

Coplanar waveguides which are often used at higher frequencies due to their relatively easy fabrication can leak power when applying them at higher frequencies. “High” in this case especially refers to a higher slot width to wavelength ratio. This power leakage does not only yield losses but concurrently leads to a reactive contribution of the characteristic impedance Z_c of the transmission line which needs to be carefully taken into account using CPWs in resonant systems.

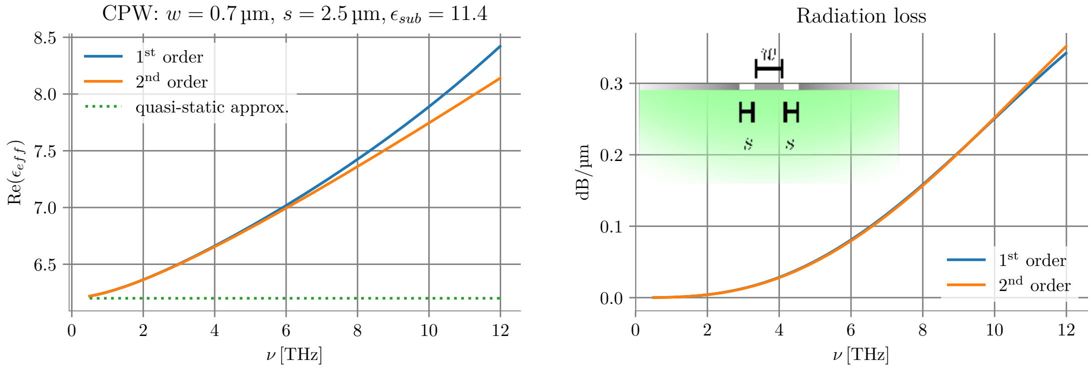

Figure 3.3.: Real part of the effective dielectric constant and radiation loss of an infinitely long CPW-line with slot width $s = 2.5\,\mu\mathrm{m}$ and a width of the inner conduction line of $w = 0.7\,\mu\mathrm{m}$. The CPW-line is placed on a infinitely large silicon substrate with substrate dielectric constant $\epsilon_{subs} = 11.4$. Both quantities are calculated based on the formalism described in the Appx. B.4.

The dominant mode of a slot line that is printed on an infinitely large dielectric substrate[4] has a phase velocity greater than the speed of light in the denser medium which leads to radiation into the substrate and thus to power leakage of the transmission line. As the conventional used definitions of the characteristic impedance become void the analytical expression for Z_c and the complex propagation constant $\gamma = k$ received by the conformal mapping method cannot be used any longer. A calculation procedure which is used instead is presented in the Appx. B.4 and is based on the solution ansatz described in [37, 56, 122, 123, 113, 55]. As dealing with higher frequencies and partly with a significantly larger ratio between the width of the CPW slot and the frequency of interest the procedure as applied in [56, 123] has been further enhanced in this work using higher order expansions of a convolution integral. The difference in the characteristics of a CPW line using the second order expansion of the formalism to the first order

---

[4] For THz receivers which are integrated with dielectric lenses the size of the dielectric lens in terms of wavelength is as large that it can be treated as an infinite dielectric for the planar wave circuits which are attached to the lens.

expansion used by [56, 123] is exemplary depicted in Fig. 3.3 on the real part of the effective dielectric constant and on the radiation loss. Figure. 3.4 gives an example of the characteristic impedance and the propagation constant of a CPW that is used for the RF-circuit designs in this work. The parameters are calculated by means of the second order approach described in the Appendix. The slot width of the CPW-line in this example is varied by ±0.1 µm to demonstrate how sensitive the characteristics of the CPW react to small changes in its dimensional sizes and to underline the importance to consider the changes in the characteristics occurring at higher frequencies.

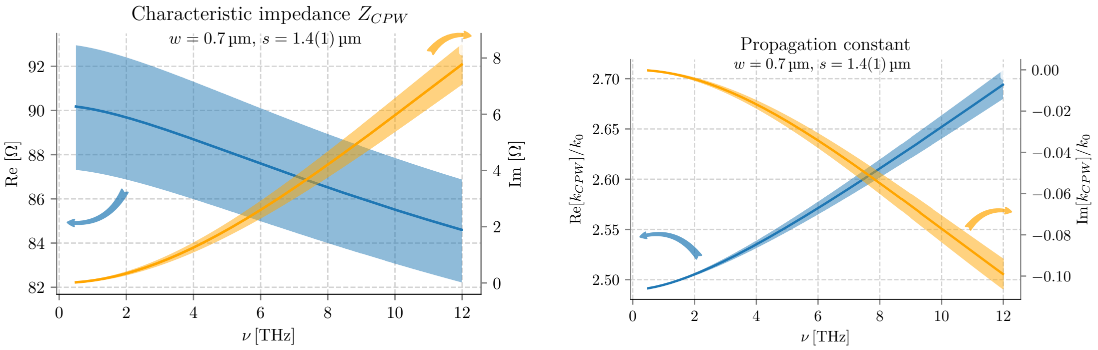

Figure 3.4.: Characterstic impedance and propagation constant calculated for a CPW consisting of a perfect conducting metal structure placed on a infinitely large silicon substrate of dielectric constant $\epsilon_{sub} = 11.4$. The inner width of the CPW is $w = 0.7\,\mu\mathrm{m}$. Both quantities of the CPW line have been calculated for three different slow width of the CPW $s = 1.3\,\mu\mathrm{m}, 1.4\,\mu\mathrm{m}, 1.5\,\mu\mathrm{m}$. It is marked in the legend of the plots as the middle value $\pm 0.1\,\mu\mathrm{m}$.

3.2.2. Narrow-band RF-circuits

The antenna used for the narrow-band RF-circuits of this work is a twin slot antenna that belongs to the resonant antennas (see Fig. 3.5). Twin antennas are especially suitable when looking for antenna configurations allowing for high directivity with a preferably low number of simple elements. Integrated in its center is the mixing element that needs to be DC-biased. Since the conduction lines for biasing and the readout of the IF-signal share the same metal-layer plane as the resonant antenna, a RF-choke is directly connected to the antenna. It blocks the high operating frequency and works as a low-pass filter for the IF and DC-signal. Antenna and RF-choke together form the entire RF-circuit as depicted in Fig. 3.5.

In an equivalent circuit model (see Fig. 3.6) similar to that proposed by [63] the antenna slots may be represented as two voltage generators in series with the antenna impedance

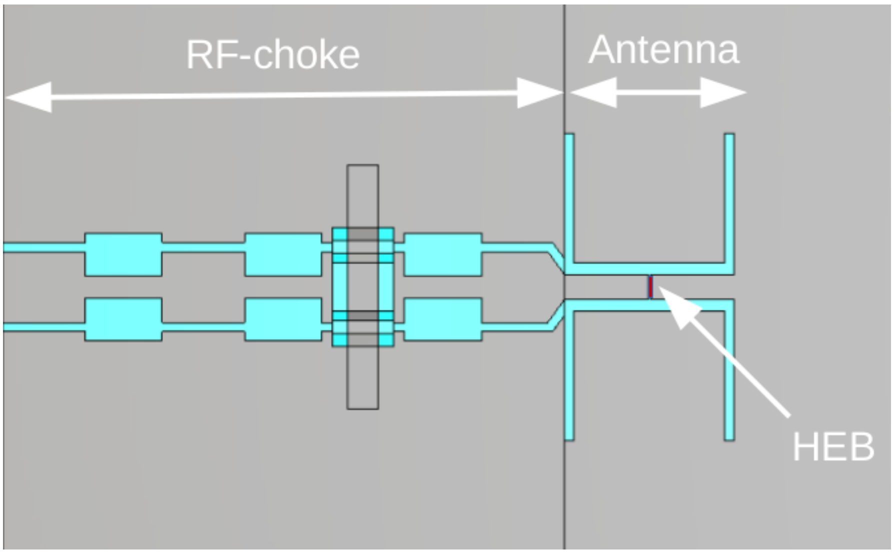

Figure 3.5.: Sketch of narrow-band RF-circuit: The RF-circuit consists of a double-slot antenna and an RF-filter that acts as a low-pass filter.

Z_{slot}. They are connected through the transmission lines of a certain characteristic impedance Z_c and of a certain length l to the HEB load with the impedance Z_{HEB}. The CPW-lines need to match the antenna impedance to the HEB-load that sits at the symmetric feeding point of the antenna. The impedance which is seen at the antenna feeding-point Z_{fp} is the HEB embedding impedance. In case that the influence of the connected RF-filter is negligible, it equals two times the slot antenna impedance after its transformation across the CPW-lines, which is given by

$$Z_{fp} = 2 \cdot Z_{emb,2} \tag{3.3}$$

$$= 2 \cdot Z_c \cdot \frac{Z_{slot} + Z_c \cdot \tanh \gamma \cdot l}{Z_c + Z_{slot} \cdot \tanh \gamma \cdot l}. \tag{3.4}$$

Equation (3.4) directly pinpoints to the fact, that the length of the connection lines determines the ratio between imaginary and real amount of the impedance at the terminal of the antenna. Certainly, as the transmission line is defined in the same plane as the antenna between the slots and cannot be infinitely small it naturally has an effect on the slot-antenna contour which cannot be prevented and is not included in this simplified representation. For the design of this work the connection lines are attempted to be kept small in comparison to the length of the antenna.

The RF-choke, that is a quarter-wavelength reflection filter for high frequencies, is directly connected to one of the slots of the antenna. It needs to block the RF-signal as

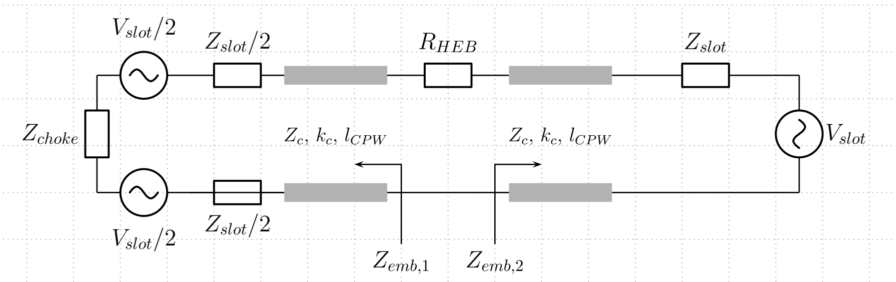

Figure 3.6.: Equivalent circuit model of the double slot antenna and RF-choke. The slots are represented as two voltage generators with the slot impedance Z_{slot}. They are connected with the HEB through CPW-lines which exhibit a characteristic impedance Z_c and wavenumber k_c and have a certain length l_{CPW}. The RF-filter impedance is in series with one of the antenna slots. The total embedding impedance Z_{fp} which is seen by the microbridge is given by the sum of

well as to present a short at the antenna interface to not disturb the antenna resonance by acting as a capacitive or inductive element and not to yield an asymmetric beam-pattern. The impedance of the filter Z_{choke} can bee seen in series with one voltage generator/antenna impedance. If it does not present a perfect short, the microbridge hence sees an impedance on one side that equals the filter and the slot impedance transformed by the CPW connection, $Z_{emb,1}$. The overall embedding impedance subsequently is given by the sum of both embedding impedances

$$Z_{fp} = Z_{emb,1} + Z_{emb,2}. \tag{3.5}$$

Double-slot antenna

The double-slot antenna is composed of two equivalent slots that are placed parallel to each other, as can be seen in Fig. 3.5. The distance to each other as well as the length of the slots varies depending on the external (e.g. coupling to a Gaussian beam in combination with a lens, suppression of coupling into certain substrate modes when placed on plane-parallel substrate membranes[144]) and internal (e.g. impedance matching to the mixing device at its feed point) boundary conditions. A brief introduction can be found in the Appx. B.5.1. The slots are fed symmetrically thus they are driven in phase to each other.

As each of the antenna designs described in this work consists of slot structures in a plane metallic ground plane, it should be mentioned that the finite dimensions of the ground plane is not taken into consideration. In point of fact, the radiation pattern of a slot antenna is a function of its ground plane geometry. Reflections of the E-field at the edges of the metal sheet results into undulations that are superimposed on the original pattern and modify the overall radiation pattern[42, 119]. The larger the dimensions of the plane, the more numerous are the waves but simultaneously their magnitudes decreases. As the metal sheet is very large in comparison to the wavelength of operation, the finite ground plane dimensions, however, can be neglected in this case.

Considering that the antennas are driven in phase, the physical distance between the slots determines the beam pattern including the beam width and directivity. That means that placing the slots too far away from each other results into a splitting of the main lobe into two equivalent side lobes. It should be noticed here that the lens has a crucial influence on the beam pattern and on the coupling behavior to the incoming radiation field that is explained in Sec. 3.4.2 and is not further discussed here. Connecting the two slots by transmission lines, that enables a symmetrical feeding of the two slots from one port, which in this work is terminated by the mixing HEB element, the electrical length of the transmission lines needs to be carefully chosen to match the impedance at both, the feeding points of the antenna and the HEB mixing device to not acting as a inductive or capacitive elongation.

RF-choke

The RF-choke behaves as a RF short circuit at the desired operating frequency and lets pass IF and DC signals. The RF-filter is a stepped-impedance low-pass filter and consists of quarter lambda pieces of CPWs with higher and lower characteristic impedances as schematically depicted in Fig. 3.5.

For an analytical approximation of the filter, the RF-choke is treated as a construct consisting of pieces of transmission lines which characteristic impedance and propagation constant have been determined by means of the high frequency approximation model earlier discussed in Sec.3.2.1. Any shunt capacities due to sudden jumps in the dimensions between adjacent CPW lines are neglected in the analytical design. The $50\,\Omega$ transmission line at the IF-output of the filter is represented by a $50\,\Omega$ load. Starting from the IF-output the input impedance Z_{in}^{i} after the i^{th} CPW element is

$$Z_{in}^{i} = Z_c^i \cdot \frac{Z_{in}^{i-1} + Z_c^i \cdot \tanh(\gamma \cdot l)}{Z_c^i + Z_{in}^{i-1} \cdot \tanh(\gamma \cdot l)}, \qquad \text{with} \quad Z_{in}^{0} = 50\,\Omega \tag{3.6}$$

3.2.3. Broadband antennas

The following sections give a short overview of the concepts of spiral antennas that are used in this work.

Logarithmic spiral antenna

The planar log-spiral antenna is one of the equiangular antennas whose shape can be entirely specified by angles[46]. Its performance essentially is non-dispersive in case of perfect conductance and an infinitely long antenna. It therefore is classified as a frequency independent antenna[146].

A plane, logarithmic spiral-curve can be defined in polar coordinates by $\rho(\phi) = k \cdot e^{a \cdot \phi}$, where a and k are positive constants. The tightness of winding can be specified by the angle Ψ between the radial vector $\rho(\phi)$ and the tangential of the spiral curvature at point $\rho(\phi)$ as depicted in Fig.3.7. For an infinitely continuing arm this angle specifies the whole spiral-curve and leads to its alternative name *equiangular spiral*[45, 46]. The constant a depicts the measure of the winding strength by $a = \frac{1}{\tan(\Psi)}$. The length of the spiral curve is given by the circumference of the spiral

$$L = \int_{\rho_{start}}^{\rho_{end}} \left[\rho^2 \left(\frac{\mathrm{d}\phi}{\mathrm{d}\rho} \right)^2 + 1 \right]^{\frac{1}{2}} \mathrm{d}\rho, \tag{3.7}$$

which can be shortened to

$$L = \sqrt{\frac{1}{a^2} + 1} \cdot (\rho_{start} - \rho_{end}). \tag{3.8}$$

The arm of a spiral antenna is defined as the area between two logarithmic spiral curves. The second edge is the identical image of the first edge but rotated by a fixed angle δ with respect to the first curve. The angle δ determines the filling factor or the metalization area of the arm.

A complete mathematical description of the logarithmic spiral antenna with two spiral arms correspondingly is given by the equations for all four conductor edges

$$r_1 = r_0 \cdot e^{a \cdot \phi} \tag{3.9}$$

$$r_2 = r_0 \cdot e^{a \cdot (\phi - \delta)} \tag{3.10}$$

$$r_3 = r_0 \cdot e^{a \cdot (\phi - \pi)} \tag{3.11}$$

$$r_4 = r_0 \cdot e^{a \cdot (\phi - \delta - \pi)} \tag{3.12}$$

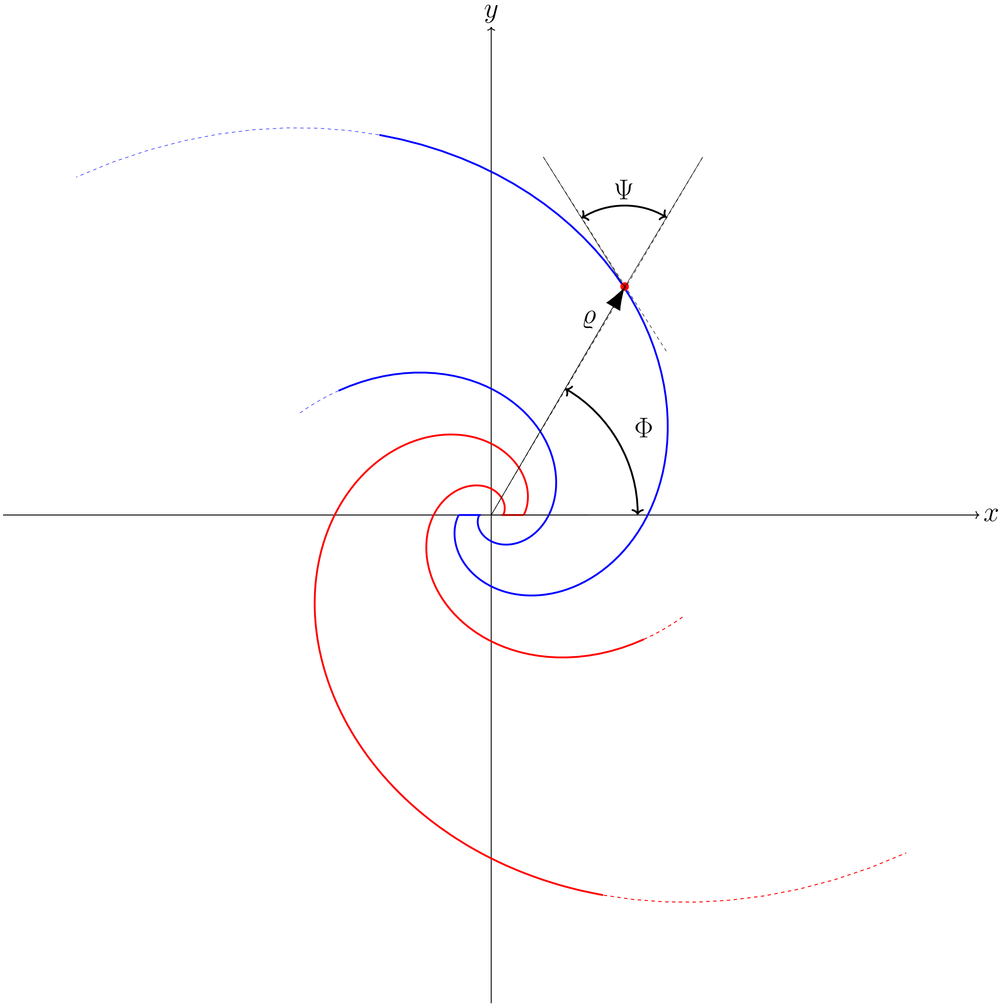

Figure 3.7.: Schematic of a logarithmic spiral antenna with two spiral arms

If $\delta = \frac{\pi}{2}$ the antenna has a self-complementary geometry.

The spiral antenna exhibits a broadside, bidirectional pattern with its maximum normal to the antenna plane [4]. The number of turns of the spiral arms influences the antenna pattern only insignificantly [46]. Typical values for the winding strength a are in between 0.2-0.4. If a gets large the spiral arms rotate only slowly and yields a radiation pattern which becomes similar to that of a dipole. A convenient selection criterion for the lower cutoff frequency of the antenna's bandwidth is the change in its polarization near the axis of its main lobe. If the wavelength becomes large compared to the total arm length of the antennas, the radiated field of the antenna changes from elliptically to linearly polarized. According to Balanis [4] the corresponding lower cutoff frequency is chosen as the frequency where the axial ratio of the polarization ellipse drops below 2 which is reported to typically occur when the overall arm-length is about one wavelength. Taking into account that ρ_{start} is considerably small compared to the maximum arm length, and that the effective wavelength of a spiral antenna placed on a substrate of dielectric constant ϵ_r may be estimated by $\lambda^{eff} = \lambda/\sqrt{\frac{\epsilon_r+1}{2}}$ this limit can be specified using Eq. (3.8) and is given by

$$\lambda_{max} = \frac{D}{2}\sqrt{\frac{\epsilon_r + 1}{2}} \cdot \sqrt{(1 + \frac{1}{a^2})}, \tag{3.13}$$

where D is the diameter of the smallest possible circle compassing the whole spiral curves, $D = 2\rho_{end}$.

Archimedean spiral antenna

The Archimedean spiral antenna is known to exhibit a broadband characteristic with a rather constant feed point impedance over its frequency bandwidth [26]. Therefore, it is sometimes classified as a frequency independent antenna[45] although it does not fulfill the theoretical requirements of scale-independence specified by [146].[5]

The chosen design contains two spiral arms as depicted in Fig. 3.8 which are specified by four analytical curves defining the rims of the arms. In polar coordinates these functions describe the radius of a spiral curve in dependence of three quantities: the winding angle Θ in radians, the radius change rate a and the inner radius of the spiral r_0. It is given by [171]

$$r_{in}(\Theta) = a \cdot \Theta + r_0. \tag{3.14}$$

The radius change rate $a = \frac{\Delta r}{2\pi}$ is the radius change for one turn of the spiral arm Δr per radian. The corresponding outer boundary of the arm is determined by the constant shift of the winding angle by an offset angle Θ_{off}:

$$r_{out} = a \cdot (\Theta + \Theta_{off}) + r_0. \tag{3.15}$$

A rotation of the first spiral arm by 180 ° gives the second spiral arm.

The total extent D of the Archimedean spiral is described by the outer radius after N

---

[5] Even if this classification is justifiable from an experimentally point of view, the Archimedean spiral does not show the necessary identical electrical behavior at different frequencies due to physical congruence of its surface when being scaled to another frequency[4, 146].

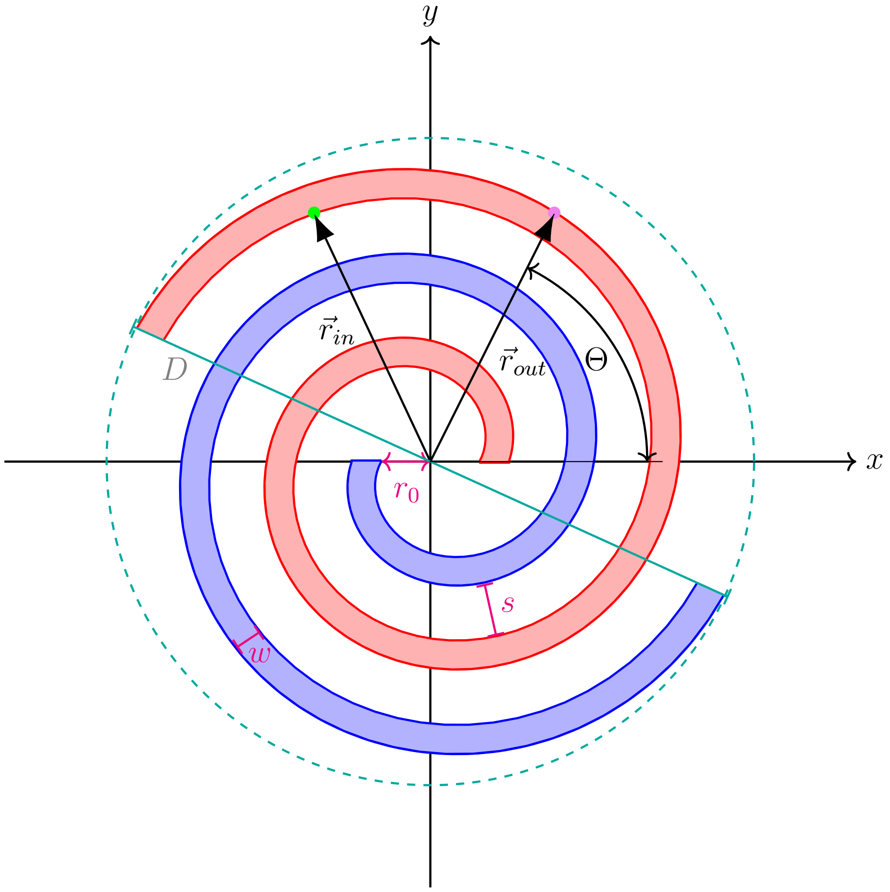

Figure 3.8.: Schematic of the Archimedean spiral antenna with two arms. The inner and outer spiral curve of each arm is defined via the analytical functions, r_{in} and r_{out}, in polar coordinates given in Eq. (3.14) and Eq. (3.15).

turns

$$D = 2 \cdot r_{out}(\Theta_{end}) = 2\pi N a + r_0. \tag{3.16}$$

In contrast to the logarithmic spiral antenna the width w of each spiral arm as well as the slot width s between the arms are constant. The width of an arm can be obtained by subtracting the inner and outer radius functions

$$w = |r_{out} - r_{in}| = \Theta_{off} a. \tag{3.17}$$

The slot width s is given by

$$s = \pi a - w. \tag{3.18}$$

The invariable width of the arm and the slot allow the definition of the metalization ratio X assigned by

$$X = \frac{w}{w+s}. \tag{3.19}$$

The length of the unwounded spiral arm $L(\Theta)$ can be found by integration over the initial and final winding angle Θ_{in} and Θ_{end}, respectively:

$$L(\Theta) = \int_{\Theta_{in}}^{\Theta_{end}} \sqrt{r^2 + a^2}\mathrm{d}\Theta \tag{3.20}$$

A common model to explain the radiation behavior of the Archimedean spiral is given by the band theory developed by Kaiser [93]. In this simplified model the radiation is thought to occur from a localized band on the spiral arms. The two spiral arms are approximated as a two-wire transmission line of negligible wire width whose spiral geometry enables its transformation into an antenna. For a typical straight two-wire transmission line with a wire-spacing much smaller than the wavelength the currents in the wires are 180 degree out of phase. Consequently, the corresponding radiation from both lines cancels each other. Wrapping of the two wires yields so called active regions, where the currents of adjacent arm parts are in phase to each other and their radiation contributions add up. For a tightly wrapped Archimedean spiral this happens where the circumference equals about one wavelength[93]. Following this principle radiation likewise occurs for higher-order active regions where the circumference equals odd multiple integer of lambda. However, as the power of the outward traveling wave is reduced after passing an active region, the contributions based on the higher-order regions typically are neglected.

Retaining the concept of active regions the lower and upper frequency, f_{low} and f_{high}, of the antenna band is determined by the outer and inner radius of the spiral antenna, respectively, by

$$f_{low} = \frac{c_{phase}}{2\pi r_{out}} \tag{3.21}$$

$$f_{high} = \frac{c_{phase}}{2\pi r_{in}}, \tag{3.22}$$

where c_{phase} is the phase velocity.

In practice the bandwidth is smaller than predicted by this theoretical limits. The actual lower cutoff is determined by the frequency where back reflections at the cut ends become negligible. The upper cutoff is given by the frequency from where the size of the feeding structure at the center of the antenna becomes insignificant and resembles a point like feed.

Although it is reported that the Archimedean antenna exhibits a higher loss compared to the logarithmic spiral antenna [4], it is the concept of choice for 10.7 THz as the Archimedean spiral geometry allows to design both, an input impedance at the antenna feed-point that matches the resistance of the HEB element and a footprint geometry that at the same time matches the dimension of the HEB element, respectively.

Frequency dependent input impedance at antenna base

For self-complementary antennas in their operational band the input impedance according to Babinet's principle [4, 146] is assumed to be $Z_{sc} = \frac{\eta_0}{2} \approx 188\,\Omega$ in free space, where $\eta_0 = \sqrt{\frac{\mu_0}{\epsilon_0}} \approx 376.7\,\Omega$ is the impedance of free space. Placed on a thick substrate with an electric permittivity, $\epsilon_{r,sub}$, whose width is large in comparison to the largest wavelength of the frequency band the input impedance of the antenna can be calculated from the effective dielectric constant using

$$\begin{aligned} Z_{sc}^2 &= \eta_{eff}^2/4, \text{ with} \\ \eta_{eff} &= \frac{\eta_0}{\sqrt{\epsilon_eff}}. \end{aligned} \tag{3.23}$$

The input impedance of both kinds of broadband antennas introduced in the previous two sections accordingly is reduced when placing them on a dielectric substrate dependent on the corresponding effective dielectric constant (as mentioned in Sec.B.2). Since this effective dielectric constant is frequency-dependent the resultant input impedance, as well is a function of frequency. It means that even an ideal, self-complementary logarithmic spiral antenna in free space loses its frequency-independent characteristic when being placed on a dielectric. The frequency dependency might be estimated resorting to the representation of both antenna types as two parallel striplines on a dielectric substrate that are separated by a narrow gap, and are called coplanar striplines. Retaining to the band theory[93] the Archimedean antenna consisting of two winded-up arms exhibits a field distribution similar to the propagating waveguide mode of striplines when driven in its balanced mode[25]. Based on this statement Chen et al. [25] derived an expression for the input impedance of the Archimedean antenna [6] The expression is proofed to be accurate up to frequencies of 20 to 40 GHz[24] and is used in this work with an effective dielectric constant modified for higher frequencies.

From the mid-infrared range an analogy between logarithmic spiral antennas and coplanar transmission lines has been justified for instance in the work of [60] recognizing that the conformal transformation from the w plane to the complex z plane ($z = \ln(w)$) of a self-complementary spiral yields into a coplanar strip line where the strip width equals the width of the center-slot of the spiral antenna [100]. A semi-empirical, frequency-dependent expression of the effective permittivity of a coplanar strip line with two parallel strips of same width w_{cps} with distance s_{cps} to each other has been derived by [82] and is given by

$$\sqrt{\epsilon_{eff,cps}(\nu)} = \sqrt{\epsilon_{qs}} + \frac{\sqrt{\epsilon_{r,sub}} - \sqrt{\epsilon_{qs}}}{1 + a\left[\frac{\nu}{\nu_{tc}}\right]^{-1.8}}, \tag{3.24}$$

where

$$\nu_{tc} = \frac{c_0}{4d\sqrt{\epsilon_{r,sub} - 1}}$$

is the cutoff frequency of the TE_1 mode, and d is the thickness of the substrate. The parameter a is empirically related to the geometry of the strip line by

$$\begin{aligned} \log(a) &\approx u \log(s_{cps}/w_{cps}) + g, \text{ with} \\ u &\approx 0.54 - 0.64q + 0.015q^2 \\ v &\approx 0.43 - 0.86q + 0.54q^2 q = \log(s/d) \end{aligned}$$

Equation(3.24) is used for both kinds of broadband antennas in this work to estimate the frequency-dependent effective dielectric constant and enables to qualitatively pinpoint to another important relationship between input impedance and dimensions of geometrical parameters. It is worth to notice that Eq. (3.24) converges to the quasi-static value for the low and to the substrate's dielectric constant for the high frequency limit as to be expected. In between both limits it is a non-linear, frequency-dispersive function whose curve is dependent on the parameters specifying the geometry of the lines. The qualitatively curve of ϵ_{eff} can be used to optimize the antenna's input impedance. Aiming e.g for an input impedance as constant as possible over a large frequency range the geometrical antenna

---

[6] The respective expression is deduced from a closed-form solution of the characteristic impedance of periodic coplanar waveguides (PCPW) by conformal mapping.

parameters accordingly should be chosen such that the effective electric permittivity is a maximum flat curve in the operational frequency bandwidth. Striving for a greatest possible input impedance, the curve should increase the least possible with frequency.

3.3. Matching between antenna and mixing element

The choice of the material used for the mixing element (approximately 5 nm thick NbN) and the silicon RF-circuit substrate results in RF-circuit dimensions which are at the limit of the resolution that can be achieved with fabrication. RF-structures which shall be manufactured with e-beam lithography need to meet certain dimensional requirements. For the required metal thickness of about around three times the skin depth at the operating frequency the typical distances between metal structures must not fall below is 0.5 µm. The silicon substrate used for the lens and the chip-wafer, roughly reduces any planar antenna dimension by a factor of $\sqrt{\frac{11.4+1}{2}} \approx 2.5$. That means that an antenna structure being of the size of the operational wavelength $\lambda_0 = 28\,\mu\text{m}$ shrinks to 11 µm. Hence, as being integrated within the chip the feed lines from the HEB mixing element consisting of the NbN microbridge to the antenna are limited in dimensions by the antenna size to not disturb the antenna geometry. Consequently, the width w and length l of the microbridge are limited by the antenna design and by fabrication limitations. Firstly, its length should not fall below 100 nm to 120 nm due to the resolution of the E-beam lithography, and secondly, its width cannot be larger than the width of its contact pads w_{cp} that is determined by the antenna design. Using a phonon-cooled HEB bridge the thickness of the film additionally needs to be as thin as possible. The target size for a NbN film is about 5 nm, which is the smallest possible thickness to obtain a uniformly thick and smooth film producible with the resources of our laboratory. The sheet resistance $R_\square$ that could be achieved for the NbN-bolometers of comparable thicknesses t in the upGREAT receiver[17] is about 1200 Ω/sq. The resistance of a microbridge made of thinnest possible NbN layer thickness thus is determined by its width and length, more specifically by its aspect ratio. It is given by

$$R_{\text{HEB}} = \rho \cdot \frac{l}{A} = \rho \cdot \frac{l}{t \cdot w} = R_\square \cdot \frac{l}{w}, \tag{3.25}$$

where A the surface perpendicular to the current flow. Since the aspect ratio of the bolometer bridge cannot be chosen arbitrarily the resistance of the mixing element which can be achieved is restricted to a certain range. The minimum the resistance of the bolometer is given by the maximum achievable width of the bolometer, $w_{max} = w_{cp}$:

$$R_{\mathrm{HEB}}^{min}(w_{max}) \geq R_{\min} \tag{3.26}$$

Ideally, the impedance of the HEB should match the footprint impedance Z_{fp} of the antenna. To enable a reasonable power transfer at the feedpoint of the antenna to the HEB element the design criterion is that the reflected amount of power shall not exceed $-12\,\mathrm{dB}$ which corresponds to a reflection coefficient $\Gamma \leq 0.25$ in amplitude. Thus the upper limit which the resistance of the HEB shall not exceed is given by $R_{HEB}^{up} = \frac{(1+\Gamma)}{1-\Gamma} \cdot Z_{fp} = 1.67 \cdot Z_{fp}$.

3.4. RF-designs of 10.7 THz and 4.7 THz mixers

This section presents the designed RF-circuits of 10.7 THz and 4.7 THz mixers and their implementation into the RF-chips and introduces the lens used for the quasi-optical receiver.

3.4.1. Introduction of lens and RF-chip outline

Extended hemispherical silicon lens

In total, two lenses of same dimensions have been ordered from the company *SUMIPRO Optical solutions*[159]. They are depicted in Fig. 3.9(a). Both lenses are extended hemispherical silicon lenses with a length-to-radius ratio of 0.328, a radius of $r_{lens} = 0.5\,\mathrm{mm}$, and an extension length of $L_{ext} = 0.164\,\mathrm{mm}$ as depicted in Fig. 3.9(b).

For reasons of cost only one type of lens can be ordered. To nevertheless maintain the opportunity of modifying the effect of the lens on the beam pattern of the antenna, different lens types can be synthesized by adding a cylindrical extension to the flat backside of the lens. It is the thickness of the silicon membrane of the RF-chip that works as an additional extension of the cylindrical length. This way, by choosing different membrane thicknesses for the RF chip it is possible to change the length-to-radius ratio within the range which is expected to be favorable. For a single unit antenna it has been reported that a high Gaussian-coupling efficiency around about 50% to 60% can be achieved within $L_{ext}/r_{lens} = 0.32$ to 0.35 [52] with moderate high f-numbers.[7] The thickest Si-membrane within this optimum range is thinner than 12 µm and thus lies in the range of available and processable membrane-sizes at our micro-fabrication facility. If needed for later test purposes the chosen lens geometry additionally allows to approach

---

[7] The receiver of this work shall be integrated in setups with Gaussian beam-optics with moderately high f-numbers (10-25).

the properties of an elliptical lens. A synthesized elliptical lens (see also Appendix B.1) can be attained using a cylindrical extension length about $L_{ext}^{ell} = \frac{r_{lens}}{n_{lens}-1} = 210.4\,\mu m$ [52] and requires a 46 µm thick membrane which is a feasible option. The thickness of the actual RF-chip membrane is 9 µm which corresponds to a ratio of $L_{ext}/r_{lens} = 0.342$. The respective extension length synthesize a shape closer to the hyperhemispherical lens which is preferable to reduce the reflection losses within the lens (see also Appendix B.1), especially as the lens will be used without a matching cap-layer on the lens surface. As has been demonstrated in [52] the reflection losses within an integrated elliptical lens-antenna can easily exceed the 1.55dB which is expected from simple transmission-line theory.

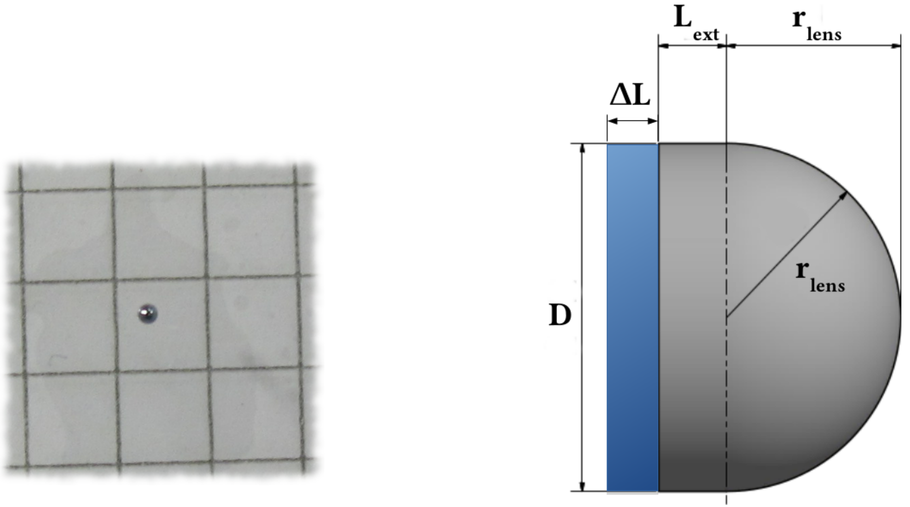

(a) (b)

Figure 3.9.: (a) Picture of the ordered silicon lens on a checkered paper; (b) Sketch of the extended hemispherical lens. Varying the length L_{ext} of the cylindrical extension the optical properties change and for example can be adapted to synthesize an elliptical or hyper-hemispherical lens. The dimensions of the ordered lenses are $L_{ext} = 164\,\mu m$ and $D = 1\,mm$. The membrane-thickness of the RF-chip, ΔL, which needs to be added to the fixed extension length of the ordered lenses, is used to obtain the desired extension length.

RF-chip outline

The RF-chip which is directly attached to the flat backside of the lens needs to provide a suitable embedding of the RF-structures into the IF-circuit, allowing to DC-bias the HEB mixing elements and transmit the IF-signal. The RF-chips developed for this work consist of circular 9 µm thick silicon membranes of 1.4 mm diameter as shown in Fig.3.10. Beamleads made of around about 1.65 µm thick gold that sticks out at the rim of the membrane are used to enable a good connection to ground via the detector housing that is made of copper. The RF-circuit of the respective design is placed on the membrane such that the antenna with the bolometer is located at its center. A large 50 Ω-CPW line for the IF-signal starting at the rim of the membrane is tapered into direction of the center. The different broadband and narrowband RF-circuits are adapted to this tapered end marked by the red ring in Fig. 3.10.

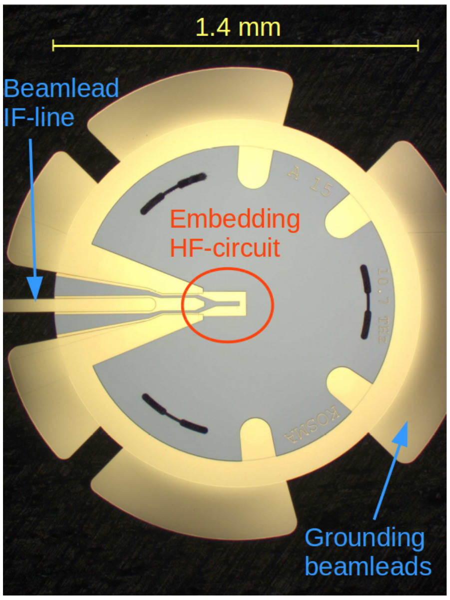

Figure 3.10.: Fabricated RF-chip: The chip consists of a 9 µm thick circle-shaped HRFZ Si membrane with gold structures on it. The RF-circuits are embedded to the IF-line at the center of the circle indicated by the red circle. This sample contains only structures defined by UV-lithography, the RF-circuit part is left blank.

- The embedding of the broadband designs into the 50 Ω-CPW happens via the IF-portal marked in the bottom picture in Fig.3.11. The four sketches on top show the individual connection to the inner line of the IF-CPW for each broadband design, respectively: Antenna *S1* directly grades into the inner CPW. Antenna *S2* and *S4* are first connected to a 1 µm thick gold line and subsequently are gradually tapered to the IF-line. *S3* is directly connected to the tapered inner line of the IF-CPW.
- The narrow-band RF-circuit designs with double-slot antennas are integrated into the IF-circuit through a long 50 Ω-CPW line that on its one end is connected to the RF-choke and on its other end widens into the large IF-output CPW-connection of the RF-chip as schematically depicted in Fig.3.12. Its length is chosen such that the antenna of each individual RF-design is in the center point of the RF-chip.

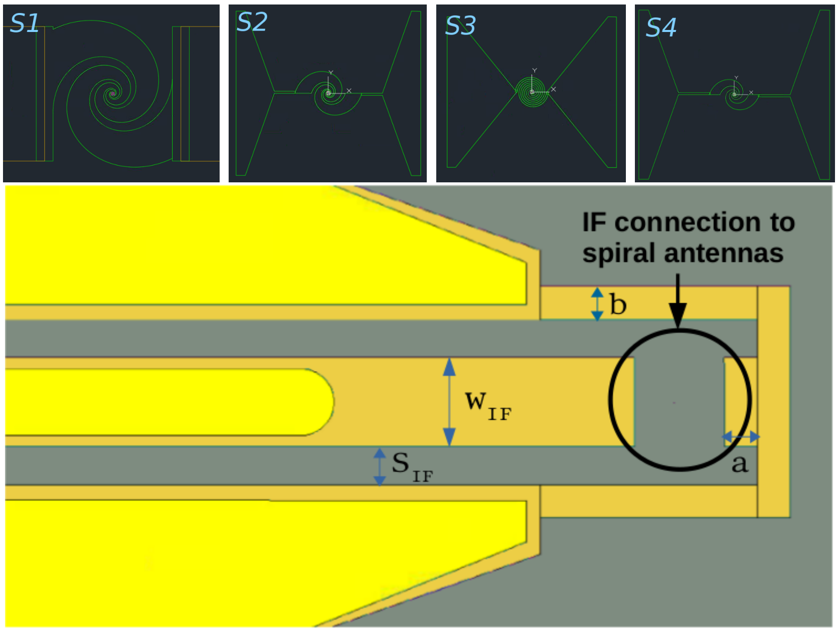

Figure 3.11.: Embedding structure into the IF circuit for the broadband antennas: The spiral antennas are incorporated to the inner line of the CPW of the IF-circuit. The terminals the antennas are connected to are marked by the black circle in the sketch. The width of the inner transmission line and the slot width of the CPW are $w_{IF} = 80\,\mu\mathrm{m}$ and $s_{IF} = 34\,\mu\mathrm{m}$, respectively. The remaining parameters are $a = 34\,\mu\mathrm{m}$ and $b = 30\,\mu\mathrm{m}$. The CPW consists of gold layers, illustrated as yellow tinged surfaces in the picture. Silicon is colored in gray. All broadband antenna versions from *S1* to *S4* with according transitional lines to the IF-terminals are depicted on top of the embedding circuit.

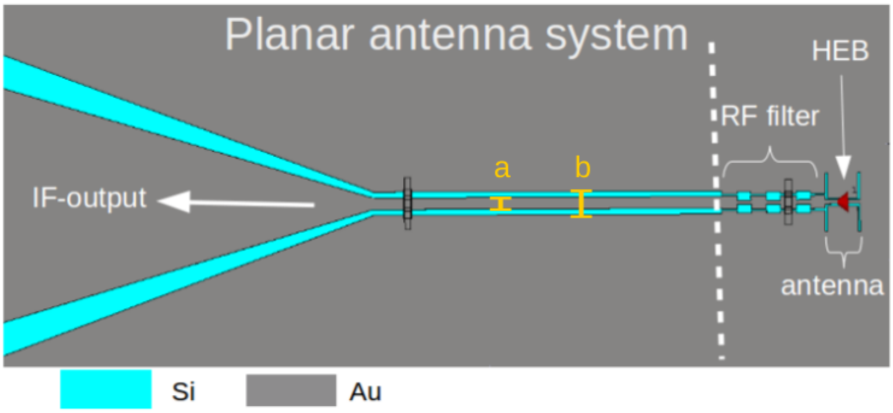

Figure 3.12.: Schematic of the RF-circuit of double-slot antennas with connection to the IF-CPW transmission line. The same schematic is used for the 10.7 THz and the 4.7 THz DS designs. $a = 2\,\mu\mathrm{m}$ and $b = 4\,\mu\mathrm{m}$.

3.4.2. Design and simulation of narrow-band RF-circuits

The antenna and RF-filter used for the narrow-band RF-circuit designs have been introduced in Sec. 3.2.2. Both components, antenna and RF-choke, undergo a separate design and optimization process before being put together. One double-slot antenna with RF-choke has been developed for 4.7 THz. For the operating frequency of 10.7 THz there are, in total, five variations of a double-slot antenna. They are all attached to the same RF-filter version that has been designed for 10.7 THz.

When designing planar circuits for receiver applications it is common to scale parts of existing, working circuits to the desired frequency range, due to the linearity of Maxwell's equations. At this point it should be mentioned that the double-slot antenna has not been designed according to the standard design parameters that are used for low frequencies [52]. This design method yields increasing down-shifts of the calculated resonance frequencies for frequencies approaching, and exceeding 1 THz. Significant deviations of the center frequency of a receiver up to 30 to 40 % [61], [55], [57] have been reported for RF-circuits relying on low frequency models. A new physical design concept introduced in 2005 by Focardi[55] among other aspects considers the changes which are expected in the charactersitics of the CPWs due to radiation effects at higher frequencies [123, 122]. All narrowband RF-circuits of this work are attempted to likewise consider the change in the CPW charactersitics for high frequencies.

Design of RF choke

The principle of the RF choke has been introduced in Sec. 3.2.2. It is composed of 7 high and low impedance coplanar waveguide (CPW) sections. The inductive and capacitive sections were chosen according to the selection criteria briefly carried out in the Appx.B.5.2. Their geometrical parameters are summarized in Tab. 3.1. The filter has a bridge over the third filter-element (counted from the antenna side of the filter) in order to suppress the degenerate odd CPW mode (the slot line mode (CSL mode)). The bridge-substrate consists of a 350 nm thick and about 1.4 µm wide SiO_2 layer with a 1 µm wide gold bridge on top of it. To account for potential conductive or inductive contributions at the antenna-filter interface, there are versions of the RF-choke where the last filter-element is additionally shorted or elongated by 300 nm.

The input impedance of the filter, assuming a 50 Ω-load at one end of the filter, is calculated based on Eq. (3.7). The characteristic impedance and the propagation constant of the CPW sections have been estimated by the high-frequency approximation of second order. They were calculated once for the chosen geometrical parameters, and secondly, for the largest deviations from the nominal values which are to be expected due to the fabrication tolerances. Fig. 3.13 shows the respective results, using the nominal length

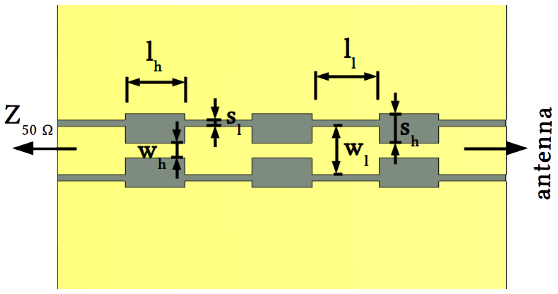

w_h [µm]	s_h [µm]	l_h [µm]	w_l [µm]	s_l [µm]	l_l [µm]
0.7	1.5	2.4	2.3	0.3	2.7

Table 3.1.: Dimensions of the high and low impedance CPWs of the RF-filter. The geometrical parameters belong to the width of the inner conduction line, the slot width and the length of the respective filter-element as depicted in the graphic above the Table.

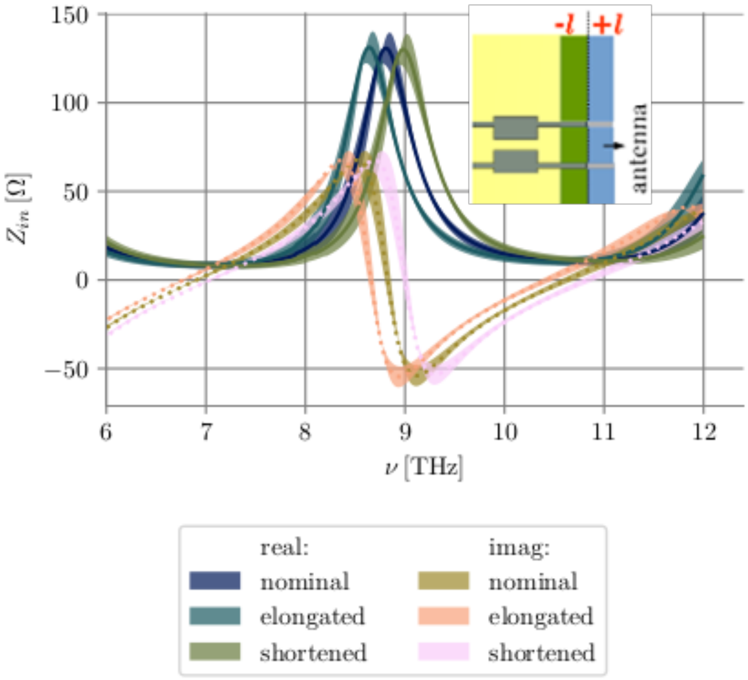

Figure 3.13.: Input impedance of the RF-choke at the antenna-interface to be expected within the fabrication tolerances. The input impedance is given for the nominal length of the filter and once with the last element being shortened and elongated by $\Delta l = \pm 300\,\mathrm{nm}$, respectively.

of the filter and once shortening and elongating the last filter element by $\Delta l = \pm 300\,\mathrm{nm}$. Thereby the phase is tuned to shift the zero-crossing of the imaginary part by about around ±200 GHz.

The final S-parameters simulated with the time domain solver in CST for the nominal dimensions of the RF-filter are represented in Fig. 3.14. The simulation overall encompasses 8 waveguide modes. The S21 parameters of all unwanted waveguide modes are below −20 dB. In particular, the quasi TEM CSL mode is successfully suppressed below the −30 dB limit and thus is not included in the figure.

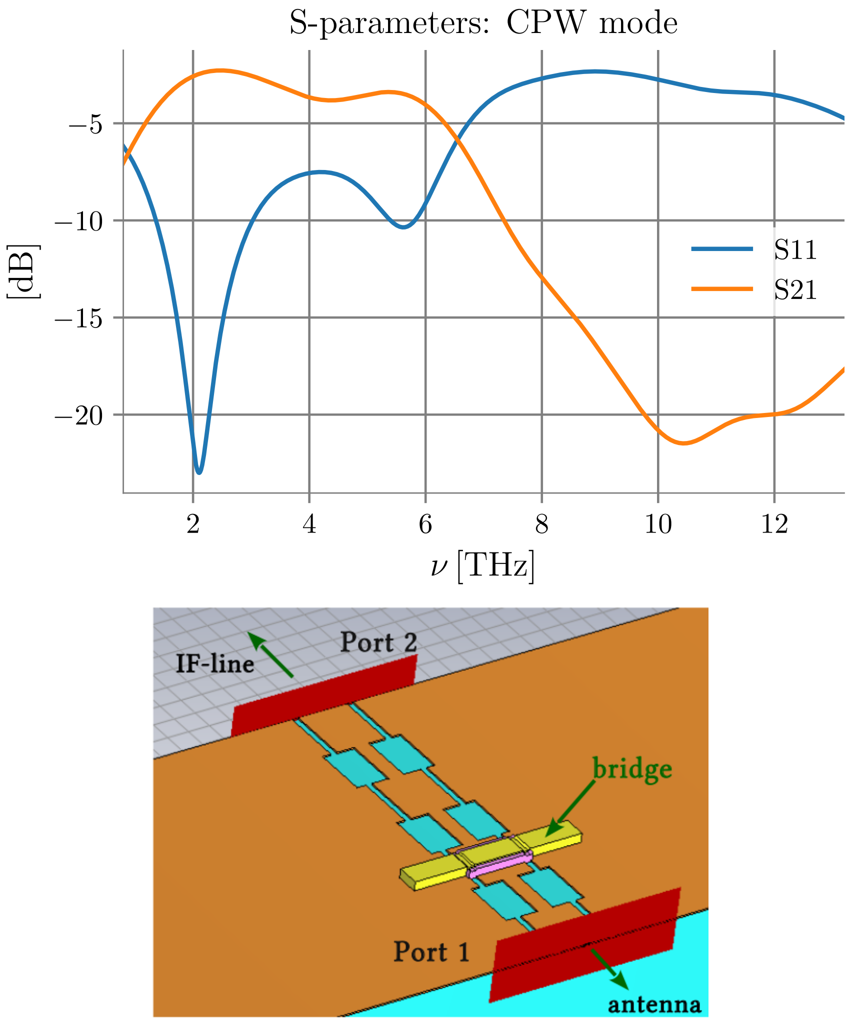

Figure 3.14.: S-parameters of the RF-choke for 10.7 THz simulated with the time domain solver in CST assuming a gold metal layer and an underlying silicon substrate with a dielectric constant of 11.4. Port 1 refers to the port of the RF-choke that is directly attached to the antenna, port 2 refers to the end of the filter that is connected to the IF-line as illustrated in the graphic below the plots.

Design of double-slot antennas

Five different designs of a double-slot antenna at 10.7 THz and one double-slot antenna at 4.7 THz have been chosen for the final optical mask. All of them are based on antenna slots of about a full effective wavelength in length. The bolometer in the antenna's center is connected to the slots by CPW-lines. For the purpose of achieving only little disturbance of the antenna geometry by the attached transmission lines, the CPWs in all designs are kept as narrow as possible within the fabrication constraints with a width constituting less than 20 % of the length of the antenna slots. The bolometer bridge connected to the CPW cannot be wider than the inner conduction line of the respective CPW. In order to allow an acceptable power transfer to the mixing element the power reflection at the antenna-HEB interface is aimed to not exceed -12 dB for all designs.

10.7 THz double-slot antenna designs:

In total five antenna versions for 10.7 THz have been designed based on the following three considerations:

1. The variations in the designs shall enable to investigate which distance between the two antenna slots emerged to be favorable for a good Gaussian beam coupling.
2. There exist a couple of factors which are able to shift the resonances of the antennas, but only can be predicted within a certain range (such as material characteristics or fabrication tolerances). The high operational frequency in conjunction with the high dielectric constant of the carrier substrate make it impossible to develop a design that is sufficiently tolerant towards all of the possible practical variations in the design parameters. Consequently, some of the antenna variations are used to anticipate potential deviations from the design parameters.
3. One safety-format of a double-slot antenna has been chosen, which according to simulations, does not exhibit a notably low power reflection, but based on the previous results of fabrication processes, has dimensions that definitely can be manufactured with high accuracy.

The impedance curves of all five designs that have been simulated with the time domain solver of CST studio suite (excluding the attached RF-filter) are depicted in Fig. 3.15. For the above-mentioned reasons the antenna resonances are located around 10.7 THz to cover a safety margin where the maximum of the resistance is spread around the frequency of operation. The respective input impedances at the antenna feeding point of the five designs ranges from about 80 Ω to 110 Ω.

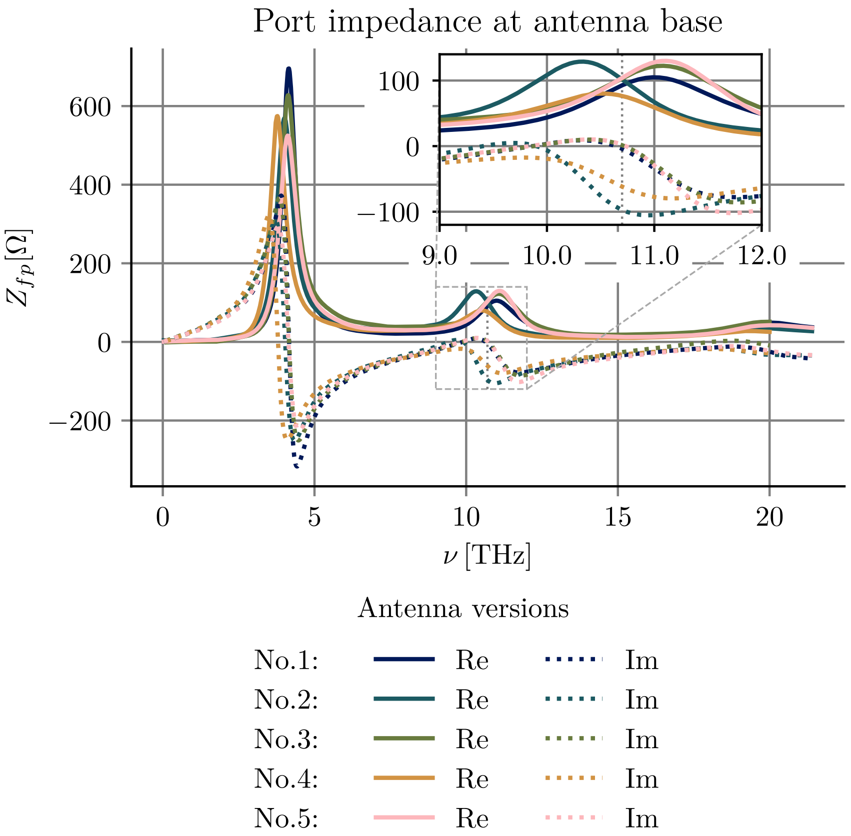

Figure 3.15.: Simulated port impedance at the HEB-antenna interface of five different double-slot antenna designs. The corresponding design parameters for each design are listed in Tab. 3.2.

For the sake of clarity, the power reflection at the antenna-HEB interface is exemplary depicted for antenna design no. 5 in Fig. 3.16, and has been calculated for the highest and lowest resistance values for the bolometer bridge which are believed to be achievable with the present NbN material (see Sec.3.3). The orange line in the plot represents the best possible impedance match assuming that the HEB resistance equals the real part of the feeding point impedance at the antenna base. It can be seen that the optimum in power coupling for this design can vary as much as 600 GHz within the span of plausible HEB resistances.

The parameters of all five designs are summarized in Tab.3.2. The numbers in parenthesis indicate the assumed maximum possible deviation in the dimensions of the fabricated

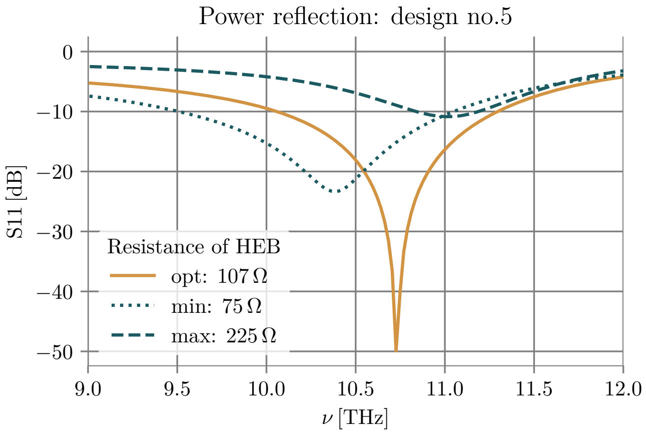

Figure 3.16.: Calculated power reflection for double-slot antenna design no.5 for the expected maximally and minimally achievable resistances of the bolometer bridge and for the optimum HEB resistance.

structures from their nominal values and refer to the last digits. The variations in the geometrical parameters are chosen as follows:

- First of all, the distance between the twin slots is varied from 5.6 µm, which correspond to about a quarter of the effective wavelength λ_{eff} according to simple static approximations with ϵ_{Si}^{4K}, to 5.0 µm. By reducing the distance between both slots an increase in the directivity of the antenna is to be expected.

- Secondly, the width of the antenna slots is varied. A more narrow slot yields a sharper resonance and a higher feedpoint impedance at the antenna-HEB interface which facilitates a good impedance matching with the resistance of the bolometer bridge.

- Thirdly, two different CPW versions are used as connection lines between antenna slots and bolometer to enable the use of different widths and lengths of the bolometer bridge.

Besides the accuracy in the dimensions of the different antenna designs, there are three additional aspects that affect the antenna performance, namely, the resistivity of the gold layer all structures are made of, the dielectric constant of the underlying silicon substrate and the attached RF-filter.

The resistivity of the thin gold-layer needs to be estimated preliminary based on measured DC resistances of dedicated test structures (long lines and squares). After fabrication of a batch devices, the DC resistivity of the gold layer is estimated again

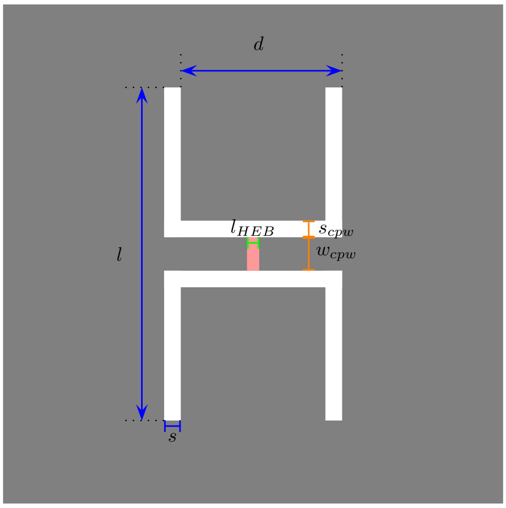

no.	d[µm]	l[µm]	s[µm]	w_{cpw}[µm]	s_{cpw}[µm]
1	5.6	9.0(1)	0.30(2)	0.80(4)	0.30(3)
2	5.2	10.3(1)	0.30(2)	0.80(4)	0.30(3)
3	5.0	10.0(1)	0.50(0)	1.00(1)	0.50(1)
4	5.0	10.2(1)	0.40(2)	1.00(1)	0.50(1)
5	5.0	9.9(1)	0.30(2)	0.80(4)	0.30(3)

Table 3.2.: Design parameters for the chosen mask versions. The length of the HEB l_{HEB} varies between 120 nm to 150 nm. The numbers in parenthesis indicate the deviation in the dimensions of the fabricated structures from their nominal values and refer to the last digits.

using the measured DC-resistivity of gold test structures present for every fabricated batch (see Sec. 7.1.3). The dielectric constant of the silicon substrate, also at cryogenic temperatures, has been estimated based on the measurements described in chapter 5 and in [9]. Two examples of how both aspects can affect the antenna performance are given in the Appx. B.5.1. The influence of the filter on the impedance curve at the antenna base is shown in Fig.3.17(a) for the antenna design no.1. The respective power reflection at the antenna-HEB interface is given in Fig.3.17(b).

The RF-filter attached to the antenna slots yields a couple of additional possibilities of the antenna-filter system to resonate at lower frequencies than 10.7 THz, where, for example, either the left or the right slot form a resonating system with the directly attached CPW-lines. This is to be expected as the RF-choke is designed to present a short-circuit for around the operating frequency, which does not extend over the whole frequency range.

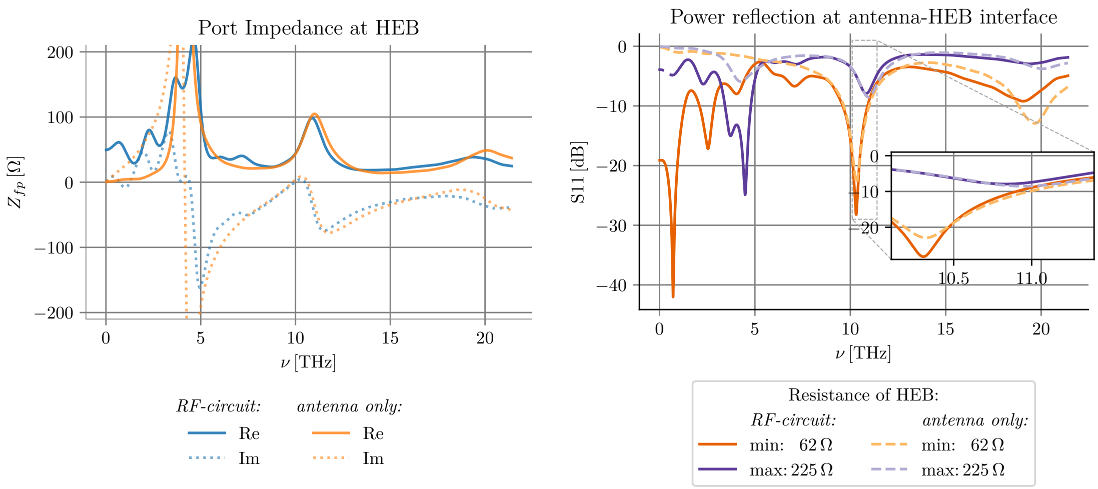

(a)

(b)

Figure 3.17.: Influence of the RF-choke on the feeding point impedance of a double-slot antenna (a) and the S11 parameters (b) for different loads at the terminal base of the antenna. The curves refer to the double-slot antenna design no.1

The influence of the distance between the slots of the antenna on the main beam of the DS antenna is approximated by calculating the far-fields for design no.1, no.2 and no.4 with the SRT based software described in Chap. 4. As has been discussed in the Optics chapter the corresponding level of the side-lobes is a subject of uncertainty, the results obtained with the software are believed to give a reasonable feedback about the variances in the width of the main beam with different distances between the slots. The spectral E-fields in k-space of the respective DS antennas are fed into the software as source fields. They have been obtained via an FFT of the E-fields at the interface between antenna and silicon surface from simulation results obtained by means of the CST software by simulating a large substrate background using a thick silicon membrane instead of the lens. The absolute magnitudes of the fields in the kx-ky plane are shown in Fig. 3.18. As can already be seen from the spectral E-fields the different distances between the slots and different lengths of the slots result in a compression and stretching of circle-shaped contour lines. From (a) to (c) the distance between the slots is decreasing from 5.6 µm to 5 µm leading to an elliptically shaped E-field spot. Based on the spectral E-fields it is to be expected that the most symmetrical beams are obtained for design no.2 and design no.1 (Fig. 3.18(a) and (b)).

The SRT software runs with a resolution of 200 000 rays over a solid angle from $0° \leq \Theta \leq 24°$,$0° \leq \Phi \leq 360°$ ($d\Phi = d\Theta = 0.21°$), with an $OR_{max} = 2$, for in total

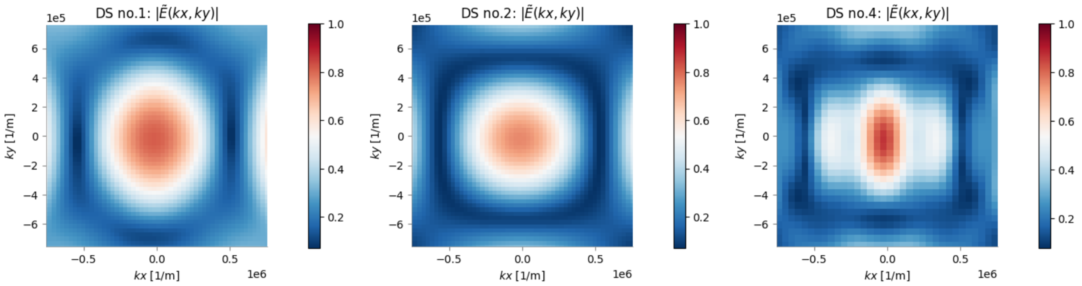

(a) (b) (c)

Figure 3.18.: Spectral E-field in k-space for different DS antenna designs at 10.7 THz

1600 observation points that are distributed on a spherical surface with its center at the origin of the center of the DS-antenna. The spherical surface has a distance about 6.327 mm($\approx$ 226 $\times$ λ_0) to the curved surface of the lens. The results for the E-field amplitude and phase along the x-direction (the dedicated polarization direction of the DS-antennas) are depicted for two sectional planes at azimuthal angles $\Phi = 0°$ and $\Phi = 90°$. The cross-polarization for all calculated E-fields is below -52 dB and can be neglected. The E-field patterns according to the software results are rather similar. A slight asymmetry of the main beam and the side-lobes is visible for antenna design no.5 as to be expected from the spectral source fields in Fig. 3.18. The high side-lobes are not taken into consideration for the reasons already discussed in Sec. 4. The -9 dB beam diameters are 3.1°, 3.2° and 3.3° for design no.1, no.2 and no. 4, respectively. The here observed differences can be neglected. The phase is acceptably flat within the main beam for all three designs which is important for a high power coupling with a Gaussian like LO beam.

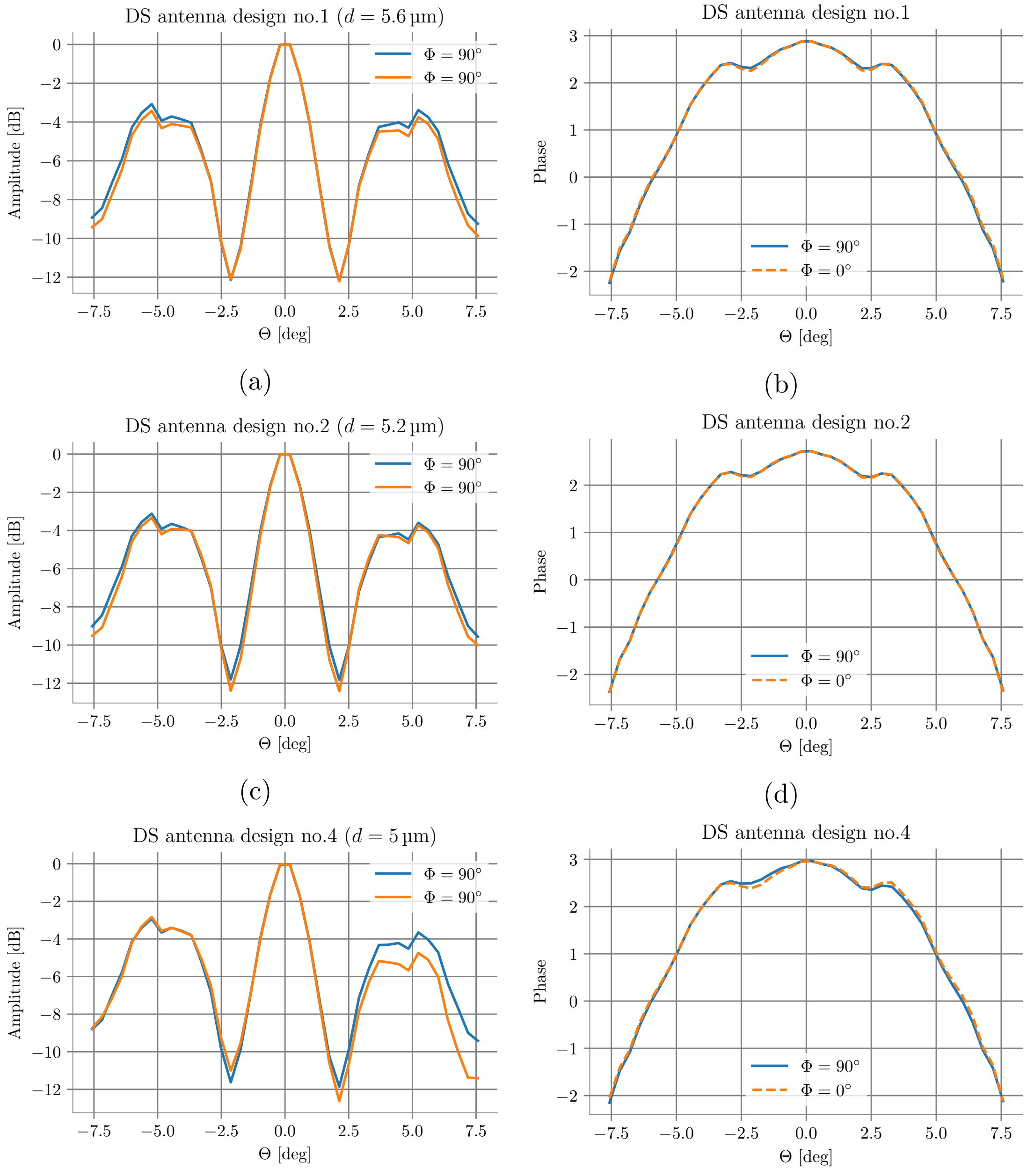
DS antenna design no.1 ($d = 5.6\,\mu$m)

DS antenna design no.1

DS antenna design no.2 ($d = 5.2\,\mu$m)

DS antenna design no.2

DS antenna design no.4 ($d = 5\,\mu$m)

DS antenna design no.4

(a) (b)

(c) (d)

(e) (f)

Figure 3.19.: Magnitude and phase of the co-polarized E-field (polarization along the x-direction, main beam direction along the optical axis (z-axis). The results have been calculated with the SRT software (see Sec. 4))

4.7 THz double-slot antenna design:

The geometrical parameters of the RF-choke and the double slot antenna can be found in Tab.3.3. The bridge dimensions are identical with those used for the 10.7 THz design. The simulated input impedance at the HEB-interface is depicted in Fig.3.20. As shown in Fig. 3.21 the RF-design exhibits a reasonable impedance matching at the HEB-antenna interface within expectation range of achievable resistances for the NbN microbridge. The mode coupling to the slot-line mode, as depicted in Fig. 3.21(b), as well as to other Hybrid, TM or TE modes is successfully suppressed and is below −20 dB.

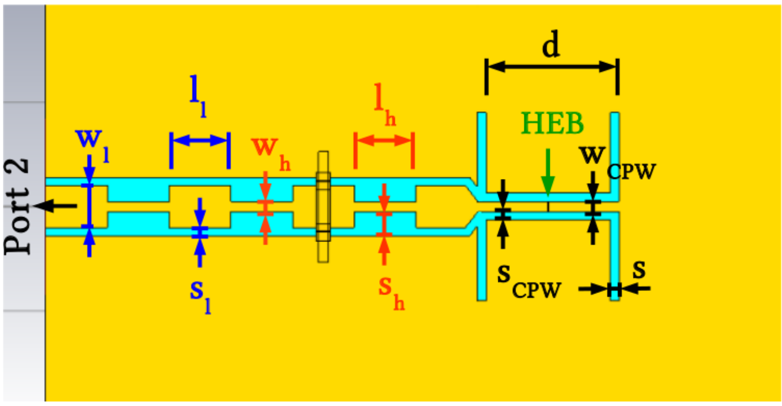

antenna					filter			
l	s	d	w_{CPW}	s_{CPW}	w_{high}	s_{high}	w_{low}	s_{low}
[µm]	[µm]	[µm]	[µm]	[µm]	[µm]	[µm]	[µm]	
18	0.8	12.7	1	0.8	1	2.3	4	0.8

Table 3.3.: Geometrical parameters of the 4.7 THz narrow-band antenna design.

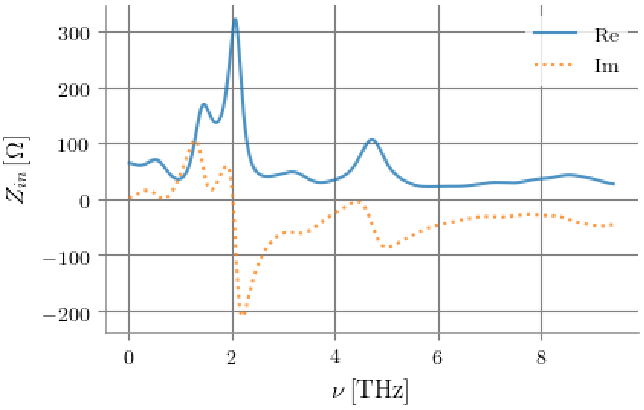

Figure 3.20.: Simulated input impedance at the HEB-antenna interface of the 4.7 THz design.

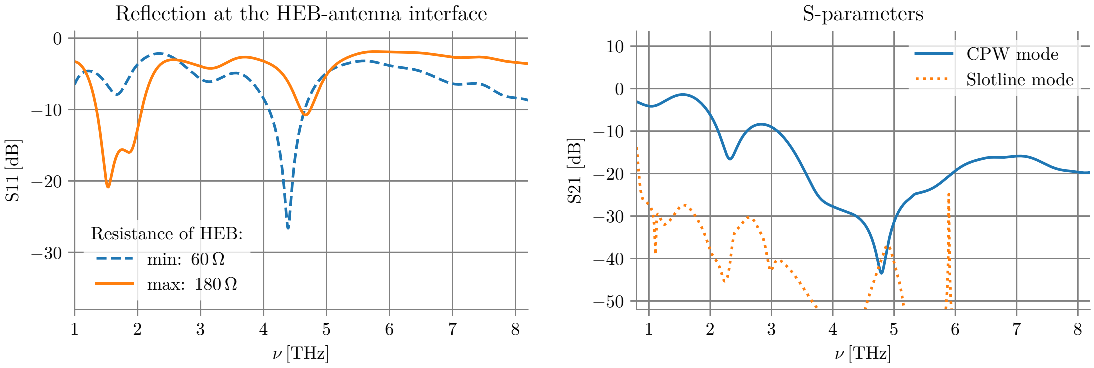

(a) (b)

Figure 3.21.: Simulated S-parameters for the 4.7 THz narrow-band antenna design. Port 1 refers to the port at the HEB-antenna interface, port 2 refers to a waveguide port that is directly attached to the end of the RF-choke filter as depicted in the upper sketch of Tab. 3.3. (a) Calculated power reflection at the HEB-antenna interface for the maximum and minimum resistance of the HEB element that is expected to be achievable based on the aspect ratio and the expectation values for the sheet resitance of NbN (see Sec.3.3). (b) S21-parameters for both quasi TEM modes, the CPW mode and the slotline mode. The filter successfully suppresses the slotline mode over the whole frequency range and reflects the CPW mode around its operating frequency (−30 dB).

3.4.3. Design and simulation of broadband antennas

The broadband antennas are designed to target two different frequencies, one around 4.7 THz, and one enclosing 10.7 THz. If possible the operational bandwidth contains both frequencies. To allow an acceptable power transfer at the HEB-antenna interface a power reflection less than -9 dB is aimed at. A lower reflection would be desirable but could not be achieved within the constraints of the HEB layer resistivity, the minimum dimensions achievable by fabrication and the restrictions in the dimensions of the contact area to the bolometer. I use a logarithmic spiral antenna design for the lower operating frequency range. To achieve an acceptable impedance matching to the HEB element at 10.7 THz I needed to switch over to a design with an Archimedean spiral antenna. Within their frequency bandwidths both broadband antennas exhibit an elliptical polarization close to a circular one that evolves into linear polarization passing their limits of their bands. The higher cutoff frequency of the antenna bandwidths is defined through this change in polarization which is determined by the feed configuration. The lower frequency limit is dependent on the length of the spiral arms and their terminations.

The following sections introduce the spiral designs chosen for the first fabrication mask. In total, there are three different spiral antennas, a logarithmic spiral antenna, a self-complementary logarithmic spiral antenna and an Archimedean spiral antenna, which are numbered consecutively from *S1* to *S4*. Spiral antenna *S1* and *S2* are identical except for their connection to the IF CPW line. They are optimized for a frequency around 4.7 THz. The Archimedean spiral antenna $S3$, optimized for around 10.7 THz, is the only spiral antenna that covers the operating frequency within its bandwidth with a safety margin such that it is expected to meet the operating frequency in any case. Spiral antenna *S4* has been developed mainly for testing purposes. It is used as a reference structure for the other spiral designs of this work and existing spiral antennas of other works (e.g. [181]).

Design and simulation of spiral antennas

The design process of the broadband antennas in this work follows the guidelines specified by the characteristic parameters which shall be optimized:

- One of the most critical design considerations is the optimization of the antenna gain by matching the impedance of the terminal base of the antenna to the mixing element in its center. At the same time the antenna-dimensions need to be kept feasible with our in-house fabrication technologies. Among other things this restricts the smallest possible value of the inner radius (see Fig. 3.22) and by this the upper frequency limit of the band of all spiral designs developed in this work. It represents the largest limitation of the antenna gain and the upper cutoff frequency. Although the broadness of the antenna bandwidth is no subject of optimization, it is aimed to achieve an upper cutoff-frequency as high as possible.

- To allow a good coupling to a Gaussian beam the antenna should further exhibit a main-beam with a possibly gaussian-shaped radiation characteristic and high directivity. This implies to design each antenna such that their main beam is as rotational-symmetric as possible.

With these optimization criteria in mind a first version of each of the antennas has been formulated according to the antenna theory and the design rules described in the previous three subsections. In the next step the antenna drafts have been investigated and optimized based on simulations performed with the Time Domain solver of CST Microwave Studio[66]. Due to the lack of computing power needed for the high frequency range and in order to save computing time the antenna is simulated without the silicon lens but is placed in the middle of the surface of a thick silicon substrate instead. All remaining surfaces of the substrate are connected to open boundary conditions that enable low reflections at these interfaces. First, all computations are performed on antennas without feeding structures and IF-connections, additionally assuming lossless materials. The metal structures being defined as a Perfect Electrical Conductor (PEC) in the first instance later on are replaced by gold whose resistivity is fed into CST manually and has been estimated separately accounting for the skin effect. The HEB is represented by a discrete edge port which is used to feed the calculation domain with power. It is treated as a lumped element with an inner impedance that is specified by the user. For the optimization process the antenna is run in its transmitting mode, actively driven via the defined discrete edge port.

Archimedean spiral antenna S3

The Archimedean spiral antenna is designed to encompass frequencies up to the operating frequency of interest about 10.7 THz. To ensure that this frequency is covered by the bandwidth of the antenna, the higher cutoff frequency is aimed to be sufficiently higher than 10.7 THz. It is set to about 12 THz. To reach this cutoff frequency according to Eq.(3.22) the inner part of the Archimedean spiral arms needs to continue until the inner circle embracing the inner ends of the spiral arms has a radius of 1.74 µm. Accounting for the width of the spiral arms, the design parameter r_0 is set to 0.8 µm such that the corresponding radius of the circle (see Fig. 3.22) touching the outer edge of the spiral arms is close to the required value and equals $r_{min} = 1.79\,\mu\text{m}$. The dimension of the spiral's outer diameter is chosen such that 4.7 THz is within the bandwidth of the antenna with a certain safety margin to the estimated lower cutoff-frequency.

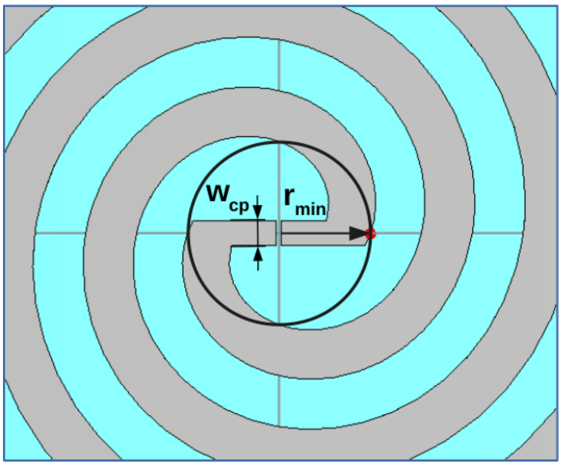

Figure 3.22.: Zoom-in into the structure of the Archimedean spiral antenna. The radius r_{min} corresponds to the minimum radius of a circle that just encompass the outer rim of the ends of both spiral arms inside the antenna. The blue colored surface indicates the silicon substrate.

Geometry specifications of Archimedean spiral antenna *S3*

r_0	0.8 µm
w	1 µm
s	1 µm
w_{cp}	0.5 µm
l_{HEB}	120 nm
N_{turns}	1.75
r_{max}	7.8 µm
r_{min}	1.74 µm

Table 3.4.: Parameters of geometry for Archimedean spiral antenna *S3*:
spiral arms: r_0: inner radius, w: width of the spiral arms, N_{turns} : number of turns of the arms, s: distance of adjacent spiral arms, r_{min} and r_{max}: minimum and maximum radius of a circle encompassing the inner and the outer extension of the spiral arms, respectively; ***feeding structure***: width of the contact pads: w_{cp}, length of the bolometer bridge l_{HEB}

To achieve a possibly rotationally symmetric pattern with acceptable directivity a rather tight winding of the spiral arms is beneficial. At the same time, the arm width of the spirals should furthermore allow an acceptable transmittance of the IF-signal (0.5-3 GHz). The final width of the spiral arms and the slot distance are chosen to correspond to a metalization ratio of $\chi = 0.5$ which conforms to a self-complementary spiral geometry. The according antenna input impedance to be expected without added feeding structure is depicted in Fig.3.23. Retaining to Eq.3.24 to estimate the effective dielectric constant (depicted in the inserted graphic in Fig.3.23) the input impedance has been estimated once using Brooker's relation Eq.(3.23) and secondly, using the expression derived by [25] for a two-armed Archimedean spiral. The results are presented in Fig.3.23 as orange and blue line. According to both models the input impedance is predicted to be considerably decreased in comparison to the prediction for the quasi-static approximation (depicted as green dashed line). In contrast to these predictions the CST simulations show a higher real part and a significant imaginary contribution to the overall feed-point impedance of

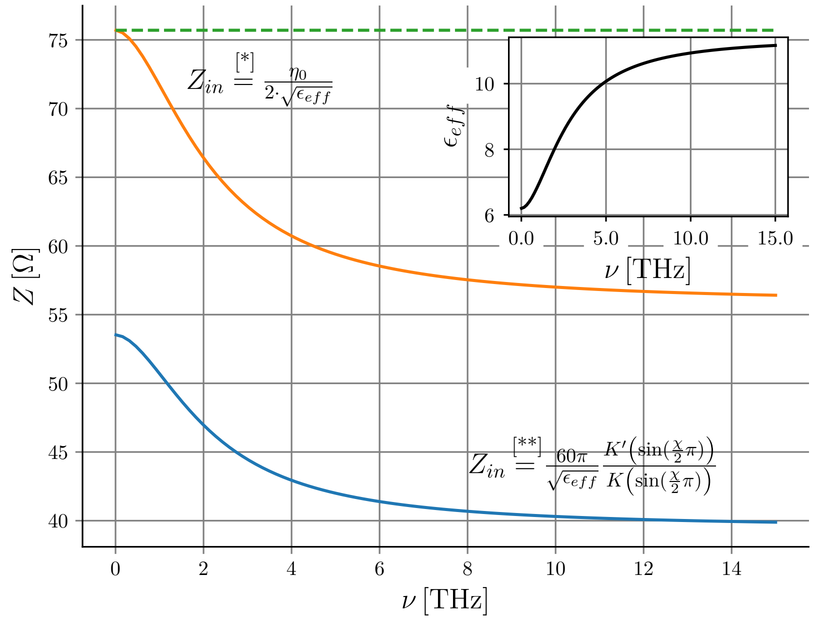

Figure 3.23.: Estimation of the Archimedean antenna *S3* without inner feeding structure (in terms of contact pads) based on [*] Brooker's relation and on equation [**] derived by Chen et al. [25] for frequencies up to 40 GHz. Instead of using the expression for the effective dielectric constant in [25] the effective dielectric constant for [**] as well as for [*] is estimated based on Eq.(3.24) and is depicted in the inserted graphic at the top, right-hand side. The green dashed line refers to the input impedance expected for the quasi-static case.

the antenna. Without additional feeding structure at the inner ends of the spiral arms the imaginary part for this configuration is approximately as large as the real part of the impedance as can be seen in Fig.3.24. Generally, the simulation results exhibit that the smaller the inner radius of this geometrical configuration the higher the imaginary part at the feed-point of the antenna. Adding the contact pads needed to connect the antenna to the bolometer enables to compensate for this high inductive impedance part but lead to a capacitive, however, significantly smaller, imaginary feed-point impedance. The contact pads which behave like an additional capacitance do not only influence the reactance at the feeding port but additionally affect the real part of the impedance. The analysis by simulations reveals that in a first, rough approximation the real part changes linearly with the inverse of the width of the contact pads. Tapering the contact pads to reduce the capacitive contribution is not possible as their width also co-determines the aspect ratio of the bolometer element in its center such that a reasonable impedance matching at the HEB-antenna interface is not possible due to the high resistivity of the HEB layer.

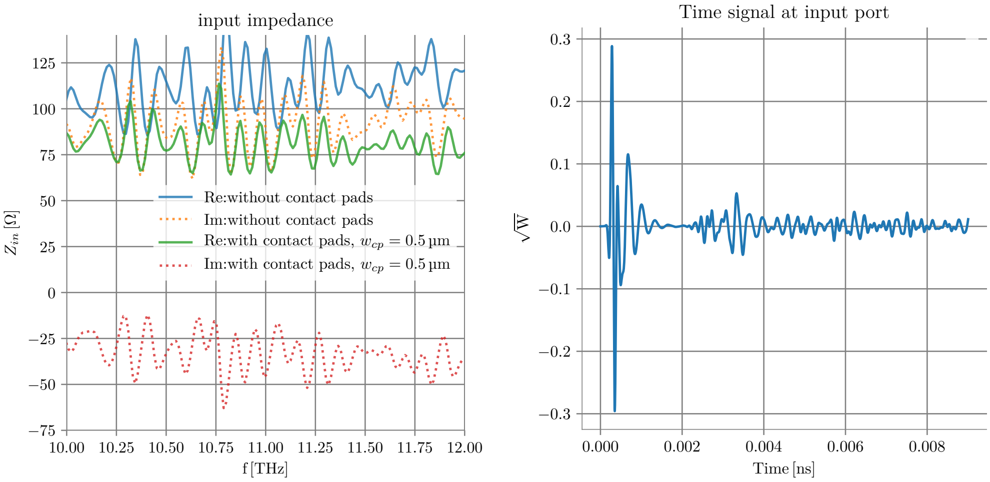

Figure 3.24.: (a) Input impedance at the center of the Archimedean spiral antenna with and without contact pads. (b) Time signal at the input port of an Archimedian spiral antenna on a thick substrate simulated in CST. The signal is not completely decayed to zero within the designated time frame of the time domain solver. The resulting truncation errors bite as ripples in the frequency domain. The impedance curve in (a) therefore exhibits an additional steady oscillating signal on top of the actual curve.

A further possibility to influence the imaginary part of the antenna's impedance is given by its geometry. The analysis by simulations yields that to reduce the imaginary part of the impedance narrow arms and little distance between adjacent arms is favorable. For an optimum feed-point impedance with a real part as high and an imaginary part as small as possible both, the contact pads and the geometry of the antenna have been optimized to the extent feasible within the above-mentioned constraints. The final dimensions chosen for the Archimedean design are summarized in Tab. 3.4. The corresponding input impedance at the feeding point of the antenna in dependence of its frequency is depicted in Fig. 3.26(a). The impedance exhibits a large oscillation for the frequency range below about 3 THz. These oscillations arise from the back reflection at the outer ends of the spiral arms for those wavelength which are larger than the effective length of the arms of the antenna. They define the lower cutoff-frequency that tallies rather well with the prediction given by Eq. (3.21). Connecting the spiral at its outer ends to the IF-line yields the same impedance curve above 3 THz but due to the changed termination conditions results into a different oscillation behavior for the lower frequencies which are outside the frequency range of interest. Furthermore the oscillation around 6 THz visible in Fig.3.26

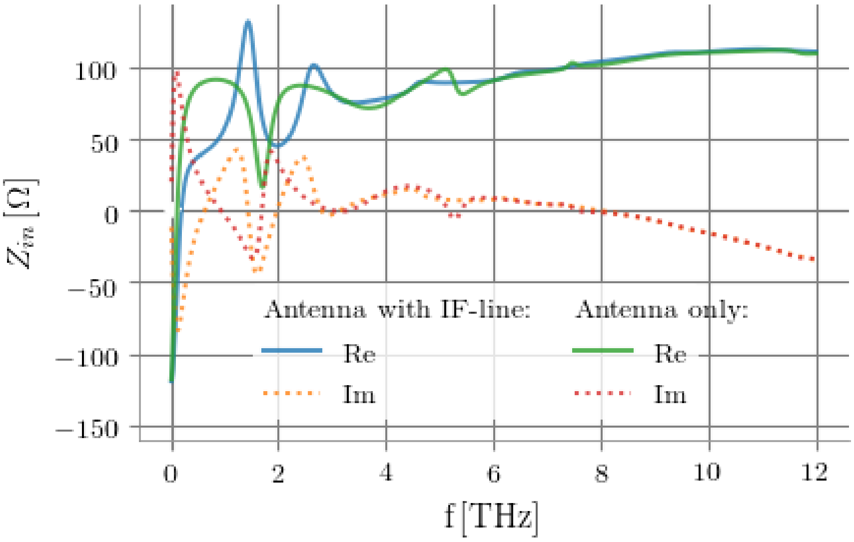

Figure 3.25.: Simulated input impedance with and without connected IF-line. The data had been smoothed by the auto-regressive filter of CST[68].

is smoothed out when connecting the spiral arms to the IF-line. It is to be expected that this oscillation likewise is the result of current reflections at the straight-cut ending of the arms used for this simulation and will be less pronounced for real case. Due to the limited computational resources it has not been possible to calculate the input impedance of the antenna connected to the IF-line based on simulations where the metal structures consist of gold. All metal parts are simulated as a perfect electrical conductor instead.

The real part of the impedance is situated between 90 Ω and 110 Ω for the frequencies above 3 THz. In contrast to its real part, the imaginary part of the antenna's input impedance is a continuously slowly decreasing function with frequency. It generally determines the higher limit of the frequency bandwidth. For an electrical termination with a resistance matching the real part of the input impedance about 100 Ω the power reflection at the antenna-HEB interface would still be below -12 dB at 12 THz, the highest frequency value the simulation has been performed for, and is about -15.1 dB at around the design frequency of 10.7 THz. In that ideal case the bandwidth from the point of view of impedance matching encompasses more than 9 THz. However, the real part of the HEB impedance cannot be chosen at this optimum value. As explained in Sec.3.3 the resistivity of the HEB layer and the possible aspect ratio restricts the the maximum and minimum values to be expected for the bolometer resistance to 110 Ω and 360 Ω, respectively. The corresponding S-parameters have been estimated using

$$S11 = \frac{Z_{in} - R_{HEB}}{Z_{in} + R_{HEB}},$$

and are depicted in Fig. 3.26(b). The respective orange and green dotted curve indicate the limits within which the actual S-parameter can be expected. At best the resulting power reflection above 2.67 THz continuously is below -12 dB.

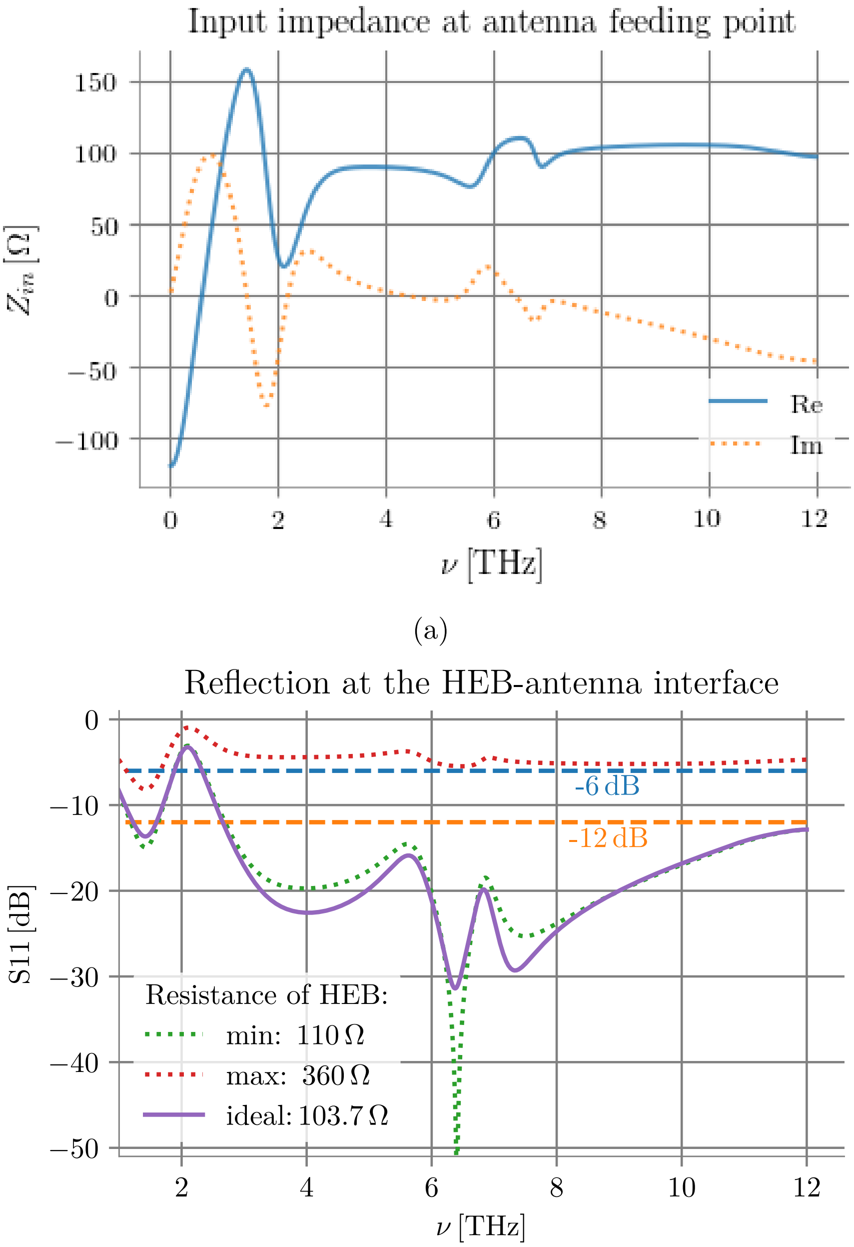

(a)

(b)

Figure 3.26.: Archimedean spiral antenne *S3*: (a) Input impedance at the feeding point. The antenna consists of a 90 nm gold layer with the dimensions and geometry given in Table 3.4. The data had been smoothed by the auto-regressive filter of CST[68] (b) Power reflection represented by the S-parameter S11 at the interface between the feeding point of the antenna and the bolometer expecting different values for the resistance of the HEB. Considered are the minimum and maximum resistance which can be expected for the HEB made from NbN, and the resistance of a HEB for the ideal case that it equals the real part of the input impedance at 10.7 THz.

Logarithmic spiral designs

The design process of broadband antennas based on the logarithmic spiral geometry showed that a realistic log-spiral antenna encompassing a frequency of about 10.7 THz with less than -9 dB power reflection at the antenna-HEB interface is not feasible under the given conditions. In general, the feeding structure at the center of a self-complementary logarithmic spiral antenna on silicon turned out to directly contribute to the imaginary part of the input impedance and by this to determine the naturally achievable bandwidth in case of perfect matching of the real part of the impedance. As a consequence, two different logarithmic spiral antennas have been designed. Log-spiral antenna *S1/S2* addresses a frequency range around 4.7 THz and is denominated *S1* or *S2* according to its respective connection to the IF-line. Test antenna *S4* is a self-complementary antenna to mark off the limits of the highest cutoff frequency achievable within the natural limits of fabrication techniques, pushing towards 10.7 THz. It further enables a better comparison with the few published log-spiral antennas used within this frequency regime [152, 151, 88] that typically exhibit a self-complementary structure.

Overall design considerations and investigations

- **inner radius**
  As a rule-of-thumb the higher cutoff-frequency according to Semenov et al. [151] is given by about $\lambda_{min} = 20 \cdot d_{in,circ}$, for their log-spiral antenna on a silicon substrate, where $d_{in,circ}$ is the diameter of a circle that just enclose the inner ends of the spiral arms (see Fig. 3.28). Accordingly, a logarithmic spiral antenna working up to 10.7 THz and 4.7 THz requires an inner radius, r_0, of about 0.7 µm and 1.6 µm, respectively. As there is evidence that for the higher frequencies the standard design rules are not completely scalable [88] the radius should be chosen such that the frequency of interest safely is covered by the antennas bandwidth. For the 4.7 THz design *S1/S2* the actual inner radius therefore is chosen to be reduced to 1.25 µm which corresponds to an upper cutoff about 6 THz according to the rule-of-thumb. For a 10.7 THz log-spiral antenna a minimum radius of $r_0 = 0.5$ µm would be desirable. However, the limits of fabrication techniques and the requirement of a reasonable impedance matching with the HEB sets a certain limit to the dimensions of the design. For this reason the inner radius of 0.7 µm is retained for the antenna design *S4*. It should be noted that the inner radius directly determines the maximum possible width of the contact area between the inner spiral arms and the bolometer bridge in its center. Due to the limits of the fabrication technique a

minimal orthogonal distance to the adjacent antenna arms of about 0.3 µm should be ensured. As a consequence the contact pads for the *S1/S2* and the *S4* designs cannot be larger than 1.5 µm and 0.5 µm, respectively.

- **complex input impedance of the antenna**
  It has been reported in [152, 151] that for self-complementary log-spiral antennas up to 6 THz the antenna impedance at the feeding point has a non-negligible imaginary component. Simulations results of this work using the CST software reveal that even without additional inner feeding structure the logarithmic spiral antennas, not restricted to the self-complementary ones, exhibit a non-vanishing imaginary part in its input impedances which leads to a reduction of the power transfer to the mixer element. Simply relying on the construction rules for a self-complementary log-spiral antenna for this high frequency range the imaginary part can constitute up to over 20% of the amount of the antenna's input impedance without any additional feeding geometry in terms of contact pads as depicted in Fig.3.27. This antenna reactance is quite considerable and needs to be compensated if possible.

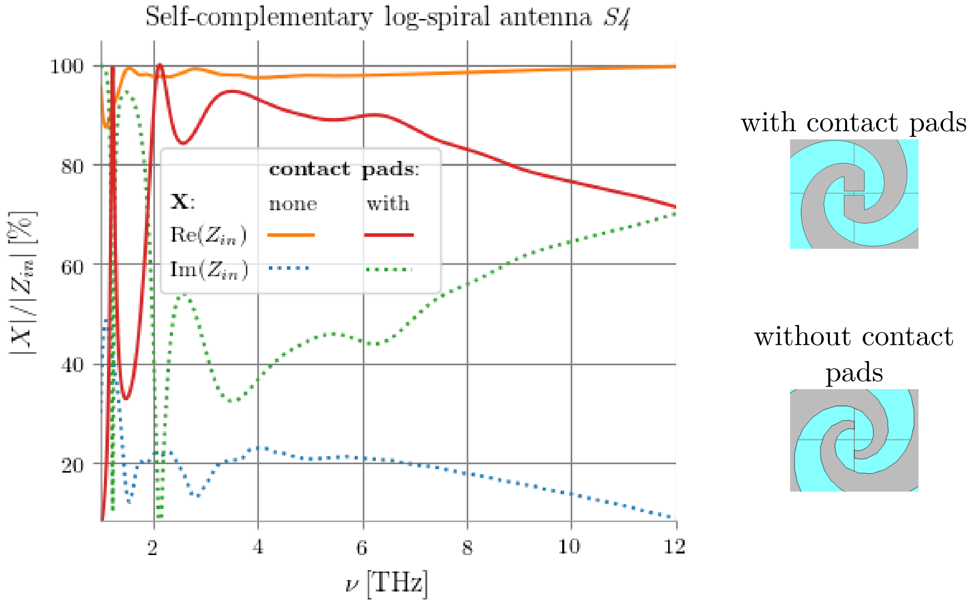

with contact pads

without contact pads

Figure 3.27.: Percentage of the imaginary and real part on the overall magnitude of the input impedance at the feeding point of antenna *S4*. The numbers have been calculated once for the antenna without any feeding structure in terms of contact pads and once adding the feeding structure that connects the inner spiral arms to the bolometer bridge.

- **feeding structure**
  Similar to the Archimedean spiral antenna, the imaginary part of the foot point impedance is further influenced by the chosen geometry of the contact pads which connect the two arms of the spiral antenna to the HEB in the center of the antenna. The contact pads behave like an additional capacitance as depicted in Fig.3.27. For that reason contact pads with an hourglass shaped geometry offers the smallest contribution to the imaginary impedance. In general, the narrower the contact pads the lower their contribution to the imaginary feedpoint impedance. The need not to fall below a minimum width in the HEB dimensions to allow acceptable impedance matching to the antenna does not allow this contact configuration for the desired frequency ranges. Therefore the geometry of the contact pads which allows for the broadest contact pads and simultaneously offer the largest distance to the winded spiral arms[8] is used for all designs of the spiral antennas. The according feeding geometry is sketched in Fig.3.28. To receive the desired width of the contact pads, w_{cp}, both spiral arms are pursued into the inner center of the antenna by the correspondingly required angle β. Mathematically, it means that the spiral curves starts at $\Phi = -\beta$ (see Sec. 3.2.3).

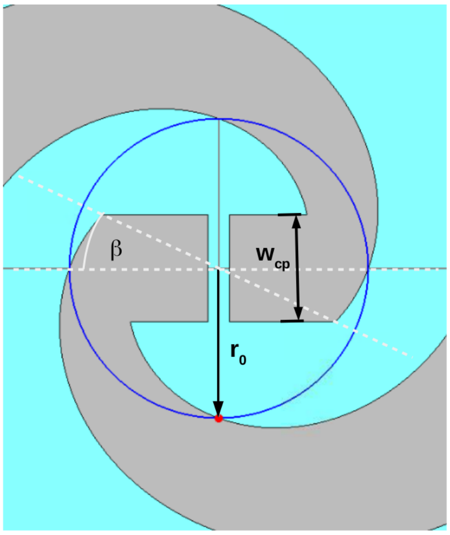

Figure 3.28.: Sketch of the geometry of the contact pads used for all log-spiral designs.

- **influence of antenna geometry**
  The input impedance of the log-spiral antenna is a function of its antenna geometry. Investigations by means of simulations revealed that a higher filling factor adjustable

---

[8] To keep the desired structure producible with the available fabrication technology

via the rotation angle δ yields a reduction of both, the real and the imaginary part of the impedance at the antennas feeding terminal. This is used to reduce the imaginary part for the *S1/S2* design where the width of the contact pads contributes considerably to the antenna reactance. A tighter winding of the spiral arms (using a constant a between 0.2 to 0.4) leads to a slightly steeper progression of the imaginary part of the input impedance and to a downward-shift of the curve of the real part of Z_{in}.

Self-complementary log-spiral antenna *S4*

The logarithmic spiral antenna *S4* is used as a test structure to figure out the limit achievable for the upper frequency within the natural limits of fabrication techniques and to provide an antenna with a self-complementary shape to allow a reasonable comparison with the few existing spiral antennas for the high THz regime, which typically exhibit a self-complementary shape. The geometrical parameters of the design are specified in Tab.3.5.

The input impedance expected by Brooker's relation (3.23) for a self-complementary antenna is approximated using the estimated effective electric permittivity given by Eq.(3.24) that is depicted in the inset of Fig.3.30. Although it correctly predicts a decreasing impedance with frequency (blue line), the real part of the input impedance of the antenna, $Re(Z_{CST})$, simulated with CST is considerably lower (see dotted gray line).

The simulation results with CST studio suite expose that the real part of the impedance is a slightly decreasing function with frequency around about $48\,\Omega \pm 13\,\Omega$ as depicted in Fig.3.32 (a) and that there is a considerable capacitive reactance around about $27\,\Omega$ which slightly increases with frequency. The high imaginary part of the impedance mainly is attributed to the contact pads as can be seen in Fig.3.31. As a consequence a power reflection below -9 dB cannot be achieved over the whole antenna bandwidth even if the bolometer element exhibits a resistance which perfectly matches the the real part of the feedpoint impedance about $38.2\,\Omega$ at 10.7 THz as illustrated in Fig.3.32 (b). The common requested condition for the inner radius to define the upper cutoff-frequency in that case hence is necessary but not sufficient as the ultimate upper limit of the antenna-bandwidth is set by the feeding structure instead. [9] Using the maximum and minimum resistance the HEB element of NbN is expected to reach for the given dimensions (see Sec.3.3) the

---

[9] It should be noted here that increasing the inner radius to 0.8 µm retaining all other geometrical antenna parameters would yield a power reflection below -9 dB over the desired bandwidth in case that the real part of the input impedance is ideally matched. However, this antenna design has been discarded in favor to focus on the ultimate limits reachable with fabrication techniques.

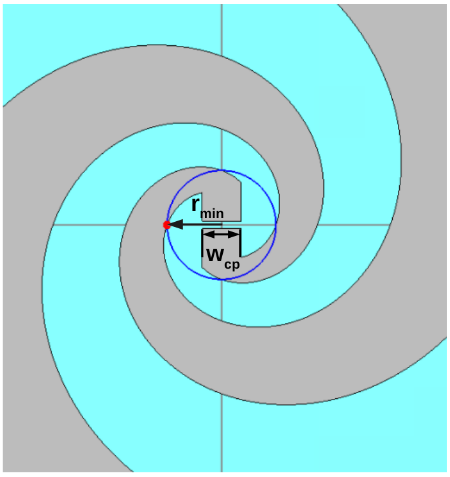

Figure 3.29.: Zoom-in into the structure of the self-complementary log-spiral antenna *S4*. The radius r_{min} corresponds to the minimum radius of a circle that just encompass the outer rim of the ends of both spiral arms inside the antenna. The blue colored surface indicates the silicon substrate.

Geometry specifications of log-spiral antenna *S4*

r_0	0.7 µm
a	0.36
δ	90°
w_{cp}	0.5 µm
l_{HEB}	100 nm
N_{turns}	1.5
r_{max}	23.6 µm
r_{min}	0.7 µm

Table 3.5.: Parameters of geometry for self-complementary log-spiral antenna *S4*: ***feeding structure***: width of the contact pads: w_{cp}, length of the bolometer bridge l_{HEB}

corresponding power reflection at 10.7 THz roughly lies in between -1.6 dB and -6 dB. The $S11$ curve calculated for the so far measured bolometer resistance of the current batch demonstrates that this antenna is only usable for test purposes.

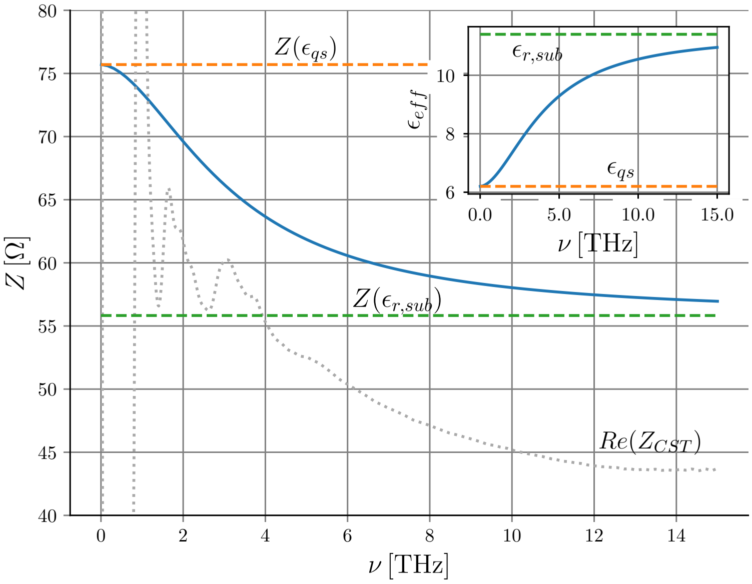

Figure 3.30.: Estimation of the input impedance of the log-spiral antenna *S4* without inner feeding structure based on Brooker's relation. The effective dielectric constant is approximated based on Eq.(3.24) and is depicted in the inserted graphic at the top, right-hand side. The orange dashed line refers to the input impedance expected for the quasi-static case the dashed green line refers to the input impedance expected for the effective dielectric constant obtained for the high frequency limit. The real part of the input impedance simulated with CST studio suite[66] is drawn as gray, dotted line.

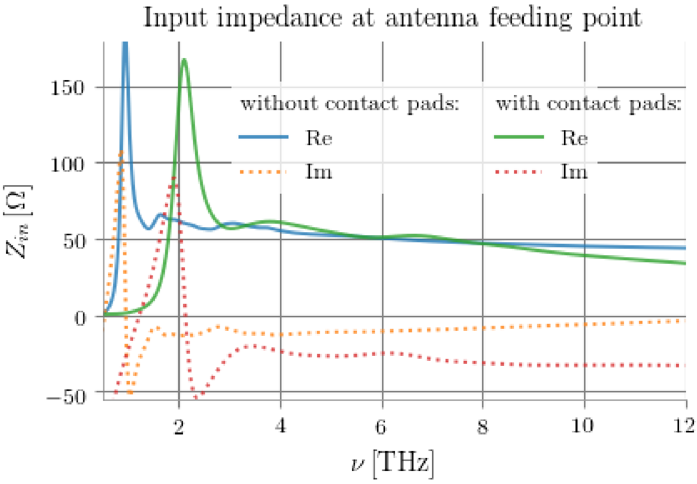

Figure 3.31.: Simulated input impedance of the log-spiral antenna *S4* with and without feeding structure in terms of contact pads which connect the ends of the spiral arms to the mixing element, the HEB. The antenna material has been treated as a perfect electrical conductor.

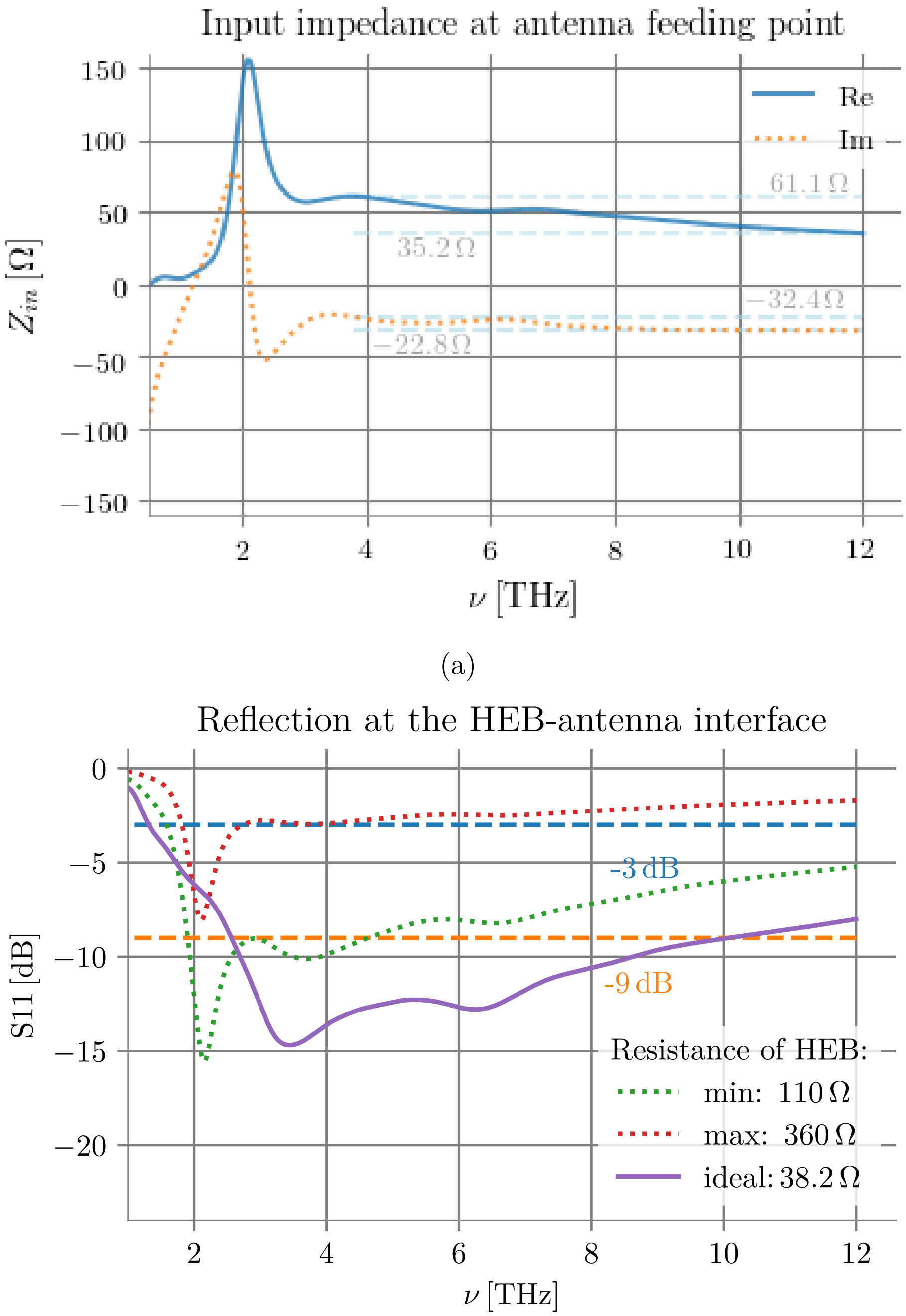

(a)

(b)

Figure 3.32.: Simulated input impedance (a) and calculated power reflection (b) at the antenna-bolometer interface for the log-spiral antenna *S4*. The material of the metal structure is gold whose electrical properties have been approximated accounting for the skin-effect based on measured dc resistance at 4 K. The S11-parameters have been calculated assuming different values for the resistance of the HEB. Considered are the minimum and maximum resistance which can be expected for the HEB made from NbN, and the resistance of an HEB for the ideal case that it equals the real part of the input impedance at 10.7 THz.

Log-spiral antenna *S1/S2*

The log-spiral antenna addressing a frequency around about 4.7 THz has been designed for two different versions of IF connections. The only difference between design *S1* and *S2* is a slightly increased number of turns about 0.5. An overview about the geometrical design parameters can be found in Tab.3.6.

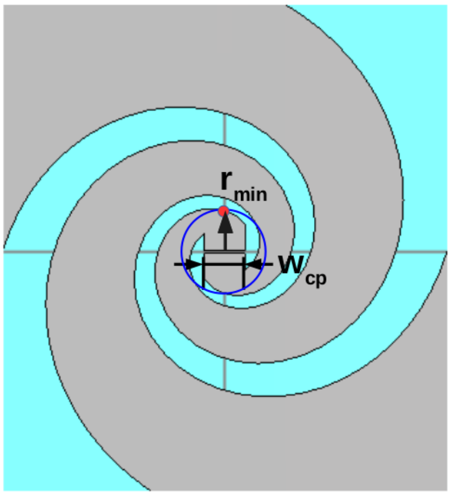

Figure 3.33.: Zoom-in into the structure of the log-spiral antenna *S1/S2*. The radius r_{min} corresponds to the minimum radius of a circle that just encompass the outer rim of the ends of both spiral arms inside the antenna. The blue colored surface indicates the silicon substrate.

Geometry specifications of log-spiral antenna *S1/S2*	
r_0	1.25 µm
a	0.3
δ	50°
w_{cp}	1.5 µm
l_{HEB}	150 nm
S1: N_{turns}	≈ 2
S2: N_{turns}	1.5
S1: r_{max}	104.4 µm
S2: r_{max}	16.26 µm
r_{min}	1.25 µm

Table 3.6.: Parameters of geometry for log-spiral antenna *S1/S2*:
feeding structure: width of the contact pads: w_{cp}, length of the bolometer bridge l_{HEB}

The simulated feed point impedance and the corresponding S11 parameters calculated for different values of the HEB resistance are shown in Fig.3.34 for the spiral antenna with 1.5 turns. Despite the non-vanishing capacitive contribution to the antenna's input impedance mainly arising from the feeding structure of the contact pads that connects the antenna with the bolometer bridge a power reflection less than -14 dB can be achieved for the best HEB resistance to be expected. The high peak in the impedance curve below 2 THz again arises due to back reflections of the current at the straight cut ends of the antenna arms which needs to be used to enable the simulation with the CST software with the existing computational resources. It is to be expected that this oscillation part is reduced due to the IF connection and is shifted to lower frequencies for the design with a slightly higher number of turns. An additional advantage of this design is the real input impedance close to 50 Ω that enables a good power transfer to the 50 Ω-IF-connection lines.

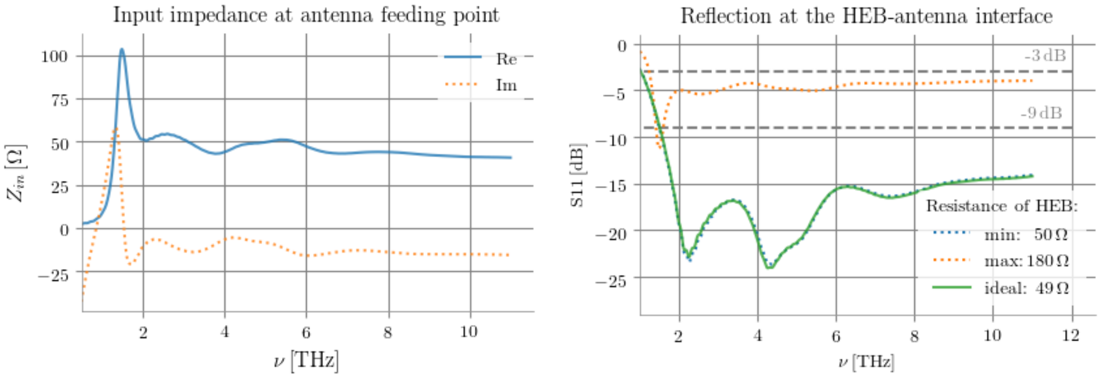

(a) (b)

Figure 3.34.: (a) Simulated input impedance of the log-spiral antenna *S1/S2*. The antenna material has been treated as gold. (b) Power reflection $S11$ at the HEB-antenna interface calculated for the maximum and minimum value for the resistance of the HEB microbridge to be expected according to previous measured NbN sheet resistances. The ideal value corresponds to the real part of the antenna's input impedance at 4.7 THz according to the simulation result shown in (a).

3.4.4. Far field properties of selected designs

In the following sections the far field properties of four of the above-introduced antenna designs (three spiral antennas and one double-slot antenna) are presented for the configuration where the respective antenna is attached to the backside of a silicon lens. The lens dimensions correspond to the lens used for the 10.7 THz double slot antennas (see Sec. 3.4.1) since this is the practical lens currently available. The results presented here are based on simulations carried out with the CST software, for frequencies below 5 THz, and do not include the calculation of the field patterns of the 10.7 THz DS antenna designs, which are discussed elsewhere in Sec. 3.4.2 based on the SRT-software results.

To allow a direct comparison of the broadband antennas with the double-slot antenna, the respective radiation patterns are exemplary depicted at 4.7 THz, a frequency which, in contrast to 10.7 THz, is within the bandwidth of all broadband antennas according to the results in the above sections. The respective E-field magnitude and its phase are depicted as orthographic projections calculated for a distance of 1 m to the center of the antenna-backside. A cut through the main beam in two sectional planes at azimuthal angle $\Phi = 0°$ and $\Phi = 90°$ is given at the right-hand side of each projection plot. To enable a more detailed view, they show a cut-out in the elevation angle Θ, ranging from $-20°$ to $20°$.

In the first part the directivity, beam-width and radiation pattern at 4.7 THz of all four antennas as well as the frequency-dependent behavior of the polarization of the spiral antennas are presented. Taking into consideration that for the operation of the antennas in a mixer module only their coupling to a linearly polarized LO source is relevant, the second part of this section discusses the properties of the antenna beams with regard to the coupling efficiency of the antennas with the radiation pattern of a linearly polarized Gaussian beam.

The calculation of the radiation patterns of the antenna-lens designs is carried out by simulations with the TD solver of the CST software[66]. As our computational resources only allow to simulate the different antenna designs with the lens up to a frequency of 5 THz the investigated frequency range is restricted to this upper frequency limit but still covers an acceptable part of the operational bandwidths of all broadband lens-antennas to identify some of the frequency-dependent characteristics. To enable the calculation of these far field properties the antenna designs need to be cut back as much as possible. An acceleration and simplification using mirror symmetry planes in the software is not possible as the spiral antennas exhibit point symmetry. The simulation is restricted to only the respective antenna made from PEC attached to the lossless silicon lens. PEC is a perfect electrical conductor, that is used instead of the material properties of Au at 4.2 K, because it uses less simulation resources. The mesh size needed to be reduced to a rather coarse resolution (a number of 461,049,600 (antenna *S3*), 721,242,336 (design *S1/S2*) and 814,364,304 (antenna *S4*) hexahedral mesh cells without adaptive mesh refinement for a bounding box of $1.3649 \times 10^6\,\mu\mathrm{m}^3$, 15 cells per wavelength) and a solver accuracy about -20 dB. The total simulation time on a PC with a Intel(R)Xeon(R) Gold 6144 3.5 GHz processor with 96 GB of RAM with a number of 16 CPU threads, and two processes running in parallel was kept below 5 days (57 h to 104 h) per spiral antenna design. For the log-spiral designs *S1/S2* and *S4* the frequencies at which the farfield pattern is calculated further needed to be restricted to seven frequency points. To enable the calculation of the far field of the 4.7 THz double-slot antenna design with CST studio suite only the antenna without attached RF-blocking filter has been simulated again assuming PEC instead of Au and excluding adaptive mesh refinement (bounding box of $1.3649x10^6$ µm, number of mesh cells is 585891684, 15 cells per wavelength, steady state crit. -25 dB).

4.7 THz double-slot antenna

The E-field of the DS-antenna is clearly linearly polarized with a negligible cross polarization of -50 dB. The respective orthographic projection and cut planes through the beam of the E-field that is polarized along the main polarization direction (the y-axis) is depicted in Fig.3.35. The directivity gain is 29.9 dBi. The main beam has a 9 dB width of 8.5° and 8.19° in the $\Phi = 0°$ and $\Phi = 90°$ cutting plane, respectively. The side-lobe level is below -11.1 dB.

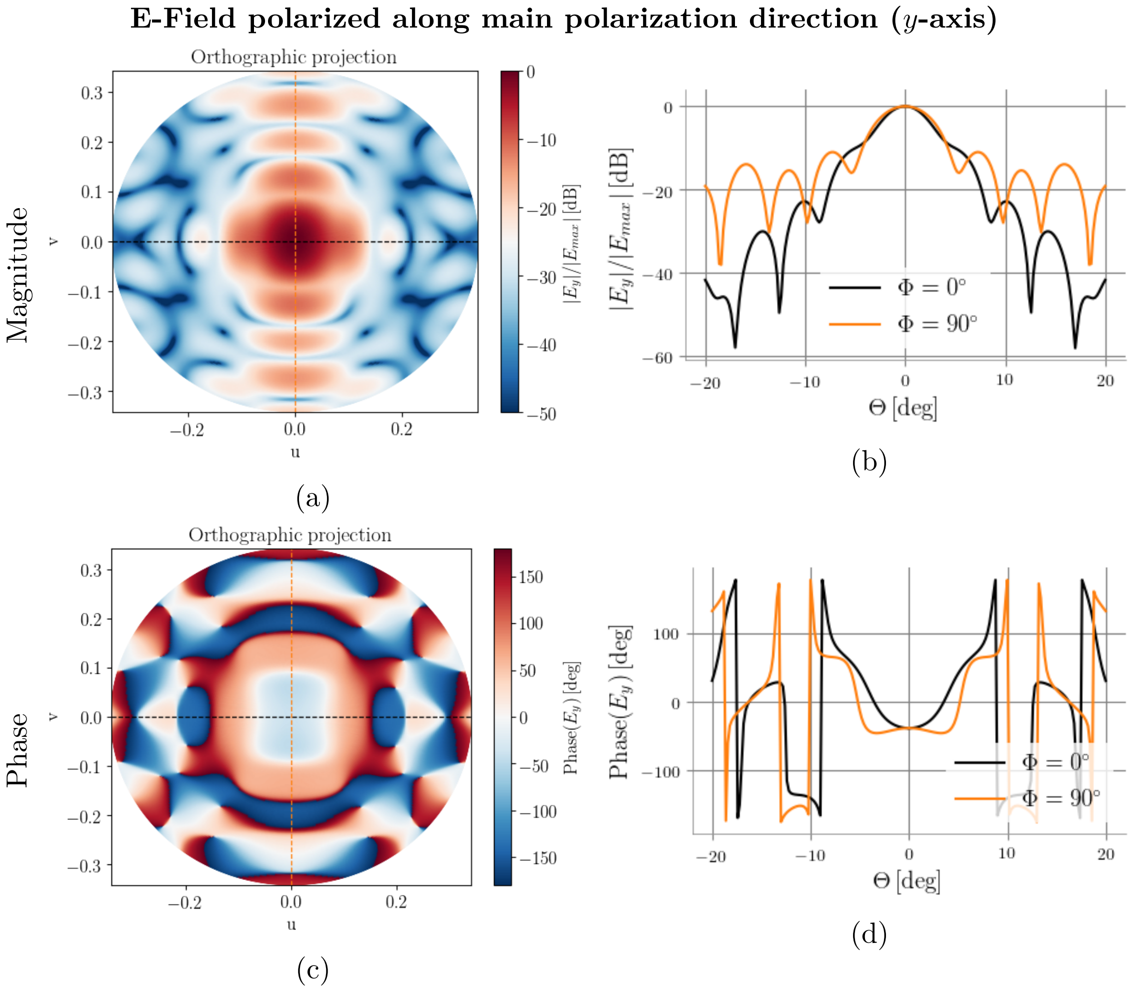

Figure 3.35.: Simulation results of E-field for the double-slot antenna at 4.7 THz. All figures show a cut-out in the elevation angle Θ from -20° to 20°. The dashed orange and black lines in the plots on the left-hand side indicate the cuts through the main beam in two sectional planes at azimuthal angle $\Phi = 0°$ and $\Phi = 90°$ that are depicted on the right-hand side.

Spiral antennas

Directivity and beam width: The directivity and the respective beam widths of the radiation patterns of all broadband antennas are plotted together in Fig. 3.36. The according 9 dB beam-width, $\Theta_{9\,dB}$, has been determined in two sectional planes in space that are orthogonal to each other, the plane at azimuthal angle $\Phi = 0°$ and $\Phi = 90°$, respectively. The directivity is an increasing function with frequency and is for all spirals considerably high with values above 28.8 dBi starting from 3 THz. Deviations in the directivity between the different antennas are less than 1 dB within the covered range. The lowest values are achieved by the $S1/S2$ spiral design.

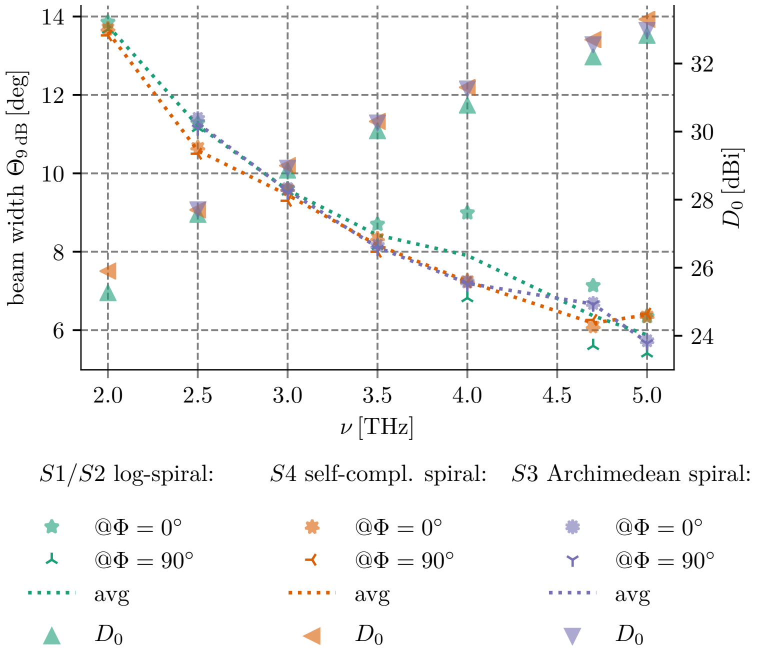

Figure 3.36.: (right axis) Comparison of the directivities in main beam direction of all three different broadband antenna designs, (left axis) 9 dB beam-width in the plane at $\Phi = 0°$ and $\Phi = 90°$.

As can be seen in Fig. 3.36 the beam widths in both planes for most of the frequency points are slightly different from each other and oscillate around the average value of both. The largest visible deviation for spiral *S3* and *S4* is 0.3°, and for spiral *S1/S2* is 2.2°, respectively, over the investigated frequency range. It is reported that for log-spiral antennas the beam-width within a fixed plane orthogonal to the antenna plane typically varies around about 10 ° due to the fact that the pattern rotates with frequency[4]. A variation of the beam-width in both planes with frequency thus is to be expected but the effect will be less noticeable due to the focusing effect of the lens.

Polarization: The logarithmic spiral antennas as well as the Archimedean spiral antenna exhibit an elliptical polarization whose sense of polarization corresponds to the winding sense of the spiral arms [93]. For a viewer placed behind the present antennas looking into the direction of the incoming signal it is left-handed polarized (LHP). For the frequency range investigated by simulations the amount of right-handed polarized (RHP) radiation is at least -12 dB smaller than the left-handed part within the operational bandwidth for all three antenna-lens constructions. It therefore is neglected for the further discussion.

The polarization ellipse at each point in space is dependent on the frequency and has its major axis tilted by a certain angle τ to the y-axis as depicted in the sketch of Fig.3.37(b). To investigate the polarization behavior of all spiral antennas, both the axial ratio AR and the tilt angle need to be considered. They are calculated using Eq.(B.21) and (B.24). A detailed look on the spatial distribution of both quantities can be found in the Appx. B.5.3. As can be seen from the orthographic projections for the self-complementary spiral antenna in Fig. 3.37(d) and (f), the spatial variations of AR and τ are mainly small with few exceptions at the edges. To visualize the frequency-dependence of the polarization of the main beam, AR and τ are investigated exclusively along the main beam direction at elevation angle $\Theta = 0°$ which corresponds to the point at $u = v = 0$ in the orthographic projection as indicated by the green star in Fig.3.37(d) and the magenta cross in (f). Within the depicted frequency range the axial ratio of all three antenna designs oscillates with frequency. Above 3 THz AR is between 1.2 and 1.9 and rather close to the AR corresponding to an ideally circular polarization which is indicated by the green dashed line in Fig.3.37(a),(c) and (e). According to the common standard radiation with an axial ratio less than 2 is considered to be circularly polarized[46] for all practical purposes. From that experimental point of view the antenna-lens designs exhibit a circularly polarized main beam within their operational bandwidths. Towards the lower cutoff-frequency of the antennas the axial ratio steeply increases indicating strongly elliptical polarization and the end of their operational ranges.

The tilt angles of the logarithmic spiral antennas varies with frequency between 49.1° and 80.6° where the variations for design *S1/S2* are considerably less than for the design *S3*. The steep in- and decrease around 4.5 THz for the Archimedean spiral *S3* is not completely understood. It is likely to be an effect due to the reflections at the straight cut ends of the arms of the Archimedean antenna that have been observed in Fig.3.26 in Sec.3.4.3.

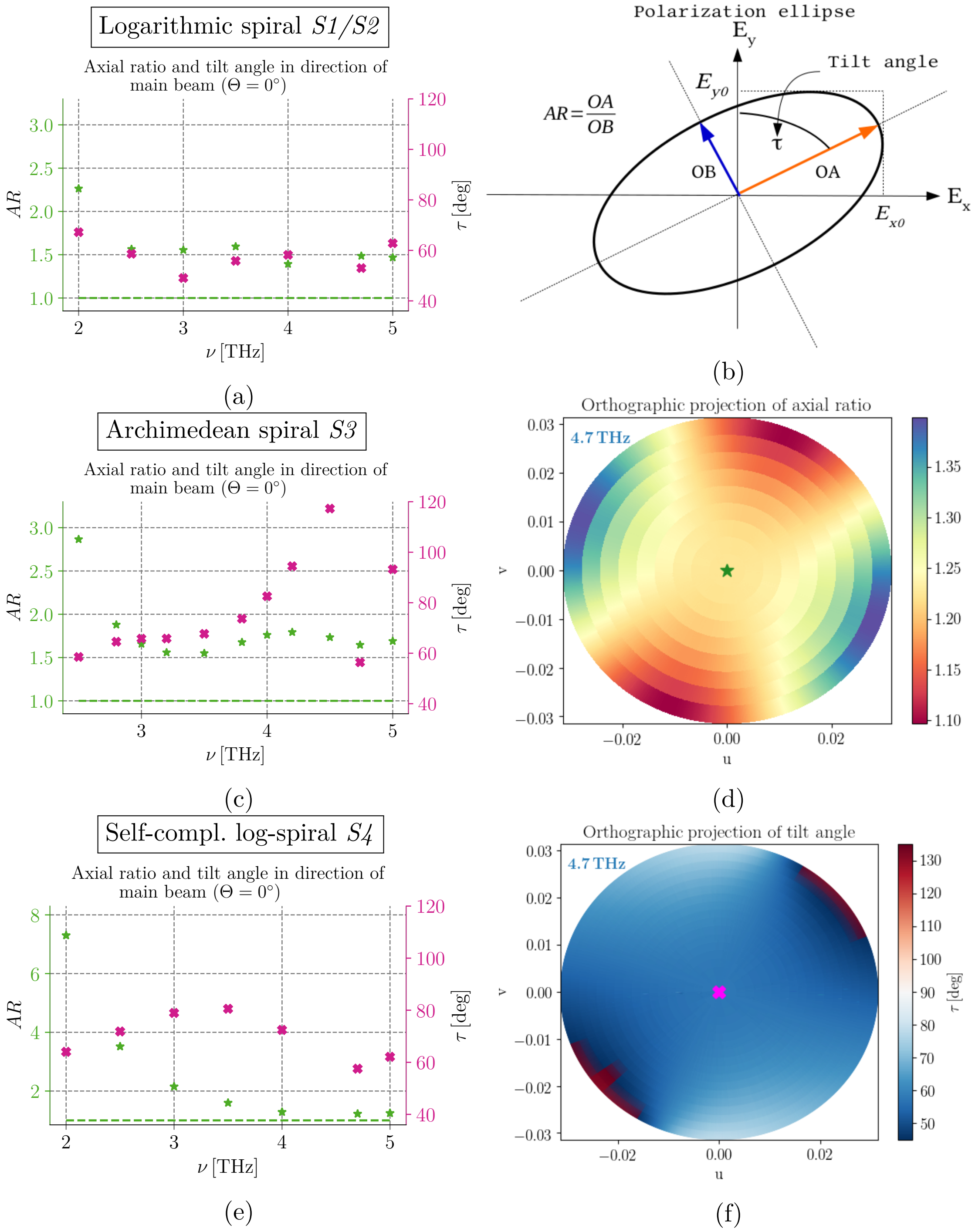

Figure 3.37.: Axial ratio, AR, and the tilt angle, τ, of the polarization ellipse as defined in sketch (b). Plot (a),(c) and (e) show both quantities determined at the point of maximum power in the direction of the main beam at polar angle $\Theta = 0°$ (marked by a green star or magenta cross in (d) and (f)) for spiral antennas $S1/S2$ to $S4$ that are placed on the silicon lens with the dimensions specified in Sec.3.4.1. The orthographic projections (d) and (f), respectively, depict the axial ratio and tilt angle of the self-complementary Archimedean spiral antenna at 4.7 THz for the polar angle Θ from $-1.85°$ to $1.85°$.

Radiation pattern: The overall LHP part of the E-fields being the primary type of polarization of the antennas is given in Fig. 3.38. The sidelobe level for all spiral antennas is at least below -10 dB with rapid trailing edges. The edges of the main beams are visible as a rapid phase change in the phase curves. Within the 3 dB beam-width of the main beams the phases varies only slightly.

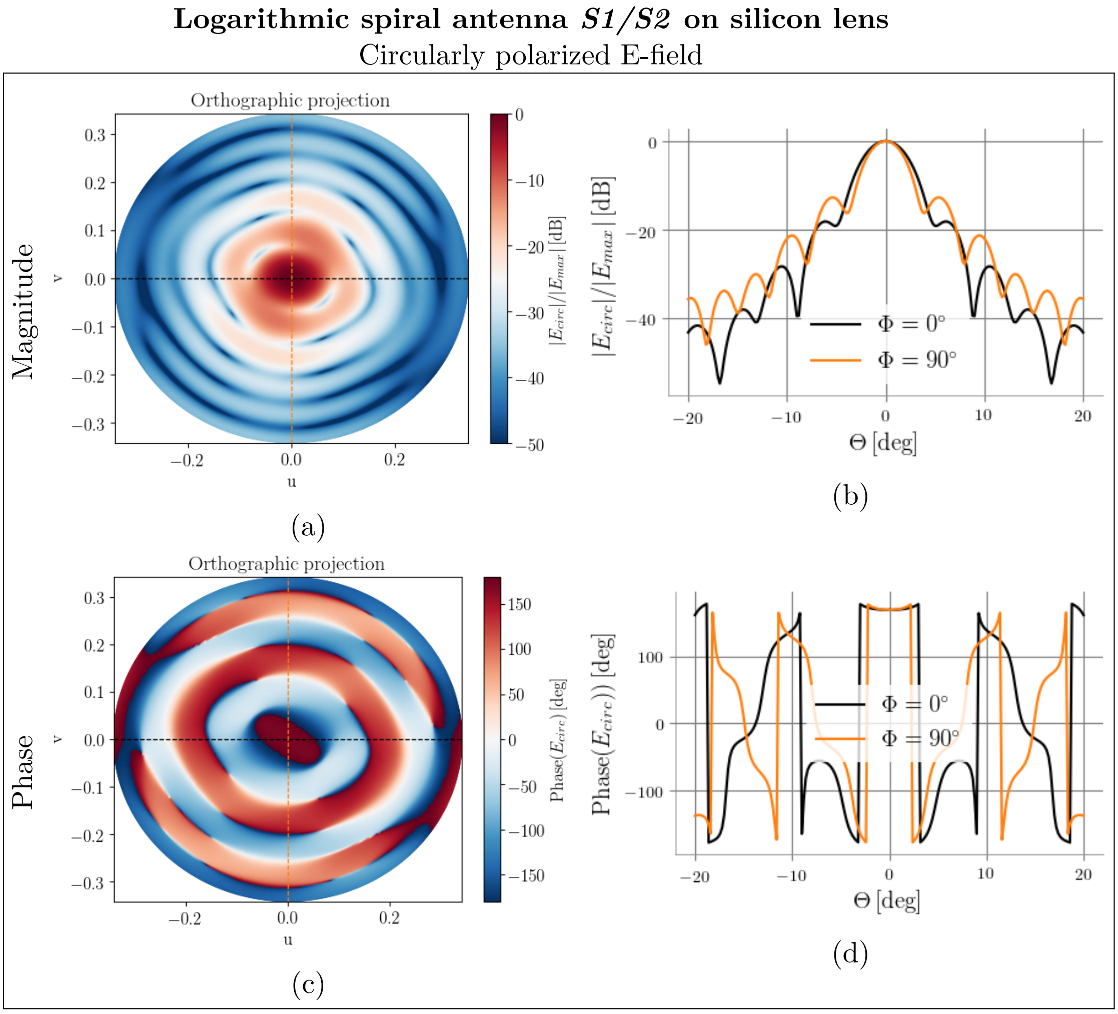
Logarithmic spiral antenna *S1/S2* on silicon lens
Circularly polarized E-field

Figure 3.38.: Simulation results of E-field for logarithmic spiral antenna design *S1/S2* at 4.7 THz. All figures show a cut-out of the radiation pattern in the elevation angle Θ from -20° to 20°. The dashed orange and black lines in the plots on the left-hand side indicate the cuts through the main beam in two sectional planes at azimuthal angle Φ = 0° and Φ = 90° that are depicted on the right-hand side.

Archimedean spiral antenna *S3* on silicon lens
Circularly polarized E-field

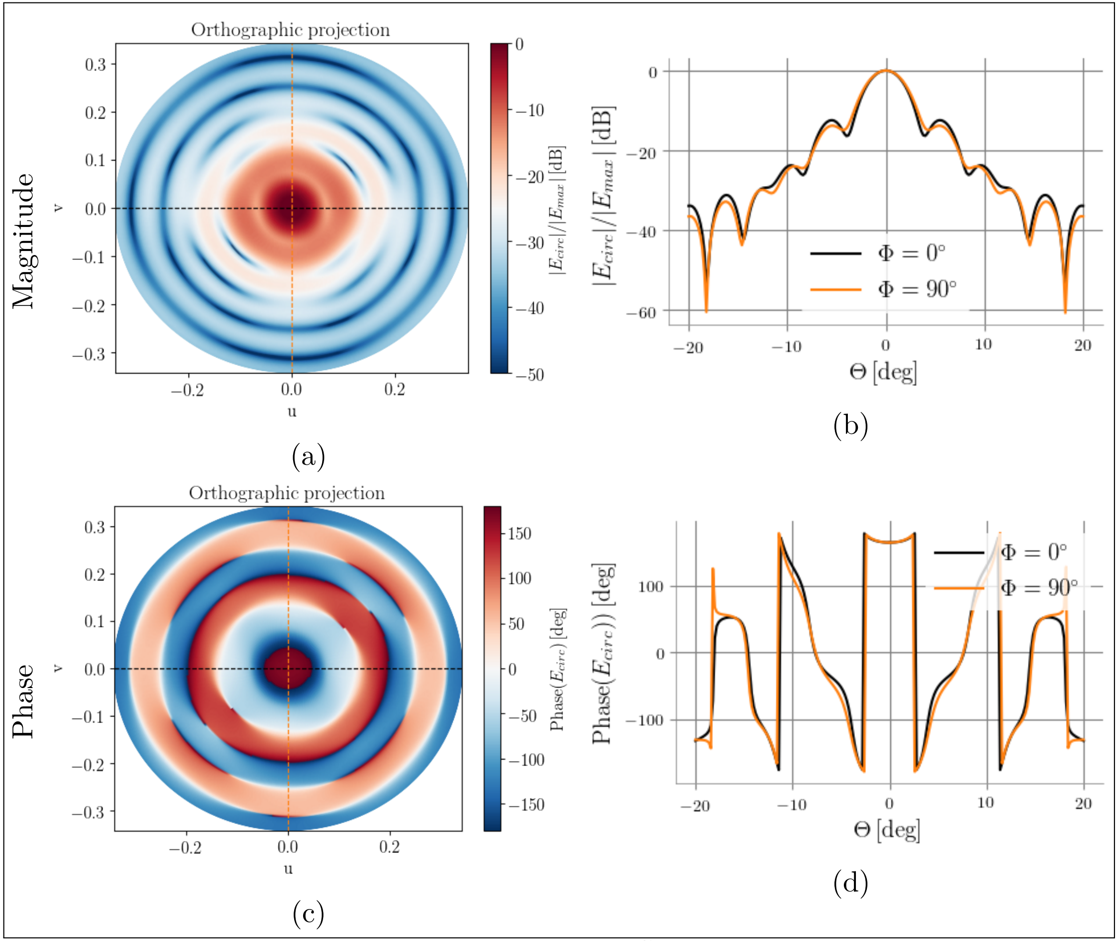

(a) (b) (c) (d)

Self-compl. Log-spiral antenna *S4* on silicon lens
Circularly polarized E-field

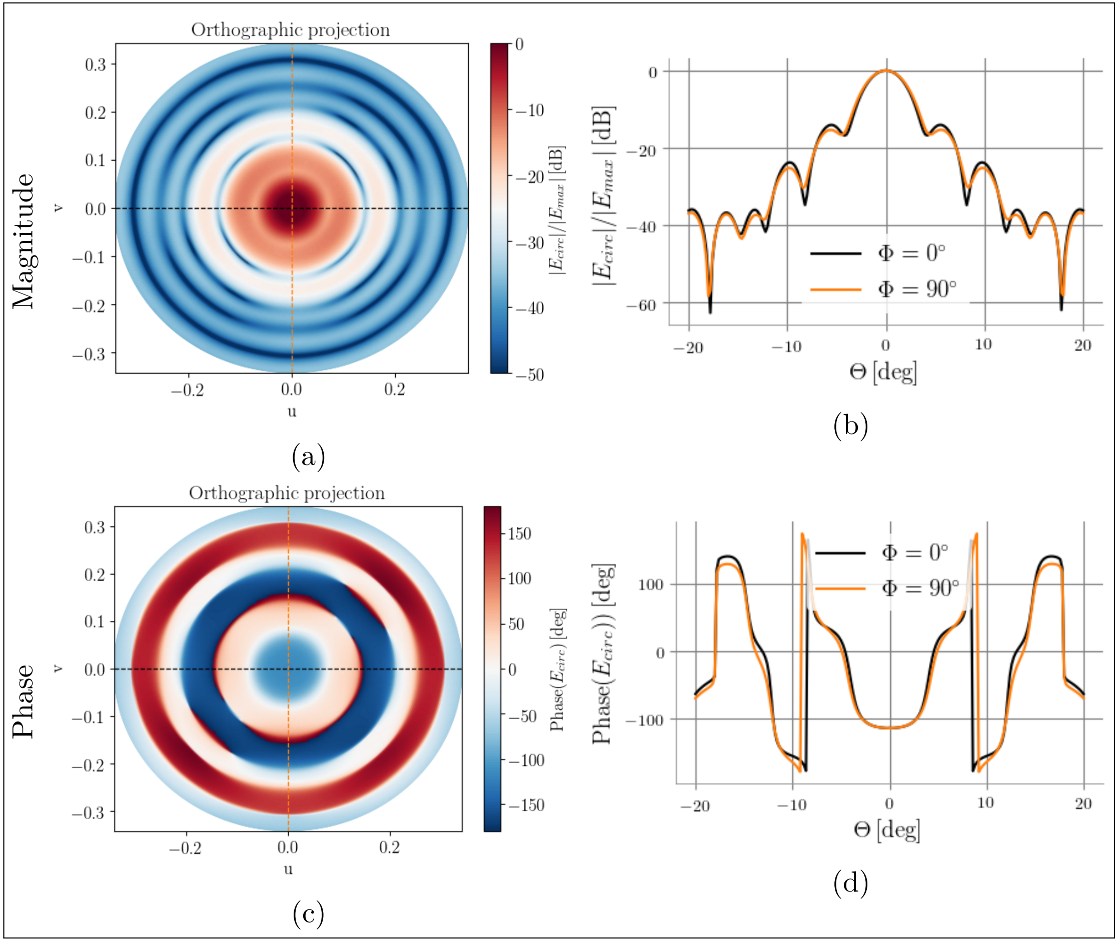

(a) (b) (c) (d)

Figure 3.38.: Continue

Coupling to a linearly polarized source

To allow a good coupling of the final receiver to the about Gaussian and linearly polarized beam of the local oscillator a good power coupling between the radiation pattern of the antenna and the Gaussian beam is necessary. A high rotational beam symmetry, high directivity with low side-lobe levels and a polarization with only little variations within the main beam of the antenna therefore is preferable. As a first quantitative measure of the antenna beam symmetry the difference in the 9 dB beam width in two different sectional planes in space can be considered.

The DS-antenna in Sec. 3.4.4 exhibit not a perfect but an acceptable rotational radiation pattern, directivity and side-lobe level.

Due to its self-complementary geometry the self-complementary logarithmic spiral antenna $S3$ shows the highest rotational symmetry in its beam patterns with frequency from all spiral antennas (see Fig. 3.36). In addition, sufficiently far away from the edge of its lower cutoff frequency its polarization is among all three spiral antennas closest to perfect circular (see Sec.3.4.4, Fig. 3.37). Consequently, for this spiral design not the highest, but the most uniformly continuous antenna pattern coupling to a linearly polarized Gaussian over its operating frequency band is expected. In contrast to antenna $S3$ and antenna $S4$ the $S1/S2$ logarithmic spiral antenna partly shows considerable deviations in the beam width for different cutting planes. For this antenna the variation in the beam width as occurring at 4.7 THz is expected to result in a reduction in the power coupling with a Gaussian beam up to 5 to 10%.

Since for the operation of the spiral antennas in a mixer module only their coupling with a linearly polarized LO source is relevant they suffer additional polarization-based power loss. The respective loss of a linearly polarized signal when coupling to a perfectly circularly polarized antenna by definition is 3 dB. Due to the slightly elliptical polarization of the spiral antennas the respective power losses will oscillate around about 3 dB according to the actual relative orientation of the major axis of the polarization ellipse and the E-field vector of the incoming signal. Additional coupling losses are possible because of a polarization-dependent reduced beam symmetry.

To depict the effect of the polarization-dependent behavior of the E-field of the spiral antennas on the coupling efficiency, in the following the radiation pattern is investigated for two different perspectives. These perspectives are chosen to visualize the antenna beam of the spirals encountered by differently linearly polarized signals. Once, for a linearly polarized signal with its E-field along the direction of the main axis of the polarization ellipse of the antenna, and second, the more realistic case, by a linearly polarized signal with the E-field along one of the orthogonal axis, in this case the x-axis.

The first view of the radiation pattern of the antennas, given in Fig. 3.39-3.41(a)-(d), depict the part of the E-field which points into the direction of the principle axis of the polarization ellipse that has been determined in main beam direction. It illustrates which part of the E-field is typically considered for potential maximum power transfer with a linearly polarized signal to couple in. The according direction of the principle axis is depicted for each antenna design in the small inset in the respective graphic (a).

The second perspective, Fig. 3.39-3.41(e)-(h), portrays the reality of the existing measurement conditions. As the receiver unfortunately will be mounted in a cryostat without the possibility to rotate it in situ during measurements and the polarization of the LO likewise is fixed with a horizontal or vertical polarization direction, in reality the LO source will only couple with the E-field either pointing into the vertical or horizontal direction.

As can be seen from Fig. 3.39-3.41 the rotational beam symmetry of all spiral antennas is considerably reduced when exclusively considering the E-field parts along one dedicated linear polarization axis, instead of the LHP part. The difference is especially obvious for the E-fields polarized along the x-axis. In comparison to the logarithmic spiral antenna S1/S2, the Archimedean spiral and the self-complementary spiral antenna S4 have a reduced but still considerably symmetric beam for the E-fields within the 9 dB beamwidth. The spiral design S1/S2, in contrast, exhibits a rather elliptical main beam as can be seen in Fig. 3.39.

An example of how this observed spatial and polarization-dependent asymmetry of the far field properties can affect the power coupling between two beam patterns is illustrated on base of the Archimedean beam pattern at 4.7 THz and a Gaussian beam with a beam waist around about 430.3 µm with its origin 71.8 µm shifted to the center of the antenna into the z-direction. The coupling efficiency of the beam patterns, the Gaussicity (see Appx. B.3), is calculated over a solid angle from $-10°$ to $10°$ for different alignments of the polarization vector of the Gaussian beam. It is about -3.4 dB if the Gaussian beam is polarized along the direction of the principle axis of the polarization ellipse of the antenna (as depicted in Fig.3.40(a)) and only -3.7 dB if the Gaussian E-field points into the direction of the minor axis instead. At first glance one might expect that these values represents the upper and lower limit for the beam coupling to be expected. However, revising that the axial ratio as well as the tilt angle are directional dependent (see Fig. 3.37), it becomes apparent that the Gaussicity can take values beyond both numbers. The same incident Gaussian beam with an E-field vector pointing into the x-direction (thus needs to couple to the E-field depicted in Fig.3.40(e)) or into the y-direction yields a Gaussicity about -4.61 dB or -5.61 dB, respectively. This example clearly demonstrates that even a slight deviation from an ideal circular polarization and a perfect beam symmetry can considerably decrease the power coupling to a linearly polarized source.

Logarithmic spiral antenna *S1/S2* on silicon lens

E-Field polarized along the major axis of the polarization ellipse

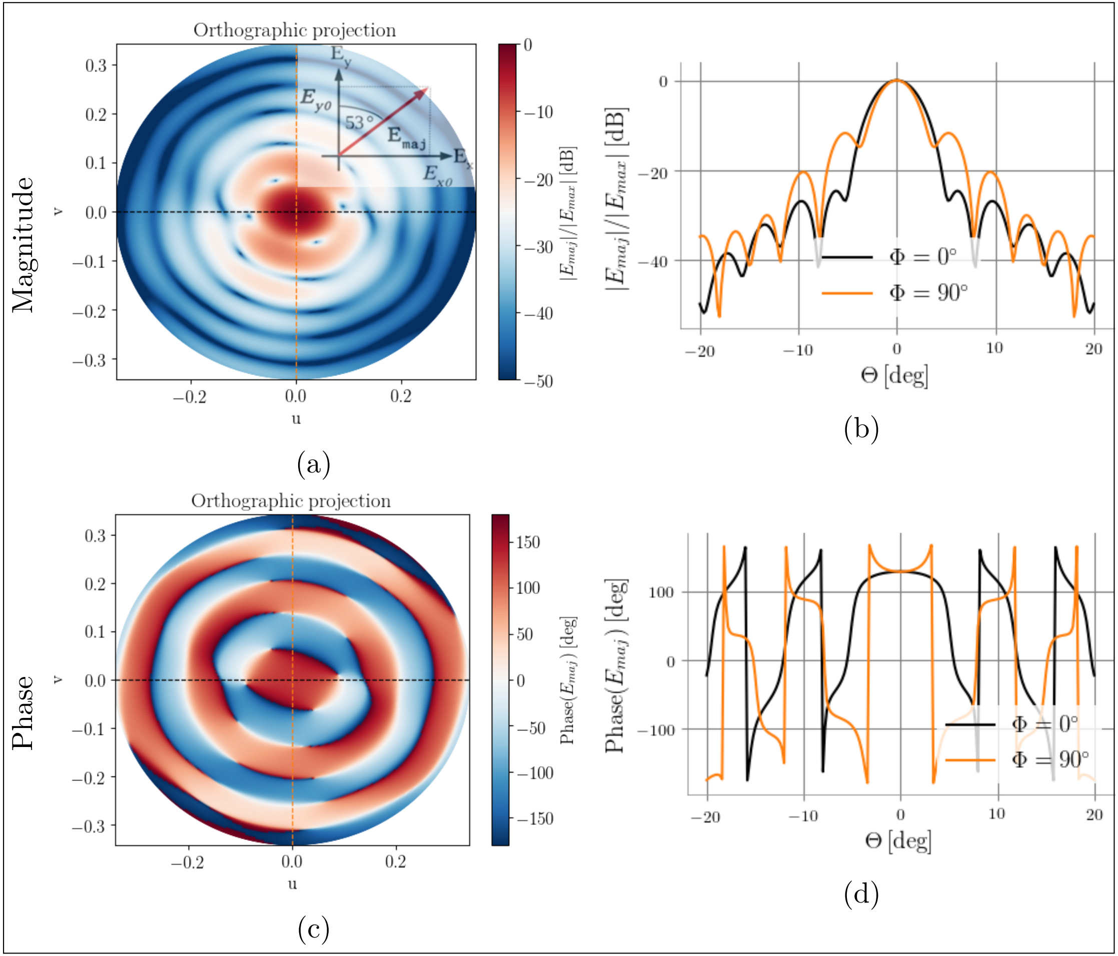

E-Field polarized along x-axis

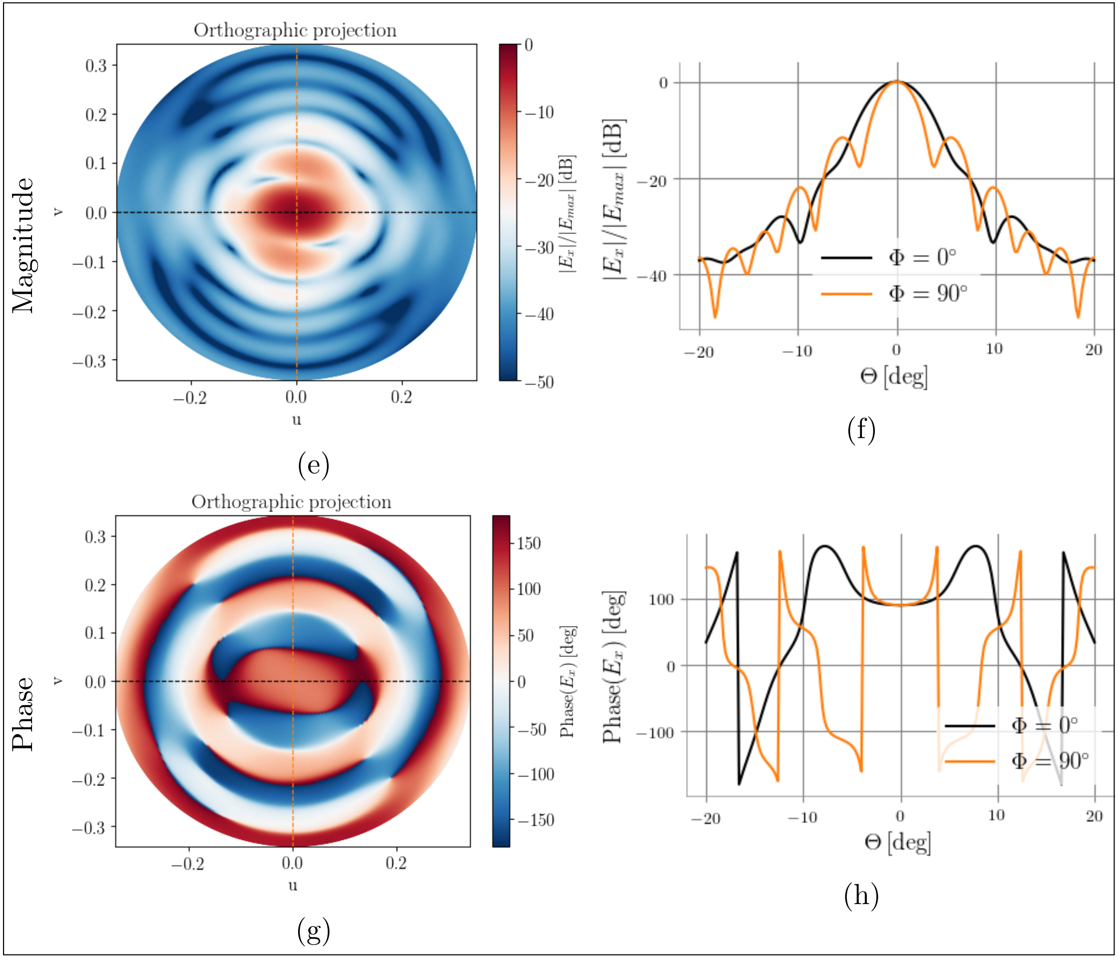

Figure 3.39.: Simulation results of E-field for logarithmic spiral antenna *S1/S2* at 4.7 THz.

Archimedean spiral antenna *S3* on silicon lens

E-Field polarized along the major axis of the polarization ellipse

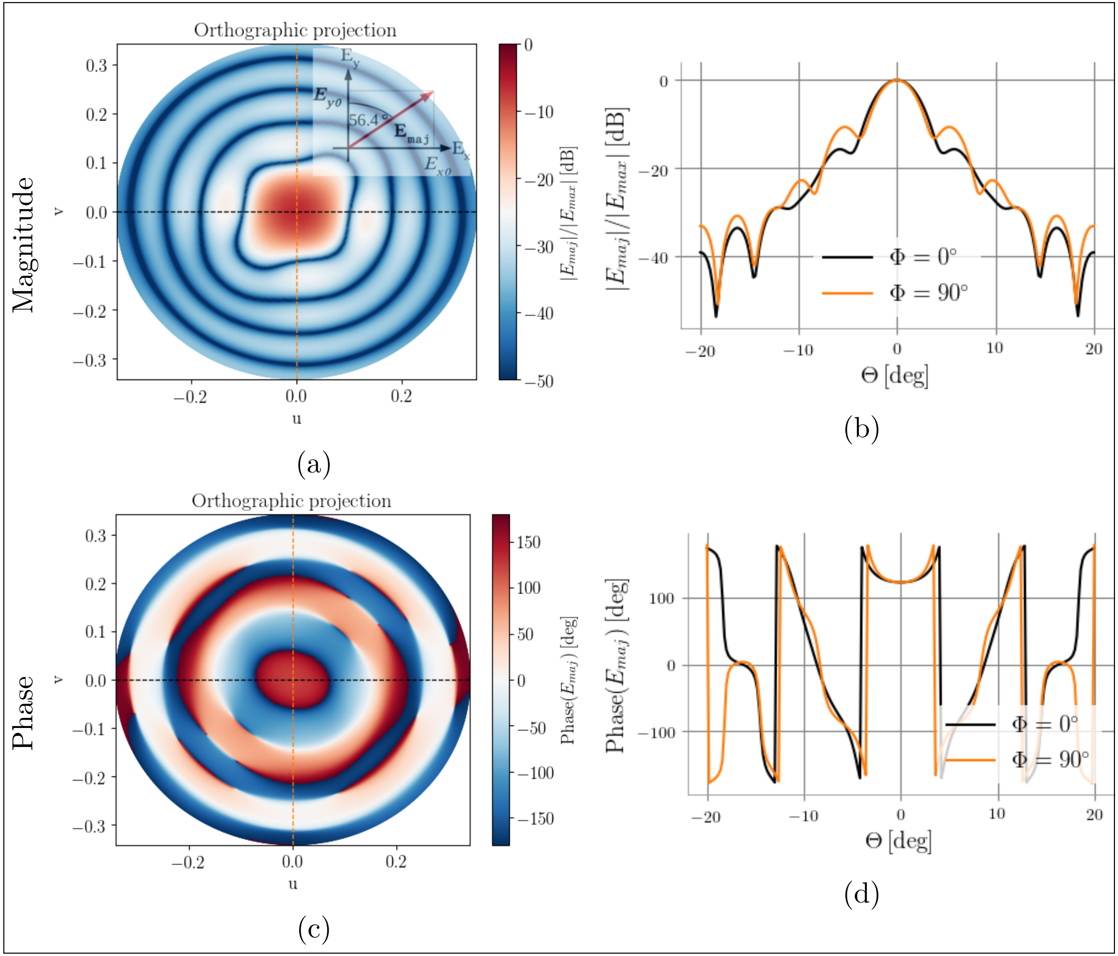

E-Field polarized along x-axis

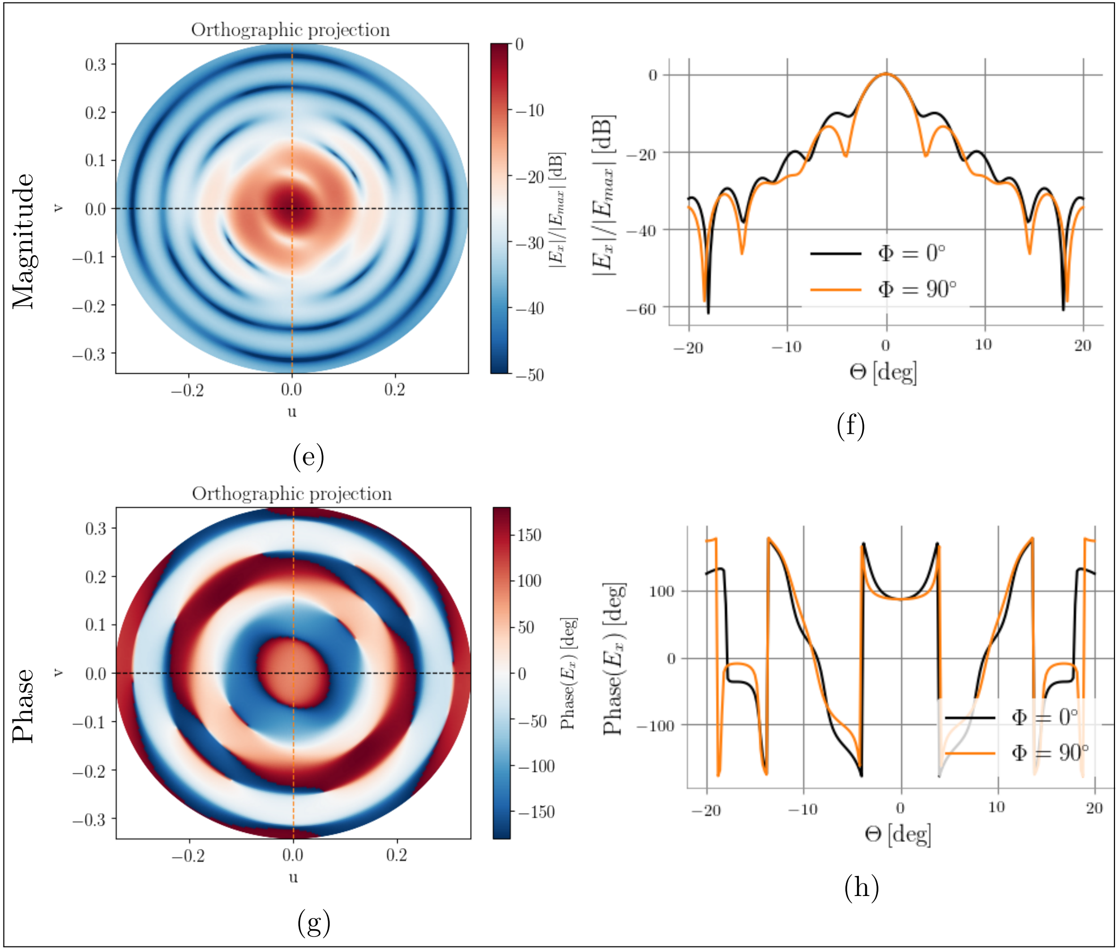

Figure 3.40.: Simulation results of E-field for Archimedean spiral antenna *S3* at 4.7 THz.

Logarithmic spiral antenna *S4* on silicon lens

E-Field polarized along the major axis of the polarization ellipse

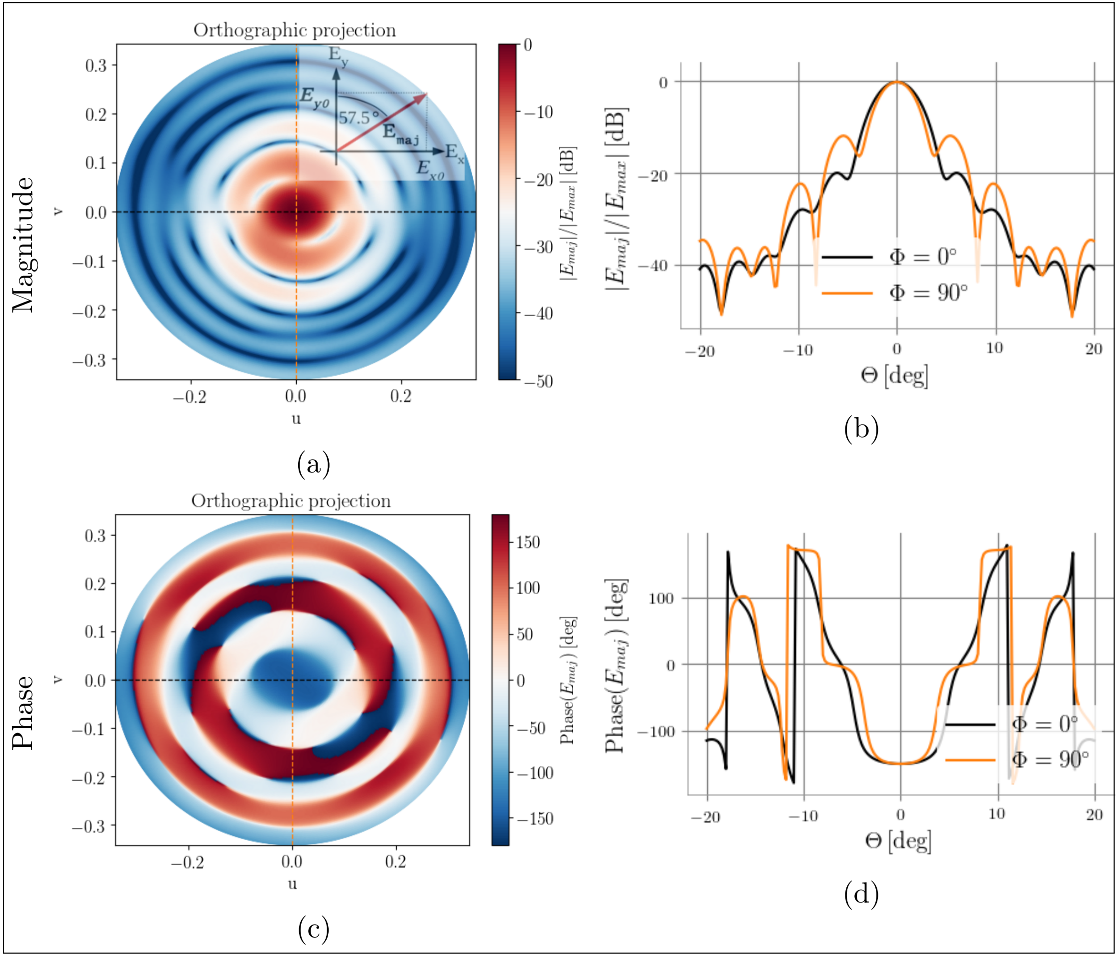

E-Field polarized along x-axis

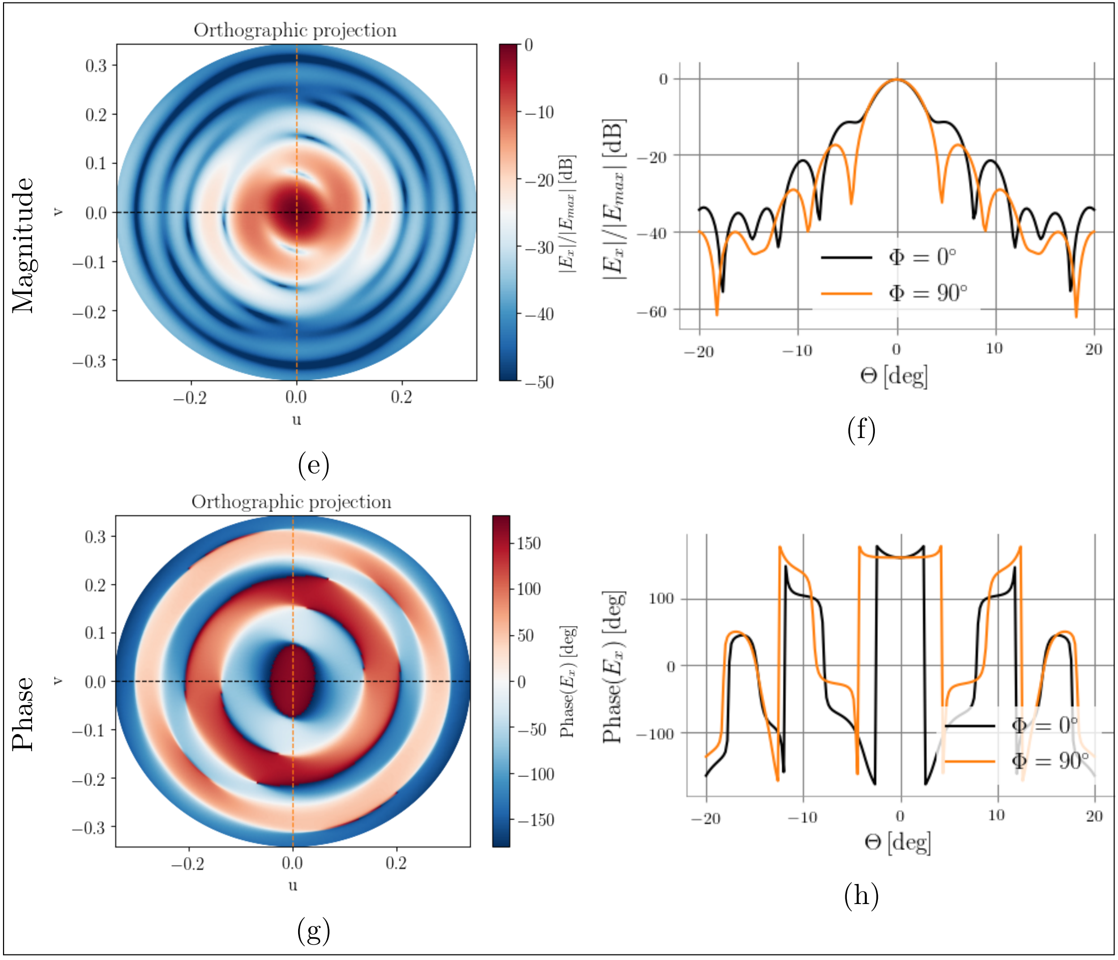

Figure 3.41.: Simulation results of E-field for self.-compl log-spiral antenna *S4* at 4.7 THz.

3.5. Summary and Conclusion

In this chapter different broadband and narrow-band RF-designs for operating frequencies around 10.7 THz and 4.7 THz have been introduced. To draw a conclusion which of the designs is the most favorable in terms of power coupling to an external Gaussian source, it is necessary to look at two key aspects that are determining for the Gaussian coupling and which to first order can be treated separately. Following the path of an incoming signal this is firstly the power coupling of an external Gaussian source to the beam pattern of the antenna, and secondly the power transfer of the in-coupled signal to the HEB-element at the feeding point of the antenna. The first aspect, the Gaussicity (see Appx. B.3), is dependent on the beam pattern of the antenna including its polarization. Because of insufficient computational resources, one has to keep in mind that the conclusions are based on modelling that could only be done up to a frequency of 5 THz. The second key quantity assesses the impedance match at the terminal base of the antenna. The according simulations are carried out on designs where the lens is replaced by a thick slab of silicon that synthesizes a semi-infinite half space of silicon by applying open boundaries with a very low reflection level at the backside of the slab. Since this requires significantly less computational resources , contrary to the beam patterns, the second aspect can be modelled up to the maximum frequency of 12 THz. The efficiency is optimal if the input impedance of the antenna at its feeding point is a conjugate match to the impedance at its termination. For this work the impedance match is restricted by the material parameters the NbN bolometer microbridge, and the fabrication constraints. It should be noted that the microbridge is assumed to offer a real-valued resistance and any possible inductance is neglected due to its large aspect ratio. An imaginary part of the input impedance of the antenna base thus directly yields a reduction of energy transfer due to reflections of the incoming signal.

The following final assessment and comparison of the different antenna designs mainly resort on both aforementioned aspects.

3.5.1. Comparison of broadband and narrow-band antennas

For a final comparison of the broadband spiral antenna designs with a narrow-band double-slot antenna design, important antenna characteristics are summarized in Tab. 3.7 for an operating frequency at 4.7 THz where the beam patterns were just computable with the available computational resources with CST. It should be noted that the Gaussicity (as defined in Appx. B.3) for the broadband-antenna spiral antennas has been optimized to the best of the knowledge and belief, however, due to the vectorial-dependent asymmetry of the beam profiles (compare Sec. 3.4.4) it cannot be excluded that there might be a more favorable Gaussian beam in terms of coupling than those that has been found out during the fit-procedure for another alignment of the polarization. Here, the best coupling was searched for with a Gaussian beam that is linearly polarized in direction of the principle axes of the polarization ellipse of the antenna beam in main beam direction. The fit-procedure further exhibited for all 4 designs that there exist plenty of local maxima for the beam coupling. The corresponding Gaussicity values are up to 10 % smaller than the optima given in the Table. These maxima exist within the here used lateral range of 8 to 10 mm which were investigated to find the optimal origin of the Gaussian-beam with beam waists between 350 to 480 µm. It justifies the assumption that there is a sufficiently large lateral range in boresight direction with enough power coupling to enable an alignment of the receiver for practical purposes (as indeed has been seen during the alignment of the assembled HEB-detectors with respect to the FTS (see Sec. 7.2.4)).

At this point it further should be noted that the reflection at the antenna-vacuum interface has not been considered yet. The comparable beam sizes and comparable radiation efficiencies of the designs (see Tab. 3.7) pinpoint to reflection losses of the same order of magnitude. In general, losses that are connected with the silicon-lenses used for quasi-optical mixer designs in literature commonly refer to reflection losses that are reduced by applying an anti-reflection coating but do not include dissipation losses in the substrate. For reasons already discussed in Sec. 3.1.2 an anti-reflection layer is not used in this work and consequently results into reflection losses around about -1.52 dB at maximum. Based on the measurement results in chapter 5 it could be demonstrated that HRFZ silicon is a low-loss substrate in the operational frequency regime. The dissipation losses to be expected in the silicon lens at cryogenic temperatures are 0.09-0.10 dB at maximum (see Sec.5.2.7 and Appx. B.1.1).

As can be seen from Tab.3.7 the Archimedean spiral antenna design is from all spiral antenna designs the most favorable in terms of both, Gaussian beam pattern efficiency and impedance matching at the HEB-antenna interface. The polarization-based coupling loss for an alignment with the principle axis of the polarization ellipse of the antenna is smaller in comparison to the other spiral antennas (compare axial ratios in the table). It enables to reach a considerably higher Gaussicity for the Archimedean spiral antenna although the beam pattern for the $S4$ design is more symmetrical. In the second place of the ranking order is the $S1/S2$ spiral design, followed by the self-complementary spiral antenna.

The same ranking order of the most favorable broadband antenna with regard to the best impedance matching between the antenna terminal and the HEB-element is also discernible over the rest of the frequency bandwidth of the antennas which could be modelled. Figure 3.42 shows the corresponding impedance match efficiency at the antenna terminals to the load for all three designs. The colored areas mark the ranges in which the power transfer is to be expected when using NbN as a bridge material. The solid lines depicts the ideal case when the mixing elements at the antennas' feeding ports exhibit a resistance equal to the real parts of the antennas' feedpoint impedances at 10.7 THz. It is obvious that the self-complementary antenna, even for the optimum case which cannot be achieved with the present NbN, suffers from increasing losses with frequency. It likewise demonstrates the need of other broadband antenna designs besides the commonly used self-complementary log-spiral antennas since the losses at the HEB-antenna interfaces to be expected with increasing frequencies outweigh the benefits of better coupling to a Gaussian beam due to high beam symmetry. The Archimedean antenna at the same time offers a favorable beam pattern and favorable impedance match conditions and therefore is believed to present an equivalent and in many cases even better candidate to achieve a high power coupling with a Gaussian beam at high frequencies than a logarithmic-spiral

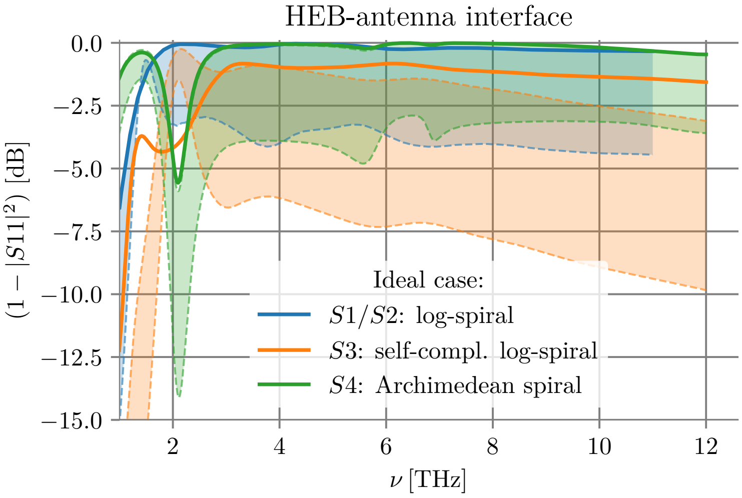

Figure 3.42.: Impedance match efficiency expected for the three broadband antenna designs $S1/S2$, $S3$ and $S4$. The power transfer is calculated based on the feedpoint impedance curves of the antennas simulated with the simulation software. The bold lines depict the optimum case where the resistance of the load at the antenna port equals the real part of the input impedances of the antenna ports at 10.7 THz ($S1/S2$: 49 Ω, $S3$: 103.6 Ω, $S4$: 38.2 Ω). The colored areas shows the regions where the efficiency can be expected when using the present NbN as HEB material.

antenna adapted for improved impedance match. Based on the results the Archimedean spiral although typically used for distinctly lower frequencies (some 10 GHz to 100 GHz) emerged to be the best choice from all spiral antennas. At 4.7 THz it reaches an overall Gaussian-coupling efficiency of 39.4 %.

The double-slot antenna compared to the other designs still exhibits by far the best power coupling to a Gaussian beam. Including the radiation efficiency the design roughly enables a Gaussian-coupling efficiency of 49 %. This efficiency is within the range that is expected for lower frequency double-slot antennas that are mounted on a lens with the respective ratio between the extension length of the here used lens and its radius [52]. By applying a lambda quarter matching-cap layer on the lens the Gaussian coupling efficiencies are expected to increase to about 64% and 57% for the double-slot antenna and for the Archimedean spiral antenna, respectively.

@ 4.7 THz	$S1/S2$ log-spiral	$S3$ Archimedean spiral	$S4$ self-compl. log-spiral	DS double-slot
Gaussicity	47.6 %	57.1 %	45.0 %	67.1 %
η_{imp} ($R_{mix} = Re(Z_{fp})$)	99.369 %	99.959 %	94.525 %	95.9 %
Gaussicity $\times\eta_{\text{imp}}$	47.3 %	57.1 %	42.5 %	64.4 %
η_{rad}	0.70	0.69	0.74	0.76
AR	1.486	1.646	1.224	–
D_0 in maj.ax.	29.8 dBi	29.6 dBi	30.0 dBi	29.9 dBi

Table 3.7.: Antenna charactersistics of four different antenna designs at 4.7 THz. The Gaussicity (the Gaussian beam pattern coupling efficiency) is calculated for the spiral antennas $S1 - S4$ assuming a Gaussian beam whose linearly polarized E-field is aligned with the major axes of the polarization ellipse of the antenna beams in main beam direction. The impedance match efficiency $\eta_{\text{imp}} = (1 - |S11|^2)$ is calculated assuming that the real part at the feeding point of the antenna $Re(Z_{fp})$ at 4.7 THz is perfectly matched by the resistance of the mixing element R_{mix} ($S1/S2$: 49 Ω, $S3$: 87.3 Ω, $S4$: 55.9 Ω, DS: 105 Ω). The radiation efficiency of the antennas, η_{rad}, refers to the reflection losses at the lens-vacuum interface and does not include potential dissipation losses in the metal sheets or the lens substrate. AR is the axial ratio of the major to the minor axes of the polarization ellipse of the E-field in main beam direction. D_0 is the directivity of the part of the antenna beam which is linearly polarized either in direction of the major axes of the polarization ellipse in main beam direction in case of the spiral antennas or in direction of the y-axis (co-polarized amount) for the double slot antenna.

4. Optics

This chapter introduces the software that has been developed to calculate the effect of a silicon lens on the beam pattern of an antenna. The first two sections give a short wrap-up of the underlying method of the software. Subsequently, the software modules are introduced and a comparison with 3D EM simulations with the commercial software CST[66] is given.

4.1. Diffraction of high-frequency electromagnetic waves

Diffraction of electromagnetic waves at arbitrary surfaces neither is a straightforward nor an easily analytically predictable issue and as such subject of numerical calculations. Standard techniques to obtain numerical solutions are based on finite element methods or methods of moments. These techniques are used for CST[66] and HFSS[89], two of the most popular simulation softwares used within HF simulation community. The drawback of those numerical methods is that they require a discretization of the total volume of the space, including objects and surrounding, into cells with typical cell dimensions of equal or less than $\lambda/10$. Predictions for increasing frequencies need a finer resolution of the space by an increasing amount of cells. As such, the limited availability of computational resources in terms of memory and computationally time restricts the calculability of numerical solutions to problems at increasing frequencies. A detailed investigation about the limitations of simulating antenna lens systems with CST is given in [5, Ch. 3]. A common volume of a silicon lens ($\epsilon = 11.4$) used for integrated lens antennas is about 270 mm^3. Its discretization into cubic cells of $\lambda/10$ size requires about $340 \cdot 10^9$ mesh cells. This large number does not even include the surrounding environment or the integrated antenna system on the backside of the lens of which some components require an especially fine resolution. The numerical simulation of the complete lens-antenna system by the commercial software CST is not possible within the computational capabilities of our work group. However, with the intent still to benefit from the highly sophisticated CST solver, the calculation is split into two parts, where the CST software is used to calculate the response of the antenna system within the near field, and the influence of the lens to the near field is solved separately with a different technique. The strategy proposes to numerically solve the antenna near field in CST by adding the largest possible substrate but not an entire lens on the antenna structures. Subsequently, the near field is used for the calculation that includes the effect of the lens. There are several methods to calculate the diffraction of high-frequency electromagnetic waves by dielectric, conducting or coated bodies which in great detail are discussed in [13]. The methods, used for the here presented software, are based on a simplified form of the Geometrical theory of diffraction (GTD) and Spectral theory of diffraction (STD). All required theoretical basics are summarized in the Appx. A.

4.2. Spectral domain Ray Tracing method

To calculate the propagation of a complex electromagnetic field, the software, developed in this work, uses a plane wave decomposition of the electromagnetic field and Geometrical Optics (GO) to trace the field through space. The combination of these two techniques was first used by Ethezazi [48] who called it the *spectral domain ray tracing method* (SRT). A big advantage of this method is that it can handle refraction at interfaces in the near and in the far field of any electromagnetic source[49]. The electromagnetic field is expressed as the superposition of plane waves[30] which are represented in terms of parallel ray tubes undergoing diffraction and reflection while propagating through space. The electromagnetic field at any point in space is given by the sum of all tubes of rays which arrive at this point. To evaluate the field along each ray-pencil corresponding diffraction coefficients given by Fresnel's equations and the divergence of the ray-pencil are taken into account (see Appx. A.1.2). Tracking all possible ray configurations from each point of the plane of the source field to investigate which of the rays arrives at a certain observation point is, unfortunately, a very time-consuming endeavor. A much more efficient treatment is to use a reciprocal computations of the trajectories. For this, rays are launched in a reverse sense, i.e., backwards from the observation point to the source plane instead of outgoing from the source (see Sec.4.3.2).

The schematic procedure of the SRT will be shortly sketched by means of an example. An electromagnetic field, $\mathbf{E_{start}} = \mathbf{E}(\mathbf{x}, \mathbf{y}, \mathbf{z} = \mathbf{0})$, is only well-known at a certain plane which without loss of generality is denoted here the x-y-plane. In a certain distance to the source plane, an optical element, a collective lens made of silicon, is placed. Using the Fourier transform $\widetilde{\mathbf{E_k}}$ of the field, the field propagating in free space can be rewritten in terms of plane waves of form

$$E_x(x,y,z) = \iint \widetilde{E_x}(k_x,k_y,k_z)e^{-i\mathbf{kr}}\,\mathrm{d}k_x\,\mathrm{d}k_y, \tag{4.1}$$

$$E_y(x,y,z) = \iint \widetilde{E_y}(k_x,k_y,k_z)e^{-i\mathbf{kr}}\,\mathrm{d}k_x\,\mathrm{d}k_y, \tag{4.2}$$

$$E_z(x,y,z) = \iint \widetilde{E_z}(k_x,k_y,k_z)e^{-i\mathbf{kr}}\,\mathrm{d}k_x\,\mathrm{d}k_y, \tag{4.3}$$

with

$$\widetilde{E_x}(k_x,k_y,k_z) = \frac{1}{4\pi^2}\iint E_x(x,y,z=0)e^{-i\mathbf{kr}}\,\mathrm{d}x\,\mathrm{d}y, \tag{4.4}$$

$$\widetilde{E_y}(k_x,k_y,k_z) = \frac{1}{4\pi^2}\iint E_y(x,y,z=0)e^{-i\mathbf{kr}}\,\mathrm{d}x\,\mathrm{d}y, \tag{4.5}$$

$$\widetilde{E_z}(k_x,k_y,k_z) = -\frac{\widetilde{E_x}(k_x,k_y,k_z)\cdot k_x + \widetilde{E_y}(k_x,k_y,k_z)\cdot k_y}{k_z}, \tag{4.6}$$

and

$$k_x^2 + k_y^2 < \mathbf{k}^2 \qquad \text{, for evanescent waves} \tag{4.7}$$

$$k_x^2 + k_y^2 > \mathbf{k}^2 \qquad \text{, for non-evanescent waves} \tag{4.8}$$

$$k_z = -i\sqrt{\mathbf{k}^2 - k_x^2 - k_y^2} \qquad \text{, for evanescent waves} \tag{4.9}$$

$$k_z = \sqrt{\mathbf{k}^2 - k_x^2 - k_y^2} \qquad \text{, for non-evanescent waves} \tag{4.10}$$

$$|\mathbf{k}| = \frac{2\pi}{\lambda}. \tag{4.11}$$

As simulations depend on a discretization of space, the integral equations are approximated by sums

$$E_x(x,y,z) = \sum_{m=-\infty}^{+\infty}\sum_{n=-\infty}^{+\infty} \widetilde{E_x}(m\mathrm{d}k_x, n\mathrm{d}k_y, k_{z,mn})e^{-i(mk_xx+nk_yy+k_{z,mn}z)}\,\mathrm{d}k_x\,\mathrm{d}k_y, \tag{4.12}$$

$$E_y(x,y,z) = \sum_{m=-\infty}^{+\infty}\sum_{n=-\infty}^{+\infty} \widetilde{E_y}(m\mathrm{d}k_x, n\mathrm{d}k_y, k_{z,mn})e^{-i(mk_xx+nk_yy+k_{z,mn}z)}\,\mathrm{d}k_x\,\mathrm{d}k_y, \tag{4.13}$$

$$E_z(x,y,z) = \sum_{m=-\infty}^{+\infty}\sum_{n=-\infty}^{+\infty} \widetilde{E_z}(m\mathrm{d}k_x, n\mathrm{d}k_y, k_{z,mn})e^{-i(mk_xx+nk_yy+k_{z,mn}z)}\,\mathrm{d}k_x\,\mathrm{d}k_y, \tag{4.14}$$

with

$$mk_x^2 + nk_y^2 < \mathbf{k}^2 \qquad \text{, for evanescent waves} \tag{4.15}$$

$$mk_x^2 + nk_y^2 > \mathbf{k}^2 \qquad \text{, for non-evanescent waves} \tag{4.16}$$

$$k_z = -i\sqrt{\mathbf{k}^2 - (mk_x)^2 - (nk_y)^2} \qquad \text{, for evanescent waves} \tag{4.17}$$

$$k_z = \sqrt{\mathbf{k}^2 - (mk_x)^2 - (nk_y)^2} \qquad \text{, for non-evanescent waves} \tag{4.18}$$

$$|\mathbf{k}| = \frac{2\pi}{\lambda}. \tag{4.19}$$

and

$$\widetilde{E_x}(k_x, k_y, k_z) = \frac{1}{4\pi^2} \sum_{j=-\infty}^{+\infty} \sum_{l=-\infty}^{+\infty} E_x(j\mathrm{d}x, l\mathrm{d}y, z=0) e^{-ik_x \cdot j\mathrm{d}x + k_y \cdot l\mathrm{d}y} \, \mathrm{d}x \, \mathrm{d}y, \tag{4.20}$$

$$\widetilde{E_y}(k_x, k_y, k_z) = \frac{1}{4\pi^2} \sum_{j=-\infty}^{+\infty} \sum_{l=-\infty}^{+\infty} E_y(j\mathrm{d}x, l\mathrm{d}y, z=0) e^{-ik_x \cdot j\mathrm{d}x + k_y \cdot l\mathrm{d}y} \, \mathrm{d}x \, \mathrm{d}y, \tag{4.21}$$

$$\widetilde{E_z}(k_x, k_y, k_z) = -\frac{\widetilde{E_x}(k_x, k_y, k_z) \cdot k_x + \widetilde{E_y}(k_x, k_y, k_z) \cdot k_y}{k_z}. \tag{4.22}$$

The final expressions (4.12) - (4.14) for the E-field can be considered as the sum over plane waves with amplitude $\widetilde{E}_{(x,y,z)} \cdot \mathrm{d}x\mathrm{d}y$ moving into the direction $\mathbf{k_{mn}} = (m\mathrm{d}k_x \; n\mathrm{d}k_y \; \mathrm{d}k_{z,mn})^\intercal$.

In the next step, the plane waves are related to tubes of rays. Each tube consists of one middle ray pointing into the direction of propagation $\mathbf{k_{mn}}$ which is surrounded by four rays defining the edges of the tube transporting the wave with amplitude $\widetilde{E}_{(x,y,z)}$ through space. The wavefront and amplitude of the wave that is carried by each tube is described by its curvature matrix, Q, and divergence factor, DF, which are defined in the Appx. A.1.2. For time- and cost-saving reasons, each ray tube starts from an observation point where its middle and surrounding tube rays converge at and ends at the source plane. The interface area between source plane and ray tube, presenting the spectral differential surface, $\mathrm{d}\mathbf{k}_t = \mathrm{d}k_x\mathrm{d}k_y$, can be calculated as the area formed by the intersection points of the four surrounding rays with the source plane. The E-field of the tube of rays which originates from point $P0$ at $\mathbf{r_0}$ with the spectral differential surface $\mathrm{d}\mathbf{k}_t$ into the direction $\mathbf{k}_{mn}$ through the empty space to point $P1$ at $\mathbf{r_1}$, where d_1 is the distance between $P0$ and $P1$, is given by

$$\widetilde{\mathbf{E}}_{P1} = \widetilde{\mathbf{E}}_{P0} \cdot e^{-i\mathbf{k_{mn}}\mathbf{r_1}} \mathrm{d}\mathbf{k}_t$$

$$= \widetilde{\mathbf{E}}(\mathbf{k}_{mn}) \cdot e^{-i\mathbf{k_{mn}r_0} - ik_{mn}d_1} \mathrm{d}\mathbf{k}_t. \tag{4.23}$$

The initial E-field amplitude $\widetilde{\mathbf{E}}_{P0}$ at the starting point of the source plane is determined by the component $\widetilde{\mathbf{E}}(\mathbf{k}_{mn})$ of the source field Fourier transform belonging to the wavevector $\mathbf{k}_{mn}$. Its phase, $\mathbf{k_{mn}r_1}$, is referred to the origin of the source plane $(0, 0, 0)$ at point $P0$. Following the convention of Appx. A.1.2 concerning the reference frames attached to the optical system, the phase $\mathbf{k_{mn}r_1}$ of the field from point $P0$ to $P1$ is given by the product of both modulus $k_{mn}d_2$.

When the tube intersects the surface of an arbitrarily shaped optical object, which in this example is a collecting lens, it is refracted. By means of Snell's law, the ray-direction after refraction is determined for all five, tube-defining rays. Using equations (A.24) and (A.25), the according curvatures after refraction are calculated. Since the field has been decomposed into plane waves at the source plane, each tube is assigned to an initial plane surface of wavefronts corresponding to an initial curvature matrix:

$$Q_{in} = \begin{pmatrix} 0 & 0 \\ 0 & 0 \end{pmatrix}. \tag{4.24}$$

The divergence factors DF_r and DF_t for the reflected and transmitted beams, respectively (see description in Appx. A.1.2), are obtained by inserting the corresponding radii of curvatures into equation (A.22). To apply Fresnel's reflection r and transmission coefficients t (see Appx. A.1.2) it is necessary to decompose the E-field amplitude into parts parallel and perpendicular to the plane of incidence which is indicated here by $\|$ and $\perp$, respectively. Using this notation, the field amplitudes arriving at point $P2$ and $P2'$ is given by

$$\begin{pmatrix} \widetilde{E}_\perp(P2) \\ \widetilde{E}_\|(P2) \end{pmatrix} = \begin{pmatrix} t_\perp & 0 \\ 0 & t_\| \end{pmatrix} \begin{pmatrix} \widetilde{E}_\perp(P1) \\ \widetilde{E}_\|(P1) \end{pmatrix} DF_2 \cdot e^{-ik_{(mn,P2)}d_2}, \text{ and} \tag{4.25}$$

$$\begin{pmatrix} \widetilde{E}_{\perp,P2'} \\ \widetilde{E}_{\|,P2'} \end{pmatrix} = \begin{pmatrix} r_\perp & 0 \\ 0 & r_\| \end{pmatrix} \begin{pmatrix} \widetilde{E}_\perp(P1) \\ \widetilde{E}_\|(P1) \end{pmatrix} DF_2' \cdot e^{-ik_{(mn,P2')}d_2'}. \tag{4.26}$$

Following this principle, the E-field can be tracked all the way along its trajectory to the observation point.

For the purpose of this work, the electromagnetic field pattern of the antenna needs to be find out in front of the lens corresponding to a distance of several hundred times of the wavelength to the source field. For such large distances, the contributions of the evanescent waves $\mathbf{E}_{evan}$ can be neglected as briefly shown in the following and are not considered in the developed software.

The contribution of the evanescent waves to the electromagnetic field at a certain point in space (x, y, z) becomes obvious considering the following estimation

$$\mathbf{E}_{evan}(x, y, z) = \sum_{n=1}^{\infty} \sum_{m=1}^{M} \widetilde{\mathbf{E}}(n \cdot \Delta k_x, m \cdot \Delta k_y) e^{-i(n \cdot \Delta k_x \cdot x + m \cdot \Delta k_y \cdot y - |k_z| \cdot z)} \Delta k_x \Delta k_y \tag{4.27}$$

with

$$k_z = -i \cdot \sqrt{(n \cdot \Delta k_x)^2 + (m \cdot \Delta k_y)^2 - k_0^2} \tag{4.28}$$

and the wavenumber $k_0 = 2 \cdot \pi/\lambda$. As the condition for the evanescent waves implies that $(n \cdot \Delta k_x)^2 + (m \cdot \Delta k_y)^2 > k_0^2$, it is convenient to write

$$(n \cdot \Delta k_x)^2 + (m \cdot \Delta k_y)^2 = k_0^2 \Delta_{n,m}^2 \tag{4.29}$$

$$\Delta_{n,m}^2 > 1 \tag{4.30}$$

With $z = \xi \cdot \lambda = \xi \cdot 2\pi/k_0$, $\xi > 1$, the term $e^{-z \cdot |k_z|} \Delta k_x \Delta k_y$ can be rewritten to

$$e^{-z \cdot |k_z|} \Delta k_x \Delta k_y = e^{-\sqrt{\Delta_{n,m}^2 - 1} \cdot \xi \cdot 2\pi} \Delta k_x \Delta k_y \tag{4.31}$$

and thus is a rapid decreasing function with increasing ξ that allows to neglect the terms of the evanescent waves for $\xi >> 1$.

4.3. Schematic of the software modules

The software is structured modularly and can be extended by *any* analytically definable geometrical bodies. A set of common two-and three-dimensional bodies is already available allowing calculations with standard types of lenses like collective , bullet, or hyper-hemisphere lenses and other common optical elements.

The ray tracing and the calculation of the E-field contribution are treated separately, in two main modules. Given an observation point, the backward ray tracing module `backtrac` calculates the beam path of those tubes of rays originating from a specified radiation source and reaching the point of observation. The user can set the ray density as well as the solid angle over which the rays are traced. The direction $\hat{\mathbf{k}}_{P_i}$ for each ray that is launched from an individual observation point P_i, by default, is defined using spherical coordinates

$$\hat{\mathbf{k}}_{P_i} = \begin{pmatrix} \sin(\Theta)\cos(\Phi) \\ \sin(\Theta)\sin(\Phi) \\ \cos(\Theta) \end{pmatrix}.$$

Given the number of rays per solid angle, defined by Θ_{max}, Θ_{min}, Φ_{max}, and Φ_{min}, the software uniformly distributes the rays with equidistant angle distances, $\Delta\Phi$ and $\Delta\Theta$, between each others as sketched in Fig. 4.1.

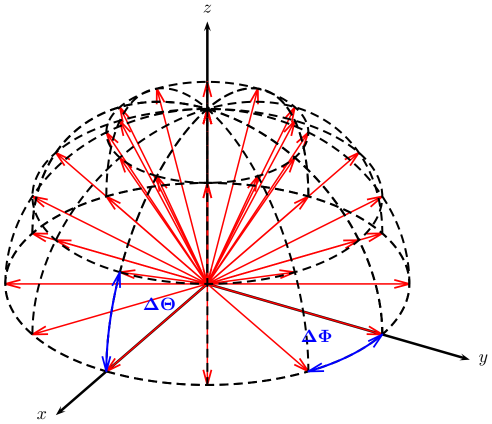

Figure 4.1.: Ray distribution undertaken by the new `backtrac` module for a given solid angle and 35 rays: The opening angle composes the whole half space. The software uniformly distributes the rays with equidistant angle-distances in $\Delta\Phi$ and $\Delta\Theta$.

The `backtrac` module stores three data sets.

1. The interaction points of the tube of rays with the objects.
2. The chronology of interaction with the objects, and
3. the dielectric constants at the interfaces of interactions.

The second main module `fical` uses the datasets compiled by the `backtrac` module to determine the E-field carried by the tubes of rays to the previously defined observation point. As the calculation of the E-field for each observation point is an independent, stand-alone process, the calculations allow for a very efficient parallelization of the software when running on suitable machines like the Cologne High Efficiency Operating Platform for Science (CHEOPS).

4.3.1. Feed-in of the field information

The information about the initial electromagnetic field can be included either by using an exact analytical expression (if available) or by providing discrete values for the field in dependence of the related location. In the latter case, which is relevant for this thesis as data are imported from the simulations software CST Studio suite, there are several requirements which need to be fulfilled to obtain a reliable simulation result. The field data which initially refer to the space domain need to be converted to the Fourier domain $\mathbf{k}$ (for instance by using a Fast Fourier Transform (FFT) algorithm). The discrete field values $\mathbf{E}^i$ in the $\mathbf{k}$-domain are stored in dependence of the respective wavevectors

$$\mathbf{k}^i = \begin{pmatrix} k_x^i \\ k_y^i \\ k_z^i \end{pmatrix}.$$

The largest value for k_x and k_y that is required to apply the spectral domain ray tracing method is given by the wavenumber $\max(k_x) = \max(k_y) = \frac{2\pi}{\lambda}$, where the smallest value is $\min(k_x) = \min(k_y) = -\frac{2\pi}{\lambda}$. Using a dataset of discrete field values it needs to be carefully considered to store enough data points to:

a) receive a sufficiently high resolution of the spectral field, and

b) assure that the absolute value of the highest and lowest value for k_x and k_y is given by the wavenumber

Using a set of uniformly distributed data points the largest value in k_x and k_y is determined by the distance Δx and Δy between two neighboring data points, respectively[135]:

$$\max(k_x) = \frac{1}{2\Delta x} \text{ and}$$
$$\max(k_y) = \frac{1}{2\Delta y}.$$

Inserting the maximum of k_x and k_y given by the wavenumber leads to the inequality conditions

$$\Delta x < \frac{\lambda}{4\pi} \text{ and} \tag{4.32}$$
$$\Delta y < \frac{\lambda}{4\pi}, \tag{4.33}$$

which must be fulfilled to apply the spectral domain ray tracing method.

4.3.2. Backward Ray Tracing module

In the reciprocal treatment of beam paths, not the entirety of all rays originating from a radiation source is considered but only rays of all possible directions from a specified point of observation are traced back to the radiation-source. By this, a huge amount of irrelevant ray paths can be excluded for calculations if only information about a certain region and not the whole space is needed. Since this is true for all practical applications, the principle of backward ray tracing is applied to the developed `backtrac` module.

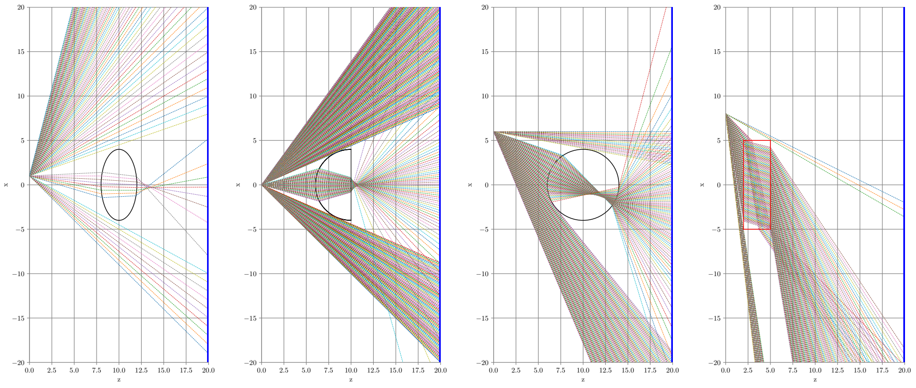

(a) Ellipsoid (b) Half sphere (c) Sphere (d) Plate

Figure 4.2.: Ray trajectories calculated with my software module `backtrac` for some geometrical bodies presenting standard candidates for optical elements. All four objects consist of silicon with a dielectric constant of $\epsilon_s = 11.9$. Given is a cross-section through the respective test setups depicting all rays which lie in the xz-plane at $y = 0$ originating from an arbitrarily chosen observation point to the screen (blue line) at z=20. The optical elements are placed concentrically around the optical axes which is the z-axis. The environment is considered to be vacuum with a dielectric constant of one. For the sake of clarity, the rays which are launched from the observation point at $z = 0$ are restricted to a certain opening angle instead of being spread over the whole half space. All rays undergoing total reflection within the objects are hidden in this example. The corresponding areas intentionally left blank demonstrates very clearly that the angle of sight is strongly restricted by total reflection for lens-shaped objects when being composed of media with a high dielectric constant such as those of silicon.

As already mentioned at the beginning of this section, the software is able to determine the intersection point of a ray with any object that can be described by analytical equations. These objects can optionally be accompanied by some additional boundary conditions. Already available in the module are spheres, ellipsoids, cylinders, arbitrarily shaped planes, circles, squares and a plate in shape of a T absorbing incident radiation.

The latter one merely is intended for testing purposes of the software, e.g., to perform standard imaging tests as shown in Fig. 4.5(a). Each optical element can be composed of any desired combinations of the existing geometrical bodies. This means, for instance, that a bullet lens is presented by a half sphere, a cylinder, and a circle-shaped plane as depicted in Fig. 4.3

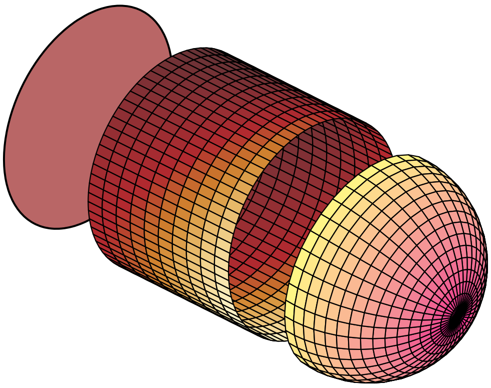

Figure 4.3.: Example for assembling optical elements in the new software: The bullet lens is defined as a circle-shaped plane plus a cylinder plus a half-sphere. By that way, each optical element in my software can be expressed as a combination of existing geometrical bodies.

To calculate possible intersection points of a ray with an object analytical geometry is used. For efficiently solving Matrix equations which occur in many cases, the highly optimized GNU Scientific Library (GSL) is integrated providing efficient algorithms for numerical computations in applied mathematics and science. The GSL library is part of the GNU Project and is freely available under the GNU General Public License [58].

The developed `backtrac` module decides which of the intersection points found within one calculation step is the causally correct one considering both, chronology and distances to the previous point of intersection. It is able to identify if the ray is within or outside an object allowing the correct treatment after total reflections events. Depending on the chosen settings, it takes into account a predefined maximum number of intersections with objects until a ray reaches the source. Furthermore, it enables to specify how often a ray is allowed to be reflected after reaching the source the first time. The maximum order of reflection refers to the total number of incidences on the source of a single ray. The ray, presented as dashed red line in Fig. 4.4, for instance is tracked as long as it reaches the source plane, that is on the backside of the cylindrical lens extension, for the sixths time. The according maximum order of reflection thus is six. The software module allows appropriate handling when a ray can only reach the source undergoing fewer times reflections than demanded. Some examples for ray-tracing being performed with the `backtrac` module through different geometrical bodies are depicted in Fig. 4.2.

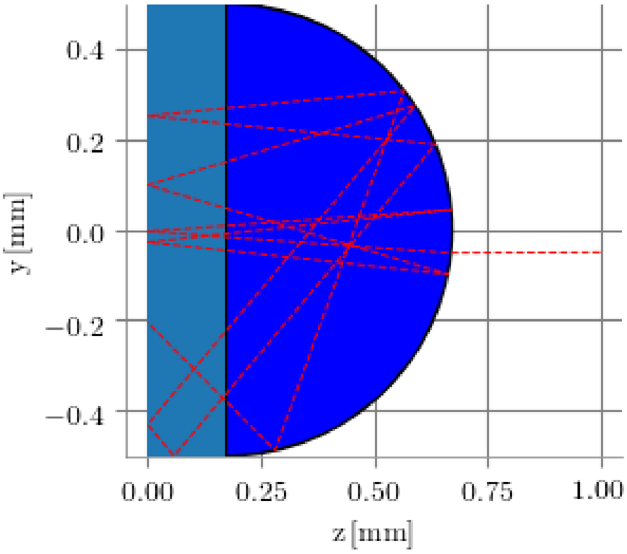

Figure 4.4.: Cross section through a silicon lens that is composed of a hemisphere and a cylindrical extension. The source plane is at the flat backside of the lens. The path of a single ray (red, dashed line) is traced until it reaches the source plane for the sixth time (maximum order of reflection $OR_{max} = 6$).

The module gives back

1. the chronology of the objects the ray is intersecting with along its trajectory,
2. the normal vectors of the intersection interfaces,
3. the corresponding dielectric constants of the interface-media
4. the intersection points and
5. the direction vectors of all five tube vectors at the source field.

Each alternative software principally can be used to calculate the trajectories of the rays as long it provides the same information as the `backtrac` module to the field calculation module.

Imaging tests

To proof the functionality of the `backtrac` module, several tests for each of the included geometrical bodies and for combinations out of them were performed.

Figure 4.5 outlines a typical imaging test performed as a verification of the computed physics. The test setup depicted in Fig. 4.5(a) shows plane-parallel rays propagating along the z-axis against the z-direction. At $z = 34.525\,\mathrm{cm}$ the rays impinge on a silicon lens (marked in red) with a dielectric constant of $\epsilon = 11.9$. Going from left to right in the picture, the two optical radii of curvature of the lens are $R_1 = 500\,\mathrm{cm}$ and $R_2 = -100\,\mathrm{cm}$, respectively. The thickness of the lens is $d = 0.5\,\mathrm{cm}$. The resulting effective focal length according to the Lensmaker's equation $\frac{1}{f} = \frac{n_{\mathrm{lens}} - n_{\mathrm{air}}}{n_{air}} \left(\frac{1}{R_1} - \frac{1}{R_2} \right) + \frac{(n_{\mathrm{lens}} - n_{\mathrm{air}})^2 d}{n_{\mathrm{lens}} n_{\mathrm{air}} R_1 R_2}$ is $f = 34.025\,\mathrm{cm}$ and is correctly delineated by the results of the `backtrac` module as can be read off from Fig. 4.5(a)). Once the focus test is passed, a second software run is performed, now with an additional T-shaped plate inserted in the setup. This plate totally absorbs all impinging radiation. The T-plate, here depicted in blue, is placed at $z = 50\,\mathrm{cm}$ in front of the lens. The generated shadow in form of the T is tracked along the z-axis. Its variable geometry and dimensions along the way are examined to meet the predictions given by analytical geometry. Cross sections of the ray trajectories are depicted in Fig. 4.5(b) for the selected part that is marked by the orange box in Fig. 4.5(a). Each ray that intersects the cross sections at $z = -4, -3, -2, -1, -0.005, 1, 2, 3$ and $4\,\mathrm{cm}$ is represented by a point colored according to the respective cross section. One can clearly see that the T-shaped gaps are turned upside down after passing the focus of the lens just as expected. A zoom of the cross section at $z = -0.005\,\mathrm{cm}$, just after the focal point is depicted in Fig. 4.5c).

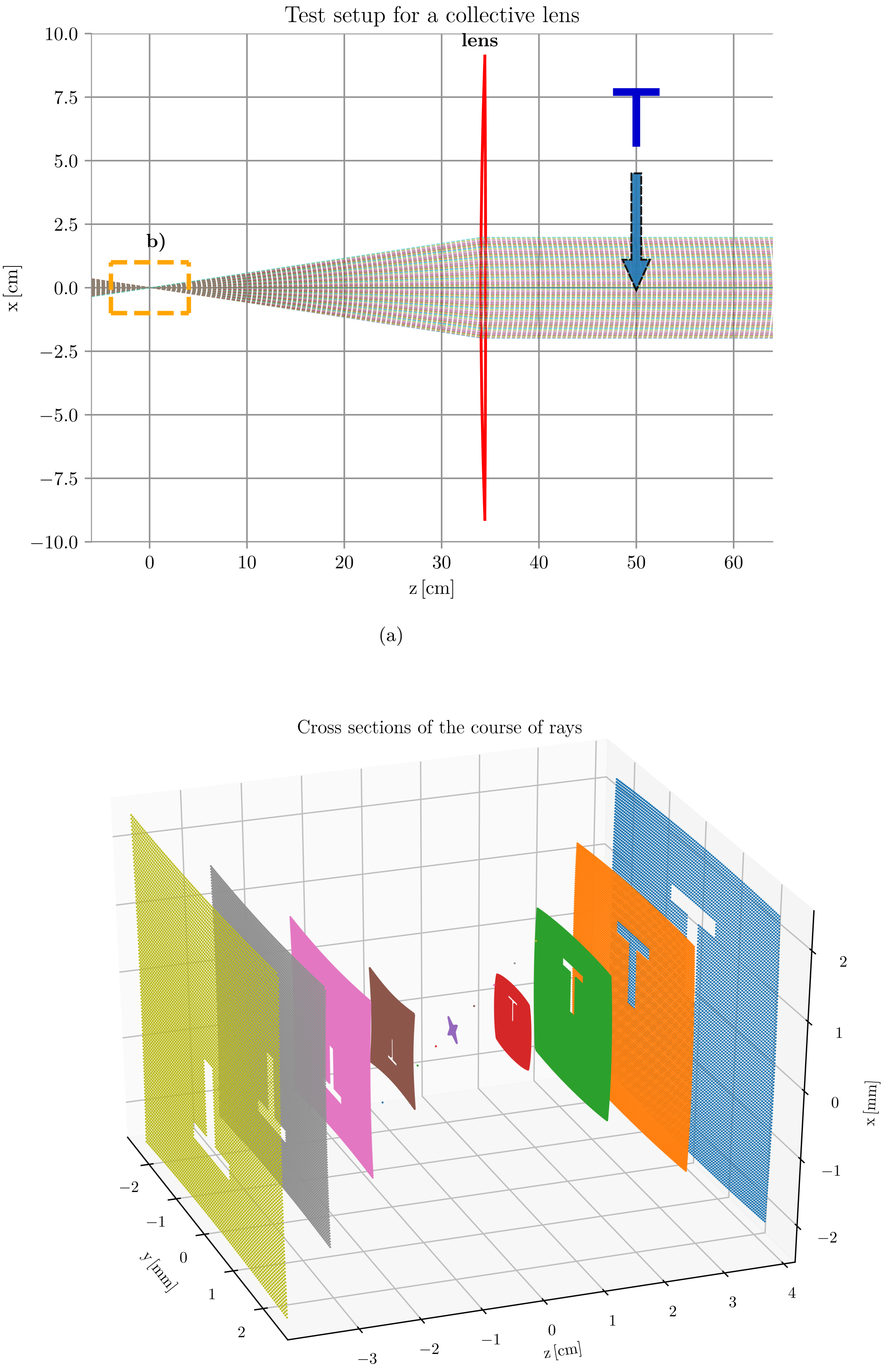
Test setup for a collective lens
lens
b)
10.0
7.5
5.0
2.5
0.0
−2.5
−5.0
−7.5
−10.0
x [cm]
0
10
20
30
40
50
60
z [cm]
Cross sections of the course of rays
−2
−1
0
1
2
y [mm]
−3
−2
−1
0
1
2
3
4
z [cm]
2
1
0
−1
−2
x [mm]

(a)

(b)

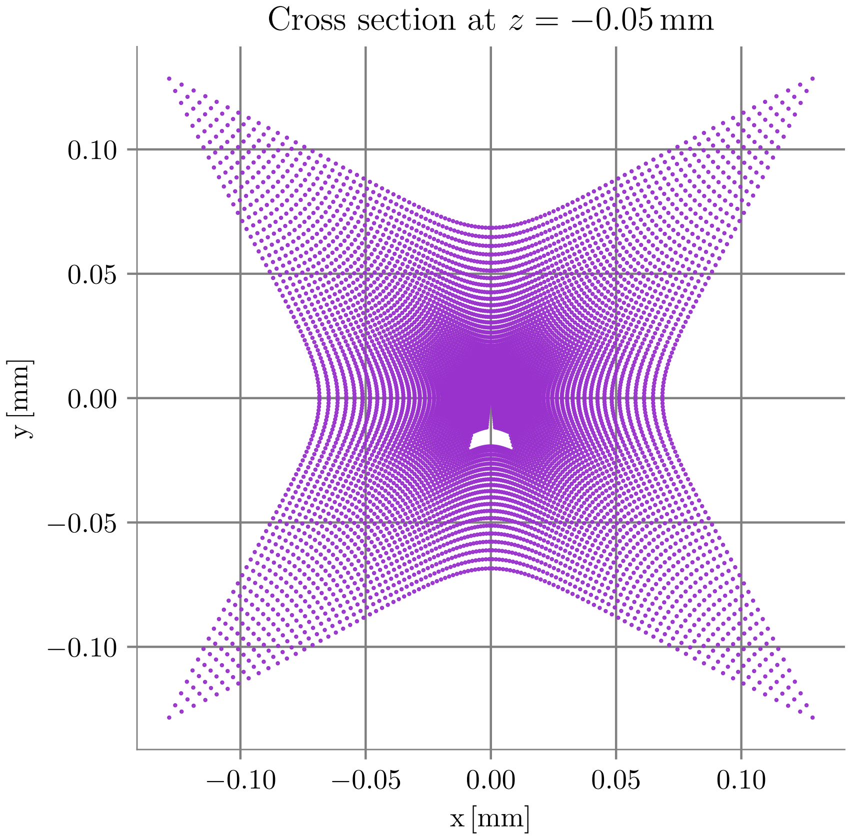

(c)

Figure 4.5.: Test setup for the `backtrac` module: a) Sketch of the setup: Plane-parallel rays are propagating along the z-axis against the z-direction where they impinge a silicon lens (marked in red) at $z = 34.525\,\mathrm{cm}$ with a focal length of $f = 34.025\,\mathrm{cm}$ which is correctly reproduced by my software. In a second run a T-shaped plate is inserted in the setup totally absorbing incident radiation. The T, here depicted in blue, is placed at $z = 50\,\mathrm{cm}$ in front of the lens. The generated shadow in form of the T is tracked along the z-axis. Cross sections of the ray trajectories are depicted in b) for the selected part that is marked by the orange box in figure a). Each ray that intersects the cross sections at$z = -4, -3, -2, -1, -0.005, 1, 2, 3$ and $4\,\mathrm{cm}$ is represented by a point colored according to the respective cross section. A zoom of the cross section at $z = -0.05\,\mathrm{mm}$, just after the focal point is depicted in c).

4.3.3. Field calculation module

To apply the field calculation module `fical`, it is necessary to know the initial field source in Fourier transform **k**-space as well as to resort to the ray-trajectories and the properties of the concerned media at the intersection points determined by the `backtrac` module. Since the calculation of the $E-$field along each tube of rays is a clearly separated, stand-alone process it is sufficient to consider the procedure per path of one exemplary tube of rays.

Having calculated the trajectory of one tube of rays by the `backtrac` module provides information about

1. all intersection points along the trajectory,
2. the chronology of the objects,
3. the normal vectors at the intersection points at interfaces,
4. the vectors spanning the surrounding ray tube at the starting point at the source plane, and
5. chronology of the refractive indexes of involved media.

The procedure per path of one tube of rays is:

1. The calculation starts at the source plane;
2. Calculate the differential spectral surface, $\Delta^2\mathbf{k} = \Delta k_x \cdot \Delta k_y$, by projecting the four vectors spanning the tube of rays at the starting point of the source plane onto the source plane (here on the k_x-k_y plane);

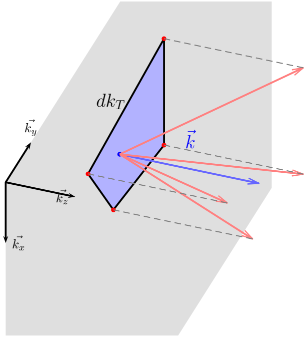

3. Calculate all bases of orthogonal vectors of the tube of ray and bases of orthogonal vectors at the interaction points of the interfaces. These are needed for later calculation of the curvature matrices and the radii of curvatures (see Appx. A.1.2);

4. Calculate the initial wavevector $\mathbf{k}_{\mathbf{ini}}^{\mathsf{T}} = (k_{x,ini}\ k_{y,ini}\ k_{z,ini})$ of the middle ray at the starting point;
5. Determine the initial E-field amplitude belonging to the initial wavevector in the $\mathbf{k}-$space at the plane of source $\mathbf{E}_{\mathbf{k},\mathbf{ini}}(k_{x,ini}, k_{y,ini})$;
6. Calculate the initial E-field contribution of the tube of rays: $\mathbf{E}_{start} = \mathbf{E}_{\mathbf{k},\mathbf{ini}} \cdot \Delta^2\mathbf{k}$.

All following steps are repeated until the observation point is reached:

7. Calculate the E field amplitude just before the next interaction point P_{i+1}: $\mathbf{E}_i = \mathbf{E}_{i-1} \cdot e^{i \cdot \overline{P_{i+1}P_i}}$;
8. Decompose the E-field into parts parallel and perpendicular to the plane of incidence;
9. Determine if the tube of rays is transmitted or reflected. Thereby all five rays defining the tube need to undergo the same refraction at the same interface, otherwise the tube of rays is discarded and excluded for the simulation.
10. Calculate matrices of curvature at the interaction point of
    a) the interface based on two tangential surface vectors (dependent on if it is a reflection or transmission),
    b) the incoming tube of ray;
11. Transform the base of the curvature matrices;
12. Calculate the curvature matrix of the tube of rays after the point of interaction;
13. Calculate the Eigenvalue of these matrices;
14. Use the Eigenvalue to determine the radii of curvatures R_i;
15. Calculate the divergence factor DF by means of the distance d and the radii R_i;
16. Calculate the resulting E-field amplitudes perpendicular and parallel after crossing the interface: $\mathbf{E}_{i+1} = (E_{\perp,i+1}, E_{\|,i+1}) = (E_{\perp,i}, E_{\|,i}) \cdot \mathbf{M}_{\mathbf{Fresnel}} \cdot D \cdot e^{(-ik \cdot d)}$, where $\mathbf{M}_{\mathbf{Fresnel}}$ is a matrix with the Fresnel coefficients, and
17. Express the field on base of the unit vectors $(\vec{x}, \vec{y}, \vec{z})$ of the coordinate space.
18. Repeat step 7 to 17 at each intersection point along the trajectory of the tube until the observation point is reached.

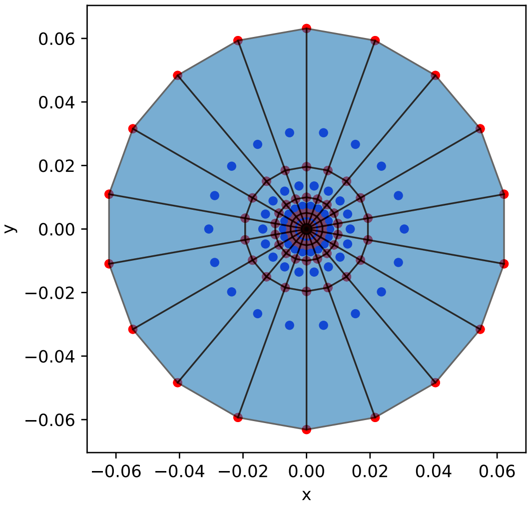

Figure 4.6.: The plot depicts the differential spectral surfaces of 100 rays that have been launched from a single point in space with a distance of 1cm to a screen over the whole half space. The dots indicate where the respective ray tubes impinges the screen. Blue dots refer to the central ray and red dots refer to the surrounding four rays which define the tube.

The total field at a certain observation point is given by the sum over the fields transported by each tube of rays that reaches the point.

Test setup

A first test run of the `ficalc` module has been performed considering the propagation of a Gaussian beam in free space along the z-axis.

Assume that the E-field amplitude points into the x-direction. When spreading through the empty space along the optical axis the amplitude can be expressed in terms of the radial distance, r, to the z-axis and the axial distance z to the smallest beam waist w_0 at $z = 0$.:

$$E(r,z) = E_0 \frac{w_0}{w(z)} e^{-\left(\frac{r}{w(z)}\right)^2} \cdot e^{-ik\frac{r^2}{2R(z)} - i(kz - \arctan(\frac{z}{z_R}))}. \tag{4.34}$$

The beam waist in dependence of the distance z is

$$w(z) = w_0 \sqrt{1 + \left(\frac{z}{z_R}\right)^2}, \tag{4.35}$$

where $z_R = \frac{\pi \cdot w_0^2}{\lambda}$ is the Rayleigh length. The radius of curvature is given by

$$R(z) = z\left(1 + \left(\frac{z_R}{z}\right)^2\right). \tag{4.36}$$

Considering the course of the amplitude at $r = 0$ for n multiple of the Rayleigh length the expression for the modulo reduces to

$$|E(0, n \cdot z_R)| = E_0 \frac{1}{\sqrt{1 + \left(\frac{n \cdot z_R}{z_R}\right)^2}} = E_0 \frac{1}{\sqrt{1 + (n)^2}}. \tag{4.37}$$

In the first run a Gaussian beam at 10.7 THz with a beam waist of $w_0 = 20\,\mu\text{m}$ and an amplitude of $E_0 = 1\,\text{V/m}$ is simulated. The corresponding analytical expression of the E-field in k-space that is used in the software reads

$$\begin{aligned} \widetilde{E_x}(k_x, k_y) &= \frac{E_0 w_0^2}{4\pi} e^{-\frac{w_0^2\left(k_x^2 + k_y^2\right)}{4}} \\ \widetilde{E_y}(k_x, k_y) &= 0, \\ \widetilde{E_z}(k_x, k_y) &= -\frac{\widetilde{E_x}(k_x, k_y) \cdot k_x}{k_z}. \end{aligned} \tag{4.38}$$

The transverse field profiles calculated with the software (see Fig. 4.7) are compared with the analytical solutions given by (4.37). The axial curve of the E-field amplitude at multiples of the Rayleigh length is shown in Fig. 4.8(a). The software results are based on a ray distribution over the half-space with an angular step-width of $d\Phi = 0.175°$, $d\Theta = 3.053°$. As can be seen from Fig. 4.8(a) the deviation between analytical and software-based field amplitudes gets smaller (less than 1 % after $z \geq 5 \times \lambda$) as soon as the distance to the source field is larger than a few wavelength since the contribution of the evanescent waves becomes negligible.

The convergence behavior as a function of the ray density is investigated for one exemplary cross section at $z = 7 \cdot z_R$ within a square plane from $-200\,\mu\text{m}$ to $-200\,\mu\text{m}$ in x and y. The numerical calculations are carried out for about 3000 rays to 500 000 rays (see Fig. 4.9) over the half space with 900 observation points. The corresponding ray density for the iteration is given in Tab.4.1.

For each observation point the difference in the E-field value from the i^{th} iteration and the $(i-1)^{th}$ iteration is calculated and the average difference over all 900 observation point is plotted against the iteration index in Fig. 4.10(a). Moreover, the average difference in the E-field value from the i^{th} iteration and the value given by the analytical expression

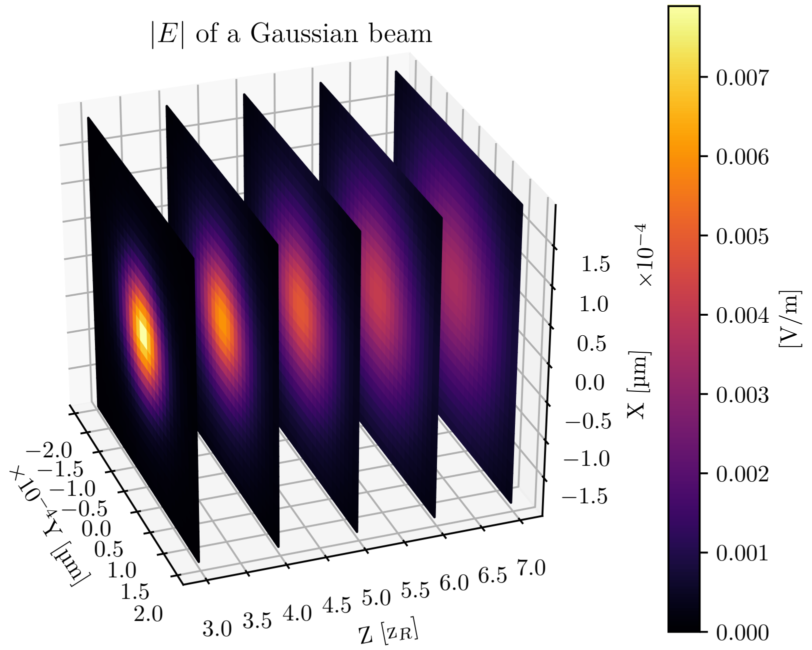

Figure 4.7.: Transverse field profiles of Gaussian beam calculated with the `backtrac` and `fical` software modules at multiples of the Rayleigh length.

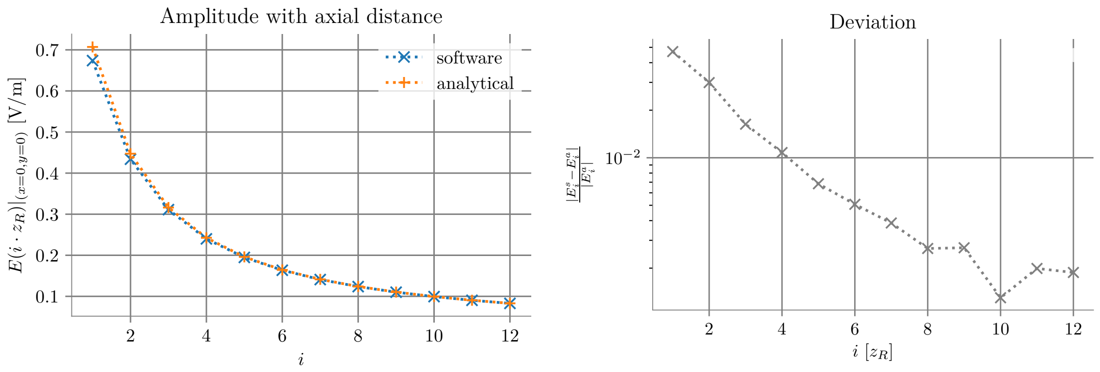

(a)

(b)

Figure 4.8.: (a) E-field amplitude of Gaussian beam at $x = y = 0$ as a function of the axial distance along the optical axis (z-axis). The E-field amplitude is plotted for multiples of the Rayleigh length z_R, once calculated with the software (999 216 rays over the half-space, angular stepwidth $d\Phi = 0.175°$, $d\Theta = 3.053°$), and once using the analytical expression in(4.37); (b) Deviation between the amplitude results calculated with the software (E^s) and obtained from the analytical expression (E^a).

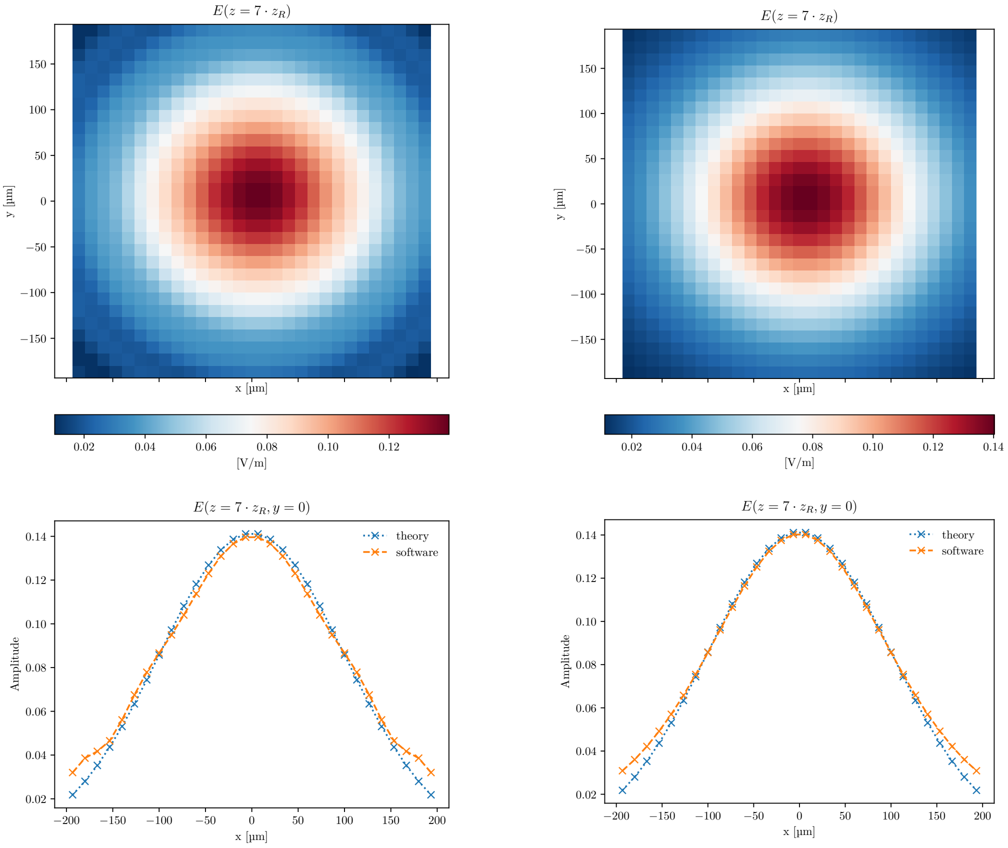

(a) (b)

Figure 4.9.: E-field amplitude of Gaussian beam at a plane perpendicular to the optical axis in a distance $z = 7 \cdot z_R$. The obtained results are based on (a) 2968 and (b) 499 140, respectively, launched rays over the half space.

(Eq.(4.34)) is depicted in Fig. 4.10(b). Both plots show that the software results converge with an increasing ray density.

i	0	1	2	3	4	5
N	2968	3968	4896	5928	6888	9900
$d\Theta$	3.214	2.813	2.500	2.308	2.143	1.800
$d\Phi$	3.396	2.903	2.647	2.368	2.195	1.818

i	6	7	8	9	10	11
N	19880	49728	69692	119712	199360	499140
$d\Theta$	1.268	0.805	0.677	0.517	0.402	0.254
$d\Phi$	1.286	0.811	0.687	0.523	0.404	0.255

Table 4.1.: Iteration index with corresponding number of rays over the half space and step width in Θ and Φ.

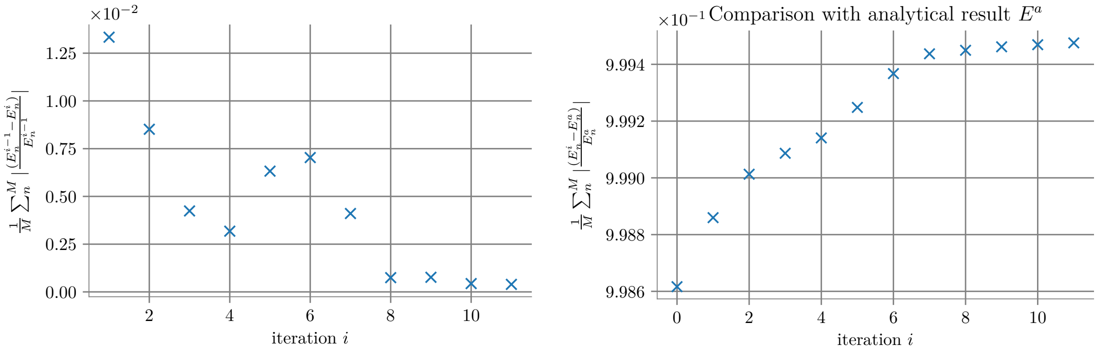

(a) (b)

Figure 4.10.: (a) Convergence of the E-field magnitude averaged over the plane with $M = 900$ observation points with increasing ray density (see iteration index in Tab. 4.1). (b) Convergence of the difference between the E-field magnitude averaged over the observation plane once calculated with the software modules and once calculated using the analytical expression E^a.

4.4. Comparison with CST

For the comparison of the SRT based software within the CST software two different scenarios at high frequencies are investigated which are just computational within the institutes resources of the CST software. The first one considers the propagation of a Gaussian beam through a silicon lens at 1 THz. In CST a Gaussian field is one of the possible built in generation options. The Gaussian E-field source that is fed to the SRT based software is based on an analytical expression. The E-field is investigated in the near field range of the lens close to the lens surface. The second test scenario considers the far-field pattern of a lens-antenna which corresponds to one of the actual RF-designs of this work (described in Sec. 3.4.3). The far-field is investigated at 4.7 THz, which besides 10.7 THz is the second operating frequency for which some RF-designs have been developed and tested for this work.

4.4.1. Silicon lens with Gaussian beam

To compare the SRT software with the Frequency domain solver of CST studio suite the propagation of a Gaussian beam through a hyper-hemispherical silicon lens at 1 THz is considered. The lens dimensions correspond to those that are used for the actual mixing block lens assembly of this work. The lens is composed of a half-sphere with 0.5 mm radius. Its flat backside is extended by a 173 µm long cylinder of the same radius 0.5 mm. The dielectric constant of the silicon is chosen to be 11.4, in compliance to the measured values at cryogenic temperatures (see Chap. 5). The Gaussian beam is linearly polarized in x-direction, has a beam waist of $w_0 = 225\,\mu\text{m}$ and has its focal point at (0,0,0). The optical axes is in z-direction and the flat backside of the lens is placed at $z = 0$ in the x-y plane with its center at ($x = y = 0$). A cross section through the lens and its alignment along the optical axis is shown in Fig. 4.4). The Gaussian beam that impinges the backside of the lens at $z = 0\,\mu\text{m}$ has an E-field given by

$$E_x(x, y) = E_0 \cdot e^{-\frac{x^2+y^2}{w_0^2}} \tag{4.39}$$

with an E-field amplitude of $E_0 = 1\,\text{V/m}$. The corresponding analytical expression of the E-field in k-space is the same used above given by Eq. (4.39).

The CST simulation of the propagation of the Gaussian beam is calculated with the FD solver using a tetrahedral mesh with a total number of mesh cells of 5 480 821 after two adaptive mesh refinements. Preferable further mesh refinements were not possible due to memory restrictions (see Sec.3.4.4). The simulation lasted about 77 hours. The results of the SRT software are based on 500 000 rays distributed over a solid angle with $\Theta_{ray} \leq 60°$ and $0 \leq \Phi_{ray} \leq 360°$ with an $OR_{max} = 1$ (for the last performed iteration step increasing the ray density from 300 000 to 500 000 yields an average deviation in the E-field over all sample points less than 0.4 %). The SRT software runs on an Intel(R) Core(TM) i5-4430 CPU @ 3.00 GHz processor. It took less than 3 h.

The E-field at a plane perpendicular to the optical axis at $z = 703.8\,\mu m$ is calculated (in a distance of 30.8 µm to the tip of the lens). The results are depicted in Fig. 4.11. As can be seen from the plots the magnitude in main beam direction of the E-field polarized along the x-direction is about similar to the magnitude predicted by the solver of the CST software. The course of the curves of the phases are rather similar from roughly −100 µm to 100 µm. An obvious deviation in the beam width is visible. The smaller beam width from the SRT result cannot be explained by the exclusion of the contributions of those rays touching the rims of the lens shapes which leads to vanishing fields in the geometrical shadow regions. In contrast to the SRT result, for the beam calculated by CST an asymmetry between the beams in the $x = 0$ and $y = 0$ planes is visible.

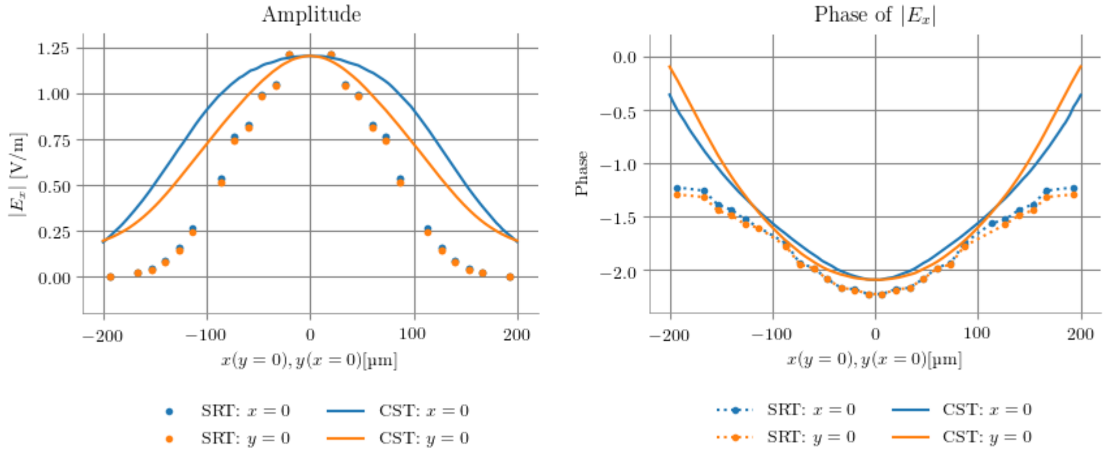

(a) (b)

Figure 4.11.: Simulation results of the E-field of a Gaussian beam after propagating through a silicon lens (dimensions and beam specifications in the text). The plots show the absolute amplitude and phase of the E-field along the x-axis and the y-axis at $z = 703.8\,\mu m$.

4.4.2. Silicon lens with self-complementary logarithmic spiral antenna

To compare the SRT software with the TD solver of CST studio suite the propagation of the E-field of one of the antenna lens designs ($S4$) for the HEB receiver is calculated for a frequency at 4.7 THz. The detailed description and dimensions of the used spiral antenna are given in Sec. 3.4.3. The lens dimensions are the same as used in the section above. The spiral antenna is attached to the flat backside of the cylindrical extension (see

Fig. 4.13(a)). The simulation of the lens-antenna with CST studio suite is only possible with a course resolution (hexahedral mesh cells without adaptive mesh refinement for a bounding box of $1.3649 \times 10^6\,\mu\mathrm{m}^3$, 15 cells per wavelength, solver accuracy about -20 dB) (see details given at the beginning of Sec. 3.4.4). For the numerical calculation with the

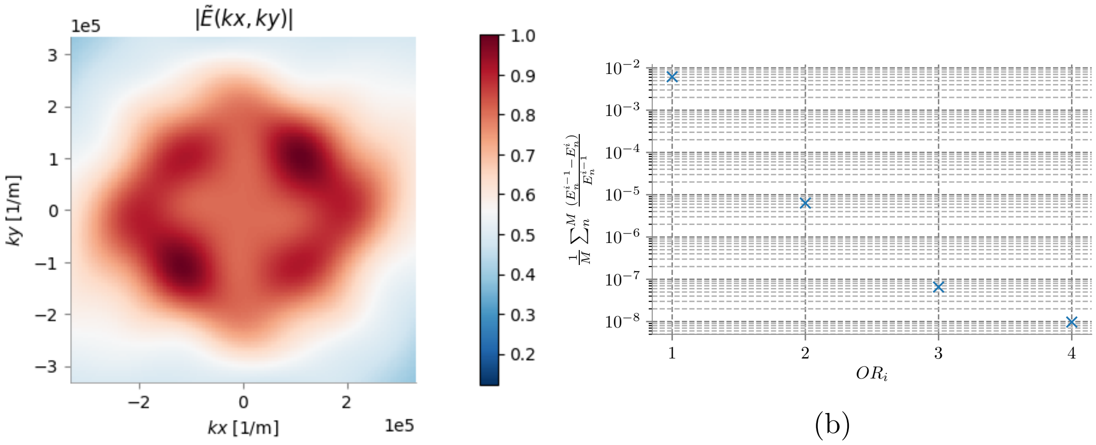

(a)

(b)

Figure 4.12.: (a) Spectral E-field in k-space of the self-complementary log-spiral antenna $S4$ at the spiral-lens interface. (b)SRT software results: Convergence of the E-field amplitude averaged over the plane with M=900 observation points in dependence of the considered E-field contributions of increasing orders of reflection.

SRT based software the spectral E-field in k-space of the spiral antenna (see Fig. 4.12(a)) is used as the source field. It is obtained by an FFT of the E-field of the spiral antenna at the antenna-lens interface received from the results from the CST-simulation. The sample distance is $\Delta k_x = \Delta k_y = 3784.17\,\mathrm{m}^{-1}$. It corresponds to the sample distance where the last iteration step increasing the resolution by a factor of four results in an average deviation less than 4 %. The software results converge with an increasing order of reflections (see Fig. 4.12(b))

The results that are shown in Fig. 4.13 are obtained from the SRT software using 50 000 rays over a solid angle with $\Theta_{ray} \leq 24°$ and $0 \leq \Phi_{ray} \leq 360°$ with an $OR_{max} = 5$ (the solid angle is chosen such that it covers the lens). They depict the amplitude and phase of the x and y-component of the E-field in two sectional planes at $\Phi = 0°$ and $\Phi = 90°$, respectively. Comparing the curves obtained from the SRT software and from the CST software the results are similar around the main beam. The side lobes predicted by the CST software are considerably lower than the ones calculated by the SRT software.

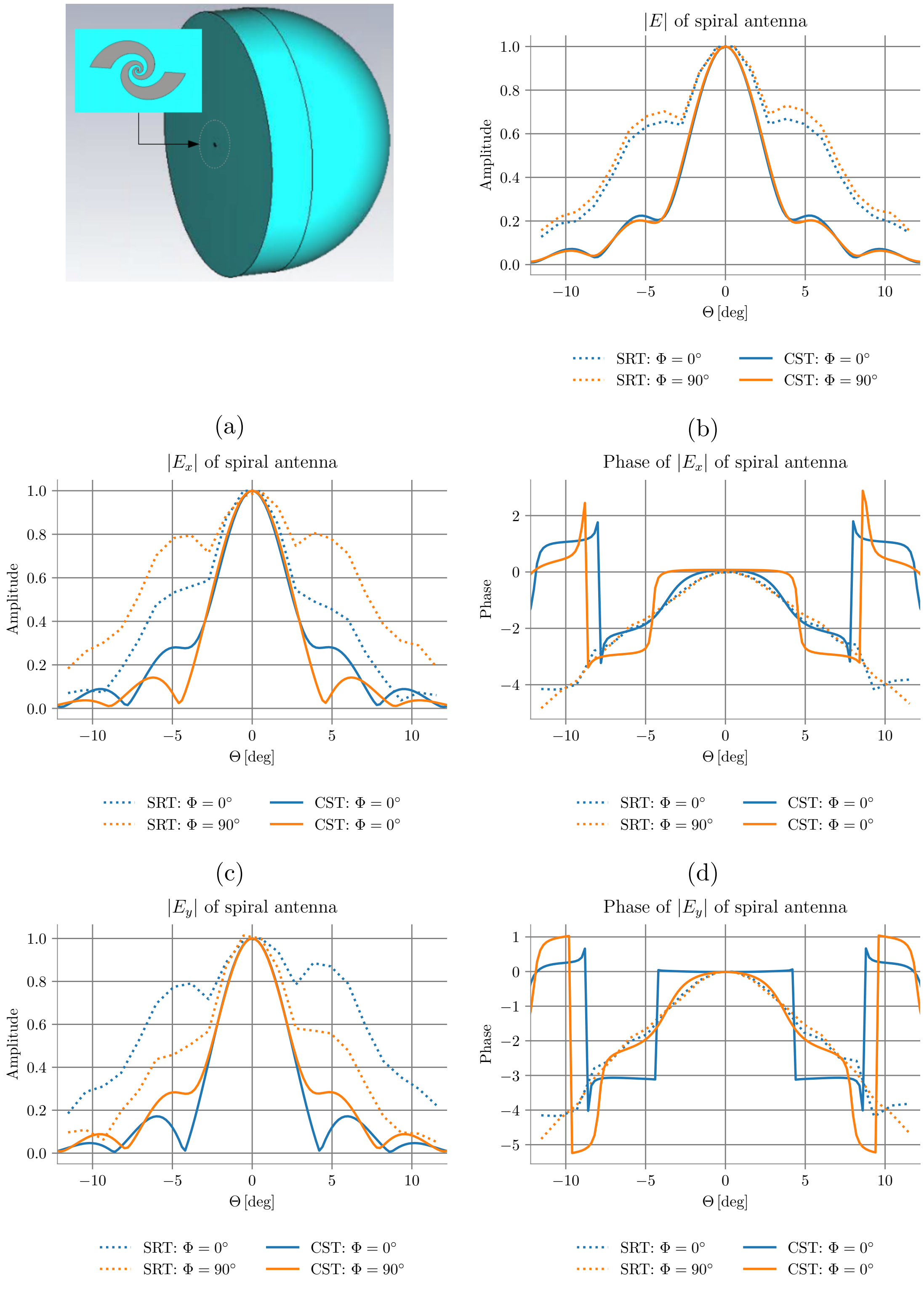

(a) (b)

(c) (d)

(e) (f)

Figure 4.13.: Comparison of far-field results calculated with the TD solver of CST studio suite and the SRT software for the spiral antenna $S4$ on the dielectric silicon lens (diameter of 1 mm) as sketched in (a)

4.5. Conclusion and Outlook

The SRT software that has been introduced in this chapter allows with its modular structure the tracing of E-fields through various objects. It contains geometrical definitions to describe elliptical, cylindrical or plane surfaces, to define various optical elements like lenses and plates that are needed to construct optical setups. The optical elements can be defined as a substrate with a certain dielectric constant, they can be specified as perfect absorbing material or as a perfect electrical conductor. The source field of the `fical` module can either be a tabulated discrete field read in from a standard text file, or it can be given by an analytical expression.

The comparison of the E-field results of two different scenarios using the CST software and the SRT based software depicts rather similar results along the main beam directions but considerable deviations in their predictions of the height of the side lobes which for designing purposes of the follow-up optics, matching the mixer to the telescope, cannot be neglected. Since the SRT software is intended for the calculation of E-field propagation at the high frequencies addressed in this work the test setups have been chosen application orientated with the actual lens dimensions of the receiver at high frequencies that were just computational with the CST software at costs of a low resolution of the simulation object. Consequently, it cannot be said which of the results is better to depict the reality without the experimental beam characterizations of the actual designs. This, however, is out of the scope of this thesis, mainly because a local oscillator source is still under development. The comparison of both softwares further show that the SRT software is able to calculate the desired E-field information in considerably less time on a standard PC than the CST on a specifically powerful PC, necessary for additional memory and a more powerful processor with more cores. For the simulation of the antenna-lens object in the example presented in the section above it took less than 4 % of the total solver time of the CST software. Within our computational resources, the SRT software, in contrast to the CST software, moreover does not have a high frequency limit in the THz regime above which the lens antennas cannot be simulated anymore.

For a more detailed investigation of the causes of the differences in the results further simulations with both softwares are necessary which have not been done so far due to time consumption reasons. A comparison with PO techniques and other simulation softwares like HFSS[89] and FEKO[3] would be a welcome addition, especially with regard that there is evidence for deviations in the results obtained by different simulation softwares and different numerical calculation techniques as has been shown in [76]. The usage of the Cologne High Efficiency Operating Platform for Science (CHEOPS) for further investigations with the full functional parallelized version of the SRT software module is the next step for extensive simulations of more antenna lens designs. A further future task is to trace the E-field of the lens antennas developed in this work through the optics of the actual used cryostat where the receivers are mounted in for measurements.

Based on the obtained results the far field results of selected RF-designs of this work are characterized with the CST software below 4.7 THz. The SRT-software is used to estimate the E-field amplitude and phase of some of the 10.7 THz RF-designs (see Sec. 3.4.2) within the main beam having in mind that a trustworthy statement about the side lobe levels to the current situation is not possible.

5. Determination of material properties for cryogenic applications

Knowing the response of a material to electromagnetic fields is crucial for the design of electromagnetic receivers and optical setups. At the operating frequency of 10.7 THz the lack of sufficient information about material properties of optical components as well as about the carrier substrate of the RF-structures required to perform according measurements using Fourier transform spectrometers (FTS). This chapter presents the results of the respective cryogenic- and frequency-dependent measurements of very pure silicon samples and the results of transmission measurements of window materials and glues performed at room-temperatures. It is divided into three parts.

In the beginning section 5.1, a brief outline of the analytic method for the extraction of material parameters from transmission spectra, and the respective metrology is given. Furthermore, the enhancement of a FTS by a test setup for measurements down to 80 K is described.

It is followed by a detailed data analysis of the transmission measurements of several HRFZ silicon samples, in section 5.2. In this second part, both aspects, the frequency- as well as the temperature-dependence of the refractive index and the absorption coefficient of pure silicon are investigated. A brief conclusion about the results, their accuracy, and the limits of the metrology is given.

The third part, section 5.3, is devoted to the transmission measurement of potential vacuum window materials and of several glues.

5.1. Dispersive refractive index from Fourier Transform Spectrometer transmission measurements

The direct measurement of the complex refractive index by means of transmission measurements requires phase and amplitude information about the transmitted, electromagnetic field. Since the Fourier Transform Spectrometer (FTS) measures an intensity as function of the position of the moving mirror of the interferometer, the spectrum does not offer directly measurable information about the phase of the transmitted radiation. A flat sample with in good approximation plane-parallel surfaces, however, produces a specific fringe radiation pattern due to interference at the sample-vacuum interfaces comparable with an optical resonator in a Fabry-Perot interferometer[84]. Being dependent on the refractive index of the material, the interference pattern in the measured transmission spectrum allows to extract the complex refractive index with certain restrictions. An outline of the underlying theory and an introduction of the fringe methods to calculate the refractive index are given in the Appx. C.3. The fringe methods, in general, rely on the information about the magnitude and the frequency of individual, local extrema of the interference pattern within the measured spectrum. Because of the limited spectral resolution of the recorded transmission spectra further data processing is mandatory for the determination of those local extrema and, by this, to receive meaningful results when applying fringe methods. A detailed description of the according data processing is given in the Appx. C.4.

5.1.1. Implementation of a new test setup

Due to the lack of a suitable cryostat integrable within the measurement setup of our FTS[1], there is no possibility of cooling down any samples to cryogenic temperatures. To get a first hint of temperature dependent changes in the sample properties I modified the setup in that manner that it allows for cooling down to 145 K as well as for alternating between reference and sample measurement during operation. The corresponding setup is depicted in Fig.5.1. It consists of a massive cooling finger of copper which is attached to a brass cylinder which can be cooled from outside by liquid nitrogen. Two highly pure, highly flexible copper ropes connect the sample holder with the cooling finger. The sample holder is mounted on a thermally isolated, rotatable rod enabling to arbitrarily switch between reference and sample measurement while maintaining the integrity of the optical path. It additionally provides a convenient mount for a heat resistor. The sample holder plates are exchangeable units which allow the direct attachment of a temperature sensor in close proximity to the sample.

To build in the new components I removed the original side panel of the FTS sample compartment and replaced it by an accordingly designed side panel where all components can be attached to. As test measurements concerning the focus of the source beam revealed that the standard sample placement predefined by the manufacturer is not exactly in the collimated spot area, the location of the sample holder needed to be

---

[1] Vertex 80 v with FIR extension[15]

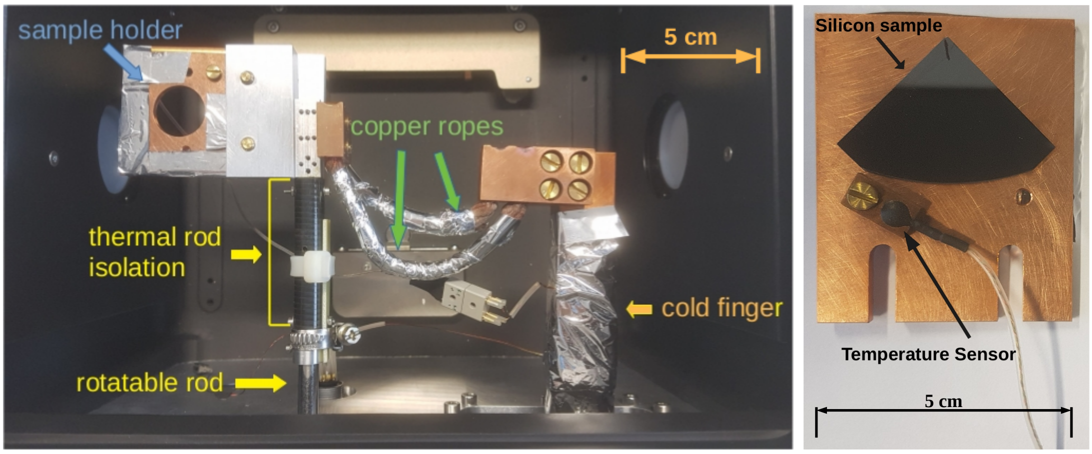

Figure 5.1.: (left) Installed setup in the sample compartment of the FTS for measurements of cooled-down samples. The rotatable rod enables to interchange the sample position and reference position in situ during operation. In the given configuration displayed in the picture the sample holder with attached sample is placed in the beam path of the optical axis of the FTS and cannot be seen as it is covered by the empty sample holder that serves as the reference. (right) Sample holder with silicon sample: The temperature sensor is attached in close proximity to the sample.

adjusted respectively that it lies in the actually focus plane. Optimizing of the refrigerating process in the setup was carefully carried out by controlling each change on the individual components of the cooling chain by means of a temperature sensor successively attached to each component.

5.2. Dispersive temperature dependent refractive index of HRFZ silicon

High resistivity float zone (HRFZ) silicon is a standard carrier material for planar RF circuits. Since its dielectric constant significantly influences the dimensions of all circuit parts it is necessary to estimate within which limits this quantity is to be expected in practice, and how it varies with temperature. Up to this time of the ongoing design work[2] only one publication from 1959 [92] reported about a temperature dependence of single crystal silicon of unspecified resistivity for radiation with a wavelength from $2 - 30\,\mu\text{m}$. Due to the lack of information about the cryogenic dielectric properties of HRZF silicon the new test setup described in Sec.5.1.1 was implemented to estimate the temperature

---

[2] We had the 18th Oct. 2019

dependence of its dielectric function. Based on these measurements the dielectric constant at 5K could be estimated to be in between 11.2 to 11.5. Subsequently, thanks to Philipp Warzanowsky from the Institute of Physics II FTS transmission measurements of one of my Si samples down to 5K could be performed in a dedicated measurement setup. Later on, Wollack et al. published a paper [179] in 2020 where they measured the refractive index of high-purity silicon at 300 and 10 K over the range from 100 to 1000 cm^{-1} (10-100 µm). Their results agree very well with the findings of this work as they get a similar relative change in the real part of the refractive index of about 0.826% for Si being cooled down to 10 K which is close to the relative change of about 0.83% measured for the silicon sample being cooled down to 5 K[9].

The following sections rely on measurements down to about around 150 to 160 K conducted with the new test setup described in Sec.5.1.1 as well as on the measurements performed by Philipp Warzanowsky from the Institute of Physics II.

5.2.1. Measurement procedure

The temperature-dependent transmission spectra of in total 5 HRFZ Si samples with varying resistivity have been measured by means of two different FTS - the in-house extended *Bruker Vertex 80* FTS and the *Bruker IFS 66v/S* FTS dedicated for cryogenic applications. The samples are p-doped with boron and have a crystal structure of <100>. The thickness of the plates was measured with a dial gauge with an uncertainty about ±1 µm and ranges from about 361 µm to about 535 µm . The thickness was determined as the average of at least four measurements at different positions on the sample plate[3] and is listed in Tab. 5.1 together with the resistivity declared by the manufacturer.

Measurements down to 150 K

For an initial assessment of the temperature-dependent refractive index, transmission measurements on silicon samples no.1 to 4 listed in Tab. 5.1 have been performed in the new test setup described in Sec.5.1.1. An overall number of more than 70 transmission spectra at different temperatures varying from room temperature to about 150 K allows a mapping of the transmission evolution with temperature in steps smaller than 20 K. Each dataset represents an average of 5 to 15 interferogram records[4] with a nominal resolution of 2.3 GHz. Depending on the number of scans and further measurement

---

[3] In this context many thanks to Stephan Wulff who culled the Si samples remained from other research projects and directly measured their thicknesses.

[4] The actual number was chosen according to the velocity with which the samples cooled down or warmed up.

settings[5] the acquisition of a single spectrum required between approximately two and five minutes. The radiation source used for the setup is a mercury-vapour lamp. The optical components consist of a Mylar multilayer beam splitter that is applicable from $680\,\mathrm{cm}^{-1}$ to $30\,\mathrm{cm}^{-1}$ and a pyroelectric room-temperature DLaTGS (deuterated L-aline doped triglycene sulphate) detector with Polyethylene-window dedicated for $700\,\mathrm{cm}^{-1}$ to $10\,\mathrm{cm}^{-1}$ according to the manufacturer[15]. The chosen setup-equipment enables to cover sufficient ambient spectral range around the wavenumber of interest at about $357.14\,\mathrm{cm}^{-1}$.

For silicon sample no.1 it was alternated between reference and sample at each temperature step of the measurement. However, the sample plate cannot be placed exactly at the same position after swapping but will be in a slightly different tilt angle at each measurement which means that the effective thickness of the sample is slightly different for each measurement. For a better analysis of the temperature-dependent thickness-variation of the plate and its effect on the spectrum and more importantly, to enable an adequate determination of the relative change in the real part of the refractive index, the plate position of the remaining samples is kept unchanged during the cool-down and warm-up processes. The recording of a reference spectrum only takes place just before and after a measurement cycle, thereby at the highest and at the lowest temperature value, respectively, which could be reached with the sample.

To get down to temperatures as low as possible the little heat resistance in the setup has been removed which however withdraws the ability to additionally regulate the temperature. The according temperature course of one cool-down and warm-up cycle of a sample as depicted in Fig.5.2 is non-linear with time and especially steep at the beginning before flattening when reaching the lowest temperature plateau. Consequently, measurements are taken over a certain temperature span that amounts to not more than a few Celsius degrees at most and is dependent on the position of the present temperature value in the temperature curve and the preset measurement settings defining the time per measurement. As the refractive index certainly does not experience abrupt jumps with temperature within the frequency range of interest and only exhibits marginal changes within this small temperature intervals, this is still acceptable. Accordingly, the temperature margin depicted with the calculated values of the refractive index always refers to the temperature interval of each individual measurement and is clearly articulated in the according evaluation.

---

[5] like mirror-velocity, pause-time between records etc.

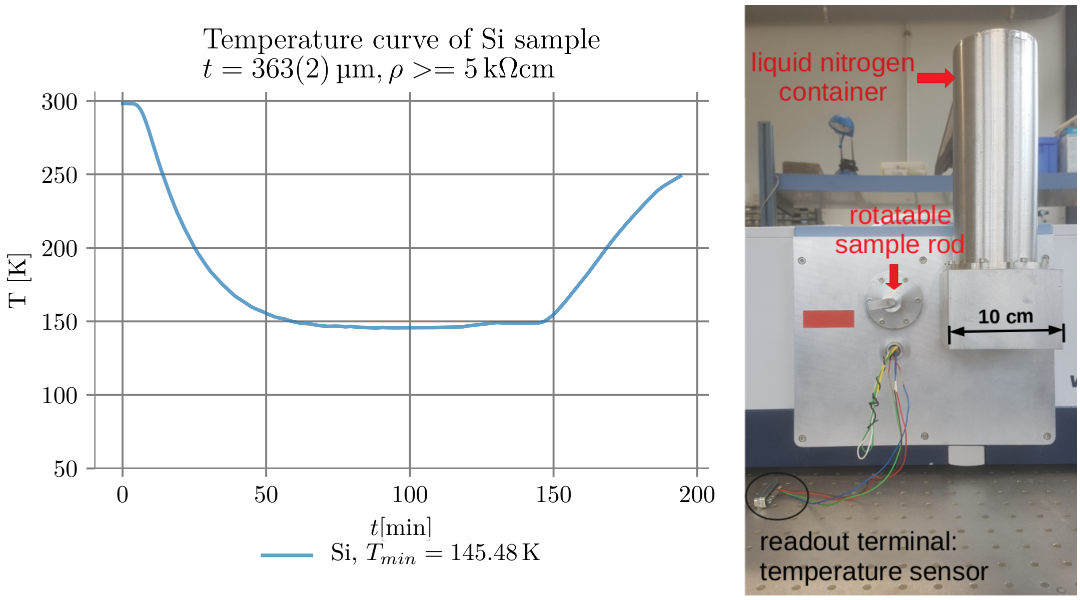

Figure 5.2.: (left) Measured temperature course of a silicon sample in the modified setup with time: Despite a continuous supply of nitrogen within the first 100 minutes the change in temperature is non-linear and varies with different velocities. The lowest temperature that could be achieved is $T_{min} = 145.48\,\mathrm{K}$. (right) Exterior view of the sample compartment of the modified Vertex 80 v FTS (see Sec.5.1.1) to enable both, the interchange of sample and reference position in situ during operation by means of an rotatable rod with two sample supports as well as cooling-down of samples by liquid nitrogen which is filled in the exterior cylindric container attached to a cold finger.

Measurements down to 5 K

The measurements of silicon sample no.5 were performed with a resolution of 15 GHz in a dedicated FTS setup in the Institute of Physics II by Philipp Warzanowski. The corresponding setup of the Bruker IFS 66v/S consists of a mercury-vapour lamp, a 6 µm Mylar beam splitter, a cryostat with two polyethylene windows and a 4 K bolometer. The cold finger in the cryostat offers two supports for sample attachments. One of the sample holder is used to mount the sample while the other empty sample holder is used as a reference. A telecontrol of the rotatable cold finger allows to interchange the sample position and the reference in situ during operation. In total, measurements at seven temperature values (5 K, 20 K, 50 K, 70 K, 100 K, 150 K and 300 K) were taken. The uncertainty in temperature is negligible as the setup allows to keep the temperature constant during the measurements. For each temperature value a transmission measurement of the sample as well as a reference measurement were taken. The variations in the effective thickness due to movements of the sample are assumed not to exceed 0.8%. The evaluations are based on normalized transmission spectra.

no.	$^*\rho$ [kΩ cm]	d [µm]	i	swap	$T^{\mathbf{meas}}_{\mathbf{min}}$
1	5	363(2)	DSP	yes	~150 K
2	5	363(1)	DSP	no	
3	>3	535(6)	SSP	no	
4	>3	533(1)	DSP	no	
5	5	368(2)	DSP	yes	~ 5 K

Table 5.1.: Specification about silicon sample plates used for measurements. The thickness was determined with a dial gauge and *the resistivity is according to the declaration of the manufacturer. The digit in brackets indicates the measurement uncertainty. The thickness was determined as the average of at least four measurements at different positions for each sample plate. The column "i" specifies if the silicon sample is double-sided polished (DSP) or single-sided polished (SSP). The column "swap" indicates if the reference and sample position were interchanged for each single temperature step measurment (yes), or if in case of "no" only a measurement of the sample spectrum was taken. No swap ensures that there is no change in the effective thickness of the sample due to movements of the sample. The last column gives the lowest temperature value down to which a transmission spectrum of the individual sample has been recorded.

5.2.2. Data extraction

The actual transmission spectrum of a sample is deduced by the normalization of the sample spectrum, that is acquired with the sample placed in the optical beam path, by the reference spectrum of the empty setup. Both FTS setups use different optics and optical elements which especially impacts the lower, appropriable frequency limit of their achievable measurement spectrum due to a diminished signal-to-noise ratio. The according effect on the reference spectra of the respective FTS setup is shown in Fig. 5.3. Absorption and interference features of optical windows and beam splitters clearly dominate the spectra of the empty setups. The consequent frequency range utilisable for the evaluation roughly spans from about 2.5 THz to 18.9 THz.

With the frequency spectra at hand the refractive index is determined based on the interference fringe pattern in the normalized transmission spectra by means of two different methods which are described in Appx. C.3. The fringe difference method using equation (C.33) yields a discrete value for n and α for each pair of two adjoined maxima or minima. The value for the respective quantity is referred to the frequency point in the middle of the frequency positions of the respective adjacent maxima or minima. The fringe order method based on Eq.(C.31) and (C.32) reveals the refractive index for

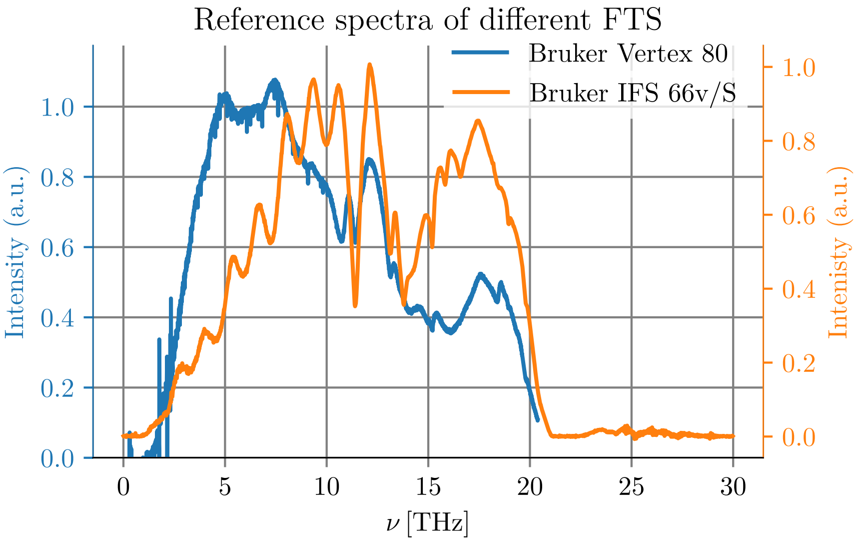

Figure 5.3.: Reference transmission spectra of the in-house extended *Bruker Vertex 80* FTS and the *Bruker IFS 66v/S* FTS of the Institute of Physics II of the University of Cologne at room temperature. Absorption and interference features are attributed to the optical elements in the setups such as optical windows and beamsplitter.

each frequency point of a local extrema. The local extrema are determined using the smoothing and fit procedure described in Appx. C.4. At this point it should be noted that the temperature-related change in the thickness of the silicon samples is taken into account using Eq. (C.40) (see Appx. C.5). An investigation by tracking individual local extrema (see Appx. C.6) in the interference pattern of the transmission spectra reveals that the dominant, temperature-related effect on the transmission spectrum still is caused by a change in the refractive index and not by the change in the thickness.

The transmission spectra of both, about 530 µm thick samples offer more than 440 local extrema and the silicon samples with a thickness around 360 µm exhibit more than 280 local extrema over the frequency span ranging from 2.5 THz to 18.9 THz. The resulting data point distance for $\hat{n}$ is between 35 GHz and 150 GHz, depending on the respective sample thickness, and sufficiently resolves the spectrum in the observed frequency range to study the course of n on the basis of the spectrum fringe rate.

A detailed description of the data processing of the transmission spectra and a comparison of the results for the refractive index of individual silicon samples using both fringe methods is given in the Appx. C.4.2.

5.2.3. Transmission spectra

Unexpected features

The transmission spectra measured in the in-house extended FTS setup exhibit two unexpected features that leap to the eye at first glance looking at the selection of spectra of either the cooling-down or the warming-up cycle in Fig. 5.4. First, the transmission of sample no.3 (Fig.5.4(c)) is the only one revealing a nearly linear decrease with frequency. Being the only sample polished only on one side this might be due to contaminations by molecules which accumulate at such coarse surfaces and still can stack to the surface for the relatively high pressure around about 2.9 hPa of the FTS vacuum. Dispersive scattering losses at the coarse surface might give an additionally contribution.

Secondly, the transmission spectra of all samples exhibit unexpected, broad absorptive features at about around 6.8 THz, 11.4 THz, 13.1 THz and 18.3 THz which are only weakly defined for sample no.3 due to the strongly reduced transmission. Those absorption peaks particularly evident at around 6.8 THz increase with lower temperatures. The most likely explanation for this phenomenon is the accumulation of ice crystals on the sample by freezing out of water vapor at the sample's surface. Those water molecules are still present in the setup after long evacuation time as can be verified in the reference spectra of the empty setup by their absorption lines spread over the whole measurement spectrum. Hydrogen-bonded ice crystals exhibit corresponding absorption lines around about the aforementioned frequencies and especially contain two strong absorption lines near 4.6 THz and 6.6 THz due to lattice vibrations [178]. The absorptive features due to foreign molecules inhibit a reliable estimation of the sample's absorption coefficient since they clearly dominate the calculated results as can be seen in Fig. 5.5(b)-(d) but cannot be separated from contributions originating from the sample itself. As depicted in Fig. 5.5(a) the transmission spectra acquired in the dedicated setup of the IFS 66v/S FTS are free from these distinct absorption lines that grow with decreasing temperature. They confirm that the interfering absorption features are due to the gathering of foreign molecules at the surface of the samples, most likely due to ice crystals. Consequently, all further evaluations concerning absorption and extinction coefficients are solely based on the dataset acquired with the IFS 66v/S setup.

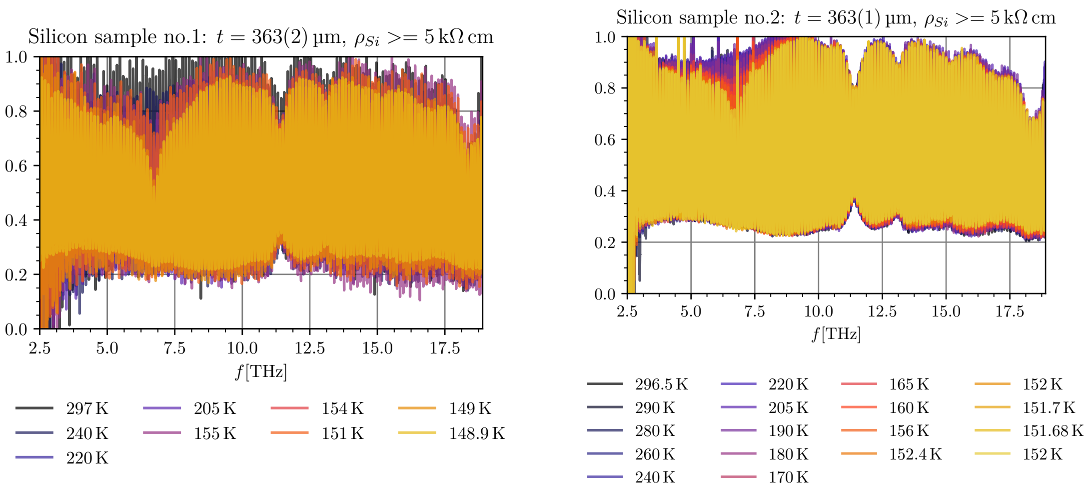

(a) (b)

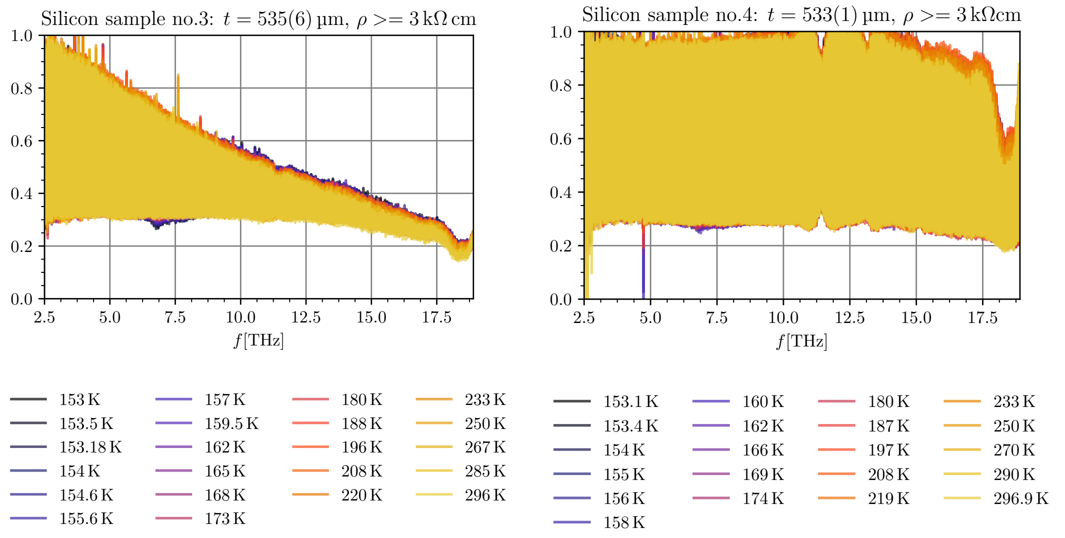

(c) (d)

Figure 5.4.: Transmission spectra of cooling cycles of four different silicon samples. Specifications about the samples can be found in table5.1

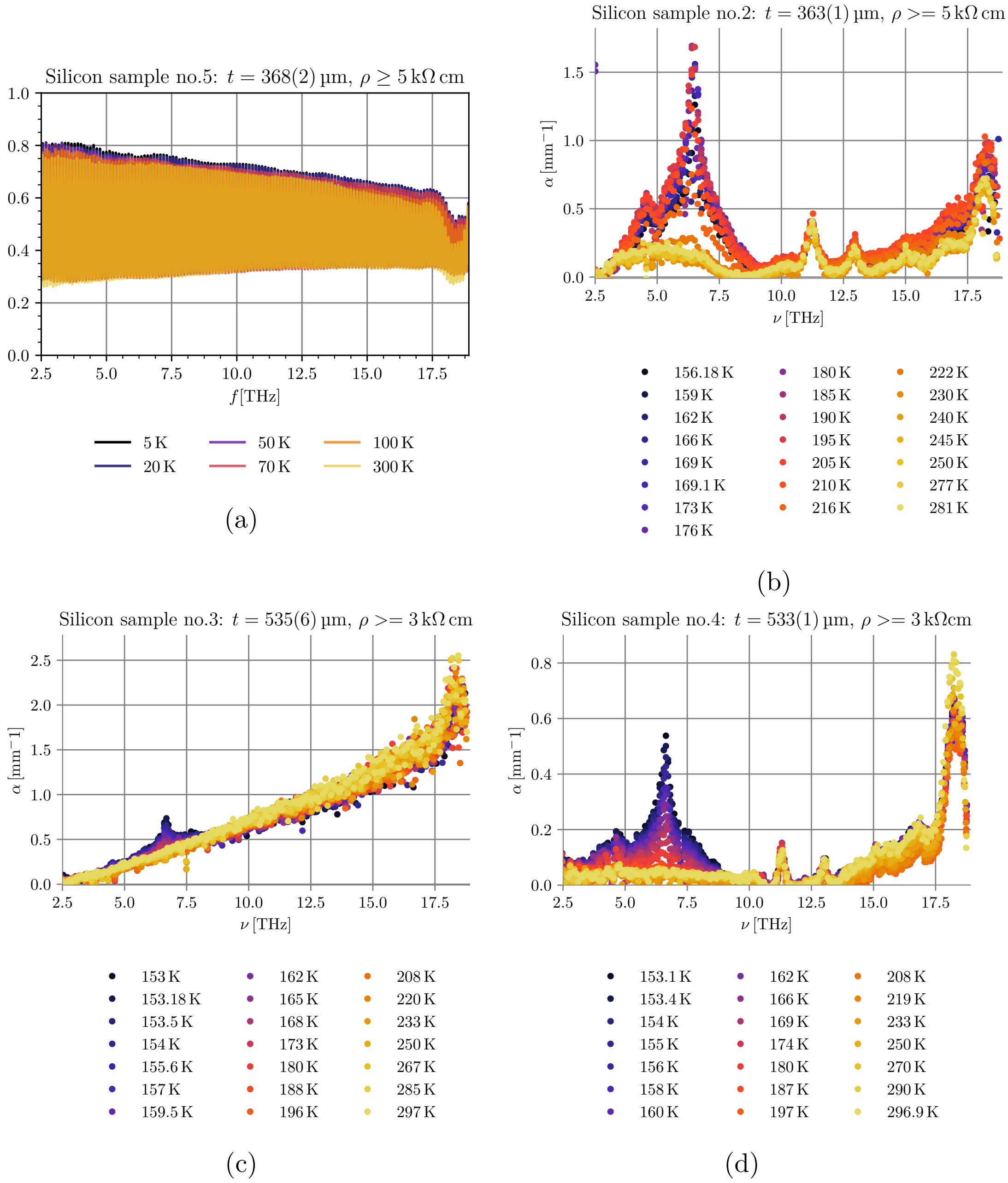

(a) (b) (c) (d)

Figure 5.5.: (a) Temperature-dependent transmission spectrum of the silicon sample measured in the dedicated setup in the Institute of Physics II. Development of the absorption coefficient of Si samples with temperature for a (b) warm-up cycle and (c)-(d) two cool-down cycles.

5.2.4. n as a function of frequency

The results of the measurements yield the same qualitative behavior of the refractive index of silicon for all investigated samples. The measurements performed in this work exhibit a real part of the refractive index that changes less than 0.002 over a frequency interval of about around 12 THz (see Fig. 5.6). Within the measured frequency range n is a weakly increasing function of frequency similar to what was reported e.g. in [47]. However, its dispersive curve shape exhibits a slightly larger gradient compared to the existing, empirically found dispersion formula of the Herzberger-type (C.18) and the Sellmeier-type (C.11), which are available for the upper and lower adjacent frequency regime [85, 109, 47]. This difference most likely arises from setup-specific features such as a frequency-dependent penetration angle on the sample surface [138] or internal reflections within the spectrometer which are not accounted for in the theoretical model.A zoom-in view in Fig. 5.6 furthermore displays some step-type resembling features. As they are only visible in the measurements carried out with the Bruker IFS 66v/S they likely show some setup-specific effects whose detailed investigation would go beyond of the scope of this work. However, it can be excluded that this features arise from the varying Signal-to-Noise ratio that is attributed to the internal FTS-beamsplitter resonances (see Fig. 5.3 in Sec. 5.2.2).

As this study is based on samples of slightly different resistivity a visible impact of the resistivity on the index of refraction is possible. The associated effect on the refractive index can be deduced by means of the Drude model. For isotropic materials the frequency-dependent expression in the Drude term in Eq.(C.7) can be rewritten as a function of the conductivity $\sigma(\omega)$ of the material $\frac{\omega_p^2}{\omega^2+i\omega/\tau} = \frac{\sigma(\omega)}{i\epsilon_0\omega}$ with $\sigma(\omega) = \frac{\sigma_{DC}}{1-i\omega\tau}$ [44]. As the DC conductivity σ_{DC} is inversely proportional to the resistivity ρ [174], a correlation between the dielectric function of silicon and its resistivity is to be expected. Generally speaking, according to the Drude model an increase in resistivity should cause a reduction of the imaginary part of $\hat{n}$ and $\hat{\epsilon}$ along with a lower absorption coefficient which could be demonstrated in Ohba et al. [127]. Likewise, the according real parts are expected to decrease with increasing resistivity. Afsar et al. [1] confirmed this relation for the sub-THz range at room temperature based on a study of silicon samples with resistivities of 1.5 kΩ cm , 2 kΩ cm and 11 kΩ cm. In accordance with the results of these publications, it would be logical to also expect a difference in the extracted results for the measured samples of 3 kΩ cm and 5 kΩ cm resistivity although this effect might be small due to the already small amount of free carriers in all probes. However, at first sight no correlation between resistivity and real part of the refractive index can be observed from the results.

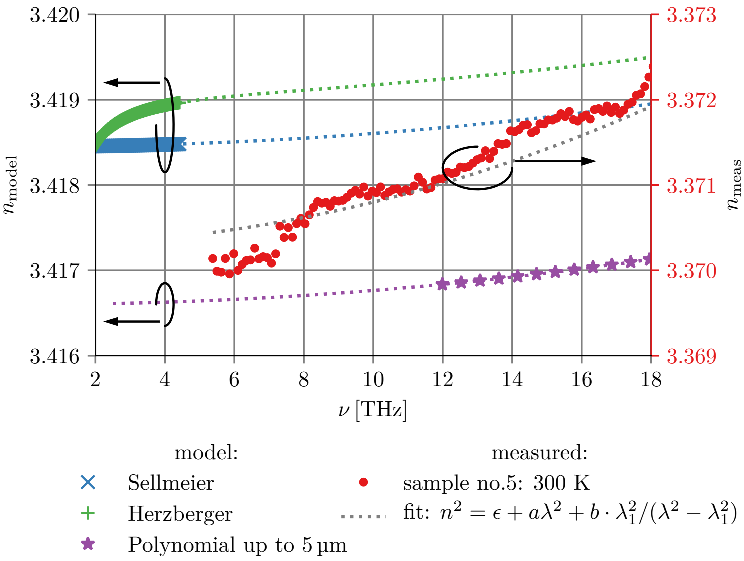

Figure 5.6.: Extracted real part of the refractive index at room temperature in comparison to three different polynomial-type models: Sellmeier [109], Herzberger [85] and Polynomial up to 5 µm [23]. The bold markers indicate the actual frequency ranges these models are based on. The dotted lines refer to the continuation of the models outside their respective frequency ranges.

Neither the calculated absolute values of $n(T)$ in Fig. 5.8(a) nor the relative change in n with temperature depicted in Fig. 5.8(b) enable to confirm a distinct dependence on the resistivity.

5.2.5. n as a function of temperature

The cool down of silicon causes a distinct reduction of its refractive index as depicted in Fig. 5.7. The curves, $n(\nu)$, ascertained from measurements at different temperatures run in a very good approximation parallel to each other within the measured frequency range. Therefore, the change in the refractive index with temperature over the large frequency range can be assumed to be the same for each single frequency value.

To simulate the temperature-dependent behavior of the real part of the refractive index the relative change of n is fitted using three different models, namely the classical Lorentz oscillator model (C.11), the single (C.23) and double oscillator models (C.20). The fit procedure is applied to the total set of all silicon samples with a resistivity of about 3 kΩ cm.

Although the change in n can be assumed to be the same for all three samples, the absolute values in n differ considerably from each other as can be seen in Fig.5.8. The fit functions of all three models, however, still contain a fit-parameter accounting for the absolute value of ϵ or n^2 either at 0 K or 300 K. To simulate the behavior of n with the Lorentz model the absolute value of $\epsilon_{0\,K}$ is extracted by a separate fit of the absolute refractive index for each single data set individually and used as a fixed value for the according data set in the subsequent fit. The remaining parameters defining the slope of the relative refractive index with temperature then are extracted by fitting the respective model over the entire data sets.

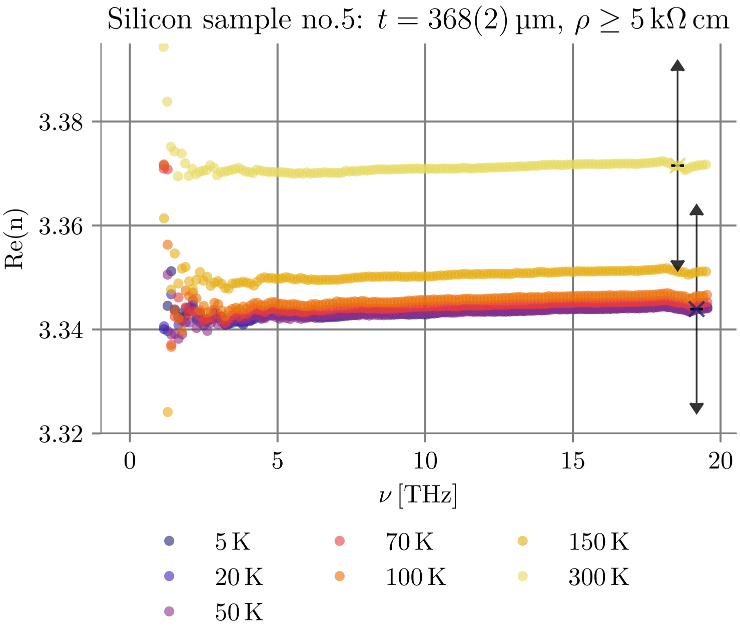

Figure 5.7.: Extracted real part of the refractive index for different temperatures. The arrows indicate the uncertainty due to the uncertainty in the samples thickness.

All fits are accomplished in *python* with the non-linear least squares fit-routine provided by *scipy.optimize.curve_fit* [148]. The values for the fit-parameter are restricted to physically reasonable intervals. For the Lorentz oscillator model the according diagonal entries of the covariance matrix of the fit result are used as the variances to approximate the 95% confidence interval, respectively, for a total of 48 data points. The according interval limits can be found in brackets next to the fit parameters in Tab. 5.2.

The amount of fit-parameters and the highly non-linearity of the fit-functions

increase the difficulty to specify the corresponding uncertainty intervals for the single and double oscillator models. Here, a standard variation of the parameters is estimated by a variational analysis of each initial fit parameter. The results are listed in table 5.2 together with fit parameters from literature published at other frequency values within the here measured frequency regime or in close vicinity to it. A reasonable correspondence between fit parameters at different frequencies can be expected, since the change in the refractive index with temperature (see Fig. 5.7) is in very good approximation the same over a large frequency range.

Lorentz oscillator	ϵ_{0K}	a_1^{eps} [K^{-1}]	a_2^{eps} [K^{-2}]	a_3^{eps} [K^{-3}]
This work	11.05-11.54	$2.94(1.56)\times10^{-5}$	$2.21(0.12)\times10^{-6}$	$-7.77(2.42)\times10^{-10}$
Ref. [109]	11.4552	2.7765×10^{-4}	1.7066×10^{-6}	-8.1423×10^{-10}

(a)

Double oscillator	α_Λ [10^{-4}eV/K]	α_χ [10^{-4}eV/K]	β_Λ [K]	β_χ [K]	G_Λ [eV^2]	G_χ [eV^2]
This work	4.00(0.78)	2.68(1.5)	600(17)	508(10)	10.1 (8.0)	140.5(16.3)
Ref. [39]	5.27(0.12)	2.67(0.04)	419(29)	302 (21)	25.3(0.8)	149.8(7.0)
Ref. [6]	–	–	–	–	23.75	159.28

(b)

Single oscillator	$E_g(0)$ [eV]	$E_p(300\,\text{K})$ [eV]	α_g [10^{-4}eV/K]	β_g [K]
This work	3.6(0.6)	9.3(1.5)	4.1(2.9)	700(220)
Ref. [39]	4.03(0.02)	13.31	3.41(0.03)	439(13)
Literature values				
Ref. [175]	1.1557	–	7.021	1108
Ref. [2]	1.1692	–	4.9 ± 0.2	655 ± 40

(c)

Table 5.2.: Fit parameters for different models describing the temperature dependence of the real part of the refractive index. Fit parameters of the classical Lorentz oscillator model are based on Eq. (C.8). Fit parameters of the single and double oscillator models refer to Eq.(C.23) and (C.20). Numbers in brackets for fit parameters of this work in table (a) refer to the 95% confidence interval and in table (b) and (c) to the estimated standard deviation.

The curves of n with temperature simulated with the different models as well as predictions from selected publications are depicted in Fig. 5.9. All three fit-models based on a classical or extended Lorentz oscillator model are suitable to describe the measured temperature dependence of the real part of the refractive index. However, the range below 70 K is the most difficult range to fit accurately. None of the models can perfectly reproduce the rather fast convergence of n in this temperature range. A comparison with the results from other publications clearly demonstrates that a reasonable prediction of n for lower temperatures roughly below 70 K is not possible if the fit-parameters have been extracted only on basis of measurement results above 100 K. That predictions would yield a considerable deviation from the here presented measurement results (see Fig. 5.9, pink dashed and purple and red dash-dotted lines). Accordingly, the fit-parameters for the classical Lorentz model deviate from existing publications. In constrast to [109] (see Tab.5.2(a)), the values found in this work propose a stronger quadratic dependence of the permittivity with temperature but a smaller linear dependency on T. Both fits based on the single and the double oscillator model yield rather similar results as can be seen from the gray dotted and the brown dashed curves in Fig. 5.9. The fit value of about 3.6 eV for the average band gap energy at 0 K is around about 30% higher compared to literature values about 1.17 eV [99], 1.1557 eV[175] and 1.1692 eV [2] but is within the same order of magnitude. As can be seen from Tab.5.2(c) the values for α_g und β_g are within the range provided by other publications.

The slope of n predicted by the empirically determined fit-function of Naftaly et al. [121] which is the only work based on measurements from 296 K to 4 K, reproduces the fast convergent behavior of n with lower temperatures. Although Naftaly et al. states that their model only gives good results for temperatures above 70 K, surprisingly, their prediction for n above 70 K yields a slightly larger reduction of the refractive than can be found from my own data (see the dotted orange curve in Fig. 5.9).

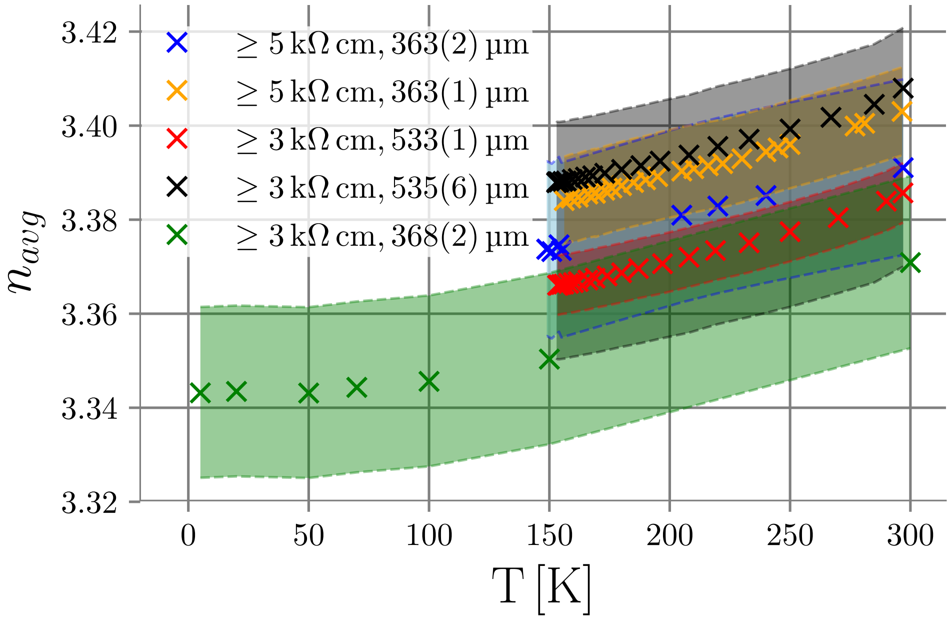

(a)

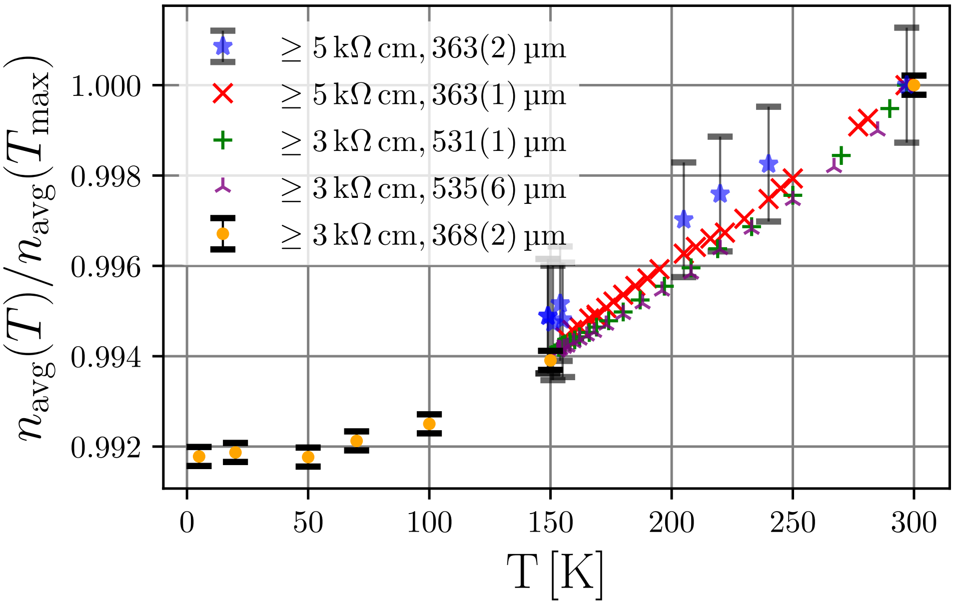

(b)

Figure 5.8.: (a) Extracted real part of the refractive indices of 5 different silicon samples with temperature and (b) according relative change in the refractive index based on the value at maximum temperature. n_{avg} represents the mean value averaged over the frequency interval from 7.5 THz to 12.5 THz. The legend indicates the resistivity and the thickness of the respective sample.

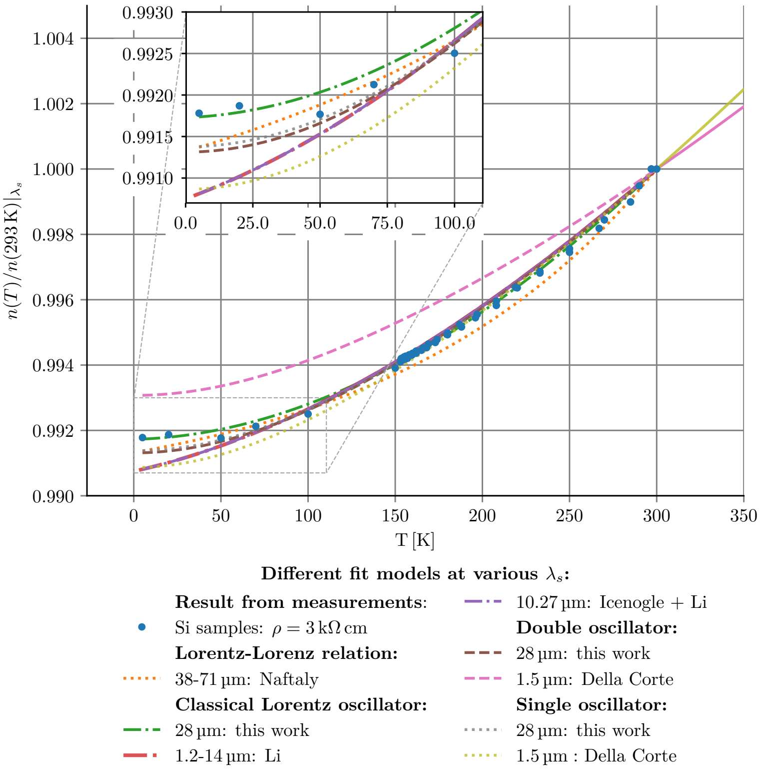

Figure 5.9.: Relative change in the refractive index with temperature: Comparison of different fit models applied to the measured results of this work and comparison with fit results of publications from Naftaly et al. [121], Li [109], and Della Corte et al. [39]. Della Corte et al. [39] applied both oscillator models to their measurement results at a wavelength of 1.5 µm for the temperature range from 300 to 600 K. The fit results of Li [109] are based on measurements down to 100 K. The respective fit curves are drawn as solid lines within the temperature range of their measurements and as dashed or dotted lines otherwise. Naftaly et al. [121] empirically determined fit-function is based on measurement results from 4 to 296 K.

5.2.6. Extinction and absorption coefficient

The transmission spectra acquired with the in-house extended FTS setup exhibit large, absorptive features which can be attributed to water molecules gathering at the sample's surface as has been reported in Sec. 5.2.3. As those features disable a reliable extraction of the absorption or the respective extinction coefficient, n' and α, all presented results solely rely on the datasets of silicon sample no. 5 down to 5 K in the IFS 66v/S spectrometer. The respective data processing is given in Appx. C.4.3.

As described in more detail in Appx. C.3, the accuracy of both quantities, the extinction and absorption coefficients, extracted from fringe methods relies on the exact determination of the magnitude of the local extrema in the interference pattern of the transmission spectrum. However, the magnitude of the transmission pattern is especially sensitive to power-variations in the radiation source between successive reference and sample measurements. A comparison of several transmission measurements (depicted in Fig. 5.10) which have been performed at the same temperature reveal an average power alteration of around about 3 % over the measured frequency range. To estimate the order of magnitude of the associated uncertainty in n' and α, therefore, a fractional drift in the source power of maximal 3 % between two successive measurements is plausible.

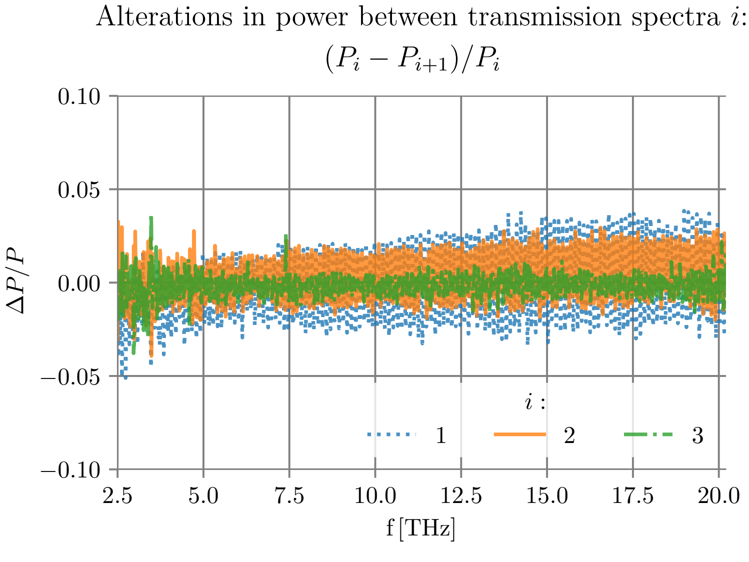

Figure 5.10.: Change in power between successive measurements due to intensity fluctuations of the radiation source: Transmission measurements i performed at the same temperature with a sample in the optical path are compared to estimate the average power fluctuation $\Delta P/P$.

To compute the spectra to be expected for a 3 % higher or 3 % lower underlying intensity level over frequency, the reference spectra are corrected by the corresponding power fluctuation $\Delta P/P = 0.03$ and are used to normalize the original sample spectra. These modified spectra represent the transmission spectra if accounting for a respective increase or decrease in the intensity due to the power fluctuation. The absorption and extinction coefficient extracted from the modified spectra give the upper and lower limit of the according uncertainty intervals.

Results:

The calculated values for the imaginary part of the refractive index and the absorption coefficient are shown in Fig. 5.11. The contribution to the overall uncertainty by the uncertainty of the sample's thickness (see blue error bars in Fig. 5.11 (c)) is neglected as it is considerably smaller than those expected due to the effect of power fluctuations (see shaded violet areas in Fig. 5.12(c), (a) and (b)).

In the vicinity of 10.7 THz a temperature change from 300 K to 5 K roughly yields a reduction of both quantities by 30 % to 35 % as can be seen from Fig. 5.11 (c) and Fig. 5.12(c). The observed change is similar to the decrease around about 62 % reported in Loewenstein et al. [111] from 300 K to 1.5 K at about 28.57 µm and the decrease down to roughly 53 % reported for a silicon sample with a resistivity of $> 5\,\mathrm{k\Omega\,cm}$ from 297 K to 4.5 K [38] for frequencies below 7.7 THz. For a better overview, a collection of further absorption or extinction values found in literature at or close to 10.7 THz are summarized in Tab. 5.3

reference	λ [µm]	T [K]	α [cm^{-1}]	n'	sample information
[32]	23.26	77K	$^{*} \approx 1$	—	p-type, $\rho \geq 1\,\mathrm{k\Omega\,cm}$
[92]	2-30	20 K,77 K	**1-2.5	—	pure, high quality single crystal grown in vacuo
[111]	28.57	300 K	3.4(2)	—	
	28.57	1.5 K	2.1(2)	—	$\rho = 0.1\,\mathrm{k\Omega\,cm}$
[38]	16.66-1249	297 K	—	$^{***}\approx 2.19 \times 10^{-4}$	$\rho > 5\,\mathrm{k\Omega\,cm}$
		4.5 K	—	$^{***}\approx 1.18 \times 10^{-4}$	$\rho > 5\,\mathrm{k\Omega\,cm}$
[156]	20	room	2.0871	3.3218×10^{-4}	bulk silicon
[179]	≤33.33	300 K	—	8.9×10^{-5}	high-purity silicon,
	≤33.33	10 K	—	4.9×10^{-6}	$\rho \approx 30 - 40\,\mathrm{k\Omega\,cm}$

Table 5.3.: Reference values from literature for the absorption coefficent α and the imaginary part n' of the refractive index: * read off from [32, Fig.3], ** read off from Figure of the section "result" in [92]), *** calculated from the values ϵ'_{∞} and ϵ''_{∞} provided in [38, Tab. 2].

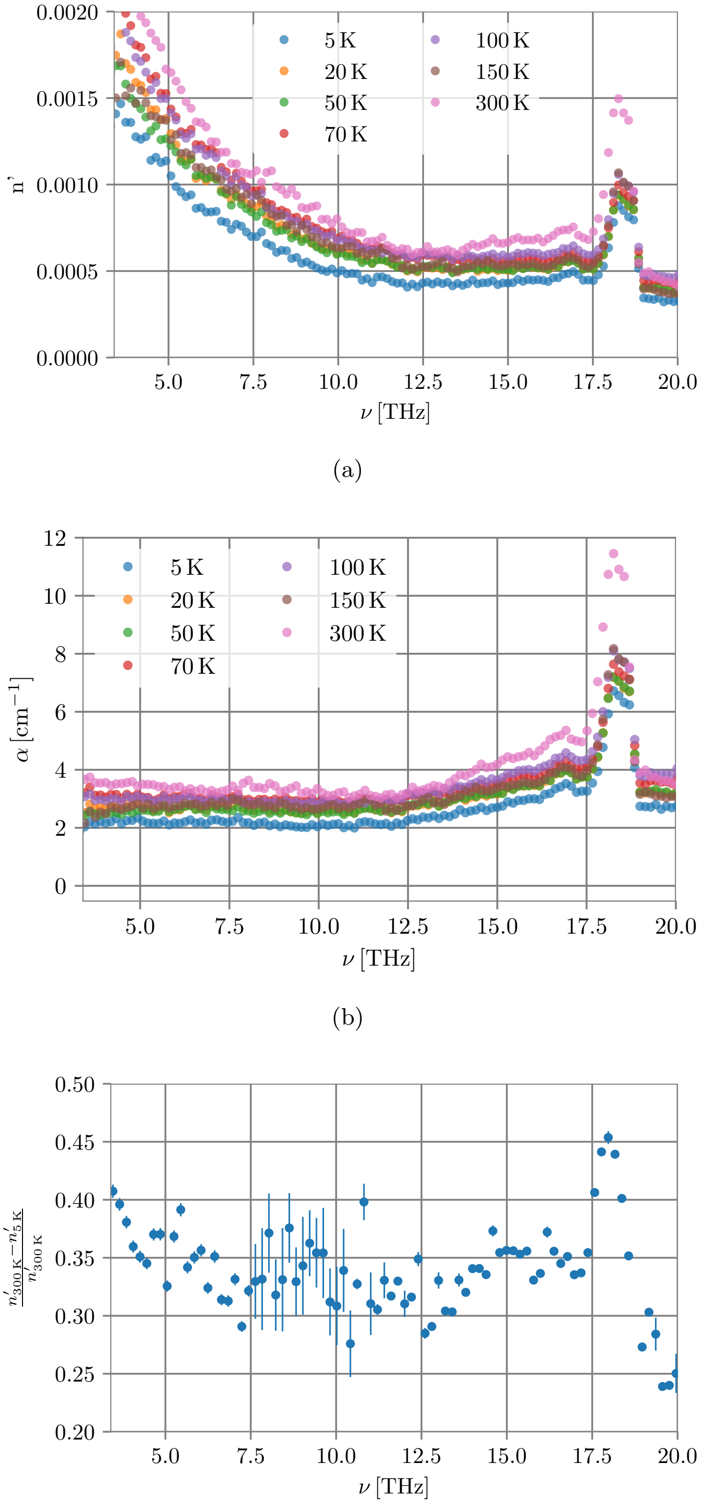

(a)

(b)

(c)

Figure 5.11.: Extinction (a) and absorption coefficient (b) of silicon extracted on basis of Eq. (C.38) for different temperatures. The relative change in n' with a reduction of the temperature from 300 K to 5 K is depicted (c). The blue error bars refer to the uncertainty expected due to the uncertainty in the sample's thickness.

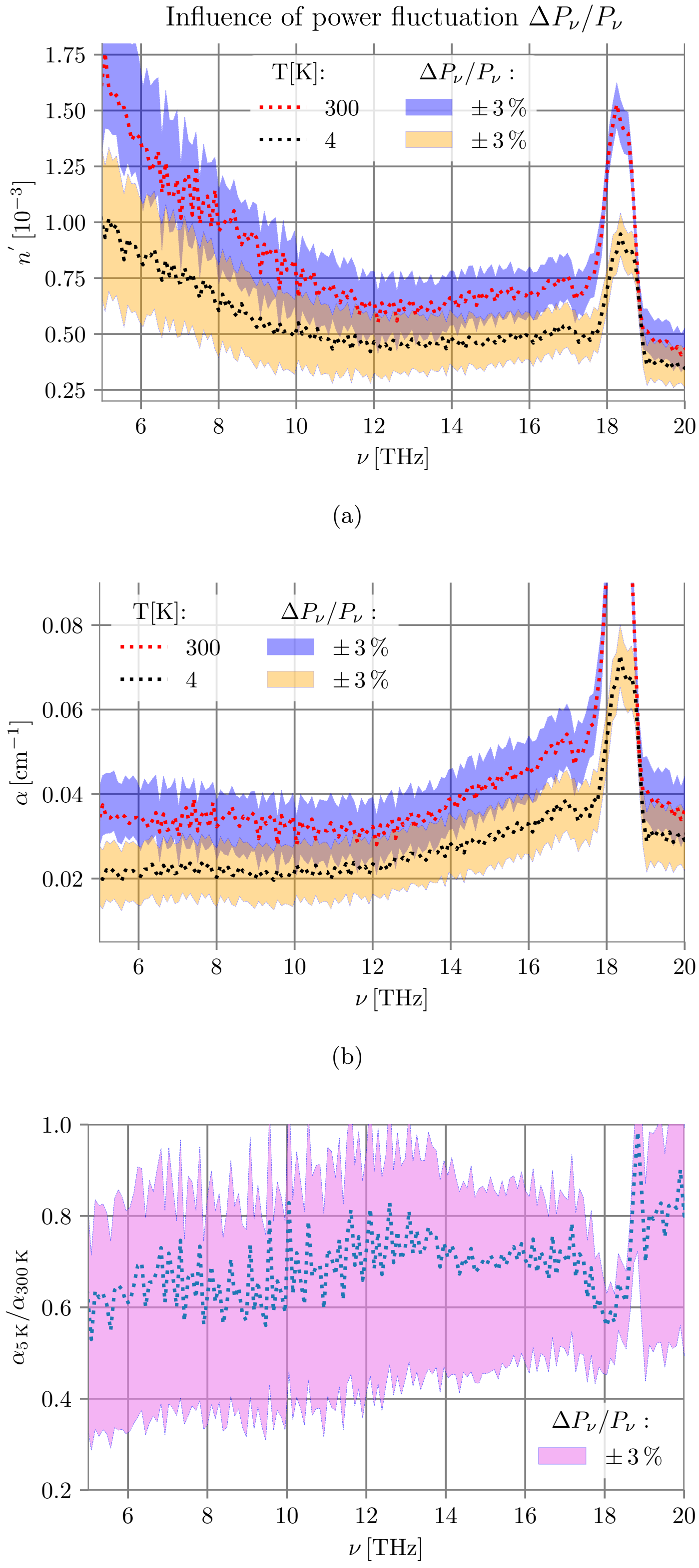

(a)

(b)

(c)

Figure 5.12.: Extinction (a) and absorption coefficient (b) of silicon extracted on basis of Eq. (C.38) at 5 and 300 K. The shaded regions indicate the uncertainty level expected due to power fluctuations of the radiation source of about ±3%. The contribution due to the uncertainty in the sample's thickness is significantly smaller as depicted in Fig. 5.11(c) and can be neglected.

5.2.7. Conclusion and outlook

The observed change in the real part of the refractive index for float zone silicon from 300 K to 5 K is about 0.83 %. The absolute values extracted by the fringe order method are spread over a range from 3.37 to 3.41 with a rather large uncertainty due to the uncertainty of the sample's thickness and cannot be used to precisely specify an absolute number for n. Relying on values from literature [179, 121, 111] and considering a frequency dependence of Sellmeier-type (C.11) the refractive index can be assumed to be around $3.417 \pm (0.008)$ at room temperature. Accordingly, at cryogenic temperatures the best estimate for the dielectric constant of silicon needed for the design of the high frequency circuits in this work is 11.4(1).

The dielectric loss estimated by means of the transmission measurements is accompanied by a considerably large uncertainty that is attributed to the power fluctuations in the radiation source expected between successive measurements. Nevertheless, a decrease of the extinction and the absorption coefficient with lower temperature is clearly visible. This is to be expected due to the freezing-out of conduction electrons with temperature and has been reported in other works [38, 179, 109, 111, 155]. Based on the extracted results the upper limit for the absorption coefficient at cryogenic temperatures is assumed not to exceed $0.03\,\mathrm{cm}^{-1}$. Using Eq. (B.4) to roughly approximate the order of magnitude for the dissipation loss expected due to the silicon lens chosen for the quasi-optical design of the receiver yields about 0.09-0.10 dB at maximum.

In comparison to other observations (summarized in Tab. 5.2 and Tab. 5.3) the results of this work are qualitatively consistent. A quantitative statement with regard to the scant data from literature is, however, difficult, as it requires the inclusion of three further aspects. These are additional material specifications like the resistivity and the type of doping which are known to influence the absorption properties of silicon[1], information about the processing like compensation for doping, and finally the measurement procedure and method. Due to a lack of adequate details in many prior works there is no basis for a quantitatively meaningful comparison.

Since the current information available is still scarce a detailed experimental study of the dispersive and temperature-dependent behavior of the refractive index on its material specifications would be welcome.

As demonstrated in this work the models to describe the temperature-dependence of n or ϵ are suitable albeit not perfectly precise. Findings from prior works for the fit-parameters, however, do not allow to predict the downward slope observed in this work correctly. Models for the prediction of the response of semiconductors are still mainly based on semi-empirical fitting instead of physics-based formulas, for instance established on the time-dependent perturbation theory of quantum mechanics [170]. To assess the quality of the predictions of those models the measured results, however, need to be as precise as possible.

The accuracy of the extracted quantities by FTS measurements relies on using a realistic model for the sample and beam configuration and correctly estimate the corresponded model parameters[23] like partial coherence[73] or a convergent beam angle[138]. The uncertainty in the extinction or absorption coefficient, respectively, especially for early publications can range from 5%[138] over even be discarded due to an error in the data as large as 20%[32]. Precise results relying on different methods, where for instance the real and imaginary part of $\hat{n}$ can be determined separately and directly from measurements, would strongly help to confidently fill this gap of scarce knowledge and scant proven correlations between material specifications and electromagnetic response of silicon. A promising candidate for experimental studies is the Terahertz time-domain spectroscopy, a phase-sensitive method to measure the complex dielectric function of materials. Ongoing development within the last years based on THz air-photonics enabled to extend the operating frequency range of this technology from around previous 4 THz up to 15 THz [35]. Terahertz time-domain spectroscopy based on the previous technology has been used to measure the complex refractive index in the far-infrared below 4.5 THz but reportedly yields an increasing uncertainty in the absorption coefficient with increasing frequency[36]. It remains to be seen if the THz air-photonics technology reveals similar observations. Finally, to safely proof and identify correlations between the material specifications and the temperature-dependent refractive index of silicon in this frequency range further analysis is necessary. This is, however, beyond the scope of this work.

5.3. Characterization of materials needed for the measurement setup

5.3.1. Cryostat windows

As mentioned earlier, at entering the high frequency regime around 10.7 THz materials are little explored for certain applications and measurement technologies. Common materials for windows, lenses, beam splitters or polarizers used for THz applications are high-density polyethylene (HDPE), polytetrafluoroethylene (Teflon), polyimide (Kapton), poly [bisphenol A carbonate] (BPC) and polymethylmethacrylate (PMMA). First investigations [34, 35] up to 9 THz indicate that those materials become opaque at higher THz frequencies. Transmission measurements of common windows materials with a Fourier Transient Spectrometer (FTS) conducted up to $17-20$ THz (see also Figure 5.13) confirm that due to their high absorption in the specified frequency range, they are unsuited for the measurement setup or the receiver. Recent investigations [34, 35] in the area of polymer research exhibits possible suitable alternatives in cyclic olefin/ethylene copolymers such as the polyethylene cyclic olefin copolymer called Topas[6]. Measurements up to 9 THz of Topas samples conducted by [34] reveal an absorption coefficient below 3 $\mathrm{cm}^{-}1$ at room temperatures. To estimate its absorption behavior around 10 to 11 THz several transmission measurements with the FTS on TOPAS samples[7] have been conducted. The transmission of the five different samples in total is depicted in Fig. 5.14 and the results are summarized in Tab. 5.4.

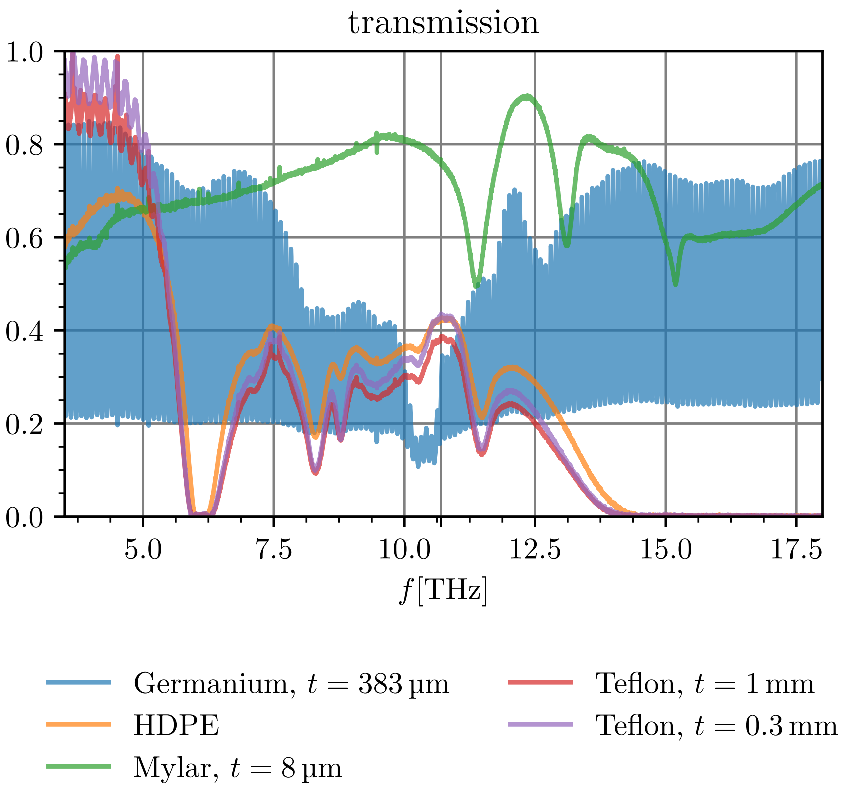

Figure 5.13.: Transmission measurement of different well-known materials, conducted with the FTS at room temperature.

As the foils seem to be prone to easily crack and quickly tear the Topas plates of 2 mm thickness are chosen as possible candidates for the cryostat window.

---

[6] Topas from TOPAS Advanced Polymers GmbH, https://topas.com

[7] In this context I would like to thank Mr Wolfram Goerlitz from the company *TOPAS* for kindly providing and sending us all different samples for testing purposes.

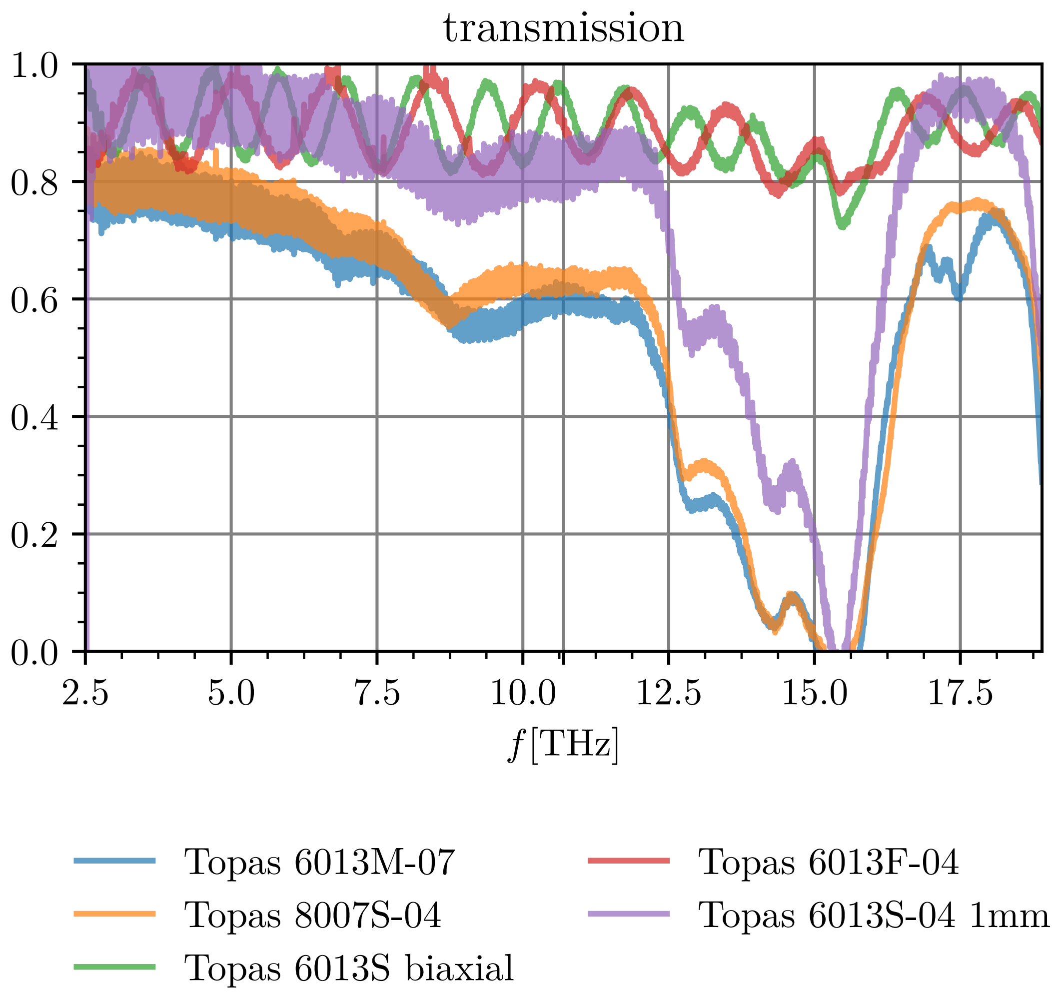

Figure 5.14.: Transmission of five different Topas samples measured in the FTS.

sample name	sample typ	thickness	$T_{10.7\,\mathrm{THz}}$
TOPAS 8007S-04	plate	2 mm	0.63(6)
TOPAS 6013M-07	plate	2 mm	0.61(6)
TOPAS 6013S-04	plate	1 mm	0.83(5)
TOPAS 6013F-04	foil	150 µm	0.90(6)
TOPAS 6013M-07	foil	10 µm	0.95(6)

Table 5.4.: Specifications of the Topas samples[1]: TOPAS 6013F-04 has an elongation at break about 3%. TOPAS 6013M-07 has an biaxial orientation due to a stretching frame and an elongation at break about 100%. The uncertainty of the transmission is given in brackets and refers to the last digit of the measured value.

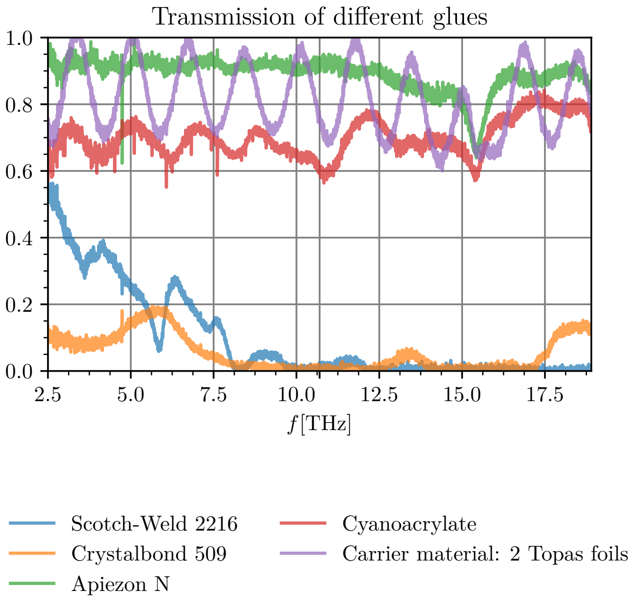

Figure 5.15.: Transmission spectrum of different glues applied at 2 Topas foils as carrier material. The transmission through the Topas foils without adhesives in between (purple line) exhibit low losses over the whole frequency range.

5.3.2. Glues

The quasi-optical receiver requires to connect the silicon lens to the thin silicon membrane that contains the high-frequency circuit with the antenna. In this work both components are stuck together by glue with the intention to attach most of the glue to the outer brim of the lens. During assembly, however, a little bit of glue needs to be applied between the lens and he antenna substrate. For this function we want to use a glue with ideally low absorption. A short study of the transmission behavior of possible glue materials have been performed by FTS measurements. For the transmission measurements different adhesives have been applied between two Topas foils which without additive exhibit a good transmission as can be seen in Fig. 5.15. The thickness of all adhesives layers have been kept roughly 1 mm. The transmission behavior of the different glues ranges from rather transparent to opaque at around 10.7 THz- Unfortunaly, Crystalbond and Scotchweld, the two glues that are most often used for assembly due to their mechanical and their curing properties are opaque.

6. Fabrication and assembly

The fully assembled mixer unit consists of several parts of which the RF-chip and the receiver housing are fabricated in-house. Additional components such as the IF-board, the silicon lens and a suitable plug IF/DC-connection have been ordered. The IF-board and the SMPMT connector are assembled into the receiver housing in a separate step and form a permanent unit that is reused for all RF-circuit designs developed in this work. Only when the RF-chip is mounted on the IF-unit the silicon lens can be attached to the RF-chip in the very last step. The following sections give a description of the fabrication process of the RF-chips. Subsequently, all components of the permanent mixer-unit are introduced and the final assembly of all parts is presented.

The fabrication of and needed process development for the RF-devices has been done by Dr.Karl Jacobs. The design of the IF-chips, the housing and assembly of the detector is the work of Michael Schultz. The IF-design of the passage between the IF-chip and the RF-chip with regards to their embedding into the copper housing has been done by Dr. C.E. Netty Honingh.

6.1. Fabrication and mask design

The RF-devices presented in this work have been fabricated in the in-house microfabrication laboratory. To manufacture the RF-chips several fabrication techniques are required including electron-beam (E-beam) lithography for the RF-structures, UV-lithography for the embedding IF-circuit and beam lead technology for thicker gold layers which are designated as contacting *beamleads* and stick out over the rim of the silicon membrane. Furthermore different etch techniques (Argon etch, O_2 etch, BHF etch and DRIE) are used either for cleaning purposes or to remove material layers or etch out structures through a 9 µm thick silicon membrane.

Per batch 80 RF-chips can be fabricated. One batch contains in total 20 different RF-chip designs. Starting base is a 30 mm × 30 mm silicon on insulator (SOI) wafer which is composed of a 300 µm thick silicon layer serving as the handle wafer, followed by a 500 nm thin SiO_2 layer and the device layer on top that consists of a 9 µm thick high resistivity silicon layer. In the very first step a 7.0(5) nm thick NbN-layer is deposited on the device layer side of the SOI wafer by Michael Schultz. From this layer the HEB microbridges of the devices are made in later fabrication steps. Subsequently in total 7 further layers consisting of Au, NbTiN, SiO_2 and some adhesion layers are deposited on the device-layer of the SOI wafer. All layer-depositions follow the same principle that in general can be devided up into 5 process steps: First a photoresist is applied on the wafer and exposed by E-beam- or UV-lithography through an optical mask that contains the negative or positive images of the structures which shall be deposited on the wafer. Depending on the used photoresist either its exposed or its non-exposed part, respectively, can be removed by development in a solvent. Subsequently, a layer of the desired material is deposited by sputtering over the whole surface of the wafer. Using another solvent the remaining photoresist is removed from the wafer. After this liftoff process the wafer surface is only covered by the deposited layer at those positions which have been defined by the image of the photo mask. After depositing all required layers on the device-layer side of the SOI wafer the alignment slots for the lens are etched through the device layer and the process wafer is diced into specified sections (see Fig.6.3 in Sec. Mask design). At this step the DC characteristics (T_c, I_c, R_N) of the HEB elements integrated into the RF-circuits (as depicted in Fig. 6.1 and 6.2(a)) are measured for the first time by recording the RT and IV-curves by dipsticking in a helium can. Subsequently, the thick handle wafer of each sector is removed by plasma etching (DRIE) and the SiO_2 is removed by a buffered oxide etch (BHF). Based on a last UV-lithography step at the backside of the device-layer the RF-chip outlines and the glue depots are defined. The RF-chips are etched out and after a thorough cleaning are ready for the assembly.

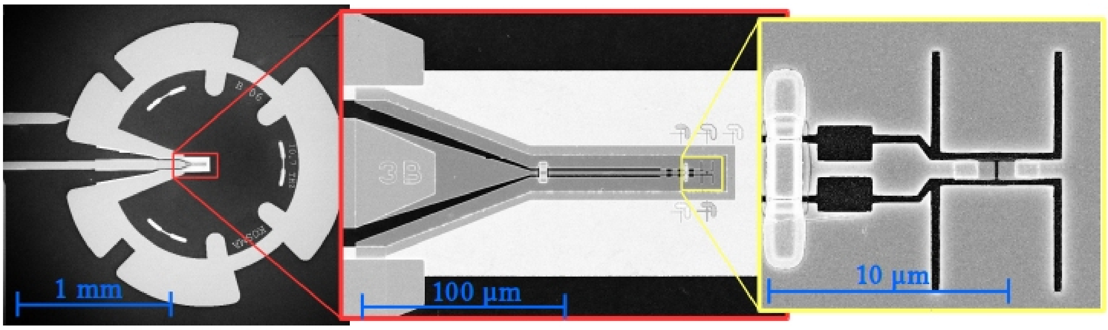

Figure 6.1.: SEM images of fabricated RF-chip before final etching step.

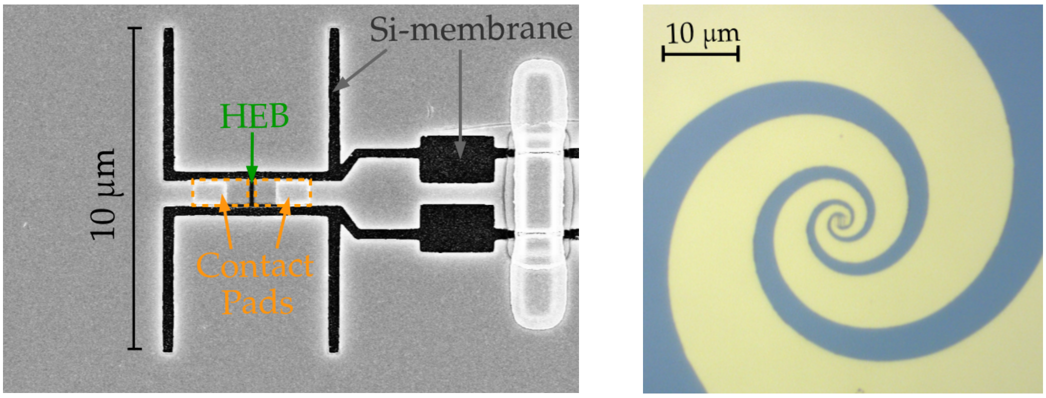

(a) (b)

Figure 6.2.: Scanning electron microscopy (SEM) image of a fabricated double-slot antenna (a) and microscope picture of a logarithmic spiral antenna (b). The grayish color in (b) is the silicon-membrane, the yellow colored surface is gold.

Mask design

The optical mask needed for the exposition with the desired circuit-structures not only provides the images of the RF-designs but also contains images of several structures to determine the quality of the NbN-film and the sheet resistance of gold layers of different thicknesses at different locations on the process wafer. Due to the limited space on the mask a careful choice of five different versions of the double-slot antennas for 10.7 THz was required as well as the restriction to one RF-filter design where aside from the nominal length the last part of the filter is additionally shortened and extended to compensate potential capacitive or inductive impedance contributions at the critical antenna-filter interface. The drawing of the corresponding mask design combining the UV as well as E-beam lithography is depicted in Fig.6.3. It is divided up into 6 sectors from A to F containing the different RF-designs and NbN test-films (zoom-in at the right-hand side of Fig.6.3). The four rim sections, indicated as AV, CV, DV and FV contain van-der-Pauw structures and lines to measure the sheet resistance of different gold layers.

6.2. Receiver Housing and IF-board

The receiver housing and the IF-board have been designed by Michael Schultz. A sketch of both components is shown in Fig. 6.4. The housing consists of a 1.8 cm × 1.8 cm × 0.6 cm copper holder made of oxygen free copper tellurium alloy (CuTe) that provides the assembly interface for the antenna chips, the interface to the fore-optics and to the IF connection. A pyramidal-shaped front section with a hole of 1.6 mm diameter in its middle is used to integrate the lens antenna into the housing. The slightly angled surfaces of the pyramidal front section are intended to reflect any interfering signal that is outside

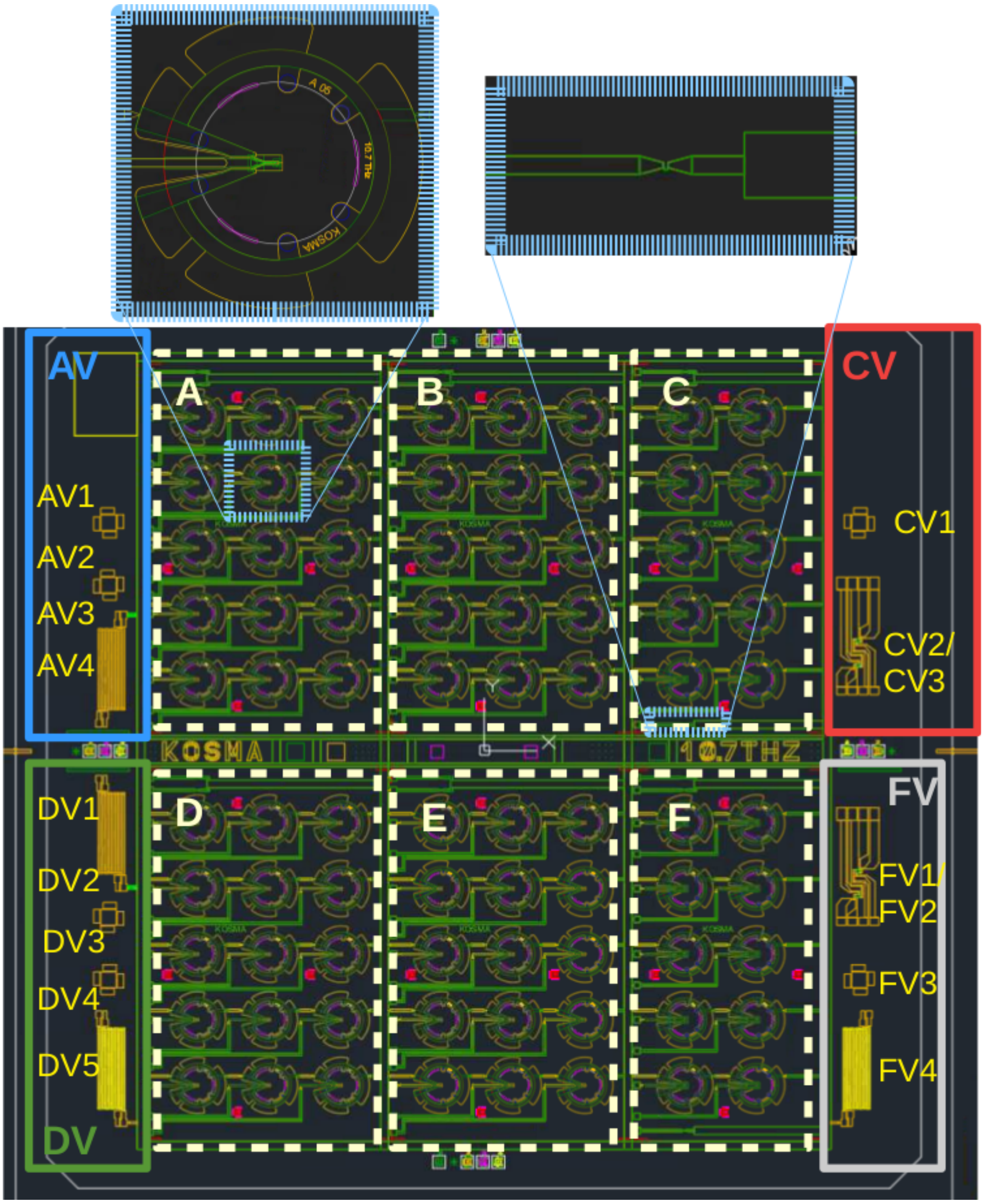

Figure 6.3.: AutoCAD drawing of the optical mask for UV and E-beam lithography. The optical mask is divided up into different sections A to F which contain the different RF-chip units (see zoom-in at the left-hand side) and some test-structures with NbN films (see zoom-in at the right-hand side). Sector AV, CV, DV and FV contain lines and van-der-Pauw structures to measure the DC resistance of gold layers of different thicknesses.

the area of the lens aperture out of the optical beam path. A recessed pocket in one of the pitched surfaces serves as socket for the IF-board. It can be accessed from the backside of the housing via a hole passage for the inner conductor of the SMPMT IF connector. The copper housing was fabricated in-house by the mechanics workshop. The triangular-shaped IF-board consists of a 50 Ω micro-stripline with a curved foot at one end to enable an easier connection to the IF-output (see Fig. 6.4(right)). The TMM10 board is glued into the block with EPO-TEK H20E.

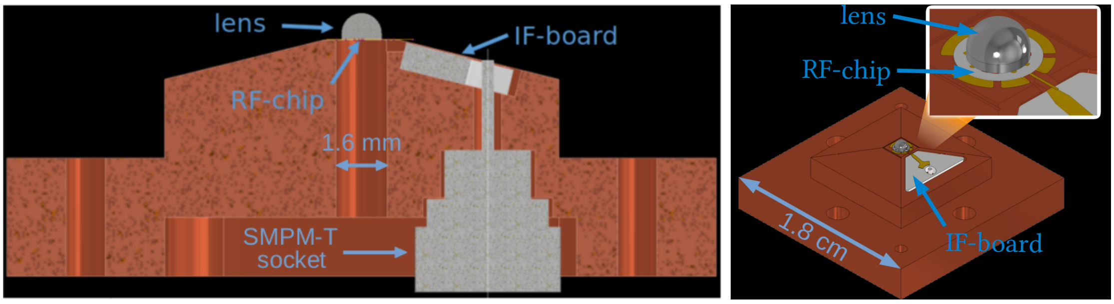

Figure 6.4.: Sketch of the fully assembled mixer block: (left) cut through the mixer block, (right) perspective view of the mixer block.

6.3. Assembly

The mixer assembly has been done by Michael Schultz. A sketch of the complete mixer unit is depicted in Fig. 6.4. First of all the IF-components need to be assembled. Therefore the IF-board is glued into the recessed pocket of the copper block. The SMPM-T-socket that is utilized as IF-output port of the detector is soldered up to the backside of the receiver housing. Its inner line is guided via the hole passage to the front-section of the housing and sticks out of the IF-pocket where it is connected to the transmission line on the IF-board. With the complete permanent IF-unit on hand, the RF-components now can be added in the next steps. In the first step, the RF-chip is centered over the middle of the copper-hole and is fixed by its grounding beamleads and some tiny glue drops to the detector housing. Its IF-beamlead line (see Fig. 6.5 (left)) is bonded to the micro-strip line of the IF-board. To attach the 1 mm diameter lens to the RF-chip, the lens is first prefixed on the chip using Crystalbond that has been filled into glue depots which are recessed in the RF-chip. The glue depots (see Fig.6.5 (left)) are closed at the device-layer side by a gold layer to prevent any contact to the RF-structures. By means of three adjustment marks in form of warped bone-shaped holes (pink-shaped features in Fig.6.5 (left)), that are etched through the whole Si-membrane, the lens is optically aligned to the RF-chip through a microscope and finally fixed with small drops of Scotch Weld at the lens-membrane interface-edges. The maximum shift of the center of the RF-chip to the center of the backside of the lens thereby is expected to be below 5 µm. The realized alignment between RF-chip and lens that could be achieved so far and is depicted in Fig.6.6 is below 2 µm.

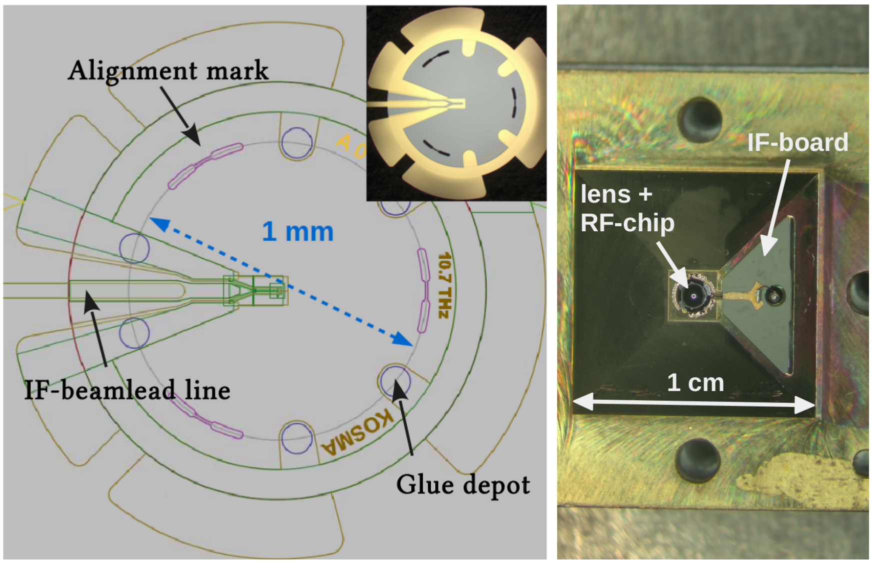

Figure 6.5.: Scheme of a RF-chip (left) and picture of the front-side of a fully assembled receiver (right). The small overlay image in the left figure is a picture of a fabricated RF-chip (yellow surfaces: gold, gray surfaces: silicon).

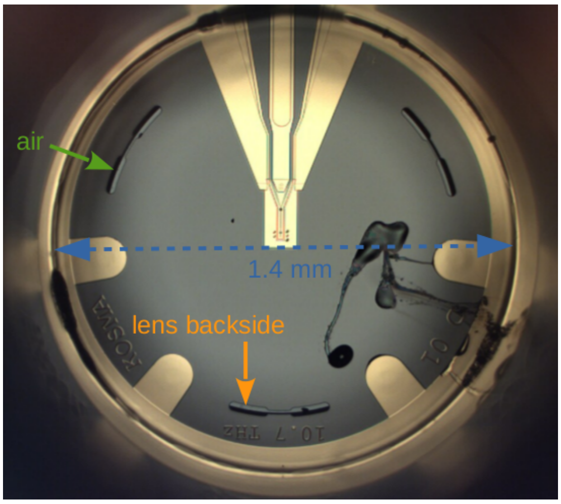

Figure 6.6.: Microscope picture of the RF-chip taken through the backside of the detector housing when the detector is fully assembled. The bright gray areas which fill out half of the alignment marks belong to the silicon lens that is attached to the backside of the RF-chip.

7. Measurements

In the following chapter the measurements to characterize the DC properties of HEB devices and the direct RF response of five assembled mixers are presented. Measurements of the mixer performance and noise could not be carried out so far due to the missing local oscillator for 10.7 THz.

7.1. DC characterization

In this section the measured IV-curves and the RT-curves of HEB elements from three different wafer sectors (section A, D and F) (see Sec. 6.1 Fig. 6.3) are evaluated regarding three quantities. These are the maximum resistance, R_{max}, the critical temperature, T_c, and the critical current, I_c, at 4.2 K at a bias current of about 10 µA (see Sec. 2.3). The DC characterization is a necessary step to allow a pre-selection of suitable candidates for the assembly before the final separation process described in Sec. refSec: Fabrication and mask design. Only after this validation the handle wafer of the sector is removed and the devices get etched out. A non-vanishing resistance-plateau in the RT-curves after the phase transition into the superconducting state is investigated in the context of an intrinsic property of the HEB device caused by a charge-conversion process at the normal-to-superconducting interface between the NbN-microbridge and its contact pads (see Sec. 2.3). Moreover, the sheet resistances of gold-layers of which the RF-structures fabricated are examined at room-temperature and at cryogenic temperatures as their surface resistivity influences the RF performance.

7.1.1. Measurements

The measurements of the DC-characteristics are performed on HEB-devices on diced wafer sectors before the final back-etching step (see Sec. 6.1). To measure the IV and the RT-curves (see Sec. 2.3) of the HEB-devices, the sector with the respective HEBs is mounted on a dipstick. The HEB-devices are connected to the printed circuit board of the dipstick head by bond wires on additional bondpads on the sector that are removed in a later stage. By slowly immersing or pulling up the dipstick in a can with liquid helium the devices are cooled down or warmed up. The according temperature is read out by a calibrated temperature sensor[1] on the dipstick. The HEB-resistance is measured using a dual lock-in amplifier setup for the current and the voltage[14] with a small current modulation of typically 9.7 µA.

The resistivity of the 70 nm and the 150 nm thick gold films and the 1.5 µm thick beamlead gold on a 150 nm thick seed gold layer is measured by means of 4-point lines consisting of 478 squares, and by square Van-der-Pauw structures (see Fig. 7.1). These test-structures are made from the same gold-layer on the same wafer as the fabricated RF-chips (see Sec. 6.1). The DC resistance is determined as a function of temperature by slowly cooling them down on a dipstick in a can with liquid helium using a four-point measurement scheme.

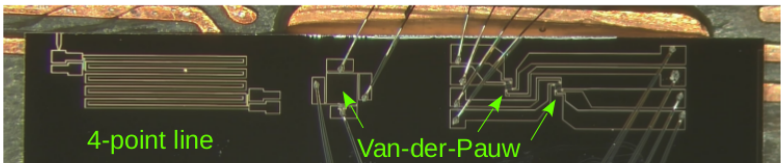

Figure 7.1.: Van-der-Pauw and 4-point line structures to determine the sheet resistance of gold-layers.

7.1.2. Analysis of the HEB IV and RT-curves

The critical DC-current at 4.2 K of the HEBs is read out from the IV-curves as described in Sec. 2.3. The critical temperatures, T_c, determined from the measured RT-curves as the midpoint of the phase transition are extracted from the smoothed RT-curves as the local maximum of its derivative $\frac{dR}{dT}$ in the temperature range from 8 K to 10 K, as shown in Fig. 7.2(a). Depending on the strength of noise the RT-data are smoothed over 10 to 31 measurement points (sample distance $\Delta t_{step} = 0.01\,\mathrm{K}$) with a Savitzky-Golay filter (polynomial order of 3).

The contacts and current path through the RF circuit structures causes an additional series resistance of less than 2 Ω in all measured RT-curves. This contribution is still visible at 4.2 K as can be seen in Fig. 7.2(b) and is subtracted from the RT-curve. The maximum resistance, R_{max}, can be directly read out from the corrected RT-curve as the highest resistance value of the curve.

The superconducting proximity effect leads to a reduced critical temperature of parts of the NbN microbridge that are close to the Au contact pads. After passing, in a downward

---

[1] DT-470 from Lake shore

temperature sweep (see Fig. 7.2), the critical temperature of the unaffected NbN film this results in two areas of the NbN microbridge in vicinity to the contact pads which are still normal-conducting and causes a resistance plateau that is visible below T_c (see Fig. 7.2(b)). The non-vanishing resistance, $R_{plateau}$, is a sloping plateau which can be approximated by a linear function. The limits of the plateau are determined by the upper and lower transition points where the approximately linear behavior of the curve is replaced by a non-linear increase or decrease, respectively. $R_{plateau}$ is defined as the resistance at the middle of the interval minus the series resistance contributed by the gold transmission lines (see Fig. 7.2(b)). The upper and lower interval limit gives the uncertainty.

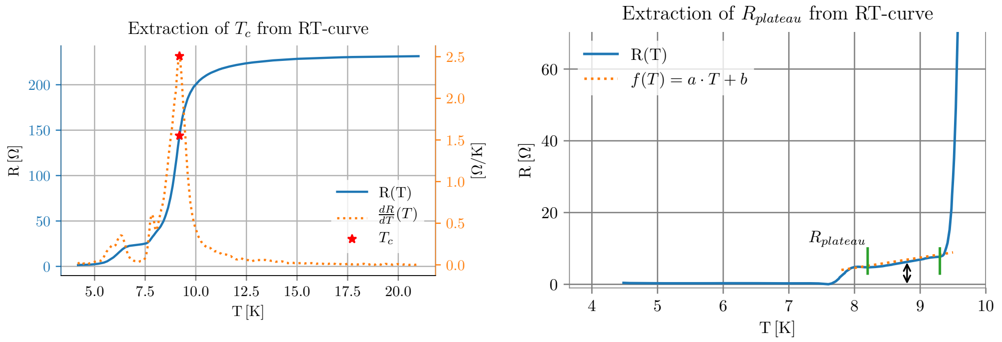

(a)

(b)

Figure 7.2.: Extraction of (a) the critical temperature and (b) the resistance plateau of the HEB from its RT-curve. The critical temperature corresponds to the maximum of the derivative $\frac{dR}{dT}$.

Assuming that the plateau resistance in the RT-curve originates from the charge-conversion process at the interface between the superconducting bridge and its contact pads, the length of the corresponding resistive part of the bridge is given by $l = 2 \cdot \xi_{NbN}$ of “normal conducting” Niobium Nitride, where ξ_{NbN} is the coherence length of the NbN film. Thus the coherence length can be estimated from the measured plateau resistance via

$$R_{Plateau} = \rho_{NbN} \cdot \frac{2 \cdot \xi_{NbN}}{w_{HEB} \cdot t_{HEB}} \tag{7.1}$$

$$\rightarrow \xi_{NbN} = 0.5 \cdot \frac{R_{Plateau}}{\rho_{NbN}} \cdot w_{HEB} \cdot t_{HEB}, \tag{7.2}$$

where w_{HEB}, t_{HEB} and ρ_{NbN} are the width, thickness and resistivity, respectively of the

HEB. The latter is estimated from the average measured resistance at around 25 K of NbN testfilms which are on the same wafer as the microbridges. The results of these measurements are given in Sec. 7.1.4.

7.1.3. Sheet resistance of gold layers

The sheet resistance, R_{sheet}, of the gold test-structures is calculated from the measured resistance values R_{meas}. For the 4-point lines it is given by the measured resistance divided by the number of squares N, $R_{sheet} = R_{meas}/N$. For the Van-der-Pauw structures it is determined via $R_{sheet} = \frac{\pi}{\ln 2} \cdot R_{meas}$.

The results of the measured averaged sheet resistances of gold-layers of three different thicknesses are summarized in Tab. 7.1. The test-structures for the about 70 nm thick film exhibit a considerably high resistance at cryogenic temperatures, with a Residual Resistance Ratio about $RRR = 2$. Due to a thin NbN layer underneath the 70 nm thick gold-layer the resistance of the test-structure for around 4.2 K could not be determined as the NbN becomes superconducting around 6.7 K (see Fig. 7.3).

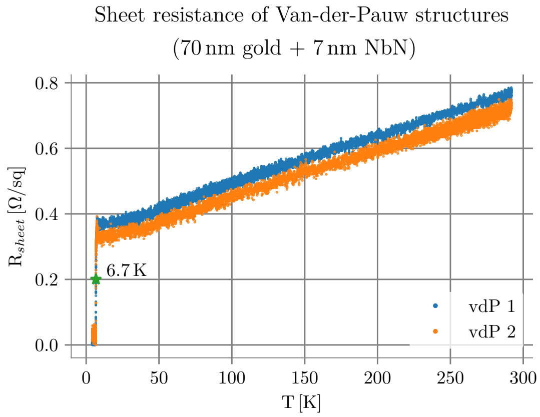

Figure 7.3.: Temperature-dependent sheet resistances of 70 nm thick gold van-der-Pauw test structures with a thin NbN-layer underneath.

7.1.4. DC Properties of NbN HEB bridges

An overview of the extracted maximum resistance, critical current and critical temperature values of individual HEB devices from sector A, D and F (see Fig. 6.3 in Sec. 6.1) is shown in Fig. 7.4(a) and (b). For the NbN testfilms the critical current values could not be measured since the occurring high current leads to an overload of the electronics of the measurement apparatus. The average resistivity of the NbN-layer all HEB-bridges are made from is determined from the testfilms at a temperature of about 25 K and is

	thickness of gold-layer		
T[K]	70(5) nm	150(5) nm	1.65(5) µm
294	0.77 Ω/sq	0.27 Ω/sq	2.6×10^{-3} Ω/sq
20	0.38 Ω/sq	—	—
4.2	—	0.11 Ω/sq	0.9×10^{-3} Ω/sq

Table 7.1.: Measured sheet resistances of gold layers of different thicknesses at room temperature and at cryogenic temperatures. The uncertainty in the thickness of the gold-layers is given in brackets and refer to the last digit of the number. The 70 nm and 150 nm thick gold layers are sputtered, the 1.65 µm thick gold layer is electroplated gold grown on a 150 nm thick sputtered gold layer.

3.8(3) µΩ m. HEB-devices that belong to the same RF-circuit design exhibit about the same resistance values as expected since the respective HEB microbridges ought to have the same dimensions.

The critical temperature values are not correlated to the dimensions of the HEB bridges but are arbitrarily spread around an average value of 9.1 K with a standard deviation of 0.1 K . Although originating from the same NbN film these variations are to be expected since variations can be ascribed to a slightly varying thickness profile of the film leading to spatially variations of the intrinsic NbN film properties. It emphasizes the need of individual DC characterizations of each single device.

The maximum value of the resistance in the RT-curves for NbN-layers usually is reached around 25 K [17]. For all measured 10 µm × 10 µm square NbN testfilms this is true. Moreover, the resistance decreases from 25 K to 100 K by roughly 3 %. Consequently, for a HEB-microbridge with the typical dimensions used in this work (length between 100 nm and 120 nm,width of 0.8 µm) and the measured average resistivity of the NbN film, a decrease about 6 Ω to 8 Ω at 100 K would be expected. Contrary to these predictions, the maximum resistance in the RT-curves of most of the HEB-devices is reached at temperatures only higher than 25 K up to 100 K (see Fig. 7.5(a)) and the resistance from 25 K to the maximum resistance value is increase by less than 5 Ω. One possible source for the observed shift of R_{max} to higher temperatures is the considerable resistivity of the 70 nm thick gold-layer (see Sec.7.1.3) which the DC-current needs to pass for the RT-measurements of the HEB-devices, but not for the measurements of the NbN testfilms. The according series resistance contributed by the gold transmission lines to the overall measured resistance behaves conversely to the NbN and increases with increasing temperature as shown in Sec. 7.1.3. The resistivity of the gold-layer further can explain the high resistance plateau below the critical temperature (see Fig. 7.5(b)) which is of the order of 23 Ω and is too large to result from the resistance caused only by the charge

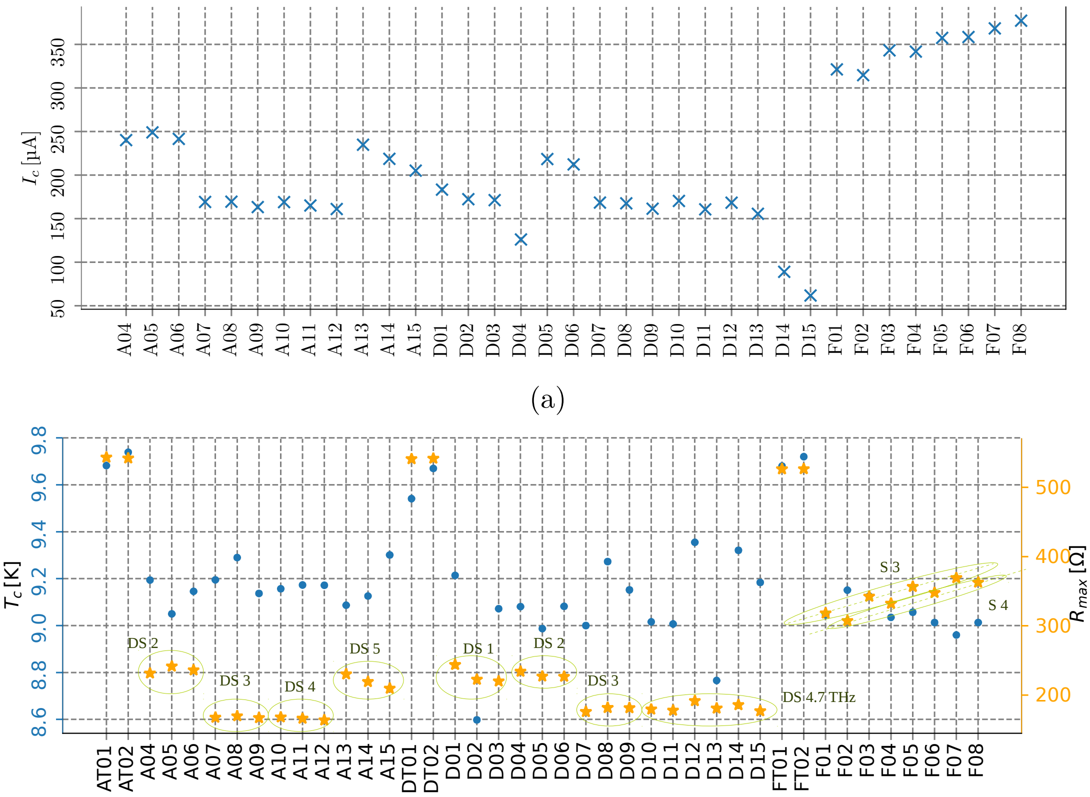

(a)

(b)

Figure 7.4.: (a) Critical current, and (b) maximum resistance and critical temperatures of HEB-devices from sector A, D and F. The HEB-devices are numbered consecutively for each sector. (Ax: HEB device number x from sector A, and so forth). The addition "T" after the sector label stands for "test-device". This test-device consists of a 10 µm × 10 µm square test-film composed of the same NbN-layer as the HEB microbridges. The green circles and green labels refer the HEB-devices to their respective RF-circuit design. (DS x: double-slot antenna of design version no.x, DS 4.7 THz: RF-circuit with the 4.7 THz double-slot antenna, S3: Archimedean spiral antenna, S4: self-complementary spiral antenna).

conversion effect. This plateau only vanishes at considerably lower temperatures than the resistance plateau that occurs for the NbN testfilms (see Fig. 7.5(b)) where no 70 nm thick Au layers are present in the measurement path. Assuming that the average path length of the current through the 70 nm thick gold-layer is between 52 to 60 squares for the double-slot antenna designs, the resistance due to the 70 nm thick Au transmission line is calculated based on the measured temperature-dependent sheet resistance of the 70 nm thick van-der-Pauw gold structures (see Fig. 7.3). The according resistance is

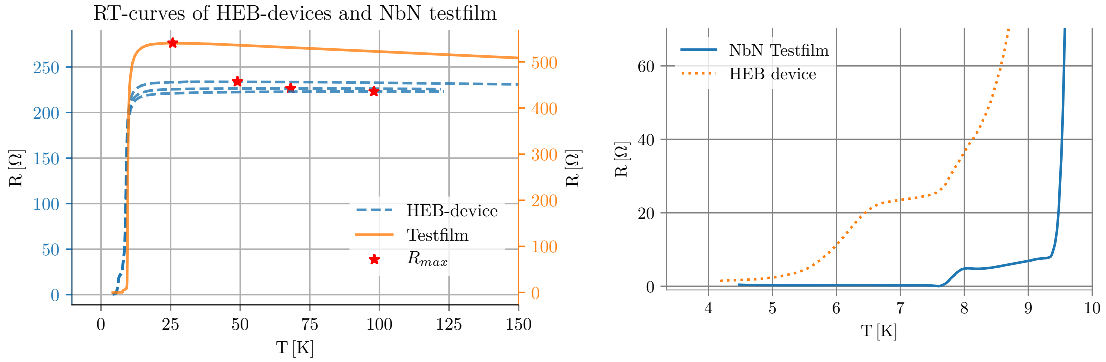

(a)

(b)

Figure 7.5.: (a) RT-curves of HEB-devices and a NbN testfilm. The maximum resistance, R_{max}, is reached at different temperatures. (b) RT-curve of an HEB-device below the critical temperature.

depicted in the inset in Fig. 7.6 with respect to its resistance value at 25 K as a function of temperature. From its curve an increase in the resistance from 25 K to 100 K by roughly 6 Ω to 7.5 Ω is to be expected and by this is of the order of magnitude to cause a shift of the maximum resistance value of the HEB-devices to higher temperatures. Subtracting the calculated temperature-dependent series resistance from the measured RT-curves of the DS-antenna HEB-devices leads to a shift of the maximum resistance values close to 25 K as can be seen in Fig. 7.6. Moreover, the series resistance contributed by the thin gold-layers below the critical temperature is of the order of the high resistance plateaus of the DS HEB-devices. In conclusion, it is a plausible explanation for the observed temperature shift of the maximum resistance and the high resistance plateau of the HEB-devices.

7.1.5. Plateau resistance and coherence length

To compare the shapes of the RT-curves of individual HEB-devices with each other, the RT-data are normalized to the extracted critical temperatures and peak resistances of the devices. This comparison at first is based on the measured raw data without accounting for any potential contributions due to gold-layers which have been mentioned in the above section. Since the non-vanishing DC resistance of the HEBs after passing the phase transition into the superconducting state is an indication for a charge-conversion between normal current and supercurrent, this resistance is further investigated. The RT-curves are therefore further rescaled with the width of the contact pads which connect

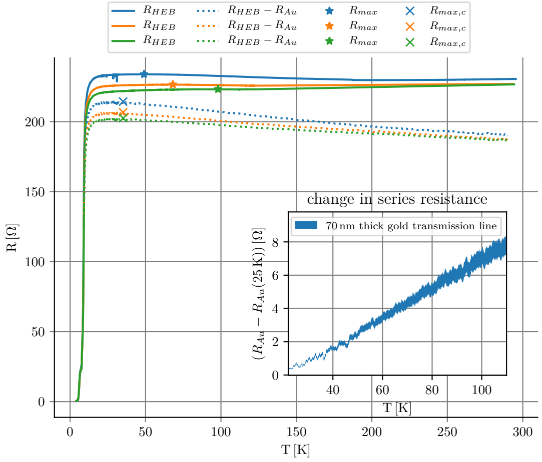

Figure 7.6.: Raw RT-data of three different HEB-devices and their RT-curves corrected for the series contribution of the gold transmission lines (see inset). Inset: Change in the DC-resistance of a 70 nm thick gold transmission line (52-60 squares long) with respect to its resistance value at 25 K.

the HEB bridge with the antenna terminal[2]. The defined width of a HEB bridge is about 200 nm smaller than the width of its contact pads, but cannot be measured for each individual device. Therefore, the width of the contact pads is the best approximation for this parameter. The according results of the rescaled RT-curves are depicted in Fig. 7.7. HEB-devices which are based on the same RF-circuit version are color-coded the same in the plot and are not listed under its individual device number but are collected under the name of the respective RF-circuit version. The geometrical dimensions of the respective circuit design are specified in Sec. 3.4.2 in Tab. 3.2 and Tab. 3.3, in Sec. 3.4.3 in Tab. 3.4 and in Sec. 3.4.3 in Tab. 3.5. Since the sectors contain several HEB-devices of each RF-circuit version there are 3 to 6 RT-curves from different HEB-devices per RF-circuit version. All curves show a step-like course below the critical temperature. Especially noticeable is that the plateau levels of HEB-devices of same RF-circuit designs are congruent with only few exceptions which points to the fact that the dimensions of the HEB-bridges are reasonably identical as required. Additionally, plateau levels from HEB-devices of different RF-circuit designs but with same nominal HEB widths are close to each other (same widths for DS 3 and DS 4 and same width for DS 1, DS 2 and DS 5, respectively).

The so far reported results refer to the measured RT-curves of the devices without

---

[2] As could be demonstrated by Boogaard et al. [11] an intrinsic contact-resistance is independent of the microbridges' length but should scale with the width of the superconducting films.

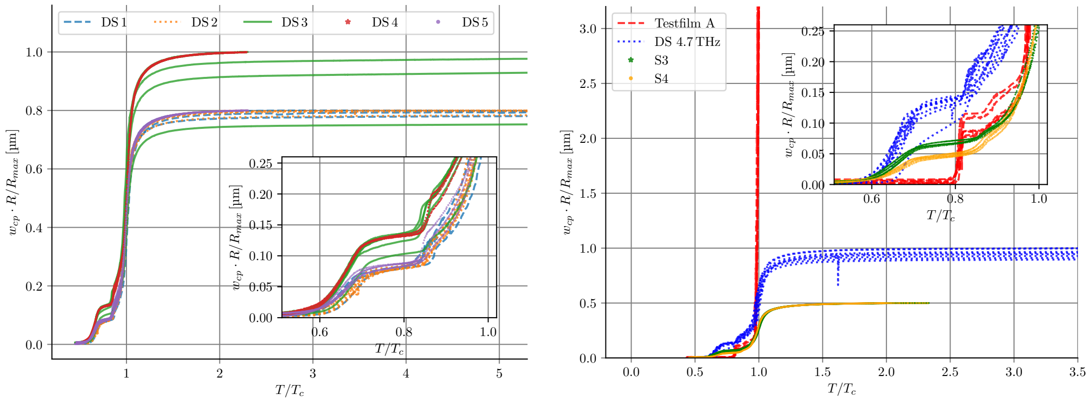

(a) (b)

Figure 7.7.: Rescaled RT-curves of different HEB-devices and NbN testfilms from sector A, D and F. Each curve represents a measurement of a different HEB-device or testfilm that is color-coded and linked to the label according to its RF-circuit version or to the testfilm, respectively. (a) Rescaled RT-curves of measured HEB devices that are integrated in a narrow-band RF-circuit for 10.7 THz. DS 1 to DS 5 corresponds to the respective doubles-slot antenna version of the RF-circuit. (b) Rescaled RT-curves of NbN testfilms and measured HEB devices which are integrated into the Archimedean spiral (S3), the self-complementary log-spiral (S4) or the double-slot antenna for 4.7 THz (DS 4.7 THz) RF-circuit.

accounting for the effect of the series resistance that is contributed by the thin gold-layer and has been described in the above subsection. To subtract the series resistance occurring due to the 70 nm thick gold layer from the RT-curves of the DS-antenna devices, the series resistance of the gold-layer down to 6 K is estimated by a linear extrapolation of the measured sheet resistance curves that are depicted in Fig. 7.3. The corresponding rescaled RT-curves corrected for the series contribution are shown in Fig. 7.8. The respective length of a normal-conducting NbN-area associated to the plateau resistance is calculated based on Eq.(7.2). For the calculation the width of the NbN HEB bridges are assumed to be 200 nm smaller than the width of the corresponding contact pad. The results are depicted in Fig. 7.9 and exhibit values between 2 nm to 6 nm. The effective length is predicted [11, 153] to be $0.96 \cdot \sqrt{\xi_0 \cdot l}$ or about the coherence length of a dirty superconductor $\sqrt{\xi_0 \cdot l}$, where ξ_0 is the BCS coherence length and l is the elastic mean free path of the electrons. Within the limits of uncertainty the calculated lengths are comparable to those predicted in the limit of dirty superconductors and are in good agreement with the estimated coherence length of about 3 nm to 4 nm given by Shcherbatenko et al. [153]. As such a proximity effect is only possible in case of a sufficiently transparent interface, the occurrence of the resistance plateaus in the RT-curves points to the fact that there

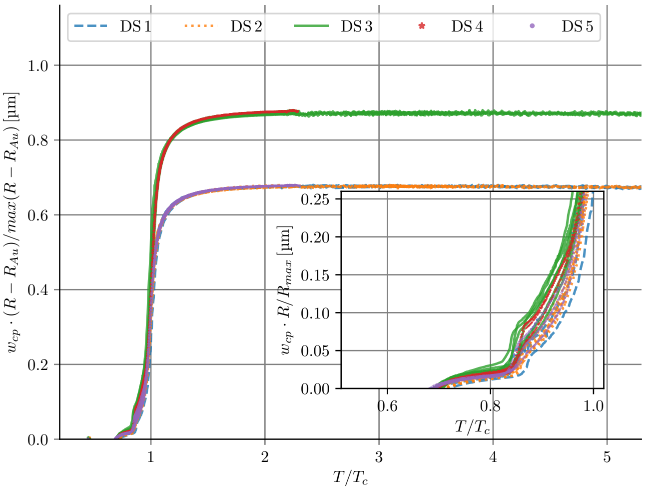

Figure 7.8.: Rescaled RT-curve of DS-antenna HEB devices that are corrected for the contribution of the series resistance given by a 70 nm thick gold layer.

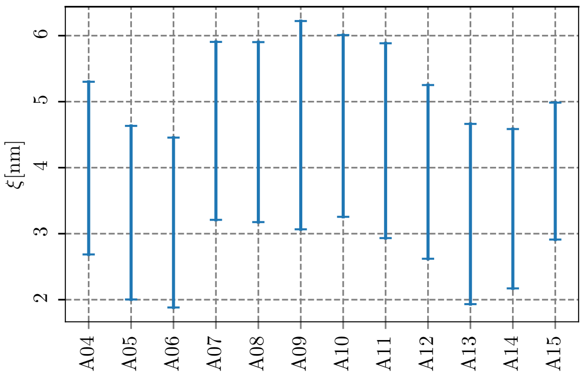

Figure 7.9.: Estimated length of the NbN-layer that is supposed to be normal-conducting below the critical temperature at each of the side of the contact pads. The upper and lower limit of each bar includes the lowest and highest values of the resistance plateau (see Sec. 7.1.2) and the uncertainties in the HEB-dimensions.

is a good electrical transparency between the NbN-layer and the interface layer of the gold contact pads.

7.2. THz Broadband response

In total, the direct RF response of five different mixer devices has been measured. The chosen RF-circuits for the receivers are the Archimedean spiral antenna circuit (see.Sec. 3.4.3 and Sec. 3.4.4), three different narrow-band designs with double-slot antenna for 10.7 THz, and the double-slot antenna based narrow-band circuit for 4.7 THz (see Sec. 3.4.2).

7.2.1. Measurement setup

The direct response of each HEB-detector to a broadband RF signal is measured using a Fourier transform spectrometer (FTS model is a Vertex 80 v with FIR extension[15]) where the mixer is used as the FTS power detector. The measurement setup is sketched in Fig. 7.10(a). The mixer block with the integrated HEB-device is placed inside a liquid Helium cooled cryostat and is mounted on a mirror sledge (see Fig. 7.11(b)) to allow for a good coupling to the Gaussian-like beam of the FTS. The interface plane of the sledge to the mixer block has been integrated with respect to the mirror position of the sledge with a machining accuracy of 5 µm. A heater attached to the mirror sledge enables to heat up the mixer block to the desired operating temperature. The temperature of the mixer block is controlled via a temperature sensor which is also mounted on the mirror sledge. The HEB device is DC-biased in the constant current mode via a Bias-T. In this operation mode the applied current is kept constant during measurements while the voltage across the HEB is changing due to the response of the bolometer to the incoming radiation of the FTS. The voltage signal of the HEB device passes a bandpass filter, is amplified and is fed to the external electronic detector input of the FTS. The low noise amplifier (LNA) (0.5 GHz - 5 GHz) that follows the Bias-T is not used for the direct response measurements but is included in the electronic circuitry as the setup already contains all components which are needed for the operation of the detector as a mixer. A removable grid between the FTS and the dewar entrance enables to perform polarization-dependent measurements.

The FTS is based on the principle of a Michelson interferometer [80]. The signal of a radiation source is splitted up by a beamsplitter and after reflection on a mirror in each beam path, is combined again. One of these mirrors can be moved to achieve a varying path difference between both beams. In this setup the response of the HEB device to the broadband THz signal of a mercury-vapor lamp is measured in dependence of the position of the internal moving FTS mirror. A Fourier transformation of the according interferogram yields the spectrum of the direct detection response of the mixer to the incoming signal. This total response contains the transfer characteristics of all optical

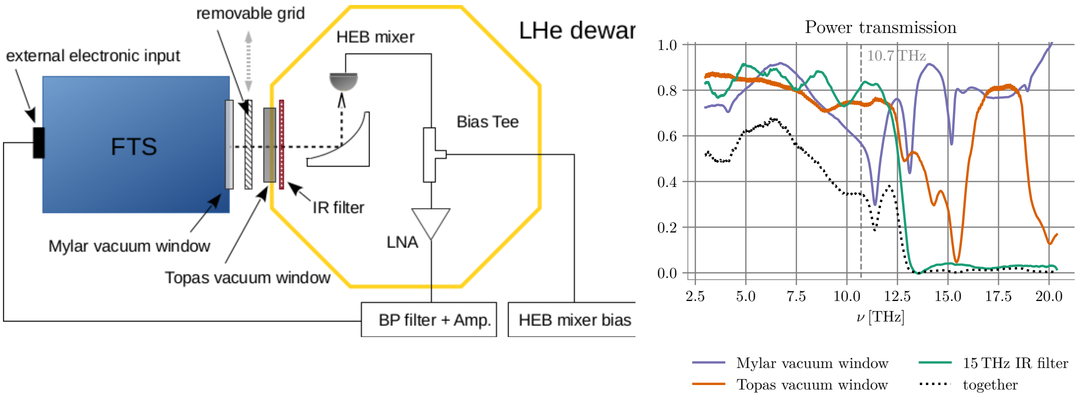

(a) (b)

Figure 7.10.: (a) Sketch of the test setup to determine direct response of the HEB devices to a broadband RF-signal. (b) Measured dispersive power transmission of 1.) the 12 µm thick Mylar vacuum window of the FTS, 2.) the Topas vacuum window of the Liquid Helium dewar (LHe dewar) and 3.) the 15 THz lowpass RF-filter. The location of the three optical elements of the test setup is depicted in the sketch given in (b).

components (beamsplitter, windows, filters) in the beam path. The actual spectral RF response of the HEB device needs to be de-embedded from the total response by correcting for the transfer characteristics of the preceding optical elements. For this purpose, I first measured the transmission spectra of the 12 µm thick Mylar vacuum window of the FTS, the Topas window of the Dewar and the 15 THz lowpass RF-filter with the internal pyroelectric room-temperature DLaTGS detector of the FTS. A measurement of the empty FTS spectrum with its internal detector is used as a reference spectrum to calibrate the direct response spectrum of the receiver for the contribution of the remaining FTS optical elements such as the beamsplitter. At this point it should be noted that the frequency-dependent detection characteristic of the internal detector is not known, but is assumed to be constant over the frequency range of interest. The measured transmission spectra of both vacuum windows, and of the heat IR-filter are shown in Fig. 7.10(b). The dotted line is the corresponding total spectral convolution function based on all three optical elements. It clearly shows that the results which can be obtained by this measurement setup are restricted to frequencies below 12.5 THz due to the sharp cut-down of the incoming signal by the IR-filter of the lHe dewar. The beam splitter that consists of multilayer Mylar coated with silicon is dedicated for 0.9 THz - 20.4 THz according to the specification of the manufacturer. In combination with the Mylar vacuum window it yields a considerable drop-down in the transmitted signal around 11.4 THz up 11.8 THz, which corresponds to the frequency where the transmission again is elevated to that level that has been reached before the transmission dip caused by Mylar. It results into an unfavorably decreased signal-to-noise ratio. For weak measured response signals during a measurement and short measurement times, the spectra obtained with the test-setup in this frequency range around 11.4 THz, need to be excluded from the assessment. [3]

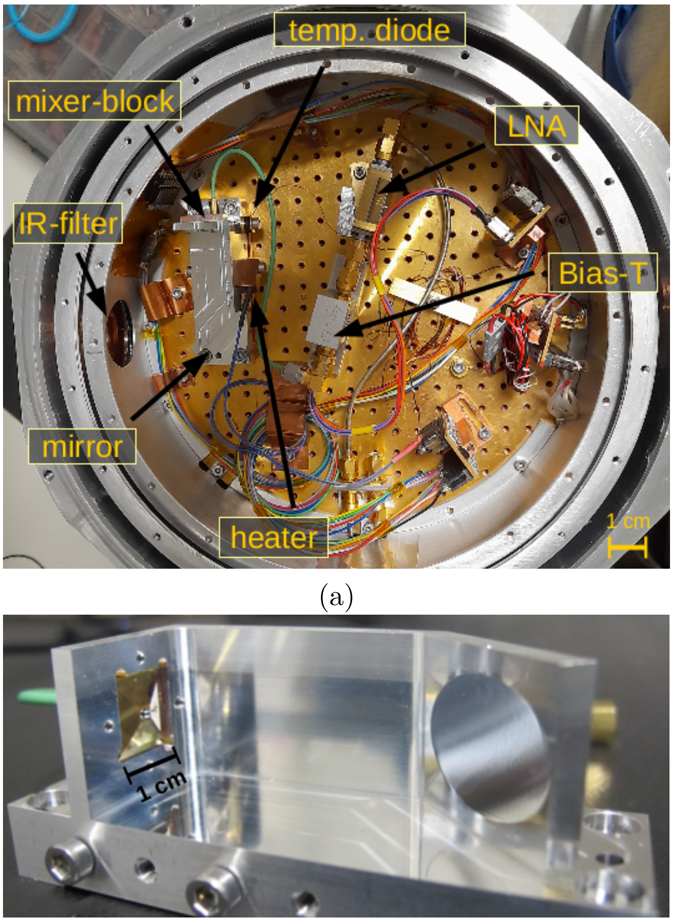

(a)

(b)

Figure 7.11.: (a) Photo of the cold optics and cryogenic electronic components of the HEB device on the cold plate of the open lHe dewar. (b) Picture of the HEB device mounted on the mirror sledge.

---

[3] The holding time of the Dewar where the mixing device inside is heated up to its operating temperature around 8 K, allows to take less then 120 spectra if the holding time would exclusively been used for spectral measurements. For a weak response feature that would require an averaging over 300 spectra similar to that reported in [180] the measurement cycle would be too short to provide the long measurement time to see potential weak features in this respective frequency range.

7.2.2. Measurement procedure

At the beginning of a measurement cycle, the mixer block, that is mounted on the 4.2 K cold-plate of the dewar, is heated up to approximately the critical temperature of the HEB film, until the hysteresis jump of its IV-curve is nearly vanished (see Fig. 7.14). The voltage bias point is set in the close vicinity of this marginally jump in the IV curve, typically at a slightly higher voltage (for positive bias voltages) than that of the hysteresis remnant . The strength of the response signal of the HEB devices is dependent on the chosen bias point and the operating temperature. During the measurement cycles different operating temperatures and bias points have been tried out. The initially set bias voltage ranges from 0.1 mV to 1.5 mV. The mirror velocity of the FTS was set between 1.6 kHz and 2.5 kHz. The spectra were measured with the maximum FTS resolution of 0.08 cm^{-1} as an average over 5 to 12 spectra. Before and after each measurement cycle a transmission spectrum of the empty FTS is measured that is needed for the later calibration process.

To estimate the resistance of the HEB elements of the narrow-band detectors during operation the IV-curve of each device has been measured at its respective operating temperature. The read-out electronics have been calibrated with a 50 Ω resistor before, which has been connected in place of the HEB mixer inside the dewar. The IV-curve of each HEB-device again is measured at 4.2 K when it is cooled down and mounted on the cold-plate in the liquid helium dewar.

To investigate if the response peaks of the narrow-band detectors are polarization-dependent a grid was placed into the beam path between the FTS entrance and the vacuum window of the dewar. The grid was once positioned in passage direction to let through the horizontally polarized radiation which in that case refers to the dedicated polarization direction of the double-slot antennas in the detectors and once into the reverse blocking direction.

Additional remarks:

- The air which lies in the beam path between the window of the FTS and the window of the dewar exhibits a transfer characteristic which contributes to the overall direct response spectrum of the HEB devices. The direct response spectra of the HEB detectors are not corrected for this contribution. A measured transmission spectrum of the air by filling the whole FTS instrument with the air of the laboratory (depicted in Fig. 7.12) allows to assign the drops in the response spectrum to the respective absorption lines of the air spectrum.

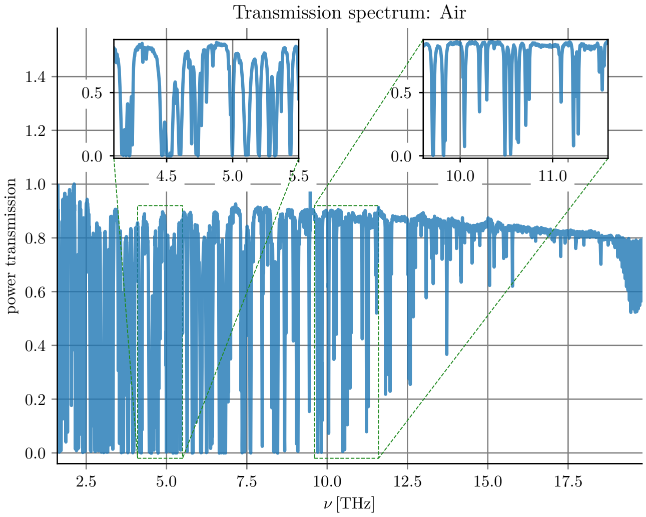

Figure 7.12.: Transmission spectrum of the air in the laboratory recorded with the FTS. For this measurement the whole FTS instrument was filled with air.

- For the first two measured mixing devices, A10 and A11, which are based on a double-slot antenna design for 10.7 THz, the measurement sensitivity is less because the measurement set-up was not yet fully optimized. The adjustment could be improved for the measurement of the third mixing device, D01, by setting the bandpass filter (see Fig. 7.10(a)) from 150 Hz to its maximum possible value of 1.5 kHz. As exactly two Si-lenses are available, there are only two assembled mixing devices at once that can be investigated. For the characterization of further devices with other RF-circuits the old RF-chip needs to be removed from the backside of the lens to make room for the new RF-chip to be attached. The removal of the RF-chips leads to the destruction of the device[4]. For this reason it was not possible to remeasure the first two mixing devices with the more sensitive set-up.

- The Topas vacuum window used for the lHe dewar needs to be exchanged every second cooling cycle as the pressure difference during the measurements leads to significant fine cracks in its surface (see Fig. 7.13).

7.2.3. Data processing

To obtain the direct response of the actual HEB-detector, the measured raw data need to be corrected for contributions like those given by the optical elements in the measurement

---

[4] The gold beamleads at its rim are destroyed, because they have to be pried loose from the copper block

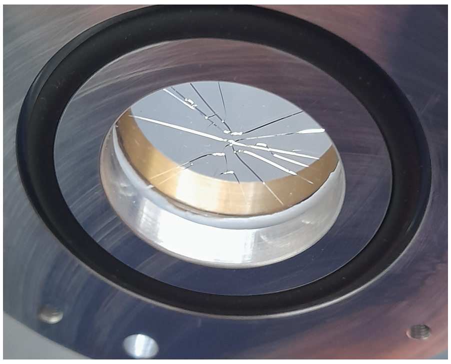

Figure 7.13.: Topas vacuum window after two cooling cycles. The fine cracks occur as a result of the pressure difference the window is exposed to. The white ring that is inserted between the brass clamp and the aluminum window flange is a teflon ring.

setup. The respective weighting function is the product of the spectral transmission characteristics of the Topas vacuum window, the Mylar vacuum window and the IR filter, and the transmission spectrum of the empty FTS instrument (see Sec. 7.2.1).

To specify center frequencies of the spectral response features from those mixing devices, which rely on narrow-band RF-circuits, the response peaks in the spectra are fitted by a polynomial of order 3 to 5 depending on the degree of asymmetry of its shape. The center frequency is determined as the maximum of the fitted polynomial.

The resistance of the HEB micro-bridge during operation is extracted from the IV-curve that has been measured at the respective operating temperature. It is approximated by the resistance value that corresponds to the bias-point chosen for the measurement (see Fig. 7.14). The change in the voltage across the HEB during each measurement has been noted and by means of the first derivative of the smoothed IV-curve over a window size of three to 5 data points is assigned to the respective change in the DC-resistance. By this the resistance range of the HEB micro-bridge is estimated within which the resistance is expected to be located during the respective response measurement.

7.2.4. Results

For all five different HEB-detectors a direct response signal could be measured. During the adjustment of all measured mixing devices in front of the FTS a considerable response amplitude could be obtained even for the largest distance between the entrance of the FTS and the dewar window of about 7 cm. Even the more critical vertical displacement of the mixing devices from the optical axis, still allowed to see enough response signal from all detectors within a few millimeters displacement from the optical axis.

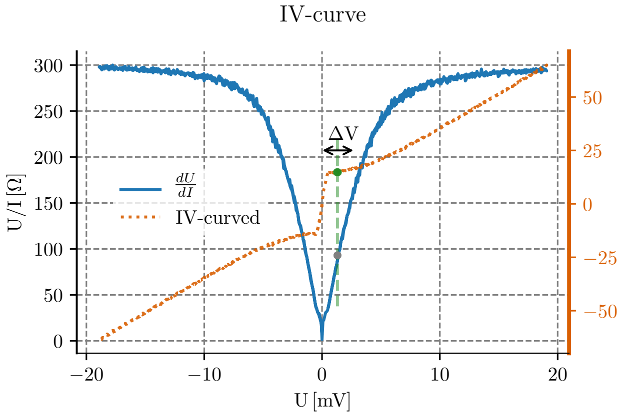

Figure 7.14.: Example: IV-curve and its derivative. The green dot depicts the typical position of the bias point set for the measurement. During a measurement the voltage varies around the bias point by ΔV.

For the 10.7 THz HEB-devices it was difficult to find an operating condition that allows to reasonably identify potential response features around 10 THz. It required a strong response of the HEB-device with a bias point close by the hysteresis remnant in the IV-curve.

The measured unprocessed data and the calibrated spectra are shown in Fig. 7.17, Fig. 7.18 and Fig. 7.20. The green dashed curves in the respective spectra showing the collective influence of the optical elements in the beam path on the transmission of the FTS radiation source reveal that most signal is transmitted between 6 THz and 8 THz and that the transmission around 10.7 THz is reduced by 70 % in comparison to this transmission maximum.

The IV-curves of the HEB-devices at 4.2 K and at the operating temperature under which the presented response spectra have been measured are shown in Fig. 7.22. The T_c of the HEB-devices is around 5 % to 10 % lower, and the I_c (compare orange and blue curve in Fig. 7.15) is up to 40 % lower than the respective values before the final etch-step and assembly (see Sec. 7.1.4). The variations of the voltage across the HEB microbridges due to its response to the incoming broadband radiation result in changes in the DC HEB resistance of up to 35 Ω during a single measurement.

All measured spectra exhibit a significant amount of structure visible as response drops over the entire frequency range. Overlaying the measured air transmission spectrum with the response spectrum as done in Fig. 7.16 reveals that these features originate from the absorption lines in the air that is in the signal path between the entrance of the FTS instrument and the vacuum window of the Dewar.

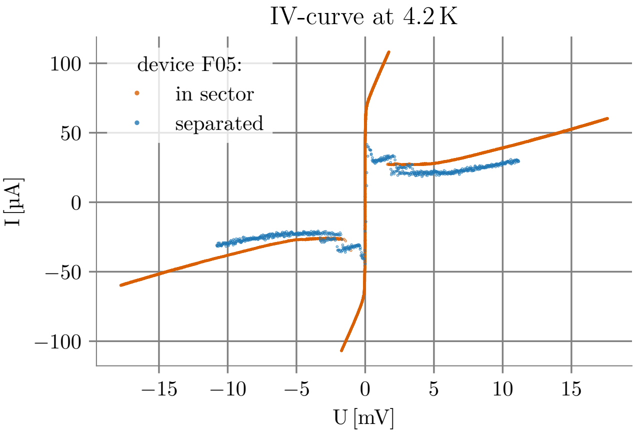

Figure 7.15.: IV-curve of the HEB-device that is integrated in an Archimedean spiral antenna. The orange curve corresponds to the IV-curve when the device is still on the sector, and the blue curve refers to the IV-curve after the device has been etched out of the sector and has been assembled in the mixer block.

From in total four narrow-band devices that have been tested in the mixer block, device D10 belongs to the 4.7 THz RF-circuit design and devices A10, A11 and D01 are narrow-band RF-circuits for 10.7 THz. The respective design version of each device is specified in Tab. 7.2 and Tab. 7.3. The individual design parameters to the design versions are given in Tab. 3.2. From all 10.7 THz HEB devices, device D01 provides the best resolved response features. This probably due to the fact that it was measured with a more sensitive set-up than has been used for A10 and A11 (see explanation in Sec. 7.2.2).

The 4.7 THz device, D10, exhibits a maximum response around 3.5 THz which is at a frequency considerably lower than expected. In contrast to this, the three double-slot antenna RF-circuits for 10.7 THz all show a response feature around 10 THz close to the intended operating frequency and have several response features below the operating frequency which are related to lower order resonances of the antenna. Although relying on the same antenna design, the center frequency of the 10 THz response feature for device A11 is approximately 200 GHz lower than those of device A10 as depicted in Fig. 7.21(a)) which is attributed to the effect of the elongated RF-filter on the antenna resonance as described in Sec. 3.4.2. The 11.4 THz features that can be seen in all calibrated response spectra probably are an artifact of the weighting function due to the transmission minimum of the optical components (see Sec. 7.2.1 Fig. 7.10(b)).

The measurements with grid confirm that the direct response of all narrow-band detectors exhibits a polarization-dependent behavior. With the grid in blocking direction

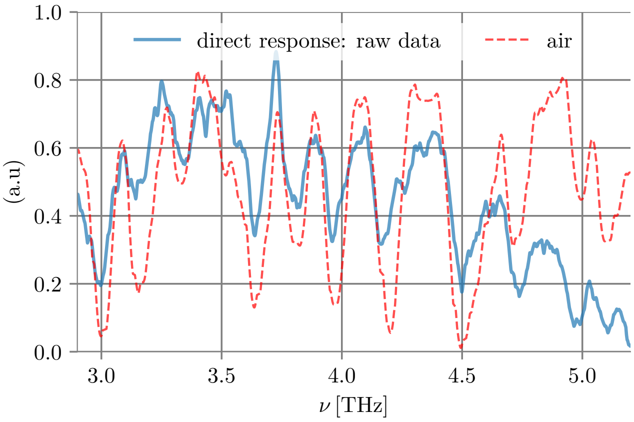

Figure 7.16.: Overlay of air transmission spectrum and measured direct response spectrum

the response features vanished for all 10.7 THz and the 4.7 THz HEB devices, whereas in passage direction referring to the dedicated polarization direction of the antenna of the detectors the spectral response features still could be seen in the measured response spectra as shown in Fig. 7.19.

The response spectrum of the broadband detector, which is based on an Archimedean spiral antenna, is depicted in Fig. 7.20. It shows a direct response over the entire measured frequency range from 3 THz to 12 THz. This broadband detector is a suitable candidate for heterodyne test-measurements at 10.7 THz.

The fit values of the maximum response features of all narrow-band detectors are summarized in Tab. 7.2 and Tab. 7.3. As the results are based on the spectra without accounting for the transmission characteristic of the air an additional uncertainty in the frequency positions of the maximum signal response of a few 100 GHz is expected. A detailed comparison with simulations is given in the following subsection.

The influence of different operating conditions on the spectral response of the HEB-devices has been investigated and is exemplarily depicted in Fig. 7.23 and Fig. 7.24. The bias voltage was set slightly higher (for positive bias voltages) than the hysteresis remnant (as depicted in Fig. 7.14) for high responsivity, but also at other bias points around the marginal hysteresis jump in the IV-curve. The operating temperature was set to values slightly below the critical temperature of the HEB where the hysteresis of the IV-curves was small enough to allow a stable operation[5]. For the response peaks which are notedly above the noise level no considerable change in their frequency position with

---

[5] Stable in this context means that during a measurement the voltage is oscillating around the initially chosen bias point without jumping to another bias point in the IV-curve

changing operating conditions could be observed (see 3.5 THz response peak in Fig. 7.24 and (8 THz response peak in Fig. 7.23). A meaningful assessment for the response peaks above 8 THz and below 5 THz for the 10.7 THz detectors is not possible due to the partly strongly merged and noisy response features. Neighbored response peaks (like the two peaks between 2 THz and 5 THz visible in the first row in the second column of Fig. 7.23) could only be separated for a high enough sensitivity.

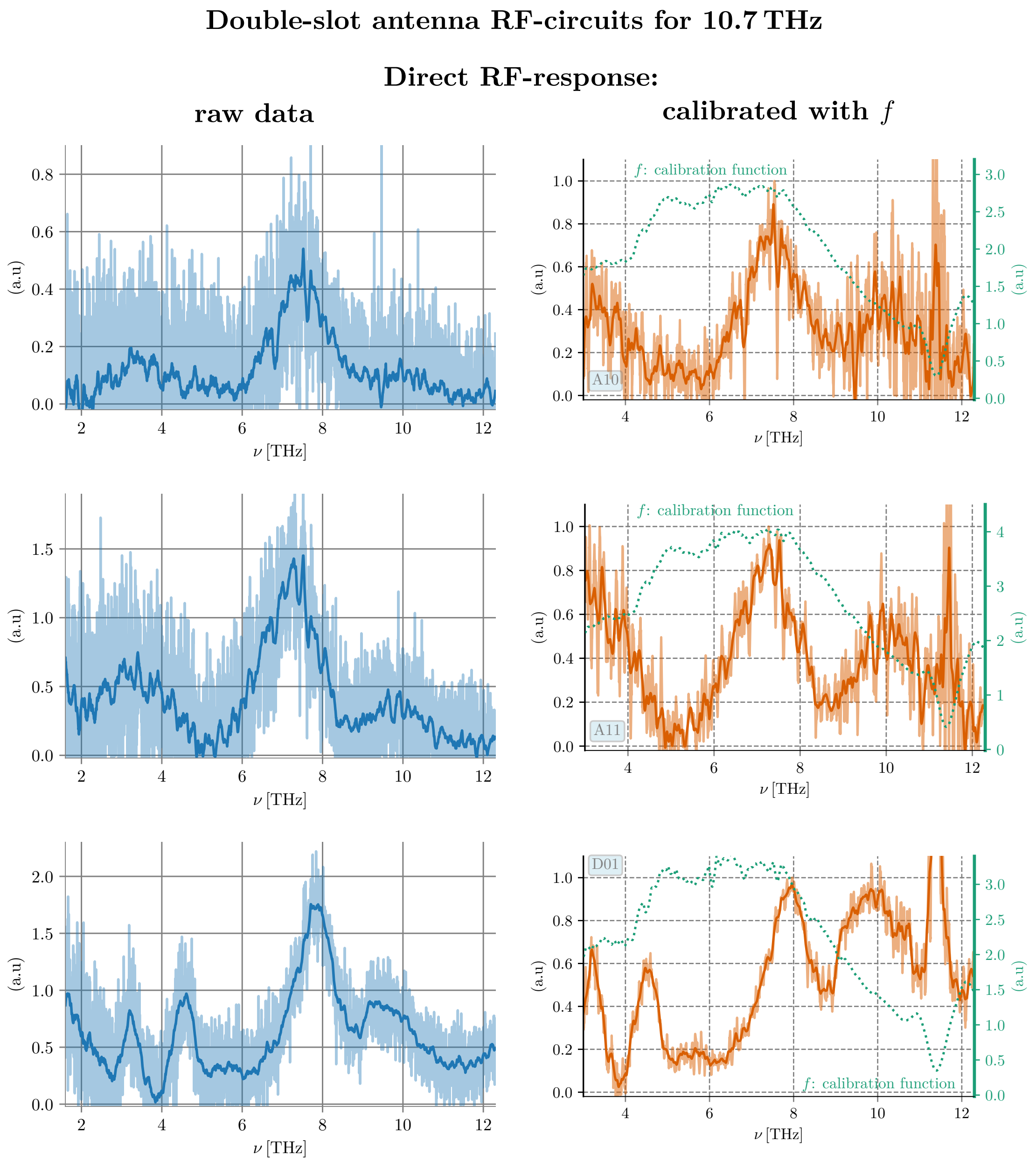

Double-slot antenna RF-circuits for 10.7 THz

Direct RF-response:

raw data

calibrated with f

Figure 7.17.: Measured total and calibrated spectral responses of three different detectors based on narrow-band RF-circuit designs for 10.7 THz. The dotted green lines in the calibrated response spectra corresponds to the according weighting function with which the raw data have been corrected for the contributions given by the optical elements of the setup and have been calibrated with the reference spectrum of the empty FTS instrument (for more information see Sec. 7.2.1).

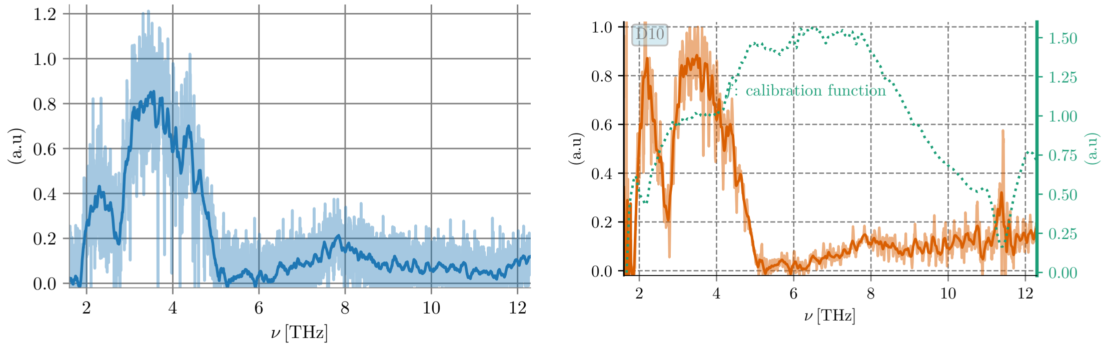
Double-slot antenna RF-circuit for 4.7 THz

Direct RF-response:

raw data

calibrated with f

Figure 7.18.: Measured total and calibrated spectral response of a narrow-band detector based on a RF-circuit design for 4.7 THz. The dotted green lines in the calibrated response spectra corresponds to the according weighting function with which the raw data have been corrected for the contributions given by the optical elements of the setup and have been calibrated with the reference spectrum of the empty FTS instrument (for more information see Sec. 7.2.1).

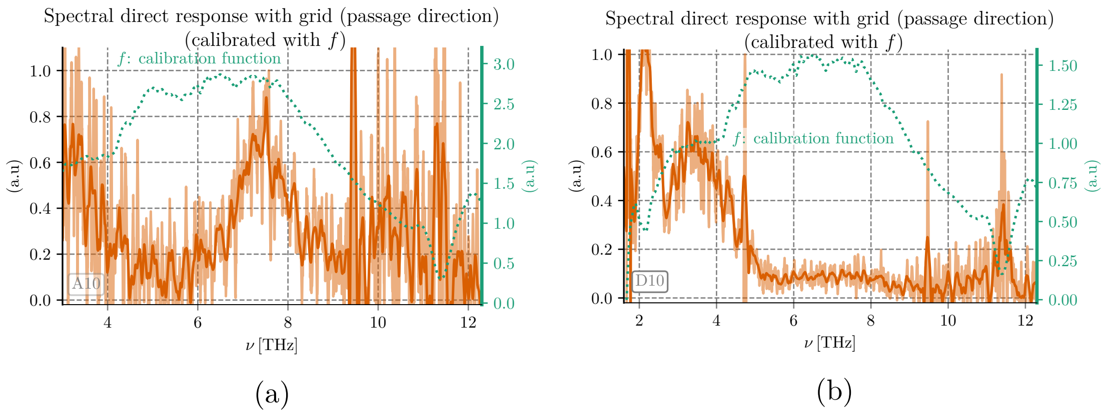
Direct RF-response with grid:

RF-circuit for 10.7 THz

RF-circuit for 4.7 THz

(a)

(b)

Figure 7.19.: Measured spectral direct response of the A10 and the D10 device when adding a grid into the beam path that let pass radiation that is linearly polarized in the polarization direction of the detectors. Compare to Fig. 7.17 and Fig. 7.18 for responses without polarization grating.

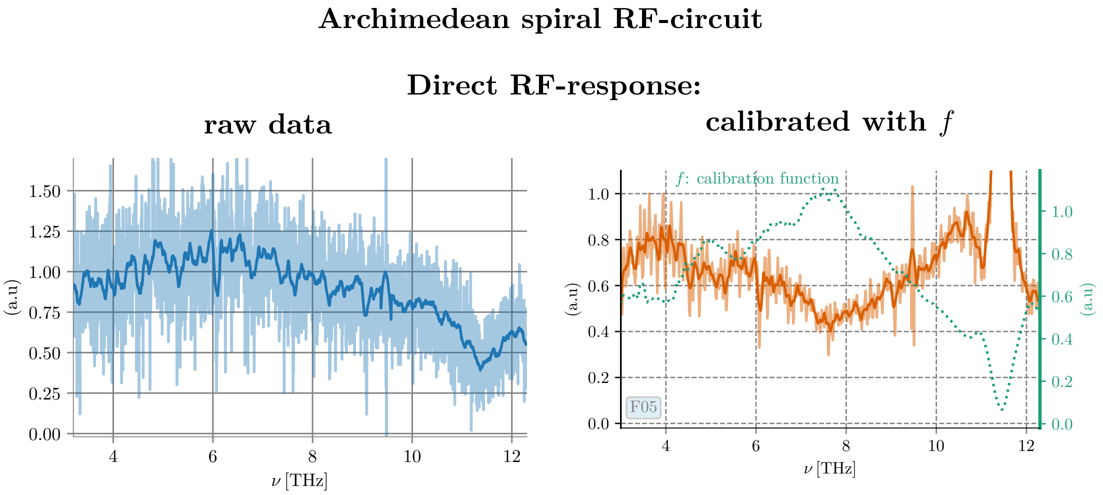

Figure 7.20.: Measured total and calibrated spectral response of a broadband detector based on a RF-circuit with an Archimedean spiral antenna. The dotted green lines in the calibrated response spectra corresponds to the according weighting function with which the raw data have been corrected for the contributions given by the optical elements of the setup and have been calibrated with the reference spectrum of the empty FTS instrument (for more information see Sec. 7.2.1).

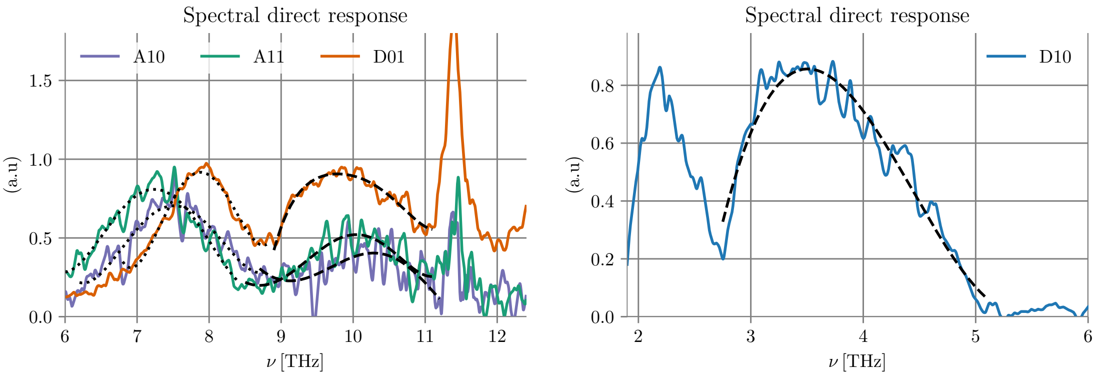

(a) (b)

Figure 7.21.: Fit of the direct RF-response features with a polynomial of order 3 to 5 depending on the degree of asymmetry of the signal curve in the spectrum. The depicted smoothed and corrected response spectra belong to investigated detectors which are based on a narrow-band RF-circuit design for (a) 10.7 THz and (b) 4.7 THz.

Double-slot antenna RF-circuits for 10.7 THz

IV curves:

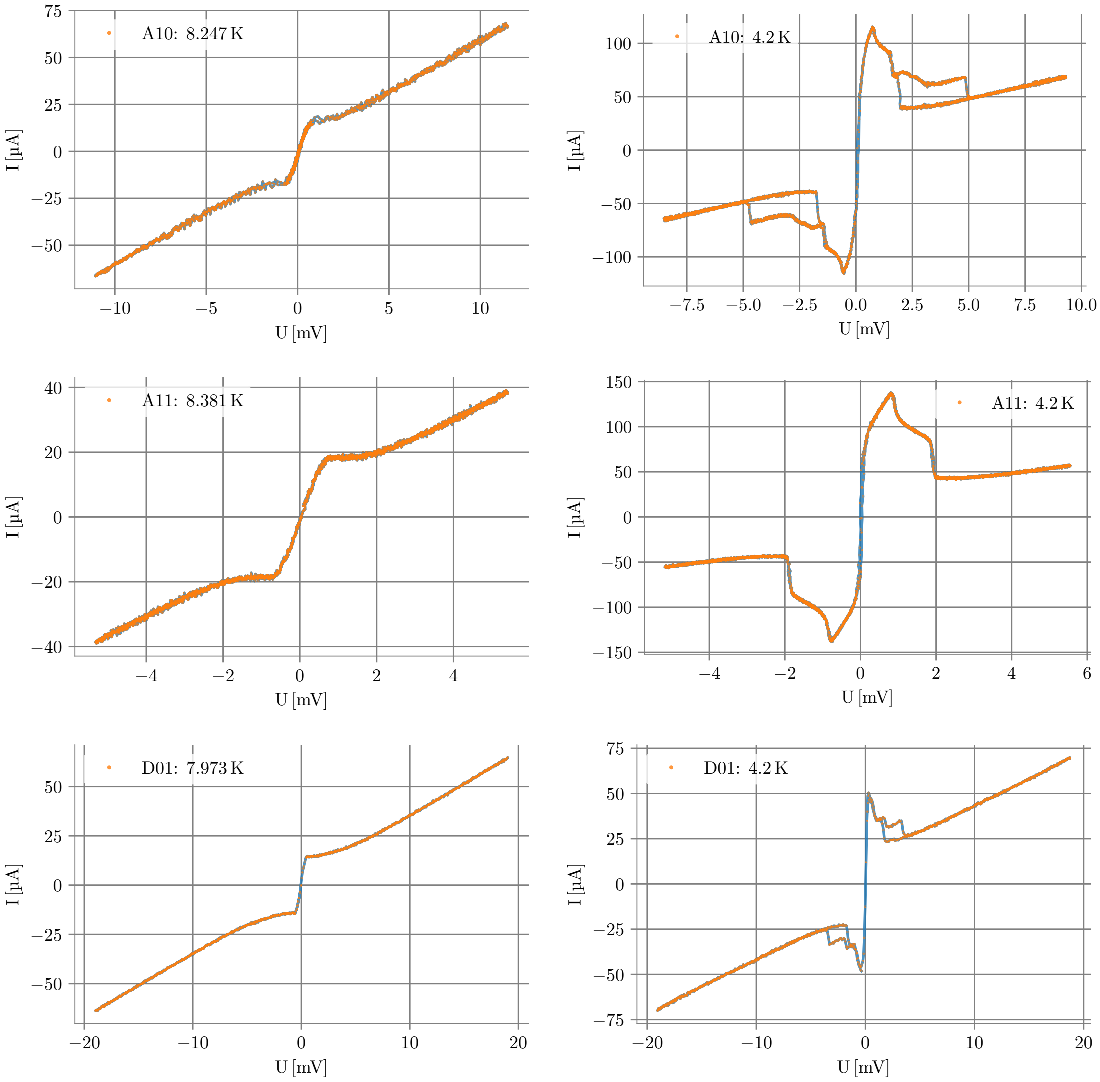

Double-slot antenna RF-circuit for 4.7 THz

IV curves:

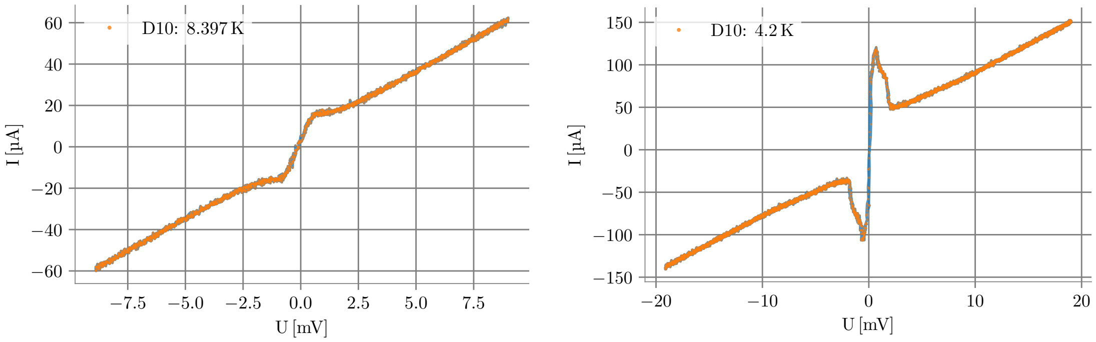

Figure 7.22.: IV-curves of the detectors at 4.2 K and at the operating temperature under which the respective response spectra in Fig. 7.17 and Fig. 7.18 have been measured.

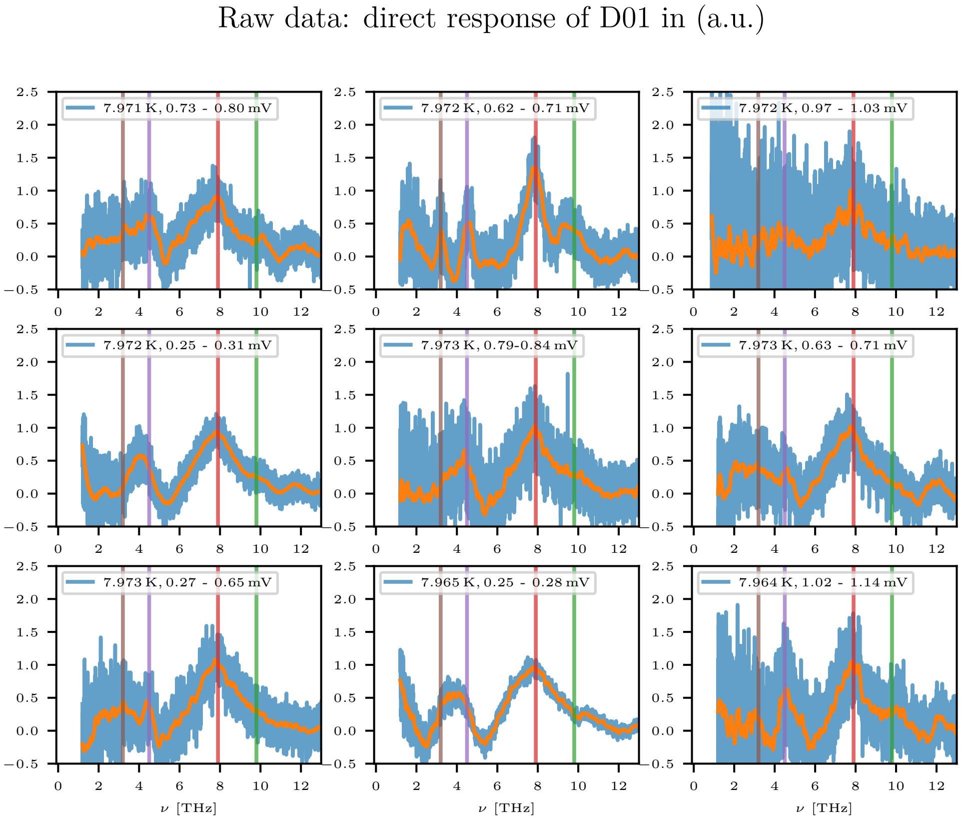

Figure 7.23.: Total response spectra of HEB device D01 at various operating conditions. The respective operating temperature and voltage bias is given in the respective spectra. The initial voltage bias that has been chosen before starting the measurement lies in the middle between the upper and lower voltage value that is depicted in each plot. The upper and lower value corresponds to the lowest and highest value of the voltage that was reached during the measurement of the respective spectra. The vertical lines are included into the spectra at same frequency positions to enable a better comparison of the locations of the different response features.

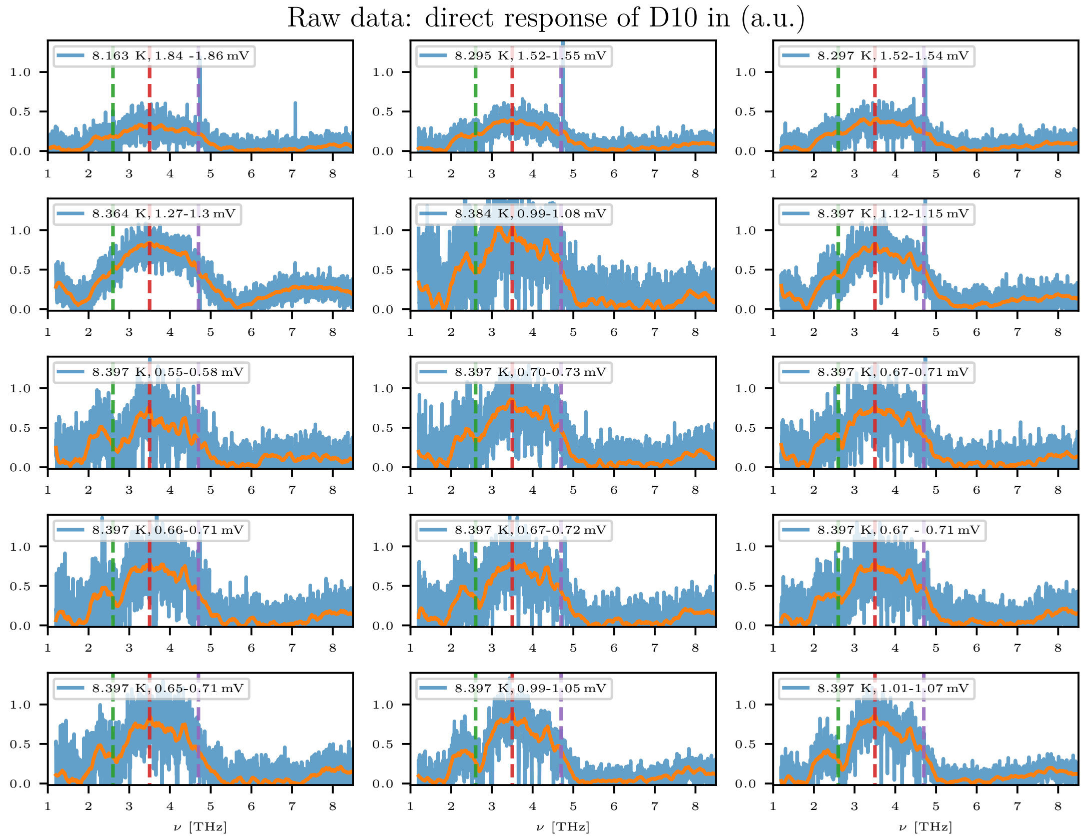

Figure 7.24.: Total response spectra of HEB device D10 at various operating conditions. The respective operating temperature and voltage bias is given in the respective spectra. The initial voltage bias that has been chosen before starting the measurement lies in the middle between the upper and lower voltage value that is depicted in each plot. The upper and lower value corresponds to the lowest and highest value of the voltage that was reached during the measurement of the respective spectra. The vertical lines are included (at 2.6 THz, 3.5 THz, 4.7 THz) into the spectra to enable a better comparison of the locations of the different response features.

7.2.5. Comparison with simulations

The measured RF-response of the HEB-devices basically is determined by two factors. The first one is the coupling of the FTS-beam with the antenna. It is called the beam coupling efficiency in the following. The second aspect is the impedance match which determines the coupling efficiency between the antenna and the HEB element at the antenna's feeding point. To compare the simulation results with the measured spectral direct RF-response of the devices it should be noted that the beam of the FTS at the entrance window is Gaussian-like but not sufficiently well characterized to allow numeric predictions about the beam coupling efficiency. Consequently, the RF-response is only compared with the predicted impedance match efficiency assuming that the incoming broadband signal sufficiently well couples to the antenna to provoke a response in the HEB-microbridge, without a significant frequency dependence.

The coupling efficiency between HEB-element and antenna is calculated using Eq. (B.16) and requires information about the input impedance at the terminal port of the antenna feed and about the resistance value of the HEB-microbridge during the respective measurement. The according frequency-dependent input impedance of the antenna is taken from CST simulations. The HEB-resistance has been extracted with the procedure described in Sec. 7.2.3. At fixed current the bias voltage variation across the HEB microbridge due to the incoming FTS radiation is over an interval that is large enough to sample various DC resistances during one measurement. The difference between the resistance values of one measurement is in the order of a few $10\,\Omega$ (see Sec. 7.2.4). For this reason the impedance-match efficiency once is calculated for the highest and once for the lowest resistance value which the HEB element is estimated to reach during the respective measurement.

The calculated impedance match efficiencies, $(1-|S11|^2)$, and the calibrated response spectra of the measured narrow-band detectors are plotted together in Fig. 7.26 and Fig. 7.27(a). The maximum in the impedance match efficiency for the upper and the lower value of the DC HEB resistance and the fitted center frequency of the response peaks are additionally summarized in Tab. 7.2.

For the 10.7 THz detectors the spectral response features around 10 THz are in good agreement with the predicted curves of the impedance match efficiencies as can be seen in Fig. 7.26. The maxima in the response features at lower frequencies in contrast are partly shifted in relation to the expected efficiency maxima, although the overall characteristic of the measured spectral response is fairly well reproduced by the simulation. According to the simulation results the pronounced response peak around 7 THz to 8 THz that occurs in the spectra of all measured 10.7 THz mixing devices corresponds to a resonance where the double slot antenna behaves as four, in-phase driven lambda-quarter slot pieces (see Fig. 7.25(a)). The lower response peaks in the spectra between 2 THz an 5 THz are based on the lambda-half resonance of the antenna slots (see Fig. 7.25(b)).

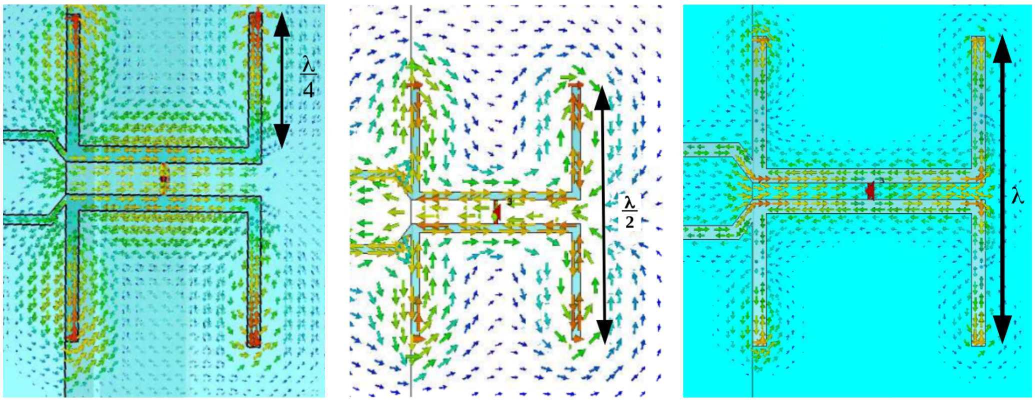

(a) (b) (c)

Figure 7.25.: Current distribution of (a) a lambda-quarter resonance (∼ 7 THz), (b) a lambda-half resonance (∼ 4 THz), and (c) a full-lambda resonance of the double-slot antenna (∼ 10.7 THz) simulated with CST-studio suite. (Red: highest current density, blue: lowest current density). The slot length of all antennas corresponds to an effective full-lambda wavelength for 10.7 THz.

The measured spectral response maximum for the 4.7 THz mixing device is 10 % to 15 % lower in frequency than the expected maximum in the impedance-match efficiency. This deviation is discussed in the following subsection.

For the HEB detector with the Archimedean spiral antenna no IV-curve at the operating temperature has been measured. To compare the response spectra with the impedance match efficiency the HEB resistance is assumed to correspond to half of the maximum resistance that has been extracted from the RT-curve in Sec.7.1.4. Since a change in the resistance of the HEB about ±50 Ω only yields a shift of the entire efficiency curve to higher or lower values, it is believed that this approximation sufficiently depicts the relative frequency-dependent course of the curve. As shown in Fig. 7.27(b) the HEB-device responds to the broadband signal of the FTS over the entire measured frequency range from 3 THz to 12 THz like expected from the predicted impedance match efficiency.

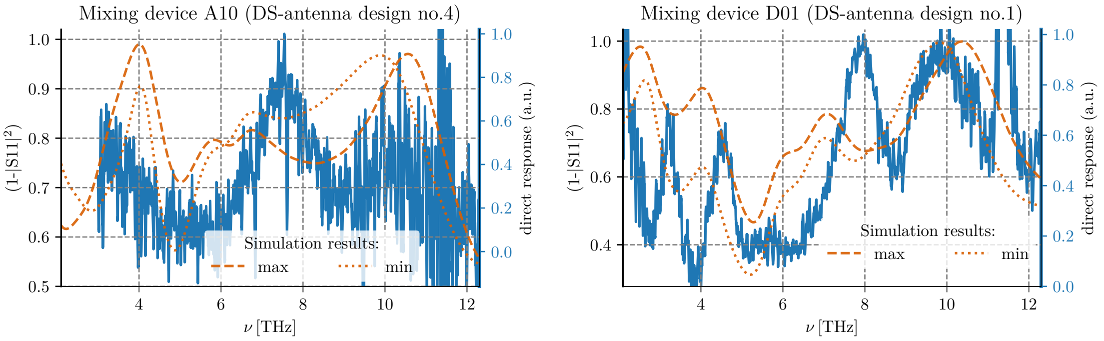

(a) (b)

Figure 7.26.: Comparison of the calibrated spectral response of the narrow-band detectors with the predicted intrinsic impedance match efficiencies between the HEB element and the antenna interface. The intrinsic coupling efficiency was calculated on base of the simulated input impedance at the antenna terminal and the resistance of the HEB micro-bridge that was determined by means of the HEB IV-curve measured at the respective operating temperature. The resistance during operation is changing due to the change in the spectral intensity of the radiation source produced by the internal moving FTS mirror. The intrinsic coupling efficiency is depicted for the highest (dashed line) and the lowest resistance value (dotted line) that the HEB element is assumed to reach during the measurement.

device	design no.	f_{fit} [THz]	f_{CST} [THz]	$f_{2nd\,peak,fit}$
A10	4	10.3(1)	9.9-10.6	7.5(1)
A11	4 (+ext.)*	10.1(1)	9.7-10.4	7.2(1)
D01	1	9.8(1)	9.8 -10.4	7.9(1)

* Filter-element of the RF-choke that is directly attached to the antenna has an additional extension in length of 300 nm (see Sec. 3.4.2)

Table 7.2.: Center frequencies of direct response maxima of three narrow-band mixing devices for 10.7 THz. The response peak denoted as the second peak refers to the pronounced response of the 10.7 THz detectors between 7 THz and 8 THz. f_{CST} refers to the center frequency of the impedance match or intrinsic coupling efficiency at the HEB-antenna interface based on the extracted resistance values of the HEB devices during operation and the simulated input impedance at the antenna terminal (for more information see Fig. 7.26).

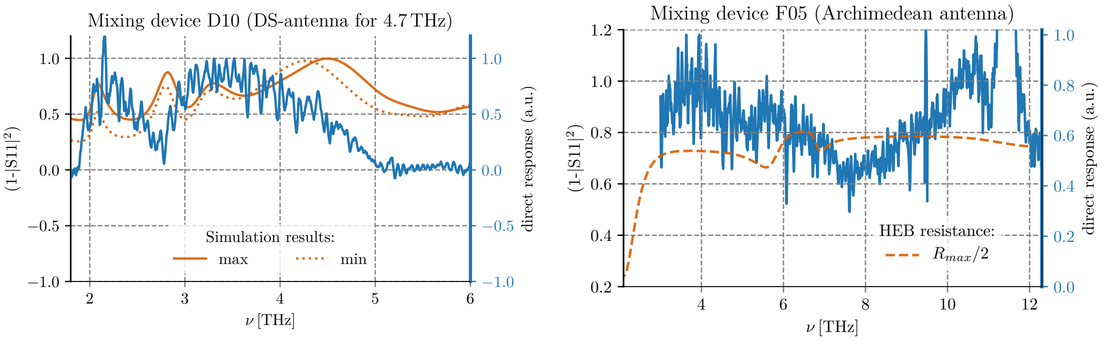

(a) (b)

Figure 7.27.: Comparison of the calibrated spectral response of (a) the narrow-band detector for 4.7 THz and of (b) the Archimedean spiral antenna based HEB-device with the predicted intrinsic impedance match efficiencies between the HEB element and the antenna interface. (a) The intrinsic coupling efficiency is depicted for the highest (dashed line) and the lowest resistance value (dotted line) that the HEB element is assumed to reach during the measurement. (b) The intrinsic coupling efficiency is calculated assuming that the resistance of the HEB-element is half of the maximum resistance that have been extracted from the RT-curve in Sec.7.1.4.

DS-antenna for 4.7 THz		
device	f_{fit} [THz]	f_{CST} [THz]
D10	3.5(2)	4.2 - 4.5

Table 7.3.: Center frequency of the direct response maxima of the narrow-band mixing device designed for 4.7 THz. f_{CST} refers to the center frequency of the impedance match or intrinsic coupling efficiency at the HEB-antenna interface based on the extracted resistance values of the HEB devices during operation and the simulated input impedance at the antenna terminal (for more information see Fig. 7.26).

7.2.6. Discussion

The comparison between the measured response spectra and predicted impedance match efficiencies reveals both, partly good conformity as well as some deviations which are discussed in the following. To begin with, for all measured 10.7 THz mixing devices the response peak around the designed operating frequency is in good agreement with the predicted curves of the impedance match efficiency. This points to the fact, that the RF-choke which is attached to the antenna, works as intended by presenting a short-circuit within the operating frequency range. Moreover, a variation of this filter leads to the expected effect on the RF-response, as can be observed in the response spectrum of device A11. exhibits a shift of its 10 THz response feature to lower frequencies of the predicted order of magnitude. Both observations support the assumption that the antenna as well as the filter work properly around the expected frequency of operation.

A deviation between the predicted impedance match efficiencies and measured response features can be found in all spectra of the 10.7 THz mixing devices for those response peaks that are located below the designed operating frequency and can be related to lower order resonances of the double-slot antennas. Based on only three measured spectra it cannot be concluded if these deviations are arbitrary or based on systematic errors. The predicted lambda-quarter resonance peak is located at lower frequencies than expected for all the measured mixing devices. On the other hand, the predicted lambda-half resonances in the response spectra occur at higher frequencies for device D01 and at lower frequencies for device A10 than the maximum response peaks in the measured spectra, where the coarse resolution in this frequency range makes it impossible to identify if the response feature below 4 THz is composed of one or two peaks. Although these lower frequency responses are not relevant for the operation of the 10.7 THz devices, they are investigated in the context of the considerable deviation between predictions and measurements that can be seen for the 4.7 THz mixing device D10. The maximum direct response for device D10 is around 10 % to 15 % lower than expected based on simulations. Since the design concept for all narrow-band circuits is the same and seems to be more accurate for the devices with a more than twice as high operating frequency it is believed that the deviation is not due to a general shortcoming of the underlying design methodology.

In the following, three different aspects that can affect the measured RF-performance are investigated, namely, the dimensional variations in the double-slot antenna, the resistance of the gold layer in which the RF-structures are defined at, and thirdly, a change in the filter characteristic.

- The dimensional variations due to fabrication tolerances of the RF-filter are too small (see analytical calculations in Sec. 3.4.2 and Fig. 3.13) to explain the shifts of the lower frequency response features. Likewise, simulation results accounting for possible changes in the dimensions of the double-slot antenna (see Fig. 7.28) do not accurately predict the positions of the lower frequency response features.

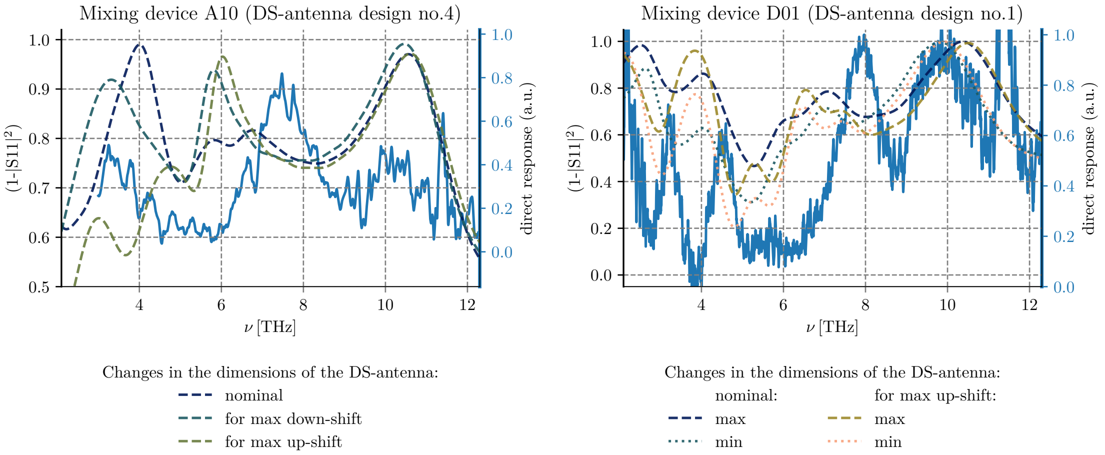

(a) (b)

Figure 7.28.: Spectral response and calculated coupling efficiencies between the HEB-element and the antenna terminal for the (a) maximum, and (b) maximum and minimum resistance value of the HEB-element during the respective response measurement. (a)The impedance match efficiency is shown for the nominal dimensions of the double-slot antenna and for deviations in the dimensions within the expected fabrication tolerances that once lead to a shift of the operating frequency to higher and once to lower frequencies.

- The effect of the gold-layer on the behavior of the RF-circuit is estimated based on the measured DC-resistivity of test-structures that are presented in Sec.7.1.3 and reveals a rather high resistance at cryogenic temperatures. [6] The respective frequency-dependent surface impedance is estimated with an internal in-house software in the anomalous limit[116], given the high frequency and the low temperature, and is fed into the simulation software. Accounting for the estimated gold resistivity leads to a shift of the expected maximum coupling efficiency to lower frequencies (see Fig.7.29) but still does not tally with the measured results.
- Basically, the filter characteristic can be changed due to a coupling of the CPW-

---

[6] In general, an increased RF surface impedance for the 4.7 THz devices is to be expected, since the thickness of the gold-layer is smaller than the actual optimal thickness around 90 nm for this frequency, as calculated from the skin depth. As the 4.7 THz and 10.7 THz devices are fabricated on the same wafer all RF-structures, however, are defined in a 70 nm thick gold-layer, instead.

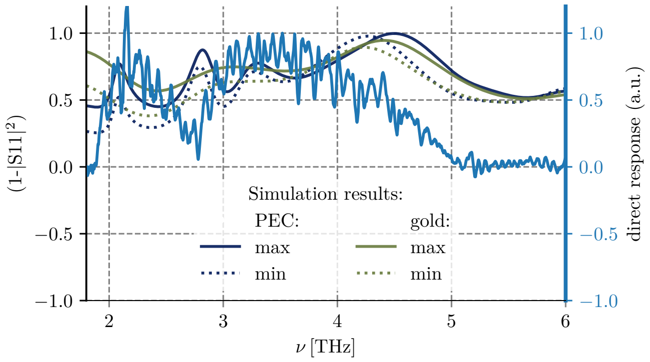

Figure 7.29.: Calibrated spectral response of the 4.7 THz device D10, and coupling efficiency between the HEB-element and the antenna terminal for the maximum and minimum resistance value of the HEB-element during the response measurement. The coupling efficiency is once calculated assuming that the metal the RF-structures consists of behaves as perfect electrical conductor (PEC), and once accounting for the resistivity of the gold-layer.

mode into unwanted modes. Such a mode-coupling could be enabled due to the existence of a gap between the lens backside and the RF-chip membrane. A respective scenario is depicted in Fig. 7.30 by introducing a gap between the backside of the RF-chip and the backside of the lens of about 2 µm. The gap leads to a shift of the operating frequency to lower frequencies. At the same time it can be observed that the lambda-quarter resonance moves to higher frequencies. Although the results reveal the shift direction of the maxima into the direction where the actual response maxima are located it cannot be used for a reasonable assessment. First a gap of 2 µm is unrealistically large, as a worst estimate of this gap is at maximum 1 µm, and secondly, any plausible gap will have an irregular thickness curve which is impossible to model.

Another candidate to change the filter-characteristic in such a way that it could explain why the predicted response maximum deviates significantly for the 4.7 THz mixing device although the same design concept yields reasonable results for the HEB detectors at a considerably higher frequency, is the bridge that is positioned over the third filter element counting from the antenna side (see Fig. 3.14). The bridge substrate, that works as an electrical insulator for the gold strip that is placed over the CPW line, consists of SiO_2 in form of fused quartz. For the design of the RF-circuits the dielectric constant of SiO_2 has been estimated to be around 3.8 with a $\tan\delta$ smaller than 0.1. This value is based on the experience value

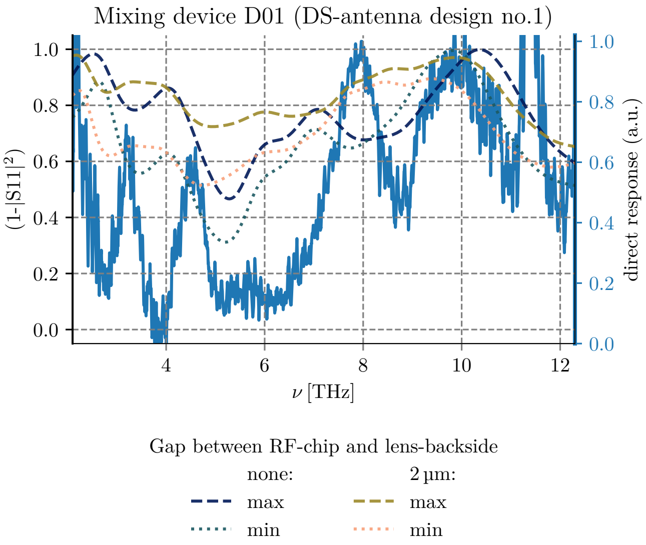

Figure 7.30.: Spectral response and calculated coupling efficiencies between the HEB-element and the antenna terminal for the maximum and minimum resistance value of the HEB-element during the response measurement. The impedance match efficiency is once calculated without and once with introducing a 2 µm large gap between the RF-chip and the backside of the lens.

of our research group and worked for the designs of former research projects for frequencies below 4.7 THz. It is further very close to the value which is provided by the internal data base of the CST simulation software. The actual frequency-dependent electric permittivity of the fused quartz layer used as a bridge substrate, however, can significantly deviate from this expectation value depending on factors like fabrication conditions and impurity levels[28, 98]. Furthermore, there is only little information about how the electric permittivity changes with temperature. In addition, absorption bands are reported for silica glass like materials [98, 78] from 21 µm to 23 µm and around 200 cm^{-1} down to around 4.2 THz (see Fig. 1 in [78]). Absorption features would cause a change in the permittivity of the bridge substrate which would affect the filter characteristic around 4.7 THz and 7 THz. Consequently, it could lead to a change in the operating frequency for the 4.7 THz device. Additionally, it could result into a shift of the lambda-quarter resonance to higher frequencies without affecting the response maximum around the operating frequency of the 10.7 THz devices. As there is too little information about these absorption features and their development with temperature it is not possible to properly predict a frequency-dependent permittivity of the used SiO_2. The overview about quartz measurements at room temperatures and the analytical formalism to describe the frequency-dependent dielectric constant that is given in [98] and is provided as a plot routine by Polyanskiy, does not cover the required frequency range down to 200 cm^{-1}. For a very rough approximation of a frequency-dependent permittivity of SiO_2 I used the plot routine provided by Polyanskiy and artificially added a small additional vibration feature at 200 cm^{-1} with a width of $\sigma = 200\,\mathrm{cm}^{-1}$. The simulation results assuming this frequency-dependence of fused quartz (see Fig. 7.31) shows that already a small change in the permittivity around 200 cm^{-1} yields a shift of the operating frequency to lower frequencies, although again not by the right amount to explain the measurements.

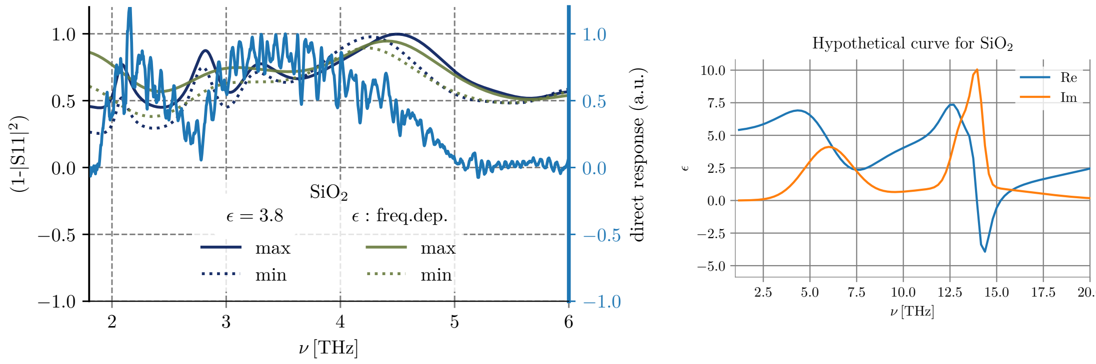

Figure 7.31.: Spectral response and calculated coupling efficiencies between the HEB-element and the antenna terminal for the maximum and minimum resistance value of the HEB-element during the response measurement. The impedance match efficiency is once calculated assuming that the bridge substrate SiO_2 has a constant dielectric permittivity of $\epsilon = 3.8$, and once assuming that the dielectric permittivity slightly changes around 200 cm^{-1} as depicted in the right figure.

In conclusion, it needs further investigations to de-embed different sources that could lead to the deviation between the predicted and the measured maxima in the response spectra of the 4.7 THz device. A change in the electric permittivity of the bridge substrate as has been reported around 6 THz down to 4.2 THz is a plausible sources to explain the observed shift of the operating frequency to lower frequencies but requires more quantitative information about the material properties of the bridge substrate to enable a reasonable assessment.

7.3. Summary and outlook

For all 5 HEB-devices which have been integrated into the mixer block lens assembly a direct response spectra could successfully be measured. The frequency range that is covered by the measurements ranges up to 12 THz. The measured broadband detector based on the Archimedean spiral antenna design responds to the broadband radiation over the entire frequency range from about 3 THz to 12 THz like it is expected from the simulation results. It thereby does not only encompass the desired operating frequency at 10.7 THz but also is suitable as a detector over a frequency range of at least 9 THz.

All measured narrow-band detectors (three 10.7 THz mixing devices and one 4.7 THz mixing device) exhibit response features that are polarization-dependent. Maximum response is observed for incoming radiation that is linearly polarized in the dedicated polarization direction of the antenna of the detectors. No response is observable for the respective polarization direction vertical to it.

The response features around the operating frequency of the 10.7 THz mixing devices have their maxima between 9.8 THz and 10.3 THz and tally with the frequency dependence of the coupling efficiencies between the antenna and the HEB-element that are predicted based on simulations and measured HEB resistances. All 10.7 THz mixing devices provide enough response around 10.7 THz to test them in a next step as heterodyne detectors at this operating frequency.

The measured maximum response peak of the 4.7 THz mixing device is around 3.5 THz and 10 % to 15 % lower than the expected maximum of the coupling efficiency between the HEB-element and the antenna. As has been investigated in the discussion section above, a plausible explanation for this deviation could be a frequency-dependent change in the dielectric permittivity of the SiO_2 bridge substrate that accordingly affects the filter characteristic of the RF-choke which is attached to the double-slot antenna. Several publications reveal that there exist various absorption features between 3 THz to 12 THz in fused quartz but there is not sufficient information, especially at cryogenic temperatures, to provide a reliable base for a quantitative assessment of the influence on the RF-circuit. A detailed study of the temperature-dependent refractive index of fused quartz layers that are fabricated under the same conditions as the here used bridge substrate therefore would be a necessary next step for the controlled optimization of the 4.7 THz designs. Another more straightforward option is the removal of bridge-substrate (air bridges) in the respective RF-chips of the next fabrication batch. This would require process development.

Up to now, the number of investigated devices is too low to allow meaningful statistics.

So far only two from in total five variations of the double-slot antenna have been tested in the mixer block. The measurement of all double-slot antenna versions thus is an important future task that will enable to better assess the individual effects and importance of different design parameters on the RF-circuit performance. Moreover, there are still three further broadband antenna versions all based on logarithmic spiral antennas that still need to be tested and are required for a comparison with the detector based on the Archimedean spiral antenna.

Finally, there are two enhancements of the measurement setup that are mandatory for future work. First of all, there is a strong reduction of the transmitted broadband signal of the radiation source above 8 THz that leads to an especially poor signal-to-noise ratio around 11.4 THz. The resulting artifact in the calibrated spectra prohibits to exploit any data around this frequency and leads to a considerably uncertain presentation of at least one side flank of the response peak of the 10.7 THz devices. The reason for this drop in the transmission is the large absorption of Mylar in this frequency range. Mylar is included into the optical beam path as part of the beamsplitter of the FTS and is used as a vaccum window at the entrance of the FTS. Although it cannot be replaced in the beamsplitter another task left for future work is to replace the Mylar window by another suitable window material. Up to now, it has not been replaced by Topas material yet, which basically exhibits a better transmission in this frequency range but also poses the risk to easily break[7] (see Fig. 7.13), even for the dewar window which is much smaller in diameter as the entrance window of the FTS. The second enhancement of the measurement setup that is necessary for future work is the implementation of a flexible vacuum tube between the FTS entrance and the Dewar window that allows to pump out the air between the windows. The strong absorption lines in the air spectrum could be clearly seen as absorption features in the response peaks of the detectors. Although these absorption features basically can be related to the actual absorption line in the measured air spectrum, the response peaks cannot be corrected for these partly considerable absorption features. These absorption features however cause an additionally uncertainty in the actual curve of the spectral response and together with the poor signal-to-noise ratio above 8 THz inhibits a unambiguous identification of the antenna RF bandwidth of the narrow-band devices.

---

[7] The sudden pressure balance that follows the break of the vacuum window leads to the destruction of the expensive commercial beamsplitter of the FTS.

8. Conclusion and Outlook

In the framework of this thesis HEB-detectors for 10.7 THz have successfully been developed, fabricated, assembled and tested according to their direct response spectrum. To the best of our knowledge this is the first work that reports about HEB-detectors that have been realized and verified as direct HEB power detectors around 10.7 THz and the first work that reports about a successful development and usage of RF-circuits based on double-slot (DS) antennas and an Archimedean spiral antenna for this operating frequency range.

The high operating frequency and cryogenic operating temperature of the detector required the development of additional software tools for the RF-circuit design as well as the examination of the temperature and frequency-dependent refractive index of the carrier material HRZF Si of the RF-circuits and other materials where still insufficient informations exist. An according detailed conclusion and outlook for each of these parts is given at the end of the respective chapter (Chapter 5 and 4) and is not repeated at this point.

The designed RF-circuits are based on 9 different antenna versions and contains narrowband as well as broadband antennas. The narrow-band RF-circuit is based on a double-slot (DS) antenna and a RF-filter- To anticipate potential deviations from the design parameters and to try out different slot-distances for an optimum coupling five different variations of a DS antenna have been developed.

The nominal resonance frequencies of the different versions are spread within a few 100 GHz around 10.7 THz. Moreover three different broadband designs have been developed based on an Archimedean, a self-complementary logarithmic and a logarithmic spiral antenna. Due to their non-resonating antenna response the broadband designs are more tolerant towards potential deviations in the design parameters than the narrowband designs. In particular, the Archimedean spiral allows to obtain an operating bandwidth where the required operating frequency around 10.7 THz according simulation results in any case will be met. Although the three different spiral antennas exhibit a quite similar frequency dependent directivity the Archimedean spiral antenna and the logarithmic spiral antenna are preferable when using NbN as HEB material as they enable a better impedance match between antenna terminal and HEB bridge than the self-complementary antenna. Although typically only being used for frequencies below 1 THz, the Archimedean spiral antenna according to the simulation results is the most favorable candidate for best power coupling to a Gaussian beam. A comparison of the spiral antennas with a 4.7 THz double slot antenna design based on simulation results shows that the narrow-band antenna design by far offers the best power coupling to a Gaussian beam and outweighs the broadband designs in terms of a feasible total efficiency. However, the fabrication of the DS-antennas is considerably more critical.

From in total 20 different RF-circuits that have been designed for this work and have been successfully fabricated from one batch in the in-house micro-structure facility four designs for 10.7 THz and one design for 4.7 THz have been assembled into the detector block and used as an external direct detector of a Fourier transform spectrometer to determine their spectral response to a RF broadband source. The observed center frequencies of the response peaks of all three different HEB-devices with a narrow-band DS-antenna for 10.7 THz tally well with the intended operating frequency with deviations of only 4 % to 8 %. The response peaks around 10 THz, moreover, are in good agreement with the predicted curves of the impedance match efficiencies. The influence of the RF-filter on the resonance frequency of the double-slot antenna that could be observed in the response spectra of two HEB-devices is adequately predicted by numerically calculations based on an formalism to determine the characteristics of CPW-lines at high frequencies that has been enhanced in this work. The HEB-device based on the broadband Archimedean antenna shows response over the entire measurement range from 3 THz to 12 THz as expected from simulations. Although to our knowledge it is the first Archimedean spiral antenna that has been fabricated and used in this high frequency range it points to its potential application for frequencies above 1 THz.

The results indicate that the underlying design methodology enables to reasonably depict the resonance behavior around the operating frequency. The good agreement with predictions further points to the fact that a dielectric permittivity of the carrier substrate around 11.4 which has been determined in the framework of this thesis is an adequate assumption for the high frequency range at the cryogenic operating temperatures. All four HEB-devices exhibit enough response around the operating frequency to be suitable candidates for future test heterodyne measurements.

The only 4.7 THz HEB-device whose direct spectral response has been measured so far exhibits a response peak around 3.5 THz that is 10 % to 15 % lower than expected according to the predictions of the curve of the impedance match efficiency. Since the RF-response around the more than twice as high operating frequency of the 10.7 THz devices could be reasonably predicted it is unlikely that this deviation is due to a general shortcoming of the underlying design. A plausible candidate to provoke such a shift in the operating frequency is a change in the dielectric permittivity around 4.7 THz of the bridge substrate SiO_2 which is used as a basement for a bridge that is placed over the RF-filter. In literature few measurements have been reported which indicate possible absorption and resonance features of fused quartz in this frequency range. However, there is by far too little information about the properties of fused quartz, especially at cryogenic temperatures to estimate a plausible frequency behavior of the bridge substrate and to adapt the design model accordingly. Since up to now only one 4.7 THz device has been characterized further measurements of 4.7 THz HEB-devices are needed to assess if the observed down-shift in the operating frequency is a general trend or an exception.

A direct comparison of the narrow-band RF-circuits with other double-slot antenna designs is not directly possible since no reports about developments of DS-antennas close to 10.7 THz range could be found in literature, to our knowledge only for frequencies below 5 THz with a successful HEB mixer operation with double slot antennas up to a frequency of 3.1 THz by Shiba et al.

The fabricated batch still contains HEB-devices with six antenna versions whose RF-response has not been characterized yet. Moreover, there are three different RF-filter variations for each double-slot antenna for 10.7 THz to further study the effect of the RF-choke on the resonance of the double-slot antenna. The characterization of those HEB-devices is the next step after enhancing the measurement setup to improve the signal-to-noise ratio above 8 THz by replacing the Mylar dielectrics in the setup. This implies a.o. to buy a different beam splitter for the FTS. In addition a IR-filter with a higher cut-off frequency than 12.5 THz would be a welcome band extension to investigate a larger part of the upper frequency bandwidth of the broadband antennas.

As soon as the 4.7 THz and the 10.7 THz LO-sources are available heterodyne measurements of suitable HEB-devices will be carried out to determine the mixer performance and noise. Since all HEB-devices are based on various antennas that are made from the same batch on the same wafer using the same fabrication process and conditions it is a good opportunity to allow a direct comparison of spiral and DS antenna mixer performances where still few works exist[62]. Even though the intended observatory SOFIA to operate a potential 10.7 THz mixer was recently terminated at the end of September of 2022[112] a mission on a balloon-borne telescope is still conceivable. The operation of the mixer for laboratory spectroscopy likewise is a feasible option.

A. Appendix: Optics

A.1. Ray tracing technique

A.1.1. Shape operator and principal curvatures

Given a surface $\sum$ that can be described by a differentiable equation $f(u,v)=w$. The tip of the vector

$$\mathbf{r} = \begin{pmatrix} u \\ v \\ f(u,v) \end{pmatrix}$$

traces all points on the surface $\sum$. The tangential vectors $\mathbf{t_1(P_i)}$ and $\mathbf{t_2(P)}$ at each point P_i on the surface which span the tangential plane at this point are chosen to be

$$\mathbf{t}_1 = \left.\frac{\mathrm{d}\mathbf{r}}{\mathrm{d}u}\right|_{P_i}$$
$$\mathbf{t}_2 = \left.\frac{\mathrm{d}\mathbf{r}}{\mathrm{d}v}\right|_{P_i}$$

To describe how the surface changes in the neighborhood of point P_i a linear shape operator is introduced which is defined on the tangent plane at P_i by a 2x2 matrix $\bar{\bar{Q}}$ called curvature matrix. As the tangential vectors neither have to be orthogonal nor be normalized the form of $\bar{\bar{Q}}$ is explicitly dependable on the chosen base vectors. Given a normal vector $\mathbf{N}$ at each point P_i of the surface which together with the vector

$$\mathbf{v} = \begin{pmatrix} u \\ v \\ 0 \end{pmatrix}$$

span up the normal-plane (see Fig. A.1). The variation of the normal vector when moving from one point in an arbitrary direction on the surface is determined by the bending of the surface in that direction. The curvature matrix describes this variation of $\mathbf{N}$ with

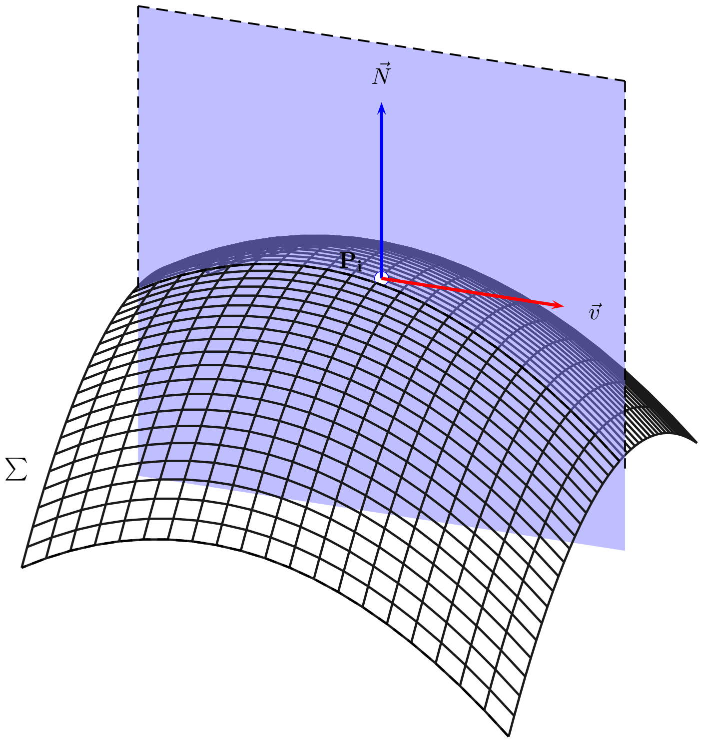

Figure A.1.: Surface $\sum$ with normal-plane spanned up by the normal vector $\vec{N}$ and $\vec{v}$ (blue area)

regard to the chosen base vectors of the tangential plane where $\mathbf{N_u} = \frac{\mathrm{d}\mathbf{N}}{\mathrm{d}u}$ is the variation in u-direction and $\mathbf{N_v} = \frac{\mathrm{d}\mathbf{N}}{\mathrm{d}v}$ is the variation in v-direction, respectively. Both vectors $\mathbf{N_u}, \mathbf{N_v}$ lie in the tangent plane at point P_i and thus can be expressed in terms of the base vectors

$$-\mathbf{N}_u = Q_{11} \cdot \mathbf{r}_u + Q_{12} \cdot \mathbf{r}_v \tag{A.1}$$

$$-\mathbf{N}_v = Q_{21} \cdot \mathbf{r}_u + Q_{22} \cdot \mathbf{r}_v \tag{A.2}$$

$$\tag{A.3}$$

Introducing the curvature matrix

$$\bar{\bar{Q}} = \begin{pmatrix} Q_{11} & Q_{12} \\ Q_{21} & Q_{22} \end{pmatrix}$$

eq. (A.3) in matrix notation can be expressed as

$$-\begin{pmatrix}\mathbf{N}_u\\ \mathbf{N}_v\end{pmatrix} = \bar{\bar{Q}}\begin{pmatrix}\mathbf{r}_u\\ \mathbf{r}_v\end{pmatrix} \tag{A.4}$$

Multiplying $(\mathbf{r}_u\ \mathbf{r}_v)$ on the right of both sides of the equation leads to

$$\underbrace{-\begin{pmatrix}\mathbf{N}_u\cdot\mathbf{r}_u & \mathbf{N}_u\cdot\mathbf{r}_v\\ \mathbf{N}_v\cdot\mathbf{r}_u & \mathbf{N}_v\cdot\mathbf{r}_v\end{pmatrix}}_{\bar{\bar{M}}_2} = \bar{\bar{Q}}\underbrace{\begin{pmatrix}\mathbf{r}_u\cdot\mathbf{r}_u & \mathbf{r}_u\cdot\mathbf{r}_v\\ \mathbf{r}_v\cdot\mathbf{r}_u & \mathbf{r}_v\cdot\mathbf{r}_v\end{pmatrix}}_{\bar{\bar{M}}_1}. \tag{A.5}$$

with the fundamental matrices

$$\bar{\bar{M}}_1 = \begin{pmatrix}E & F\\ F & G\end{pmatrix}\ \text{, and } \bar{\bar{M}}_2 = \begin{pmatrix}e & f\\ f & g\end{pmatrix}. \tag{A.6}$$

Using inversion matrix of $\bar{\bar{M}}_1$ the equation can be solved for the curvature matrix

$$\bar{\bar{Q}} = \bar{\bar{M}}_2\left(\bar{\bar{M}}_1\right)^{-1}, \tag{A.7}$$

where

$$Q_{11} = \frac{eG - fF}{EG - F^2}, \qquad Q_{12} = \frac{fE - eF}{EG - F^2}, \tag{A.8}$$

$$Q_{11} = \frac{fG - gF}{EG - F^2}, \qquad Q_{12} = \frac{gE - fF}{EG - F^2}. \tag{A.9}$$

Equation (A.5) with (A.9) are also known as Weingarten equations. The eigenvalues and eigenvectors of the curvature matrix are the principal curvatures of the surface $\sum$ and the principal directions, respectively.

A.1.2. Ray tubes

A ray as an idealization of a trajectory of a very narrow beam of monochromatic light is only a valid approximation for the propagation of an electromagnetic field if the wavelength is small compared to the dimensions of the objects it interacts with. It describes the variation of a field in the direction of propagation in terms of phase and amplitude obeying the laws of geometrical optics which shall be shortly repeated here. More detailed descriptions can be found in [40].

Phase

The phase of a ray can be found using Fermat's principle which states that a ray connecting two points r_0 and r is the curve C that makes the integral

$$S(C) = \int_C n \mathrm{d}\sigma \tag{A.10}$$

minimal or more precisely stationary where $n(\mathbf{r})$ is the refractive index and ds $= n\mathrm{d}\sigma$ is the optical length as a measure of the arc $\mathrm{d}\sigma$. The phase of the ray is given by the $k_0 \cdot S(C)$ where k_0 is the free-space wavenumber. If the refractive index is a smooth function of $\mathbf{r}$ and $\mathbf{k}$, which is the tangent vector on C at point $\mathbf{r}$ of length $n \cdot k_0$, the ray satisfies the differential equation

$$\frac{\mathrm{d}\mathbf{k}}{\mathrm{d}\sigma} = k_0 \nabla n. \tag{A.11}$$

Given that the initial direction r_0 is known the ray can be determined by the integration of (A.11) [40]. A wavefront or wave surface is defined as a surface on which $S(\mathbf{r})$ is constant. Introducing

$$\mathbf{k} = k_0 \nabla S(\mathbf{r}) \tag{A.12}$$

as the tangent vector of the ray at point $\mathbf{r}$ of length $k_0 n(\mathbf{r})$ enables to deduce that the rays are everywhere normal to the wavefronts. The eikonal equation

$$(\nabla S)^2 = n^2 \tag{A.13}$$

further states that in the vicinity of $\mathbf{r}$ the phase variation equals those of a plane wave with wave vector $\mathbf{k}$ enabling to describe the field locally as a plane wave.

Amplitude

The intensity I is defined as the energy per unit time crossing a unit surface element normal to the ray

$$I = A^2 v, \tag{A.14}$$

where $v = c/n$ is the velocity the energy in the field moves along the rays. The energy conservation in a tube of rays as depicted in Fig. A.2 with cross section areas $d\Sigma_1$ through

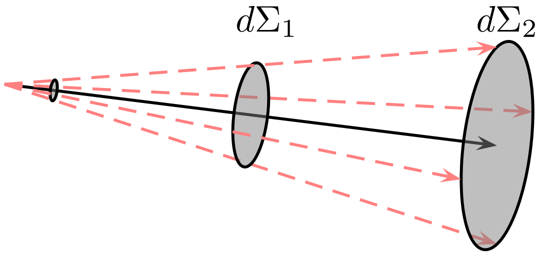

Figure A.2.: A tube of rays consisting of a center ray and four surrounding rays.

$\mathbf{r_1}$ and $d\Sigma_2$ through $\mathbf{r_2}$ states

$$I_1 d\Sigma_1 = I_2 d\Sigma_2 \tag{A.15}$$

As at each point of converging rays (source point and focus points) this equation would lead to an infinite intensity, the conversation law of energy will be rewritten in terms of energy that leaves the source per unit time, per unit solid angle

$$I_\Omega d\Omega = I_2 d\Sigma_2 \tag{A.16}$$

Geometrical parameters

Using the above-mentioned laws of geometrical optics for the phase and amplitude of rays it is possible to deduce the field carried along the rays if the initial phase $k_0 S_0(\mathbf{r_0})$ and amplitude $A_0(\mathbf{r_0})$ on some surface Σ as well as the ray direction at every point $\mathbf{r_0}$ of the surface are well-known. In a homogeneous region the phase at some point $\mathbf{r}$ is given by

$$S(\mathbf{r}) = S_0(\mathbf{r_0}) + \overline{\mathbf{r_0 r}}. \tag{A.17}$$

The amplitude at this point can be achieved considering a small tube of rays consisting of a bundel of paraxial rays near to an axial ray forming a very narrow pencil as shown in Fig. A.2. According to the energy conservation law (A.16) the intensity of the field along the axial ray varies with the cross section of the tube of paraxial rays. Without loss of generality, the axial ray going through point P_0 is attached to the z-axis. The wavefront through point $P_0 = (x, y, z)$ in the vicinity of the axial ray can be represented by

$$z = -\frac{1}{2}\mathbf{t}^T\mathbf{Q}\mathbf{t}, \tag{A.18}$$

where $\mathbf{Q}$ is the 2x2 symmetric curvature matrix with the transverse position vector (see also A.1.1) based on an orthonomal frame of reference. The gradient of $z + \frac{1}{2}\mathbf{t}^T\mathbf{Q}\mathbf{t}$ yields the normal at point P_0. Being symmetric the curvature matrix has two orthogonal eigenvectors $\hat{X}_1$ and $\hat{X}_2$ spanning up the principal planes $\hat{\mathbf{z}}\hat{\mathbf{X}}_1$ and $\hat{\mathbf{z}}\hat{\mathbf{X}}_2$ and obeying

$$\mathbf{Q}\hat{\mathbf{X}}_i = \frac{1}{R_i}\hat{\mathbf{X}}_i \quad i = 1, 2 \tag{A.19}$$

where R_1 and R_2 are the principal radii of curvature. At the focal points F_1 and F_2 the rays in the principal planes $\hat{\mathbf{z}}\hat{\mathbf{X}}_1$ and $\hat{\mathbf{z}}\hat{\mathbf{X}}_2$ converge, respectively. The rectangular cross section of a pencil defined by four tubes of rays, varies along the tube. If its foci are at $z = -R_1$ and $z = R_2$ geometrical considerations results following relation for the ratio of the cross section $\Sigma(z_0 = 0)$ at point P_0 to the cross section $\Sigma(z)$ along the z-axis

$$\frac{\Sigma(z)}{\Sigma(0)} = \frac{(R_1 + z)(R_2 + z)}{R_1 R_2} \tag{A.20}$$

Expressing the curvature matrix in the frame of its principal axes at point z

$$Q = \begin{bmatrix} \frac{1}{R_1+z} & 0 \\ 0 & \frac{1}{R_2+z} \end{bmatrix} \tag{A.21}$$

enables to easily deduce the principal radii of curvature. Applying the energy conservation (A.16) and using that the intensity is proportional to the square of the field amplitude reveals the information about the amplitude $A(\mathbf{r})$ carried along the rays to point $\mathbf{r}$ in form of a divergence factor

$$DF = \frac{A(\mathbf{r})}{A_0(\mathbf{r_0})} = \left[\frac{det\mathbf{Q}(\mathbf{z})}{det\mathbf{Q}(\mathbf{0})}\right]^{\frac{1}{2}} = \left[\frac{(R_1 + z)(R_2 + z)}{R_1 R_2}\right]^{\frac{1}{2}}. \tag{A.22}$$

The phase $k_0 S(\mathbf{r})$ at any point r for $0z$ being the axial ray surrounded by almost parallel paraxial rays forming a very thin pencil can be approximated by

$$S(\mathrm{r}) = z + \frac{1}{2}\mathbf{t}^T\mathbf{Q}\mathbf{t} \tag{A.23}$$

when the deviation in x and y direction is small.

Refraction at a curved dielectric interface

To describe the refraction of a ray field at an arbitrarily curved dielectric interface once requires the knowledge about how the curvature matrix of the wave surface changes under refraction to extract the divergence factors DF and second needs some transmission and reflection coefficients T and R. Decomposing the incident $\mathbf{E}^{in}$, reflected $\mathbf{E}^{r}$ and transmitted field $\mathbf{E}^{t}$ into parts parallel $E^{i}_{\|}$ and perpendicular $E^{i}_{\perp}$ with respect to the plane of incidence the approximated expressions for the refracted fields are given by

$$\begin{aligned}\mathbf{E}^{r} &= DF_{r} \cdot \mathbf{R}e^{(-ik_r d_r)}\mathbf{E}^{in}\\ \mathbf{E}^{t} &= DF_{t} \cdot \mathbf{T}e^{(-ik_t d_t)}\mathbf{E}^{in}\end{aligned}$$

where $\mathbf{R}$ and $\mathbf{T}$ represent the reflection and transmission coefficients for parallel and perpendicular polarization, respectively. They are approximated using the Fresnel formulas for refraction at planar surfaces. The exponent contains the wavenumbers k_r and k_t and the distances d_r and d_t between the point of refraction and the points of observations after the refraction for the reflected and transmitted case, respectively. The following subsections expand on the procedure to determine the unknown divergence factors and Fresnel's coefficients.

Curvature matrix under refraction

The determination of the divergence factor of a ray tube under refraction through a curved interface Σ (as depicted in Fig. A.3) requires to know how the surface of its wavefronts represented by curvature matrices changes. As described by [40] one method to quantitatively determine the curvature changes under refraction can be found using that according to Snell's law the phase of an incident ray pencil at every point on Σ matches the phase of the refracted pencil.

For the mathematical description of this issue it is convenient to use frames for the incident, reflected and refracted field which are attached to both, the individual ray and the diffracting object. In the following, without any loss of generality the origin of the coordinate system is placed at the point O where the ray incidents the interface between two media.

The base of orthonomal vectors of the incident, reflected and transmitted rays are $(\hat{x}_{in}, \hat{y}_{in}, \hat{k}_{in})$, $(\hat{x}_{r}, \hat{y}_{r}, \hat{k}_{r})$ and $(\hat{x}_{t}, \hat{y}_{t}, \hat{k}_{t})$, respectively. The reference frame of the surface

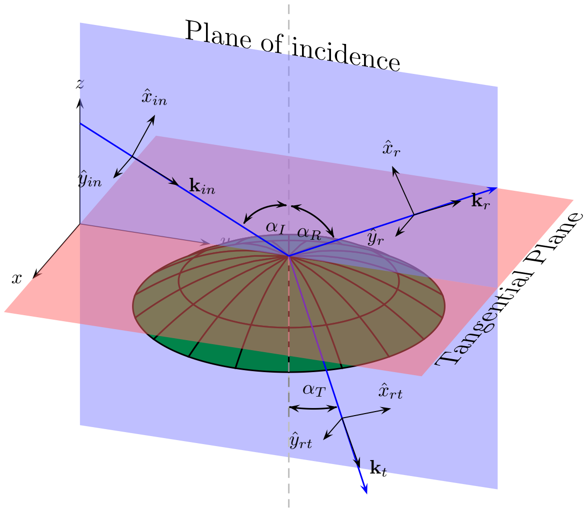

Figure A.3.: Refraction of a ray at an arbitrarily shaped interface.

at the intersection point is $(\hat{x}_\Sigma, \hat{y}_\Sigma, \hat{k}_\Sigma)$. The reference frame of the plane of incidence at the intersection point is given by the normal vector $\hat{n}$ of the surface at the intersection point, the unit vector $\hat{e}_\perp = \hat{n} \times \hat{k}_{in}$ normal to the plane of incidence, and $\hat{e}_\parallel = \hat{e}_\perp \times \hat{n}$. The curvature matrices of the incident, reflected, transmitted rays and the interface expressed in their respective reference frames are $\bar{\bar{Q}}_{in}$, $\bar{\bar{Q}}_r$, $\bar{\bar{Q}}_t$ and $\bar{\bar{Q}}_\Sigma$. Equating the second order approximation of the incident and refracted phases ,where the second order term is given in form of $-\frac{1}{2}\mathbf{tQt}$ with

$$\mathbf{t} = \begin{pmatrix} x \\ y \end{pmatrix}$$

the transverse position vector with respect to the orthonomal frame of reference [40], yields

$$n\mathbf{B}_r^T \mathbf{Q_r} \mathbf{B}_r = \mathbf{B}_{in}^T \mathbf{Q_{in}} \mathbf{B_{in}} + (n \cdot \cos(\alpha_t) - \cos(\alpha_{in}))\mathbf{A}^{-1}\mathbf{Q_\Sigma A} \tag{A.24}$$

$$\mathbf{B}_t^T\mathbf{Q_t}\mathbf{B}_t = \mathbf{B}_{in}^T\mathbf{Q_{in}}\mathbf{B_{in}} - 2\cos(\alpha_{in})\mathbf{A}^{-1}\mathbf{Q_\Sigma}\mathbf{A}, \tag{A.25}$$

with $n = n_2/n_1$.

The projection operators and transformation matrix are given by the

$$\mathbf{B}_i = \begin{bmatrix} \hat{x}_i \cdot \hat{e}_{||} & \hat{x}_i \cdot \hat{e}_\perp \\ \hat{y}_i \cdot \hat{e}_{||} & \hat{y}_i \cdot \hat{e}_\perp \end{bmatrix}, \text{for } i \in (in,\, r,\, t) \tag{A.26}$$

$$\mathbf{A} = \begin{bmatrix} \hat{x}_\Sigma \cdot \hat{e}_{||} & \hat{x}_\Sigma \cdot \hat{e}_\perp \\ \hat{y}_\Sigma \cdot \hat{e}_{||} & \hat{y}_\Sigma \cdot \hat{e}_\perp \end{bmatrix} \tag{A.27}$$

Once the curvature matrices $\mathbf{Q}_r$ and $\mathbf{Q}_t$ are determined from (A.24) and (A.25), the eigenvalues λ_i of the diagonalized matrices can be used to calculate the principal radii $R_i = \frac{1}{\lambda_i}$ and subsequently the divergence factor.

Further detailed description and additional information concerning ray techniques are provided in [13, 40, 106] .

Fresnel's equations

Fresnel's equations describe the reflective and transmitted behavior of electromagnetic waves at uniform planar interfaces. As any arbitrary polarized wave can be expressed as a superposition of waves being tangentially and perpendicularly polarized to the plane of incident, its refractive behavior is entirely captured by the determination of the amplitude ratios of the electric field vectors for both polarization cases.

Introducing the indices *in*, *r* and *t* for the incoming, reflected and transmitted parts of the field, and $\perp$ and $||$ for the perpendicularly and parallel polarized E-fields (as depicted in Fig. A.4) the corresponding Fresnel's equations used for this work (considering $\mu = 1$) are given by

$$r_{||} = \frac{1 - \frac{n_1}{n_2}\frac{\cos(\Phi_t)}{\cos(\Phi_{in})}}{1 + \frac{n_1}{n_2}\frac{\cos(\Phi_t)}{\cos(\Phi_{in})}} \tag{A.28}$$

$$t_{||} = \frac{2}{1 + \frac{n_1}{n_2}\frac{\cos(\Phi_t)}{\cos(\Phi_{in})}} \tag{A.29}$$

$$r_\perp = \frac{1 - \frac{n_2}{n_1}\frac{\cos(\Phi_t)}{\cos(\Phi_{in})}}{1 + \frac{n_2}{n_1}\frac{\cos(\Phi_t)}{\cos(\Phi_{in})}} \tag{A.30}$$

$$t_\perp = \frac{2}{1 + \frac{n_2}{n_1}\frac{\cos(\Phi_t)}{\cos(\Phi_{in})}} \tag{A.31}$$

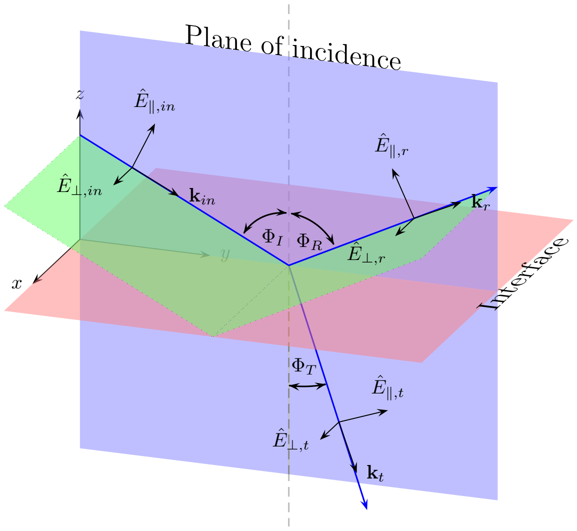

Figure A.4.: Refraction at a plane interface

B. Appendix: RF design

B.1. Extended hemispherical lenses

The choice of the lens is dependent on several parameters, like the integration of the receiver into the beam optic of the measurement setup, reflection and dielectric losses or the occurrence of undesirable aberration effects. Hyperhemispherical, ellipsoidal or extended hemispherical lenses are common lens-types used in quasi-optical receivers. The hyperhemispherical lens consists of a hemisphere that is extended by a length of $\frac{r_{lens}}{n_{lens}}$, where r_{lens} is the radius and n_{lens} is the refractive index of the lens, respectively. As it fulfills the Abbe sine condition and is aplanatic it is free of circular coma and spherical aberrations [12]. The beam pattern of an antenna integrated at its backside is bended and thereby effectively sharpened such that the antenna-gain is increased by n^2_{lens}[139]. However, it has been reported that radiation pattern from hyperhemispherical lenses turned out to be broad compared to those from ellipsoidal lenses with same radius and sometimes became multi-lobed [52]. The hyperhemispherical lens is suitable for Gaussian-beam optics, as it enables good coupling to a converging beam but not to a planar equiphase wave-front[52]. In contrast to collimating lenses the directivity does not increase with the size of the lens and as such with the aperture size[50].

The elliptical lens has an ellipsoidal surface with a major radius b and a minor radius a. The lens has two geometrical foci at $\pm c = \sqrt{b^2 - a^2}$. For a given refractive index n_l of the dielectric of the lens the geometrical and optical focus becomes identical if [83]

$$b = \frac{a}{\sqrt{1 - \frac{1}{n^2}}}, \text{ and} \tag{B.1}$$

$$c = \frac{b}{n}. \tag{B.2}$$

Beeing fed at its second focus point the lens transforms the radiation pattern into plane waves in the air medium. As such it provides good coupling with a Gaussian-beam at its planar equiphase front at the beams's minimum waist[52]. The beam pattern of a planar antenna attached to the more distance focus of the lens is diffraction-limited by the aperture of the elliptical lens which have been proven for a various of different antenna types [173, 53, 52]. Providing the opportunity to gain very narrow beam patterns the ellipsoidal lens is compatible with large f-number systems, as can typically found in Cassegrain focus telescopes [20]. The third lens type is an extended hemispherical lens that consist of a hemisphere with a certain cylindrical extension. Depending on the extension length an elliptical lens or an hyperhemispherical lens can be synthesized [52, 20] with the advantage that it is easier and less expensive to manufacture. The gaussicity, directivity, phase, beam waist and reflection loss (see definition in Sec.B.2) are a function of the extension length L_{ext}[52]. All five quantities need to be considered for achieving a good coupling to the respective beam optics, but cannot be optimized independently from each other as they have their optima at different extensions length. Thus a compromise needs to be found.

B.1.1. Dissipation loss in a lens

Considering a spherical wave that is traveling from the plane surface center of a dielectric half sphere with radius r_{lens} to the outer bend surface of the lens, the power loss due to the dissipation in the dielectric material in case of low loss material can be roughly estimated by the power decay of the wave for a loss angle $\delta << 1$:

$$P = P_0 \cdot e^{-\delta \frac{2\pi}{\lambda} \cdot z}, \tag{B.3}$$

with $\lambda = \lambda = \lambda_0/\sqrt{\epsilon_r}$ and $z = r_{lens}$.

Rearranging the equation, the loss in decibel is given by:

$$L = -\frac{10}{\ln(10)} \cdot 2\pi \frac{r_{lens}}{\lambda_0} \epsilon_0 \,[\mathrm{dB}] \tag{B.4}$$

B.2. Antenna basics

The description of the performance of an antenna requires the introduction of some fundamental antenna parameters. The here used definitions comply with the international standards, basically those of the International Electrotechnical Comission (IEC) and the IEEE Standard Definitions of Terms for Antennas [143].

Graphical representation

The graphical representation of a radiation pattern or far-field pattern of an antenna consist of a two- or three-dimensional spatial distribution of the respective radiation property of interest. Two common graphic representations are the *amplitude* or *field pattern*, which shows the spatial distribution of the field strength at a constant large radius, and the *power pattern* that depicts the power per unit solid angle at a constant radius. The typical coordinate system used for antenna analysis is a spherical coordinate system with an elevation and an azimuth plane or a polar coordinate system to describe a two-dimensional distribution. In this work, furthermore an orthographic projection of some directional-dependent antenna properties of the far field is used. The projection from spherical coordinates into the uv-plane is given by

$$\begin{aligned}
&u = \sin(\theta) \cdot \cos(\phi) \\
&v = \sin(\theta) \cdot \sin(\phi), \text{ where} \\
&\sqrt{u^2 + v^2} < 1 \text{ and} \\
&r = (u, v, 1 - \sqrt{u^2 + v^2})
\end{aligned}$$

A radiation pattern can be designated isotropic, directional and omnidirectional. Isotropic refers to a hypothetical lossless radiator whose radiation is equally distributed in all directions. It typically is used as a reference for the directive properties of an antenna which for a power pattern is indicated by adding an i to the units as in for instance dBi. A directional antenna is defined as radiating or receiving more effectively in some directions than in others[143]. If a pattern is nondirectional in one principle plane (e.g. the elevation plane) and directional in any other orthogonal principle plane (e.g. the azimuth plane) it is classified as omnidirectional. The major lobe of the radiation pattern is called the *beam* of the antenna.

Antenna on a dielectric substrate

An planar antenna placed on a substrate radiates most of its power into the dielectric. The amount of emission into the substrate side is directly dependent on the relative electric permittivity of the substrate, $\epsilon_{r,sub}$. For an elementary slot antenna the ratio of power radiated to the substrate side to that power on the air side is $\left(\frac{\epsilon_{r,sub}}{\epsilon_{r,air}}\right)^{3/2}$ [147]. Considering all antennas of this work in a first approximation as a combination of elementary slots or dipols up to 38.5 times more power is expected to be emitted into the silicon substrate with an electric permittivity around about $\epsilon_{r,sub} = 11.4$ in its operational frequency range and temperature. Power coupling via the substrate side accordingly is an attractive way to increase the energy transfer especially to weak signals.

Another effect of the substrate is the break of the symmetry of the radiation pattern present in free space that goes hand in hand with a change in the antenna's current distribution, its wave velocity and by this in the antenna's input impedance. The resulting current velocity is directly determined by the effective relative electric permittivity ϵ_{eff} by

$$v = \frac{c_0}{\sqrt{\epsilon_{eff}}}. \tag{B.5}$$

For antennas in the millimeter-wave range this effective permittivity in a good approximation is given by the value received for a quasi-static field assumption that is

$$\epsilon_{qs} = \epsilon_{eff}(0\,\mathrm{Hz}) = \frac{\epsilon_{r,sub} + 1}{2}. \tag{B.6}$$

Above a few GHz, however, this approximation needs to be extended accounting for a frequency dispersive part. A corresponding estimations for each antenna design is carried out separately in the respective design section.

Directivity and directivity gain

For directional antennas a fundamental parameter is the *directivity D*. It specifies how large the highest power density $S_{max}(r)$ radiated in the main radiation direction of the antenna is compared to the power density $S_i(r)$ of an ideal isotropic radiator. The power density of an isotropic radiator in a distance r is given by

$$S_i(r) = \frac{P_{\mathrm{rad}}}{4\pi r^2}, \tag{B.7}$$

where P_{rad} is the total radiated power of the antenna. Accordingly, the directivity reads

$$D = \frac{S_{max}(r)}{S_i(r)} = \frac{4\pi r^2 S_{max}(r)}{P_{\mathrm{rad}}}. \tag{B.8}$$

The directivity is the maximum of its directive gain, which is the ratio of the radiation intensity in an arbitrary, given direction to the radiation intensity average over all directions [143]. Designating $U(\Theta, \Phi)$ as the radiation intensity, the power per unit solid angle $\mathrm{d}\Omega = \sin(\Theta)\mathrm{d}\Theta\mathrm{d}\Phi$, the directivity gain is given by

$$D(\Theta, \Phi) = \frac{U(\Theta, \Phi)}{P_{\mathrm{rad}}/(4\pi)} \tag{B.9}$$

where

$$P_{\text{rad}} = \int_0^{2\pi} \int_0^{\pi} U(\Theta, \Phi) \sin(\Theta) \mathrm{d}\Theta \mathrm{d}\Phi. \tag{B.10}$$

The directivity follows from the maximum of the directive gain found among all possible solid angles.

$$D = D\left(\Theta, \Phi\right)|_{max}. \tag{B.11}$$

Antenna gain and antenna efficiency

The *antenna gain* is a measure for the power gain that takes into account the efficiency of the antenna. It is defined as "the ratio of the radiation intensity, in a given direction, to the radiation intensity that would be obtained if the power P_{acc} accepted by the antenna were radiated isotropically"[143].

$$G(\Theta, \Phi) = 4\pi \frac{U(\Theta, \Phi)}{P_{\text{acc}}} \tag{B.12}$$

In case of a hypothetically perfect radiator it is simply the directivity gain. Utilizing that the total radiated power is related to the accepted power by the *antenna radiation efficiency* $\eta_{c,d}$ via

$$P_{\text{rad}} = \eta_{c,d} \cdot P_{\text{acc}}, \tag{B.13}$$

the antenna gain can be further rewritten as

$$\begin{aligned} G(\Theta, \Phi) &= \eta_{c,d} \cdot 4\pi \frac{U(\Theta, \Phi)}{P_{\text{rad}}} \\ &= \eta_{c,d} \cdot D(\Theta, \Phi). \end{aligned} \tag{B.14}$$

The antenna gain, defined by the IEEE Standards, does not include reflection losses at the antenna's input terminal which arise in case of an impedance mismatch between the transmission line of the antenna and its terminal base. An antenna input impedance of Z_{in} and a characteristic impedance of the transmission line of Z_0 yield a voltage reflection coefficient Γ, or S-parameter at the input terminal of

$$\Gamma = S_{11} = \frac{Z_{\text{in}} - Z_0^*}{Z_{\text{in}} + Z_0^*}. \tag{B.15}$$

The consequent *reflection mismatch efficiency* [4], or *impedance match efficiency*, η_{match}, can be calculated by

$$\eta_{\text{match}} = 1 - |S_{11}|^2. \tag{B.16}$$

To account for both, the radiation losses as well as those arising from the impedance mismatch at the antenna's input terminal, a *total antenna efficiency*, η_{tot}, is defined as

$$\eta_{\text{tot}} = \eta_{c,d} \cdot \eta_{\text{match}}. \tag{B.17}$$

It relates the radiated power to the stimulated power P_{stim}, that is delivered to the antenna terminal,

$$P_{\text{rad}} = \eta_{\text{tot}} \cdot P_{\text{stim}}. \tag{B.18}$$

The according *realized antenna gain*, that is one of the decisive parameters for the overall receiver performance, is given by

$$\begin{aligned} G_{realized}(\Theta, \Phi) &= \eta_{\text{tot}} \cdot 4\pi \frac{U(\Theta, \Phi)}{P_{\text{rad}}} && \text{(B.19)} \\ &= \eta_{\text{tot}} \cdot D(\Theta, \Phi). && \text{(B.20)} \end{aligned}$$

Polarization

An antenna is sensitive to the direction of the electric and magnetic field vector of an impinging wave. As a consequence the strength of its coupling to an external electromagnetic wave depends on the polarization of the antenna. The polarization of a radiated wave describes the "time varying direction and relative magnitude of the electric field vector"[4]. In general, the polarization of the antenna field pattern is directional dependent which is important to note when estimating the power coupling to an external singal. If not stated otherwise, the polarization of the antennas designed in this work is referred to the E-field orientation in the direction of maximum gain. For a *linearly polarized* wave the electric field oscillates in a single direction. If the tip of the electric field vector, however, traces the course of an ellipse while moving through the space, it is said to be *elliptically polarized.* If the course of the E-field vector describes a circle the wave is called *circularly polarized.*

For an elliptically polarized wave, the curve drawn by the tip of the E-field vector in a plane orthogonal to the propagation direction at a given position in z, is called the

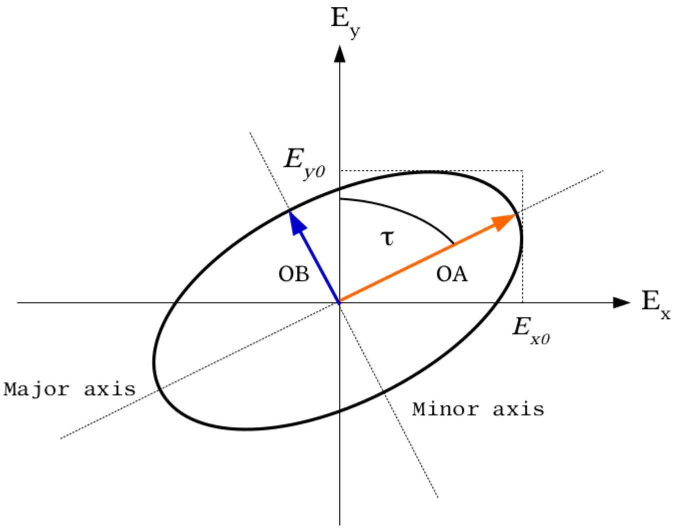

Figure B.1.: Polarization ellipse of the electric field vector of an electromagnetic wave in the x-y-plane at a fixed position in z-direction (similar to [4]). The major axis is tilted relative to the y-axis by an angle τ.

polarization ellipse and is sketched in Fig. B.1. The axial ratio, AR, of the major axis OA to the minor axis OB of this polarization ellipse is a measure for the extent of elliptical manifestation and is given by[4]

$$AR = \frac{OA}{OB}, \quad \text{with } 1 \leq AR \leq \infty. \tag{B.21}$$

An axial ratio of 1 means the polarization is circular, whereas an AR approaching infinity is tantamount with a linear polarization. Values in between indicate an elliptical polarization characteristic. The major and minor axis can be directly deduced from the phase difference between the E-field components by[4]:

$$OA = \left(\frac{1}{2}\left[E_{x0}^2 + E_{y0}^2 + C^{\frac{1}{2}}\right]\right)^{\frac{1}{2}} \tag{B.22}$$

$$OB = \left(\frac{1}{2}\left[E_{x0}^2 + E_{y0}^2 - C^{\frac{1}{2}}\right]\right)^{\frac{1}{2}} \tag{B.23}$$

$$\text{with} \quad C = \left(E_{x0}^4 + E_{y0}^4 + 2E_{x0}^2E_{y0}^2\cos(2\Delta\Phi)\right).$$

Generally, the major axis is tilted relative to the y-axis by an angle given by[4]

$$\tau = \frac{\pi}{2} - \frac{1}{2}\arctan\left(\frac{2E_{x0}E_{y0}}{E_{x0}^2 - E_{y0}^2}\cos(\Delta\Phi)\right). \tag{B.24}$$

To enable an optimal energy transfer between an antenna and an incident wave, the polarization of the antenna and the wave ought to be the same. If this is not the case, the *polarization mismatch*[4] reduces the amount of power which can couple into the antenna. As for this work the receiver system needs to be coupled to Gaussian beam optics, the polarization mismatch is already considered within the calculation of the Gaussicity.

B.3. Coupling efficiency

The coupling efficiency of the receiver's beam with a reference field can be stemmed from the field coupling coefficient. The field coupling coefficient of any two fields Ψ_a and Ψ_b is given by

$$c_{ab} = \int\int \Psi_a^\star \Psi_b \mathrm{d}S, \tag{B.25}$$

where the surface integral usually refers to a plane perpendicular to the optical axis. The coupling efficiency η of the beam profile of the receiver E_{re} with a specified field distribution E_{ref} is expressed by the field coupling coefficient normalized by the absolute square of the single field distributions. Designating the z-axis as the optical axis of the system the corresponding efficiency at a surface plane perpendicular to the optical axis at $z = z^*$ reads

$$\eta = \frac{\left|\int\int E_{ref}^\star(x, y, z = z_0) E_{re}(x, y, z = z^*) \mathrm{dxdy}\right|}{\int\int |E_{ref}(x, y, z = z^*)|^2 \,\mathrm{dxdy} \int\int |E_{re}(x, y, z = z^*)|^2 \,\mathrm{dxdy}} \tag{B.26}$$

. Since the calculated beam profile of the receiver consists of a set of discrete values $E_{i,rec}(x_i, y_i, z_i)$ the surface elements dx and dy are determined by the distance of adjacent points. In this work they are defined as

$$\mathrm{dx}_i = \frac{|x_{i+1} - x_i|}{2} + \frac{|x_i - x_{i-1}|}{2} \text{ and} \tag{B.27}$$

$$\mathrm{dy}_i = \frac{|y_{i+1} - y_i|}{2} + \frac{|y_i - y_{i-1}|}{2} \tag{B.28}$$

The coupling efficiency of an antenna to a Gaussian-beam is called *Gaussicity* and usually refers to the ground mode of a Gaussian beam. In the near-field representation from paraxial optics the Gaussian E-field is given by

$$E_{Gauss}(r) = \hat{e}_{Gauss} e^{-\left(\frac{r}{w(z)}\right)^2} e^{-ik\left(z+\frac{r^2}{2R(z)}\right)+i\arctan\left(\frac{z}{z_R}\right)} \tag{B.29}$$

with vector $\hat{e}_{Gauss}$ representing the polarization, the curvature radius

$$R(z) = z \cdot \left(1 + \left(\frac{z_R}{z}\right)^2\right), \tag{B.30}$$

the beam width

$$w(z) = w_0 \sqrt{1 + \left(\frac{z}{z_R}\right)^2} \tag{B.31}$$

where the amplitude of the transversal profile drops to e^{-1}, the beam waist w_0 which is the smallest beam width and the Rayleigh-length

$$z_R = \frac{\pi w_0^2}{\lambda}. \tag{B.32}$$

The corresponding Gaussicity with the field of interest in the aperture plane can be expressed by

$$\eta_{Gaussicity} = \frac{\left| \int\int \hat{e}_{Gauss} \cdot E_{re}(r,\Phi) e^{-\left(\frac{r}{w(z)}\right)^2} e^{-ik\frac{r^2}{2R(z)}} r\mathrm{d}r\mathrm{d}\Phi \right|^2}{\int\int \left|E_{re}(r,\Phi)\right|^2 r\mathrm{d}r\mathrm{d}\Phi \int\int e^{-2\left(\frac{r}{w(z)}\right)^2} r\mathrm{d}r\mathrm{d}\Phi} \tag{B.33}$$

To determine the Gaussian beam with the highest coupling efficiency both, the amplitude and phase terms, needs to be optimized. It further needs to be regarded that the location of the smallest beam waist of the Gaussian beam and the source of the electric field does not coincide with each other. In this specific case, the antenna on the backside of the lens is placed at the origin of the coordinate system and the optical axis arbitrarily is chosen to be the z-axis as depicted in Fig.B.2. The aperture plane S_a^{lens} is perpendicular to the optical axis and directly attached to the tip of the lens. With a lens of d in thickness this plane thus is located at $z = d$. The origin of the Gaussian beam of interest is shifted in z-direction by an unknown distance z_0. Equation (B.33) needs to be modified accordingly.

It should be noted that the Gaussicity specified here only refers to the coupling efficiency between the receivers' E-field profile with a Gaussian beam either in a far field expression or in the aperture plane of the lens which is the plane directly attached at the end of the lens' concave side perpendicular to the optical axis. The actual coupling efficiency to the receiver additionally includes losses due to back reflections of the impinging beam, losses in the lens' substrate, losses due to impedance mismatch at the antenna's feedpoint with

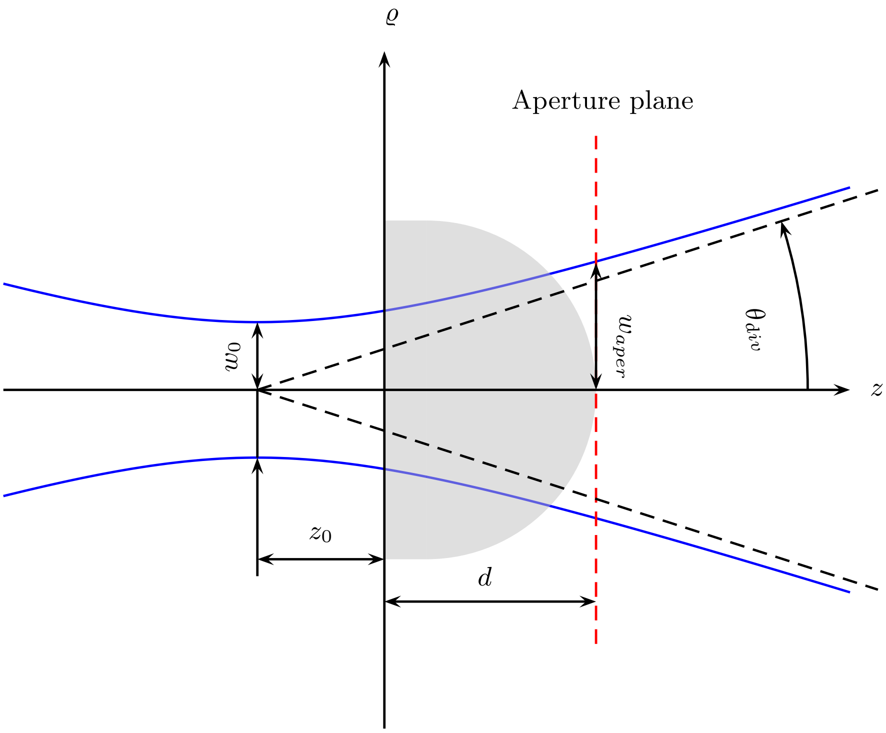

Figure B.2.: Sketch of the chosen coordinate system for the HEB receiver and the related Gaussian beam: The origin of the coordinate system is attached to the center of the backside of the lens. The lens is d thick. The optical axis is in z-direction. The Gaussian beam (blue) of interest is aligned to the optical axis but its origin where it has its smalles beam waist w_0 is shifted from the origin of the coordinate system by z_0. The aperture plane is the plane perpendicular to the z-axis directly at the tip of the lens.

the HEB and any other system losses.

B.4. Characteristics of a lossless, infinitely thin CPW on an infinitely thick dielectric

The here presented calculation follows the calculation ansatz introduced in [56, 123, 122]. Dealing with scenarios like slot regions where physical models already have been introduced for the counterpart, namely strip lines, it is common to replace the slot regions by conducting surfaces, and electrical currents by fictitious magnetic currents. The magnetic currents can be treated analogous to electrical currents. Proceeding in this manner the slot regions of the CPW are replaced by infinitely thin perfectly conducting metal strips with two magnetic current distributions $m(x, y)$ just above and below of each fictitious strip. As the tangent electric field in the actual slots are continuous the magnetic currents in each strip need to have equal amplitudes and opposite signs. Further it is considered that the magnetic currents can be expressed in functional separable longitudinal and transverse terms $m(x, y) = m_x(x) \cdot m_y(y)$ where the transverse magnetic current respects a quasi-static edge-singularity.

$$m_y(y) = \frac{2}{s\pi} \cdot \left(\frac{\Pi(\frac{y}{w+2\cdot s})}{1 - \left(\frac{2\cdot(y+d)}{s}\right)^2} - \frac{\Pi(\frac{-y}{w+2\cdot s})}{1 - \left(\frac{2\cdot(y-d)}{s}\right)^2} \right) \tag{B.34}$$

As depicted in Fig. B.3 w is the width of the inner conducting line and s is the width of the slots of the CPW. The rectangular function Π is given by

$$\Pi(x) = \begin{cases} 0 : |x| \leq \frac{1}{2} \\ 1 : |x| > \frac{1}{2} \end{cases} \quad . \tag{B.35}$$

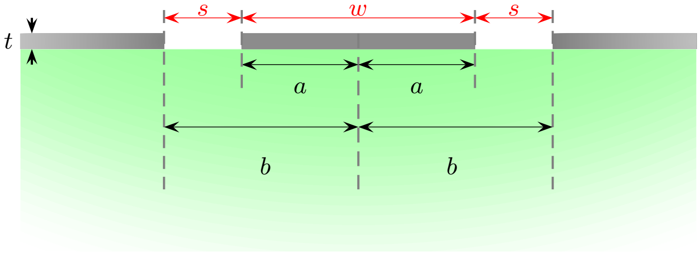

Figure B.3.: Symmetric, coplanar waveguide on an infinitely large dielectric substrate (green). The metal sheet (gray) is infinitely large.

The transverse term $m_y(y)$ is normalized by $\frac{2}{s\pi}$ such that $m_x(x)$ represents the voltage drop between the inner conducting line and the ground planes at any cross section of the CPW. To enforce the total magnetic field to be continuous through the slot axes the problem is formulated as a continuity of magnetic field integral equation (CMFIE)

$$\iint_{\Gamma} g(x - x', -y') \cdot m(x', y') \mathrm{d}x' \mathrm{d}y' = \delta(x), \tag{B.36}$$

where Γ represents the slot region and $g(x, y) = 2 \cdot g_{x,y} + 2 \cdot g_{x,x}$ with $g_{x,y}$ and $g_{x,y}$

are the homogeneous space Green's function of medium 1 and medium 2, respectively. Performing a Fourier transform of the integral equation with respect to the coordinate x the integral equation can be rewritten as

$$\frac{1}{2\pi}\int_{-\infty}^{\infty}\int_{-\infty}^{\infty} M_x(k_x)\tilde{G}(k_x,-y')\cdot m_y(y')\mathrm{dy}' e^{-ik_x x}\mathrm{dk}_x = \frac{1}{2\pi}\int_{-\infty}^{\infty} e^{-ik_x x}\mathrm{dk}_x \tag{B.37}$$

with the Fourier transformed $M_x(k_x)$ and $\tilde{G}(k_x,-y')$ of $v(x)$ and $g(x,y)$ with respect to the variable x, respectively.

Using the fact that the Fourier transform of the transversal magnetic current $M_y(k_y)$ can be related to the Bessel function of zero order J_0

$$J_0(\frac{1}{2}sk_y) = \int_{-\frac{s}{2}}^{\frac{s}{2}} \frac{2}{s\pi}\frac{e^{ik_y y}}{\sqrt{1-\left(\frac{2y}{s}\right)^2}}\mathrm{dy}, \tag{B.38}$$

the space-convolution integral can be introduced as

$$D(k_x) = \int_{-\infty}^{\infty} \tilde{G}(k_x,-y')\cdot m_y(y')\mathrm{dy}' \tag{B.39}$$

$$= \frac{1}{2\pi}\int_{-\infty}^{\infty} G(k_x,k_y)J_0(\frac{1}{2}sk_y)\cdot 4\,sin^2(k_y\cdot y)\mathrm{dk}_y \tag{B.40}$$

where

$$G(k_x,k_y) = \frac{k_1^2-k_x^2}{k_0\cdot Z_{0,free}\sqrt{k_1^2-k_x^2-k_y^2}} + \frac{k_2^2-k_x^2}{k_0\cdot Z_{0,free}\sqrt{k_2^2-k_x^2-k_y^2}} \tag{B.41}$$

is the xx component of the dyadic Fourier transformed of $g(x,y)$. k_0 is the free-space wavenumber, $Z_{0,free} \approx 376.73\,\Omega$ is the free-space characteristic impedance and $k_i = k_0\cdot\sqrt{\epsilon_i}$ with index $i = 1,2$ represents the wavenumber of each semi- infinite medium with relative permittivity ϵ_i. Utilizing furthermore the expression for the zeroth-order second kind Hankel function

$$H_0^2(K\cdot|y|) = \frac{1}{\pi}\int_{-\infty}^{\infty} \frac{e^{-ik_y y}}{\sqrt{K^2-k_y^2}}\mathrm{dk}_y \tag{B.42}$$

the convolution integral can be rewritten as

$$D(k_x) = \sum_{i=1}^{2} \frac{k_x^2 - k_i^2}{sk_0 Z_{0,free}} \left(\underbrace{\int\limits_{2d-s/2}^{2d+s/2} \frac{H_0^2(K_i \cdot |y|)}{\sqrt{1 - \frac{4\cdot(2d-y)^2}{s^2}}} \mathrm{dy}}_{A_i} - 2 \underbrace{\int\limits_{0}^{s/2} \frac{H_0^2(K_i \cdot |y|)}{\sqrt{1 - \frac{4y^2}{s^2}}} \mathrm{dy}}_{B_i} \right). \tag{B.43}$$

K_i is given by $K_i = \sqrt{k_i^2 - k_x^2}$ and $d = (w + s)/2$. It is important to notice at this point that the term within the square root either is a negative or complex number thus offers multiple solutions for K_i. This need to be taken into account when choosing the correct branch in the complex plane for the integrals to obtain a physical reasonable solution. According to [123] the spectral solution for $D(k_x)$ is an excellent approximation whenever $s < 0.2\lambda_d$, where $\lambda_d = \lambda/\sqrt{\epsilon_2}$ relates to the wavelength in the denser medium. In consideration of the fabrication limits of optical lithography which prescribe the slot width of the CPW not to fall below 0.5 µm the inequality relation is still fulfilled at about 10 THz using silicon as substrate material. Assuming a typical dielectric constant of 11.9 for a high resistance silicon wafer the limit for the slot is set to $s < 1.6\,\mu\text{m}$. A representative expression for the voltage drop $V(x)$ is obtained by an inverse Fourier Transform of $V(k_x) = 1/D(k_x)$

$$V(x) = \frac{1}{2\pi} \int\limits_{-\infty}^{\infty} \frac{2}{D(k_x)} e^{-ik_x x} \mathrm{dk}_x. \tag{B.44}$$

In absence of an excitation $D(k_x)$ is zero and leads to the dispersion equation for the x-propagation constant of the CPW

$$-\frac{K_1^2}{K_2^2} = \frac{A_2 - 2B_2}{A_1 - 2B_1} \tag{B.45}$$

For a slot width converging to zero ($s \to 0$) the dispersion equation results to the quasi-static expression of the wavenumber $\beta = \sqrt{(k_1^2 + k_2^2)/2}$. Increasing the width of the slot the wavenumber is approximated by adding a small correction term $k_x = \beta + \Delta k$. The correction term Δk thereby is approximated using the two first terms of the Taylor expansion of $D(k_x)$ around β by $D(k_x) = D(\beta) + D'(\beta) \cdot (k_x - \beta) \approx 0$. This yields the expression $k_x = \beta - \frac{D(\beta)}{D'(\beta)}$ for the complex wavenumber. As the wavelength to slot width ratio chosen for the CPW used in this work can be considerably larger than given in

[123] a higher order expansion additionally is carried out in the following and compared to the results which are obtained for the lower order expansion. The Taylor expansion of third order

$$D(k_x) = D(\beta) + D'(\beta) \cdot (k_x - \beta) + \frac{D''(\beta) \cdot (k_x - \beta)^2}{2} \approx 0 \tag{B.46}$$

solved for the complex wavenumber leads to

$$k_{x,CPW} = \beta - \frac{D'(\beta)}{D''(\beta)} \pm \sqrt{\frac{D'^2}{D''^2} - 2 \cdot \frac{D}{D''}}. \tag{B.47}$$

The solution with the plus sign before the square root represents the wavenumber of interest taking into account following selection procedure. As mentioned before the expression K_i offers several solutions thus there is no unique solution for $D(k_x)$ and V(x). To find the physical meaningful solution it is necessary to make a pole analysis. V(x) depends on quadratic terms of k_x and the square root terms of k_x in the Hankel functions. Thus $V(k_x)$ exhibits poles k_x at different locations of the Riemann sheet. The combinations are listed in table xy. The integration contour of the integrand $V(k_x)$ runs on the real axis of k_x. The subsequent path on the Riemann sheet of the complex expression for k_x needs to be carefully chosen considering the poles. For an asymptotic representation of the currents the integration path is deformed in steepest descent paths through the points $k_x = k_i$ $(i = 1, 2)$. The only pole which is captured by these paths is for the case that $Im(\sqrt{k_1^2 - k_{x,CP}^2}) < 0$, $Im(\sqrt{k_2^2 - k_{x,CPW}^2}) > 0$ and $Im(k_{x,CPW}) < 0$ and therefore leads to the only physical reasonable solution for $D(k_x)$. Applying Cauchy's residue theorem to the integral equation of $V(x)$, it can be separated into different integration terms along the steep descent paths and the residue of the pole

$$V_{CPW}(x) = -i\frac{2}{D'(k_{x,CPW})}e^{-ik_{x,CPW}x}. \tag{B.48}$$

The electrical current flowing in the middle of the CPW conductor line is given by the circulation of the y-component of the magnetic field. The contribution due to the pole is

$$I_{CPW}(x) = \frac{ik_{x,CPW}}{\pi k_0 Z_{0,free}} \sum_{i=1}^{2} \int_{-\infty}^{\infty} \frac{J_0(k_y \frac{s}{2}) sin(k_y \cdot d) k_y}{\sqrt{k_i^2 - k_{x,CPW}^2 - k_y^2}} \int_{d-s/2}^{d+s/2} e^{-ik_y y} dy dk_y\,. \tag{B.49}$$

The characteristic impedance of the CPW associated with the previously calculated complex wavenumber is defined as the ratio between the voltage and current contributed by the CPW mode $Z_c = V_{CPW}/I_{CPW}$. Using B.48 and B.49 the characteristic impedance can be expressed as

$$(Z_c)^{-1} = \sum_{i=1}^{2} \frac{2k_{x,CPW}}{i\pi k_0 Z_{0,free} s} \left(\int\limits_{2d-s}^{2d} \frac{H_0^2(\sqrt{k_i^2 - k_{x,CPW}^2}|y|)}{1 - \frac{4(2d-s/2-y)^2}{s^2}} \mathrm{dy} - \int\limits_{0}^{s} \frac{H_0^2(\sqrt{k_i^2 - k_{x,CPW}^2}|y|)}{1 - \frac{4(s/2-y)^2}{s^2}} \mathrm{dy} \right) . \tag{B.50}$$

B.5. RF-design

B.5.1. Slot antennas

In this work the most important RF-design is based on twin-slot antennas. For a first understanding, at this point, it is useful to look at the behavior of a single slot element that is fed by a port located in the middle between the left and right edge as depicted in Fig. B.4(b). The slot is placed on a semi-infinite silicon substrate with $\epsilon_r = 11.9$. It has a length l that equals the effective wavelength λ_{eff} at frequency $f_1 = 10.7\,\mathrm{THz}$. The impedance measured in the middle of the slot at port has been calculated using the Time domain solver of CST studio suite for a 96 µm squared PEC metal plate on a 70 µm thick, 98 µm squared, lossless silicon substrate ($\epsilon_r = 11.9$). To approximate an infinite substrate, open boundary at all direction except for the interface between the metal plate and vacuum are added, to enable most possible reduction of the reflection at the interfaces.

Similar to a wire antenna - its complementary equivalent -, a single slot offers several resonances related to its harmonics. In accordance with the principle of linear antennas those resonances are the result of standing waves. At the resonant frequency the antenna has its minimum reactance which for an ideal case is zero. The impedance of the slot antenna behaves inversely to the impedance of its counterpart antenna which is to be expected considering Babinet's law. As can be seen in Fig. B.4 the resonance at f_1 (slot length corresponds to a full effective wavelength) exhibits a low impedance over a broad bandwidth whereas the second resonance f_2 (slot length l corresponds to the half wavelength of an operating wavelength that is about twice of λ_{eff}) is a narrow-band but high-impedance resonance. The resonance at f_1 - the one-wavelength resonance- therefore has the advantage of a good power coupling at its feed point with a low impedance load over a quit broad frequency band. In contrast, driving the antenna at the resonance f_2 - the half-wavelength-resonance -, the respective feed impedance needs to be considerably higher than for full-wave resonance for a good impedance matching.

A closer look at the curve of the imaginary part of the impedance shows that it already strongly changes when slightly moving away from the second resonance frequency, whereas it experiences only a slow change around the first resonance frequency. That means that the half-wavelength resonance of a slot is more sensitive to impedance mismatch since any small inductive or capacitive addition results in a noticeable frequency shift understandable as a inductive or capacitive elongation of the antenna.

Placing two slots parallel to each other results into a shift of the antenna impedance at each slot induced by the mutual coupling between the antennas. As depicted in Fig. B.4, the minimum reactance of the dipole resonance $f_{2,d}$ is shifted to higher frequencies whereas it is lowered for the full wave resonance $f_{1,d}$. The overall input impedance at the antenna ports Z_{ant} when being driven in phase is the sum of the self and the mutual impedance of the antenna [63].

Both resonances, the full and the half-wave resonances, are commonly used in twin-slot configurations. In this work an attempt with dipol-slots had been made. The corresponding input impedances at the center of the dipol slots roughly ranges from 100 Ω to 160 Ω. Connecting both dipol-slots to the bolometer via lambda-quarter pieces of CPW-lines with an available characteristic impedance around about 50 Ω yields an impedance at the feeding point of the double-slot antenna around about 50 Ω to 31 Ω. To sufficiently match this impedance by resistance of the bolometer bridge, the width of the bolometer under the given boundary conditions explained in Sec. 3.3 would require a bolometer with a width roughly up to 5 µm which is about the same size as the length of the dipol slot and is inconvenient.

Consequently, all designs are based on antenna slots of about a full effective wavelength in length. Since the impedance curve with frequency at the center of a slot at its full-wave resonance additionally is relatively flat and broad in comparison to the dipol-resonance (see Fig. B.4 the full-wave resonance furthermore enables a more tolerant design as well as an impedance matching over a broader bandwidth. For the ful-wavelength slot designs the characteristic impedances of the CPW-connection lines (chosen according to the selection criteria described in B.5.2 and calculated based on the formalism explained in 3.2.1) roughly ranges from 54 Ω to 41 Ω with an imaginary part smaller than 1.5 Ω for the 10.7 THz design. The impedance at the middle of each slot at the full-wave resonance is about 10 Ω to 20 Ω. Again, assuming that the length of the CPW connecting lines is close to $8\pi/k_c$, in a first approximation the CPW-connections function as lambda-quarter impedance transformers. A rough estimate (using Eq.(3.5)) confirms that the respective feeding point impedance at terminal base of the antenna from 168 Ω to 583 Ω is convenient to connect NbN bolometers which at the same time sufficiently match the antenna impedance and exhibit appropriate dimensions to fit in between the antenna slots (see Sec. 3.3).

Two examples: Influences on the DS-antenna performance

The influence on the feedpoint impedance at the antenna base of a resistive gold-layer instead of a nearly perfectly conducting gold layer is depicted in Fig. B.5(a) exemplary for antenna-design no.5 based on gold sheet resistances which were obtained for the upGreat receiver [16]. As can be seen a higher resistance of the gold layer generally yields an out-smearing of the resonances and leads to a less pronounced maximum for the power transfer at the HEB-antenna interface, a lowering of the port impedance of the antenna and within the expectation range for the resistivity of the gold layers to a very slight shift of the maximum impedance to lower frequencies.

An increasing dielectric constant of the underlying silicon substrate results in a shift of the antenna resonances to lower frequencies what is to be expected as the effective wavelength correspondingly decreases. This effect likewise is depicted for the double-slot design no.5 in Fig. B.5(b). Within the uncertainty of the range which needed to be considered for the dielectric constant before being approximated by measurements (see Chapter 5), the frequency shift in the resonance for the presented designs is about 4 % to 5 %. It should be noted that the shown impact only restricts to the effect on the double-slot antenna itself and does not include the influence of the attached lambda-quarter RF-filter whose performance likewise is affected by a change in the dielectric constant of silicon and certainly would yield to a more pronounced frequency-shift (see Sec. 3.2.2 Eq. (3.4) and (3.5))

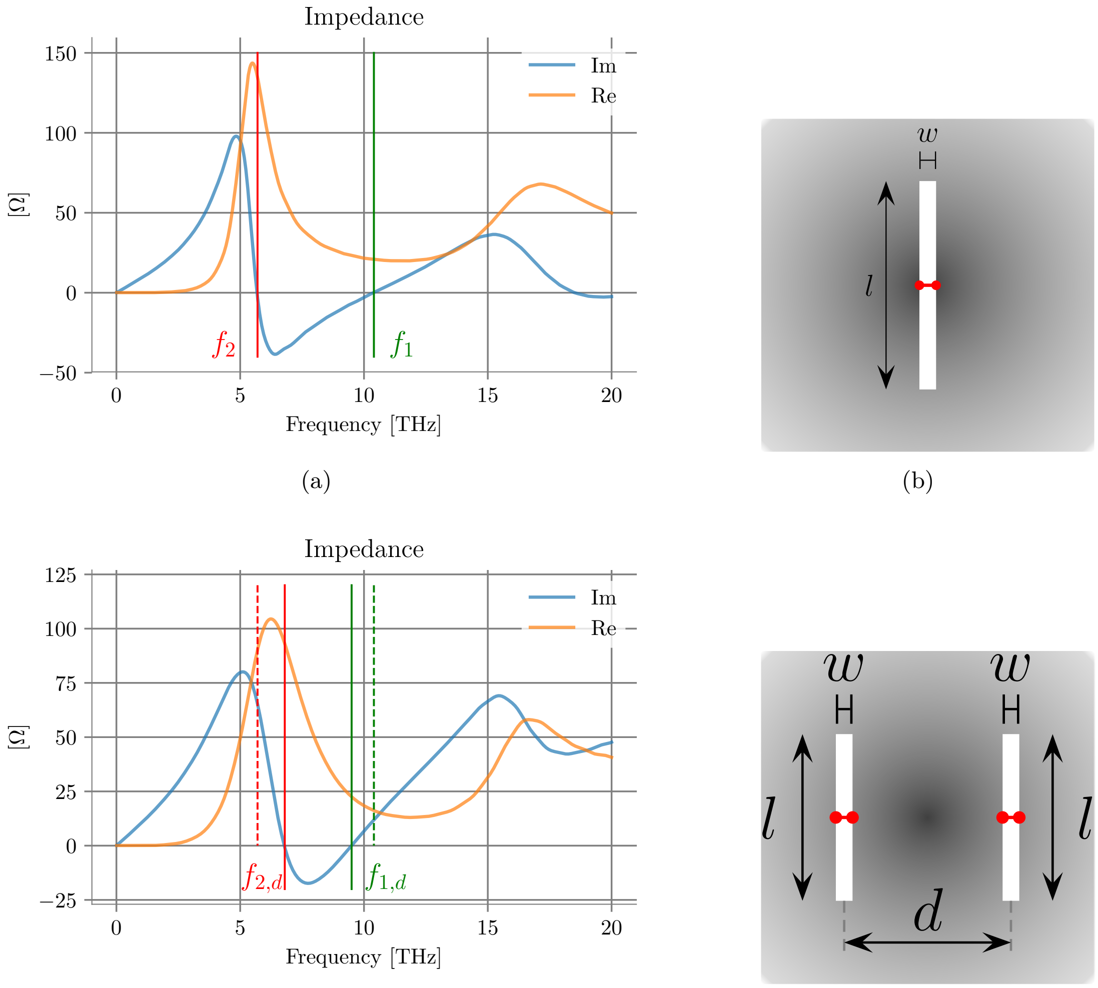

(a) (b)

(c) (d)

Figure B.4.: Frequency dependent impedance courses of a single slot antenna (a) and a double slot antenna (b) at its feeding points located as depicted in (b) and (d), respectively. The slot antennas (considered as perfect electrical conductor) are placed on a silicon substrate. The first and second resonance of the single slot, f_1 and f_2, and of the double slot antenna, $f_{1,d}$ and $f_{2,d}$, respectively, are marked by the vertical lines. The dashed lines in (c) show the positions of the resonances of the single slot. The impedances have been calculated using the Time domain solver of CST studio suite for a 96 µm squared PEC metal plate on a 70 µm thick, 98 µm squared, lossless silicon substrate ($\epsilon_r = 11.9$) with open boundary at all direction except for the interface between the metal plate and vacuum where additional space is added. The open boundary conditions introduce phase matched layers (PML) at the bounding box, which allows that waves can pass the boundary with minimal reflections. For the simulation the minimum distance to the structure is recalculated for each resonance frequency and the center frequency of the whole frequency range. (b) Schematic representation of a single slot line antenna driven by a voltage source placed between the left and right edge in the middle of the slot (red line). (d) Schematic representation of a double slot antenna simultaneously driven by two voltage sources placed between the left and right edge in the middle of the slots (red line).

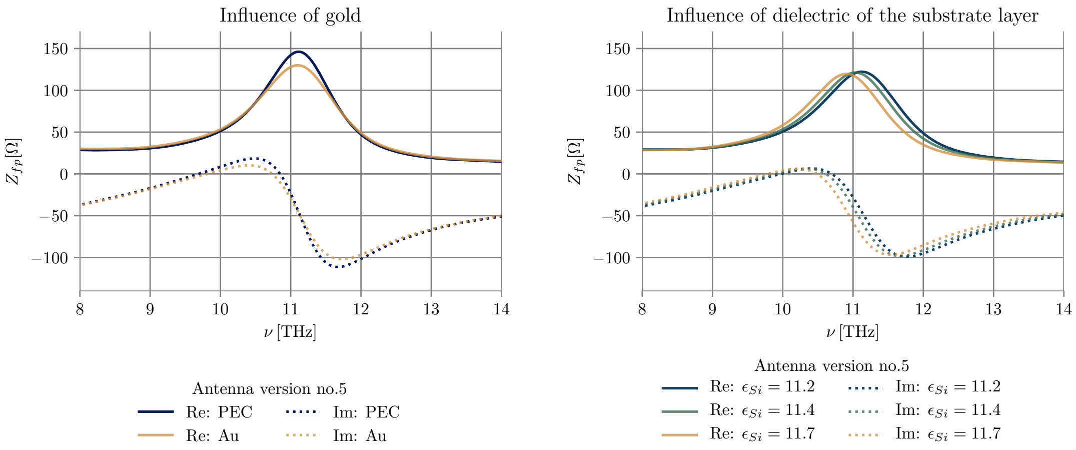

(a) (b)

Figure B.5.: Effect of resistive gold layer (a) and change in the dielectric constant of the substrate layer (b) on the port impedance of the double-slot antenna of design no.5.

B.5.2. RF choke details

The RF-choke is a low-pass filter designed to present a short circuit at the interface between antenna and filter reflecting at the operating frequency. This is a critical interface because the operating frequency of the antenna as well as the beam pattern are sensitive to any non-vanishing capacitive or inductive impedance contributions in the reflectance of the filter. If the RF-choke has a non-vanishing imaginary input impedance at the interface to the antenna slot, it will provoke a shift to lower or higher frequency resonances (depending on its capacitive or inductive character). It furthermore leads to an asymmetric current distribution in the antenna.

The filter components of the RF choke are high and low impedance CPW transmission lines. The minimum and maximum realizable line impedances of a CPW depend on several parameters. The here-used CPWs are chosen according to the following selection criteria:

1. First of all, the width of the inner conduction line of the CPW commonly does not fall below $w_{\mathrm{m}in} = 0.7\,\mu\mathrm{m}$ for both, fabrication reasons and to not increase the conduction losses for the IF signal.

2. Secondly, to prevent that any of the CPW elements forming the filter might be seen as individual little $\lambda/2$ 0r $\lambda/4$ antennas for the incoming signal due to their aspect ratio, the effective widths of the inner conductor line and CPW gap individually, as well as the combination of both are restricted. Effective widths are chosen to be at least 10% to 15% apart from the half-integer or quarter-integer of the wavelength of operation. For a nominal value of $epsilon_{si} = 11.4$ this requires $1.5\,\mu\mathrm{m} \leq w \leq 2.4\,\mu\mathrm{m}$ or $w \leq 1.2\,\mu\mathrm{m}$ or $w \geq 3.2\,\mu\mathrm{m}$.

3. Thirdly, the CPW elements needs to be chosen and combined such that mode-coupling from the CPW propagation mode, the even CPW mode, to the odd, slot line mode is prevented. As the filter is deposited on a $9\,\mu\mathrm{m}$ thick silicon substrate it might be that coupling to TM or TE surface modes is possible in case that the silicon membrane partly is not completely attached to the backside of the silicon lens. Those modes likewise needs to be considered.

During the design process simulations with CST showed that there are considerable losses and shifts of the operating frequency due to high coupling into unwanted modes in the CPW lines even for the smallest slot width. The most promising way of reducing the mode coupling is to reduce the slot size of the CPW lines below the given fabrication limit of $0.5\,\mu\mathrm{m}$ minimum gap width between the inner conductor and flanking ground planes for the desired metalization thickness. Corresponding process[1] development enabled to decrease this limit down to 0.3 µm. The geometrical parameters of the finally chosen high and low impedance CPW lines are summarized in Tab. B.1.

To calculate the characteristic line impedance in CST either a long CPW line made of a perfect electrical conductor on a silicon substrate or a CPW line with a shortened end has been excited by a waveguide port of dimensions following the geometry rules proposed by CST[67].

The geometrical parameters of the finally chosen high and low impedance CPW lines are summarized in Tab. B.1, once calculated with the static and high frequency approach (see Sec.3.2.1) and secondly simulated in CST to draw attention to the effect of radiation losses.

method:	k [m^{-1}]	Z_c [Ω]
high impedance CPW: $w_h = 0.7\,\mu\text{m}$, $s_h = 1.5\,\mu\text{m}$		
static. approx.	$5.610e5$	73.3
h.fr. approx. second order	$6.012e5 - 0.205e5j$	$87.5 + 7.2j$
CST TDS	$5.432e5$	≈ 75
low impedance CPW: $w_l = 2.3\,\mu\text{m}$, $s_l = 0.3\,\mu\text{m}$		
static. approx.	$5.610e5$	33.6
h.fr. approx. second order	$5.865e5 - 0.162j$	$32.9 + 3.3j$
CST TDS	$5.107e5$	≈ 35

Table B.1.: Characteristic impedance and wavenumber of high and low impedance CPWs used for the RF-filter for 10.7 THz. The properties have been calculated based on three different methods: a model with static approximation, a model with high frequency approximation of the second order and using the simulation software CST (see text for detailed explanations). The geometrical parameters belong to the width of the inner conduction line and the slot width of the respective filter-element.

It is obvious that there are discrepancies between the results obtained by the different methods. Although the design of a low-pass filter based on static approximations is possible it is not sufficient to simultaneously design a short-circuit resembling input impedance at the antenna side of the filter. It highlights that the high frequency approximation is mandatory to estimate the imaginary part of the input impedance.

---

[1] performed by Dr. Karl Jacobs

B.5.3. Spatial variations of polarization properties of spiral antennas

The Archimedean and the logarithmic spiral antennas are elliptically polarized. Figure B.6 demonstrates that the tilt angle as well as the axial ratio are clearly directional dependent for all three antenna designs. Especially the side lobes exhibit values which strongly deviate from those of the main beam. It emphasizes the importance of correctly focusing the signals which shall be coupled into the receiver. A detailed look on all orthographic projections for 4.7 THz shows that within the main beam the changes with direction are bearable. For the Archimedean spiral design *S3* and for the logarithmic spiral design *S1/S2* the variation of the axial ratio and of the tilt angle around the main beam direction within the range of the 3 dB beam-widths is less than 0.4 and 7°, and less than 0.2 and 9.3°, respectively. The tilt angle within the 3 dB beam-width of the logarithmic spiral design *S4* is less favorable with regard to a high power coupling to a linearly polarized LO source and experiences changes up to 20° except for a little part at the outer rim. The axial ratio is rather constant over the range with variations smaller than 0.4.

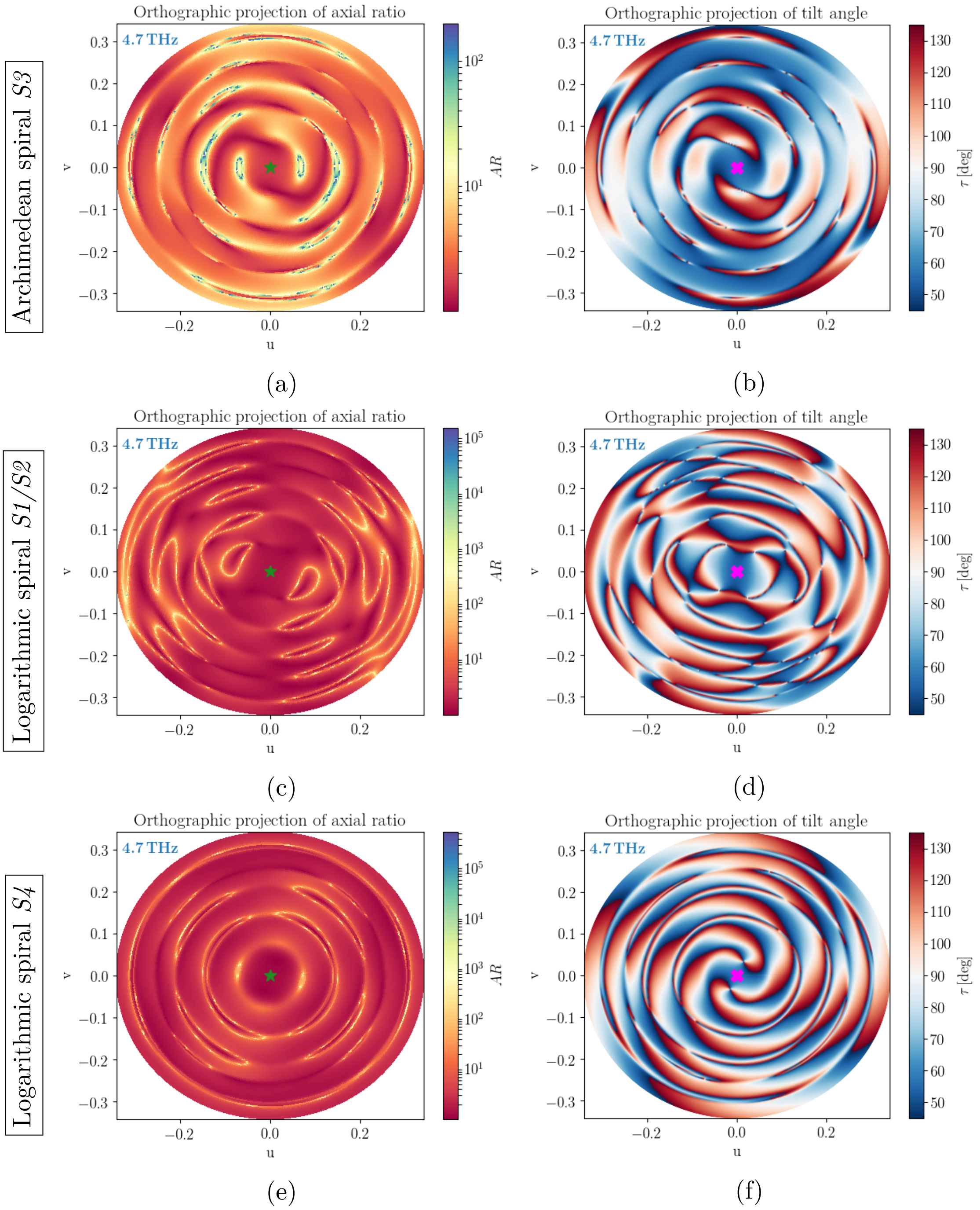

(a) (b)

(c) (d)

(e) (f)

Figure B.6.: Axial ratio and tilt angle calculated from the far field results at 4.7 THz simulated with CST Microwave studio[66] for spiral antenna design *S3* and *S1/S2* by using Eq.(B.21) and (B.24). The antennas are placed on the silicon lens that originally is intended for the 10.7 THz double slot antennas. The orthographic projection (a) and (b) show the axial ratio, the orthographic projections (c) and (d) depicts the tilt angle for the polar angle Θ from −20° to 20°, respectively.

C. Appendix: Determination of material properties at cryogenic temperature

C.1. Material parameters for the description of electromagnetic response

The refractive index, $\hat{n} = n + in'$, of a material is a complex function of wavelength and temperature. Its real part indicates the ratio of the speed of light c in vacuum to its phase velocity in the material of interest [90]. So it determines by which factor the velocity as well as the wavelength of an electromagnetic wave is changed with respect to their values in vacuum. The imaginary part of the complex refractive index is called extinction coefficient and takes account of the losses in the medium leading to an attenuation of the radiation. It is connected to the attenuation coefficient [44] by

$$\alpha = 2n' \frac{\omega}{c}, \tag{C.1}$$

which is a dispersive function due to the multiplicand ω, the angular frequency of the electromagnetic wave. The refractive index is the direct consequence of the polarizability of a material by electromagnetic fields. It is related to the relative magnetic $\mu_r = \mu/\mu_0$ and the relative electric permittivity $\epsilon_r = \epsilon/\epsilon_0$ by[99]

$$\hat{n}^2 = \epsilon_r \cdot \mu_r, \tag{C.2}$$

where μ_0 and ϵ_0 are the magnetic and electric permittivity in vacuum. The polarization response in dielectric materials to an applied alternating field generally lags in phase. Therefore, the electric permittivity is a complex function

$$\epsilon_r = \epsilon_r' - i\epsilon_r''. \tag{C.3}$$

The imaginary part represents a measure for the inherent dissipation of electromagnetic energy in the material for instance due to bound charge and dipol relaxation processes.

Another common representation of the dielectric loss is given by the loss angle δ or the loss tangent $\tan(\delta)$[134] which generally includes losses attributed to free charge conduction σ. It depicts the ratio of the lossy to the lossless counterparts

$$\tan(\delta) = \frac{\omega\epsilon'' + \sigma}{\omega\epsilon'} \tag{C.4}$$

For non-magnetic materials with $\mu_r \approx 1$ the relation between the refractive index and the relative permittivity also called dielectric constant is given by [99]

$$\epsilon_r' = n^2 - n'^2 \tag{C.5}$$

$$\epsilon_r'' = 2nn' \tag{C.6}$$

C.2. Models for the refractive index in semiconductors

The refractive dispersion in pure crystals is dominated by molecular vibrations and rotations for longer wavelengths described by phonon frequencies, and determined by electronic excitations in the vicinity of the optical frequency regime. In semiconductors the effects of point defects further play an important role in their electrical and optical properties [109, 169]. Generally, many components like the type of doping or the manufacturing process can additionally influence the final properties of e.g. silicon [174, 1, 127]. A simple theoretical model for a first insight into the dispersive dielectric properties of a semiconductor in dependence of the angular frequency of the incident radiation ω is provided by the Drude model [127, 174] extended by Lorentz:

$$\hat{\epsilon}_r(\omega) = \epsilon_\infty - \frac{\omega_p^2}{\omega^2 + i\omega/\tau} + \sum_j \frac{s_j}{\omega_j^2 - \omega - i\omega\gamma_j} \tag{C.7}$$

ϵ_∞ is the permittivity at infinite frequency. The Drude term, that is the second term in the dielectric function, accounts for the free conduction carriers considered as point charges and subject to random collisions. The plasma frequency, ω_p depends on the charge density of free carriers N_e with effective mass m and elementary charge e by $\omega_p = \sqrt{\frac{N_e e^2}{\epsilon_0 \epsilon_r m}}$. The damping rate $\Gamma = 1/\tau$ is defined by the average time between a collision τ of free-moving charges. The Lorentz term accounts for the response of bound charges at characteristic angular frequencies ω_j caused for instance by lattice vibrations called phonons or interband transitions. The parameter $s_j = \omega_p^2 f_j$ contains the measure for the strength, f_j, of the corresponding absorption term j. γ_j is the damping rate.

An analytical description of the temperature dependence of $n(\lambda, T)$ of semiconductors commonly is attempted on base of an oscillator approximation either classically treated after Lorentz [109] or extended by connecting the oscillation parameters to the quantities of semiconductor's band model [6, 39]. A solid composed of a series of independent oscillators according to the Lorentz theory exhibits a complex index which can be described by [109]

$$n^2 - n'^2 = 1 + \sum_j \frac{N_j \left(\nu_j^2 - \nu\right)}{\left(\nu_j^2 - \nu^2\right)^2 + \gamma_j^2 \nu^2} \tag{C.8}$$

and

$$2nn' = \frac{1}{\nu} \sum_j \frac{N_j \gamma_j^2 \nu^2}{\left(\nu_j^2 - \nu^2\right)^2 + \gamma_j^2 \nu^2}. \tag{C.9}$$

N_j, γ_j and ν_j are the oscillator strength, the damping constant and the resonant frequency of the $j-$th oscillator, respectively.

The upper of both equations can be simplified in the transparent frequency region, where $n' << n$, to a classical Sellmeier type equation

$$n^2 = 1 + \sum_j \frac{a_j \lambda}{\lambda^2 - \lambda_j^2} + \sum_l \frac{b_l \lambda^2}{\lambda^2 - \lambda_l^2}, \tag{C.10}$$

where the first and second summation contain all contributions from the ultraviolet absorption bands and those from the infrared absorption bands, respectively[109]. λ_j and λ_l are the wavelength of the respective jth and lth oscillation. In the frequency range of interest a further reduction can be obtained considering a negligible effect of free carriers and infrared absorption bands and only accounting for the absorption peak in the closest vicinity of the transparent region. The resulting expression reads[109]

$$n^2 = \epsilon(T) + \frac{A}{\lambda^2} + \frac{B\lambda_1}{\lambda^2 - \lambda_1^2} \tag{C.11}$$

with $\lambda_1 = 1.8703\,\mu\text{m}$ and temperature-dependent parameters

$$A(T) = e^{-3\Delta L(T)/L_{293}} \left(A_0 + A_1 \cdot T + A_2 \cdot T^2\right) \tag{C.12}$$

$$\tag{C.13}$$

and

$$B(T) = B_0 \cdot e^{-3\Delta L(T)/L_{293}} \tag{C.14}$$

and the temperature-related thickness variation $\Delta L(T)/L_{293}$ as defined in Eq. (C.39). The temperature-dependence of A and B stems from the fact that the weighting a_j of each single oscillator is proportional to its density. Since the temperature-dependent change in density directly correlates with the temperature-dependent change in volume, a_j can be related to the temperature using

$$a_j = a_{j,293\,\mathrm{K}} e^{-3\Delta L(T)/L_{293}}. \tag{C.15}$$

The temperature dependence of $\epsilon(T)$ frequently is approximated by a polynomial of third order of form[109]:

$$\epsilon(T) = \epsilon_{0K} + a_1^{eps} \cdot T + a_2^{eps} \cdot T^2 + a_3^{eps} \cdot T^3. \tag{C.16}$$

An alternative formulation to the Sellmeier-type dispersion formula is the Herzberger-type equation[85] used in Edwards [47] to describe the dispersion of silicon at room temperature from 1.12 to 588 µm. It is given by

$$n = A_H + \frac{B_H}{\lambda^2 - 0.028} + \frac{C_H}{(\lambda^2 - 0.028)^2} + D_H \cdot \lambda^2 + E_H \cdot \lambda^4, \tag{C.17}$$
$$\lambda \text{ in } [\mu\mathrm{m}]$$

with constants

$$\begin{aligned} A_H &= 3.41906 \\ B_H &= 0.123172 \\ C_H &= 2.654\,56 \times 10^{-2} \\ D_H &= -2.665\,11 \times 10^{-8}, \\ E_H &= 5.458\,52 \times 10^{-14} \end{aligned} \tag{C.18}$$

where the wavelength λ is in units of micrometers.

By analogy to Eq.(C.8) for $n' << n$ the dispersion and temperature dependence of n can be expressed in terms of energies by [39]

$$n^2 = 1 + E_p^2 \sum_{\vec{k}} \frac{f_{cv}(\vec{k})}{E_{cv}^2(\vec{k}) - E^2}. \tag{C.19}$$

$E_p = \sqrt{N_{osc} h^2 e^2 / m}$ is the electronic plasma energy, where N_{osc} is the number of oscillators per unit volume, and E is the photon energy. $E_{cv}(\vec{k})$ and $f_{cv}(\vec{k})$ refer to the transition energy and the interband oscillator strength between the valence and conduction band, respectively. $\vec{k}$ is the reciprocal lattice vector. Restricted to the infrared and ultraviolet regime terms as done before, the refractive index for a semiconductor such as silicon with indirect gap[1] can be approximated based on a double oscillator model as described in [132, 39, 6] by

$$n^2 - 1 = \sum_{j=\Lambda,\chi} \frac{G_j}{E_j^2 - E^2}, \tag{C.20}$$

where $j = \Lambda, \chi$ refers to the critical points of the Brillouin zone. The critical points are points of high symmetry within the Brillouin zone which is the primitive cell in reciprocal space of the crystal[99]. G_j is the corresponding dispersion parameter which is assumed to be proportional to the oscillator strength $G_j = E_p^2 f_{cv}(\vec{k}_j)$. Similar to the consideration of the classical Lorentz oscillator model, the temperature-dependence can be assumed to be related to the temperature-dependent volume via

$$\frac{dG_j}{dT} = -3 \cdot \alpha_{exp} G_j, \tag{C.21}$$

where α_{exp} is given by Eq.(C.40).

A simplified single oscillator model considers only the average band gap energy E_g with the frequently used, empirical relation of [175]

$$E_g(T) = E_g(0) - \frac{\alpha_g T^2}{T + \beta_g}, \tag{C.22}$$

where $E_g(0)$ is the average band gap energy at 0 K. This empirical relation (C.22) also applies for the gap values E_Λ and E_χ of the corresponding transition energies in the

---

[1] A direct band gap means that both, the lowest energy state in the conduction band as well as the highest energy state in the valence band, is at the same momentum. For an indirect band gap those momentums of the minimal and maximal energy states of the bands differ from each other. In an indirect band gap semiconductor the transition of a valence electron to the conduction band therefore needs both, a photon with energy larger than the bandgap energy and a phonon as momentum needs to be transfered to the crystal lattice.

critical points of the Brillouin zones. The approximation based on a single oscillator model for the real part of the refractive index yields[39]

$$n^2 = 1 + \frac{E_p^2}{(E_g^2 - E^2)} \tag{C.23}$$

A third ansatz which has been used in [121] is based on the Clausius-Mossotti equation[99] that relates the relative permittivity to the polarizability α_{pol}. It is given by

$$\frac{\epsilon_r - 1}{\epsilon_r + 2} = \frac{N\alpha_{pol}}{3\epsilon_0}, \tag{C.24}$$

where $N = N_A \rho_m / M_m$ is the particle density given by the molar mass M_m, the Avogadro constant N_A and the mass density ρ_m. Replacing $\epsilon_r = n^2$ in (C.24) results the Lorentz-Lorenz equation that depicts the respective relation in dependence of the refractive index. Naftaly et al. [121] approximated the temperature-dependent polarizability using an exponential term of form

$$\alpha_{pol} = p_0 + A \cdot (e^{\beta T} - 1), \tag{C.25}$$

with

$$\begin{aligned} p_0 &= 0.7775 \\ A &= 0.000572 \\ \beta &= 0.00636 \end{aligned}$$

which according to their statement gives a good fit for above 70 K but does not describe the temperature-dependence for lower temperatures, where a clearly non-linear course of the dielectric constant is visible (compare Fig. 2 in [121]).

C.3. Frequency Domain Fringe Methods

The transmission spectrum through a plane-parallel plate is characterized by a material-specific interference pattern. To get an impression how the plane-parallel shape of a sample affects the transmission spectrum, some fundamental and simplifying assumptions are made:

1. Firstly, it is assumed that the sample's response to radiation is independent of

polarization.

2. Secondly, the sample consists of a perfectly smooth, plane-parallel plate.
3. The surface areas of the sample's broad faces are considerably larger than the irradiated beam diameter so that any diffraction effects at the sample's faces which are in line with the optical axis can be ignored.
4. The radiation is represented by planar waves with a propagation direction perpendicular to the sample surface.
5. Although in praxis there is only partially self-coherence between the multiple back and forth reflected fractions of a wave in the plate, the transmitted radiation is assumed to be the outcome of wave parts perfectly coherent to each other.

For radiation incident perpendicularly on an interface between two different media of refractive index $\hat{n}_1 = n_1 + i \cdot n_1'$ and $\hat{n}_2 = n_2 + i \cdot n_2'$ Fresnel's equations for the reflection r and transmission t read

$$t_1 = t_{1 \to 2} = \frac{2\hat{n}_1}{\hat{n}_1 + \hat{n}_2} \tag{C.26}$$

$$r_1 = r_{1 \to 2} = \frac{\hat{n}_1 - \hat{n}_2}{\hat{n}_1 + \hat{n}_2} \tag{C.27}$$

The amount of transmittance through a sample of thickness d as illustrated in Fig. C.1 is composed of the radiation which directly goes through the sample as well as those terms of radiation that goes through the sample after being reflected twice, fourth, sixth times and so on at the sample-to-vacuum interfaces. The transmission of an incoming planar wave of amplitude $E_{\text{in}} = |\vec{E_{\text{in}}}|$ thus can be expressed as the square of the sum over all relevant contributions

$$T = \frac{E_{\text{trans}}^2}{E_{\text{in}}^2}, \tag{C.28}$$

with

$$E_{trans} = \sum_m E_{\text{in}} \cdot t_1 \cdot t_2 \cdot A^{1+2\cdot m} \cdot r_2^{2\cdot m}$$
$$\text{and } A = e^{i\cdot\left(\frac{2\pi\nu\cdot\hat{n}_2\cdot d}{c}\right)}.$$

The index m indicates the m^{th} contribution of the $2 \cdot m^{\text{th}}$ times reflected E-field to the total field.

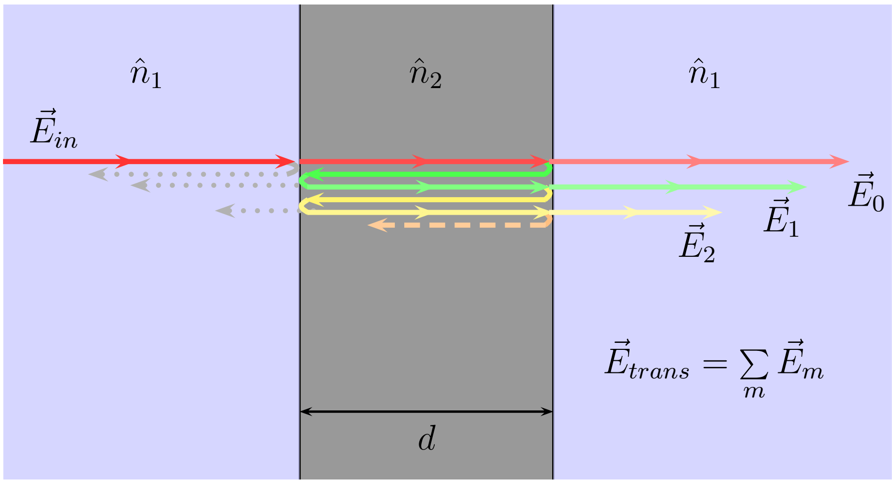

Figure C.1.: Schematic illustration of the contributions to the E-field of a planar wave after the transition through a plane-parallel sample plate with refractive index n_2. The propagation direction of the incoming field is perpendicular to the sample-surface. The transmitted E-field is composed of the radiation directly going through the sample and those parts of the wave which have been reflected for two, four, six and so on times at the sample-vacuum interfaces.

As can be seen from Eq.(C.28) the contributions of the reflected radiation lead to an intricate, dispersive fringing pattern exemplary illustrated in Fig. C.2. The depicted transmission patterns calculated according to Eq.(C.28) portray the development of the transmission spectra when considering an increasing number of field contributions stemmed from reflections. In the absence of reflections (0^{th} order) the transmission spectrum is a smooth function of frequency. Accounting of reflections leads to an dispersively oscillating transmission pattern where the magnitude of local peaks and values converges with increasing the order number m of reflected parts that are considered.

Equation (C.28) directly pinpoints the impossibility to determine the thickness d and the refractive index $\hat{n}$ independently from each other based on a fit with the respective analytical expression. In consequence, the thickness d needs to be specified by independent measurements and most commonly gives the largest contribution to the uncertainty error of the refractive index. Provided that the thickness of a plane-parallel sample is well-known, the refractive index may be estimated on base of the fringes in the transmission pattern generated by the transmission contributions of reflections.

The according transmission function $T(\nu)$ of a sample of thickness d and refractive index $\hat{n}$ with plane-parallel surfaces in vacuum under the assumptions taken above reads[114,

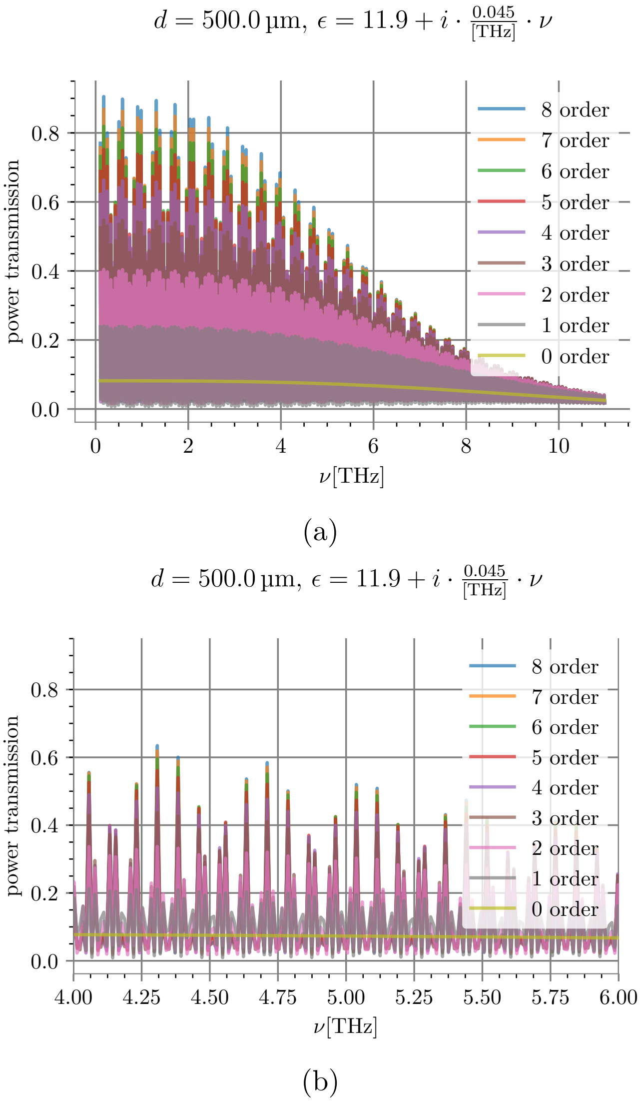

Figure C.2.: (a) Expected transmission (and zoom in (b)) based on Eq.(C.28) through a 500 µm thick plate with a dielectric constant with a non-dispersive real part of $\epsilon = 11.9$ and a linearly dispersive imaginary part $\epsilon' = \frac{0.045}{[\mathrm{THz}]} \cdot \nu$. The transmission is illustrated considering contributions of reflected radiation parts up to different order numbers. The transmission spectrum of 0^{th} order corresponds to the transmission solely obtained by the directly transmitted E-field. The power transmission of order number m additionally contains all contributions due to reflections up to the order of m. In other words, it takes into consideration those parts of the incoming E-field after $2 \cdot l$ times reflection with $l = 0, \cdots m$.

167, 84, 79]:

$$T(\nu) = \frac{\frac{(n^2+n'^2)}{n^2}(1-R)^2 e^{-\alpha \cdot d}}{1 + R^2 e^{-2\alpha \cdot d} - 2 \cdot R \cdot e^{-\alpha d}\cos(\Theta)}. \tag{C.29}$$

The absorption coefficient is given by $\alpha = 4\pi n'/\lambda$ and the phase is $\Theta = 2 \cdot \Phi + 2n\nu\frac{2\pi}{c}d$. The surface reflectance R as well as the phase shift Φ due to internal reflection are functions of the refractive index specified by

$$R = \frac{(1-n^2)+n'^2}{(1+n)^2+n'^2}, \text{ and} \tan(\Phi) = \frac{2n'}{n^2+n'^2-1} \tag{C.30}$$

Inspecting Eq. C.29 it can be seen that as long as the absorption coefficient and by this the extinction coefficient is small enough with respect to the real part of the refractive index, $n' << n$,there are local transmission minima T_{min} and maxima T_{max} at frequencies f_{min} and f_{max} occuring when the cosine of the phase is zero or one, tantamount with

$$\Phi + n \cdot f_{min}\frac{2\pi}{c}d = \pi(m+\frac{1}{2}) \tag{C.31}$$

$$\Phi + n \cdot f_{max}\frac{2\pi}{c}d = \pi m, \tag{C.32}$$

where $m = 0, 1, 2, \ldots$ is the order of the fringe. The fringe order is given by $m = \frac{2d}{c}\int_0^{\nu_a} n(\nu')\mathbf{d}\nu'$ which means that the fringe of order 1 refers to the frequency ν_a whose wavelength equals a round-trip in the sample and gives the first local maximum in the frequency spectrum due to interference of the directly transmitted wave-part with those wave-part being reflected twice at the vacuum-sample interface and all multiple internal reflections which constructively superimpose. If Φ and m are known, the refractive index may be deduced from both equations for the corresponding frequencies f_{max} and f_{min}. In this work this method of extraction is referred to as the *fringe-order method.*

Assuming that the refractive index is varying only very slowly between neighboured maxima or minima the expression to find the refractive index between the m^{th} and $(m+1)^{th}$ order fringe can be simplified to

$$n \cdot (f_{(m+1),max} - f_{m,max})\frac{2\pi}{c}d = \pi \tag{C.33}$$

However, if there is a substantial change in the refractive index in between two neighbored extrema, the result contains systematic errors. Following the notation of [27] using Eq.(C.33) to determine the refractive index is called the *fringe-difference method.* A more detailed view about fringe-based extraction techniques and their systematic errors can be found in [27], [97],[138],[81], [22], [167]. [2]

For the detailed analysis of the refractive index of silicon both fringe-based methods were applied and compared in Section C.4.2.

To extract the imaginary part of the refractive index, Eq. C.29 can be further simplified neglecting terms with n'^2 since $n' << n$ is to be expected over the frequency range of interest. It yields

$$T(\nu) = \frac{(1-R)^2 e^{-\alpha d}}{1 + R^2 e^{-2\alpha d} - 2Re^{-\alpha d}\cos(\Theta)}, \text{ with} \tag{C.34}$$

$$R = \frac{(1-n)^2}{(1+n)^2}. \tag{C.35}$$

Following again the same principle as before by looking at local extrema for the transmission the equation can be expressed as

$$e^{-2\alpha d} - \frac{(1-R)^2 + 2 \cdot R \cdot a \cdot T_a}{T_a R^2} e^{-\alpha d} + T_a = 0, \tag{C.36}$$

where $a = 0, \pm 1$ according to if it is an inflection point, a maximum or a minimum in the transmission. The solution of the quadratic equation[3] is of the form

$$e^{-\alpha d} = \frac{(1-R)^2 + 2 \cdot R \cdot a \cdot T_a \pm \sqrt{((1-R)^2 + 2 \cdot R \cdot a \cdot T_a)^2 - 4T_a^2 R^2}}{2T_a R^2} \tag{C.37}$$

Since the absorption coefficient and the thickness of the sample in the equation occur together in the form of a product, it is easy to see that the uncertainty of the absorption coefficient extracted by this equation largely depends on the accuracy of the measured sample's thickness. In contrast to the real part of the refractive index the absolute magnitude of the spectrum amplitude plays an essential role for the determination of the absorption and extinction coefficient and thereby predisposed this extraction method particularly towards instabilities of the power source and partial incoherence between multiple reflections inside the sample. An estimate of the influence of non-perfect coherence in the sample's Fabry-Perot interference on the transmission spectrum can be done by introducing a frequency-dependent coherence factor g. It equals one for perfect coherence and zero in case of no coherence between multiple internal reflections among

---

[2] It should be noted that in literature the interference spectrum and the corresponding fringe methods frequently are referred to as channel spectrum and channel spectrum methods.

[3] The evaluation of the frequency specrum in this work is mainly based on the local maxima. Here the quadratic solution with the "-"-sign needs to be applied as can be seen by the distinction of cases and the consideration that the absorption coefficient should be zero for a fully transparent sample.

each other and between reflections with the incident beam. The factor g can be thought as the coherence of the ith and $(i \pm 1)$th reflection introduced by a phase-front distortion during a back-and-forth trip. The according coherence of the ith and $(i \pm m)$th reflections is g^m. Following the notation of [73] an analytic expression for the partially coherent transmittance of a dielectric lamellae is given by

$$T = \frac{16\left(n^2 + n'^2\right) e^{-2 \cdot b'}}{\left[(n+1)^2 + k^2\right]^2} \left(\frac{1 - g^2|a|^2}{1 - |a|^2}\right) \frac{1}{1 - g \cdot (a + a^*) + g^2|a|^2}, \tag{C.38}$$

where

$$a = R^2 e^{2 \cdot i \cdot \beta},$$

$$a + a^* = \frac{2\left[\left(n^2 + n'^2 - 1\right)^2 - 4n'^2\right] \cos\left(2 \cdot b\right) - 8n'\left(n^2 + n'^2 - 1\right) \sin\left(2 \cdot b\right)}{\left[(n+1)^2 + n'^2\right]^2},$$

$$|a|^2 = e^{-4b'} \frac{\left[(n+1)^2 - n'^2\right]^2}{\left[(n+1)^2 + n'^2\right]^2}$$

and

$$\beta = b + i \cdot b' = \frac{2\pi}{c}\left(n + i \cdot n'\right) \cdot d \cdot f$$

Figure C.3 depicts the development of a transmission spectrum with the introduction of partial coherence according to the indicated, analytical formula for an exemplary dielectric sample with a non-dispersive refractive index. It demonstrates that a decreasing coherence between involved beam parts leads to a decrease of constructive and destructive superpositions within the dielectric lamellea. The result are peaks with lower amplitudes and higher vales while the actual frequency positions of the extrema virtually are unaffected. In case of no coherence, $g = 0$, the interference pattern in the transmission spectrum vanishes. As long as the contrast in the oscillating spectrum amplitude is sufficiently high to depict the fringe rate, a non-perfect coherence thus has a negligible effect on the extraction of the real part of the refractive index on base of the fringe methods. A precise determination of the imaginary part of $\hat{n}$, however, is significantly limited by partial coherence effects.

In general one needs to be aware that a drawback of extracting n' by FTS transmission measurements is that the intensity amplitude is prone for additional error sources. It can be easily influenced by power fluctuations of the radiation source[73] during a sample and reference measurement, internal reflections in the spectrometer, borderline signal-to-noise ratio in the recorded frequency regime or scratches and other little defects on the sample surface [111, (Sec.C.)].

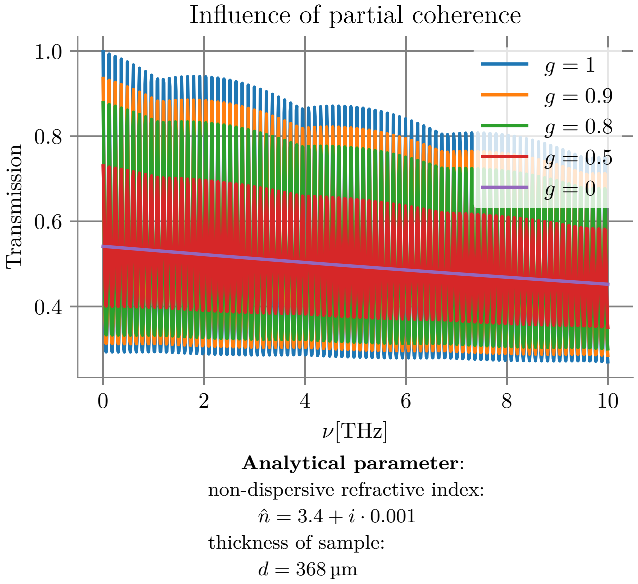

Analytical parameter:
non-dispersive refractive index:
$\hat{n} = 3.4 + i \cdot 0.001$
thickness of sample:
$d = 368\,\mu\text{m}$

Figure C.3.: Transmission spectra for different degrees of partial coherence of the multiple reflections in a Fabry-Perot etalon among each others and with the incident radiation. The transmission spectrum is calculated according to Eq.(C.38) for an exemplary plane-parallel, dielectric sample of a certain thickness and a non-dispersive refractive index specified in the graph. The coherence factor g indicates the degree of coherence and ranges from 1 (perfect coherence) to 0 (no coherence).

C.4. Data processing

C.4.1. Fit procedure of local extrema

The detection and determination of local extrema is the basis for the extraction of the refractive index by means of fringe methods which belong to the simplest set of possible methods for the determination of n. The accuracy in the determined frequency locations of the minima and maxima directly influences the accuracy of the resultant refractive index. It thus requires a spectral resolution fine enough to sufficiently depict all alterations in the transmission course as well as a suitable smoothing and fitting of the extrema to encounter unpreventable discretization errors as illustrated in Fig. C.4.

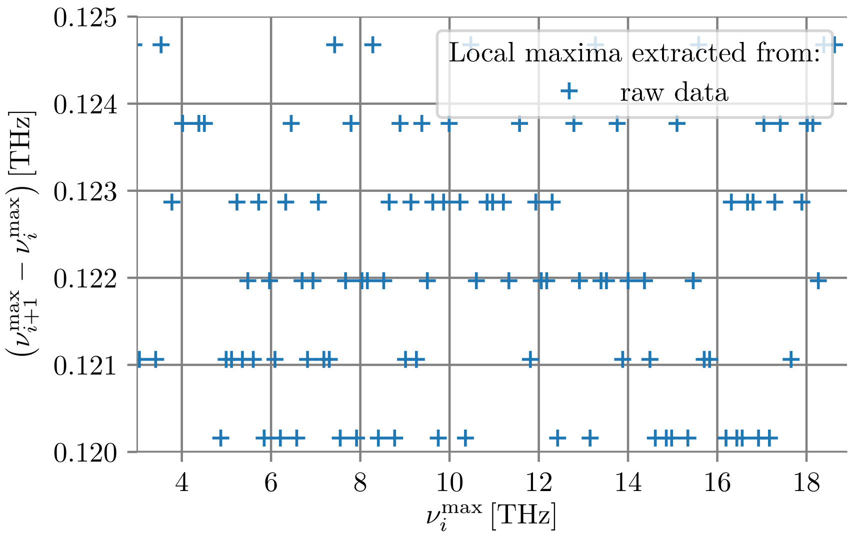

Figure C.4.: Distance in frequency between neighboured local maxima $T_{i+1,max}$ and $T_{i,max}$ in dependence of the frequency position of the maximum at $\nu_{i,max}$. As the spectrum is composed of discrete data points local intensity extrema directly determined from the raw data exhibit a systematic error within the size of ± one discrete frequency step. Hence, the distances in frequency between neighboured maxima or minima as well can only take discrete values as can be seen from the distribution of the blue crosses in the plot.

To determine the actual local minima and maxima of the interference fringe spectrum each hill and vale is first interpolated with a cubic spline function. By this the density of data points is artificially increased while preserving existing data points. Subsequently, a Savitzky-Golay filter of polynomial order 3 is applied for smoothing[4]. The window size over which the polynomial is applied by the method of linear least squares encompasses about 15% of the overall data points till each of both adjacent extrema, respectively. The final maximum or minimum is given by the extremum of the smoothed cubic spline and determined by a peak-finding function. An example of a fitted fringe pattern is shown in Fig. C.5. The impact of the data processing on the extraction of the local extrema is depicted in Fig. C.6.

It can be clearly seen that the fitting procedure is mandatory as due to the discrete distances between frequency points in the raw data the intensity extrema in between systematically are missed leading to frequency distances between neighboured extrema

---

[4] The Savitzky-Golay filter has the advantage that the locations of local extrema are preserved.

which apparently also can only take discrete values as already shown in Fig.C.4. A careful analysis of the extrema is however important as constituting the basis for all subsequent calculations concerning the refractive index and the absorption coefficient. Nevertheless, it should be noticed that the largest contribution to the error range is given by the uncertainty of the measured sample-thickness.

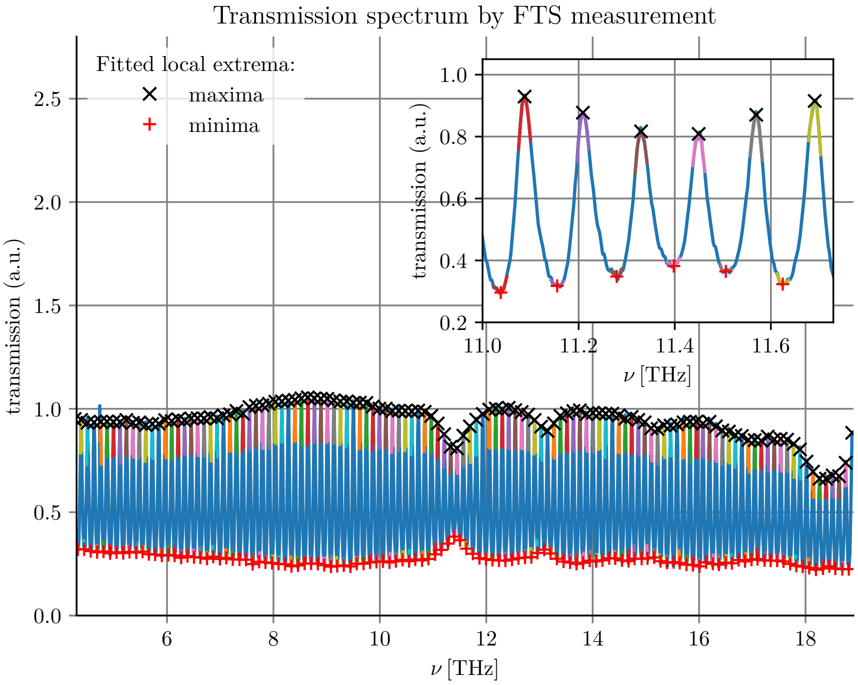

Figure C.5.: *Transmission spectrum measured with an FTS* with marked local extrema determined by the fitting procedure: The original transmission curve (blue line) is interpolated by a cubic spline function and smoothed around the extrema with a Savitzky-Golay filter by a polynomial of order 3 over a window length encompassing about 15% of the overall data points till the next extrema. The fitted polynomials over the according window sizes are displayed as colored curves drawn over the transmission spectrum as can be seen in greater detail in the enlarged section in the inset.

C.4.2. Refractive index

The real part of the refractive index was calculated on base of both fringe methods described in Appx. C.4. As can be seen in Fig. C.7 the fringe order method yields a much smoother course of the refractive index than the fringe difference method and additionally offers distinctly smaller fluctuations due to systematic discretization errors. It highlights that the fringe difference method is already prone towards small variations

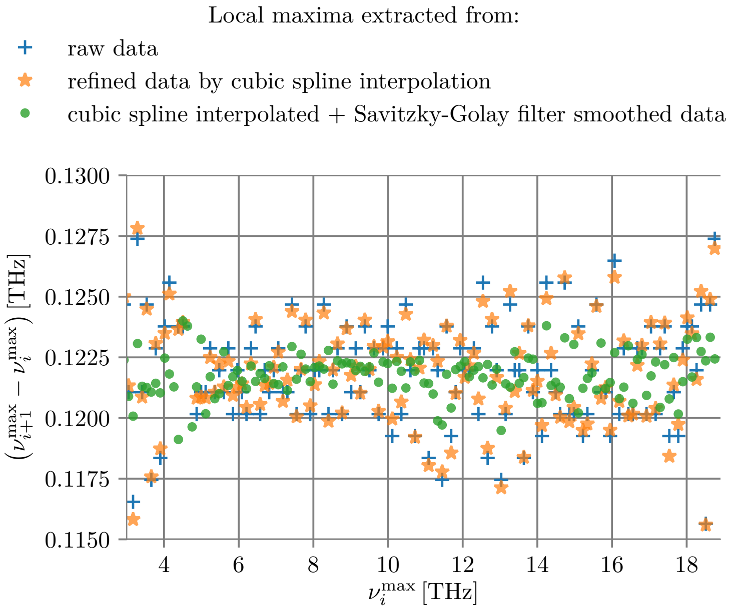

Figure C.6.: *Effect of the data processing on the locations of local extrema:* The plot shows the distance in frequency between neighboured local maxima $T_{i+1,max}$ and $T_{i,max}$ of the spectrum given in Fig.C.5 in dependence of the frequency position, $\nu_{i,max}$, of the maximum. Local intensity maxima extracted from the raw data exhibit a systematic error based on the resolution of the spectra within the size of ± one discrete frequency step. This error is propagated to the calculated distances in frequency between neighboured maxima or minima, here displayed as blue crosses, which consequently can only take discrete values. Although the refinement by a cubic spline function tackles the issue of discretization (orange stars), it can be clearly seen that the last step of the data processing, the smoothing of the refined data by a Savitzky-Golay filter, is effective to further reduce the spread in the distribution of the distance values (green dots).

in the real part of the refractive index with frequency. Since the measured frequency spectrum extends to sufficient low frequencies to enable an adequate estimation of the fringe order, the fringe order method proves to represent the firmer and more accurate method in the present case which is consistent with the results of [27]. In addition, the refractive index calculated on the unprocessed raw data shows a larger spreading of and a restriction to discrete values for n and clearly demonstrates the importance of a careful interpolation and smoothing procedure. This is especially true for the data obtained in the *Bruker IFS 66v/S* FTS (see Fig.C.7 (c)) as it provides a notedly lower resolution about seven times lower than those of our in-house enhanced FTS.

To determine the development of n with temperature in the range of interest n is averaged from 7.5 THz to 12.5 THz. The according refractive indices are depicted in Fig. C.8. It can be seen that the fringe difference method tends to yield larger values then the fringe order method. With both methods a clear decrease in n with lower

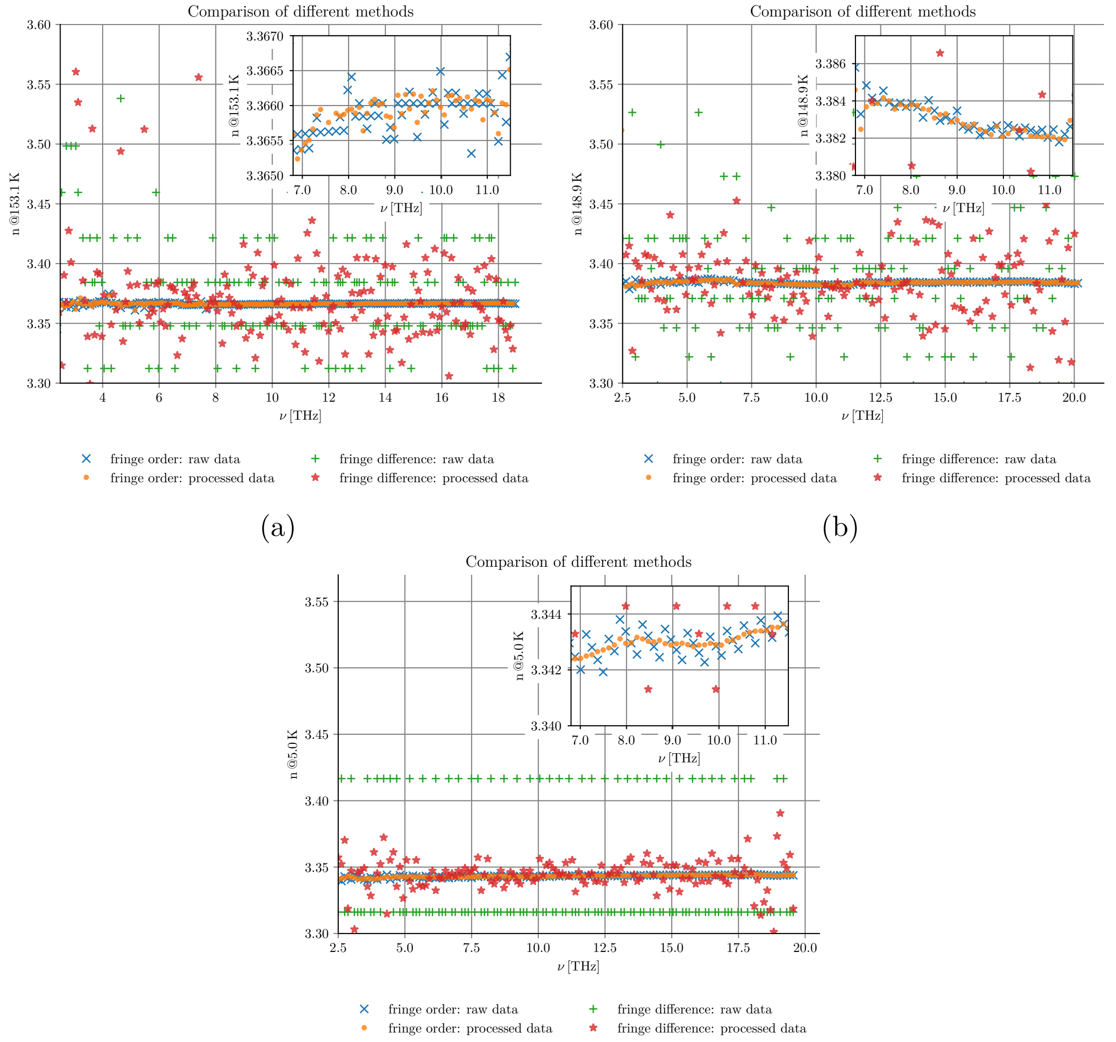

(a)

(b)

(c)

Figure C.7.: Refractive index calculated with both, the fringe difference and the fringe order method, once based on the raw data and once based on the processed data for measurements of different silicon samples with different FTS. Silicon sample no.4 (a) with a thickness of about 533 µm and silicon sample no.2 (b) with a thickness of about 363 µm have been measured in the new setup (Sec.5.1.1) with a nominal resolution of 2.3 GHz. Silicon sample no.5 with a thickness about 368 µm have been measured in a dedicated setup by Philipp Warzanowski with a nominal resolution of 15 GHz.

temperatures is visible. For the sake of clarity subsequent calculations corresponding the relative changes in the quantities of interest are restricted to values obtained by the fringe order method.

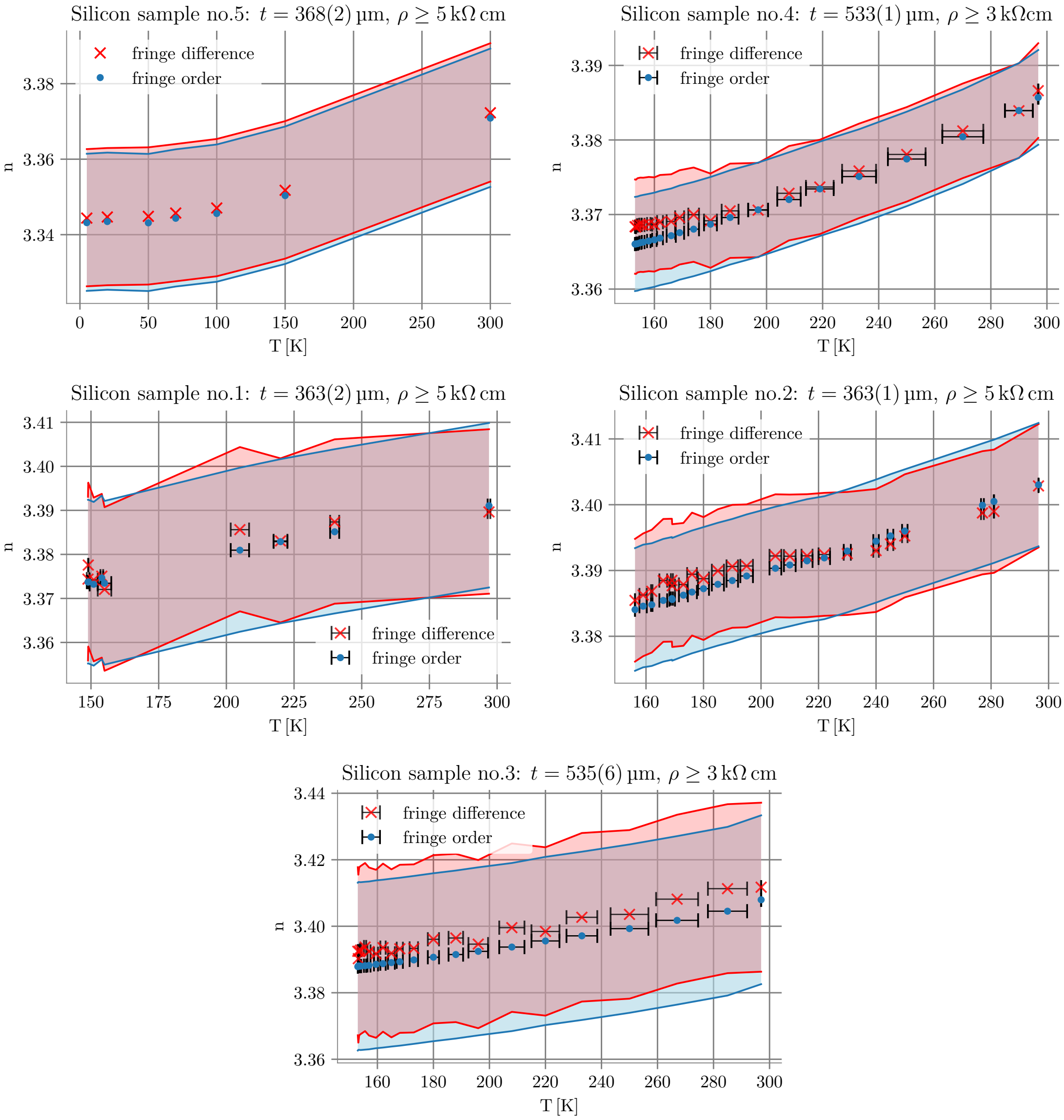

Figure C.8.: Temperature-dependent refractive indices of different Si samples calculated using two different methods, the fringe order and the fringe difference method.

C.4.3. Extinction and absorption coefficient

The extinction and absorption coefficients, n' and α, have been calculated on base of the model described in Appx.C.3 which includes the effects of partial coherence between multiple reflections and directly transmitted radiation inside the sample.

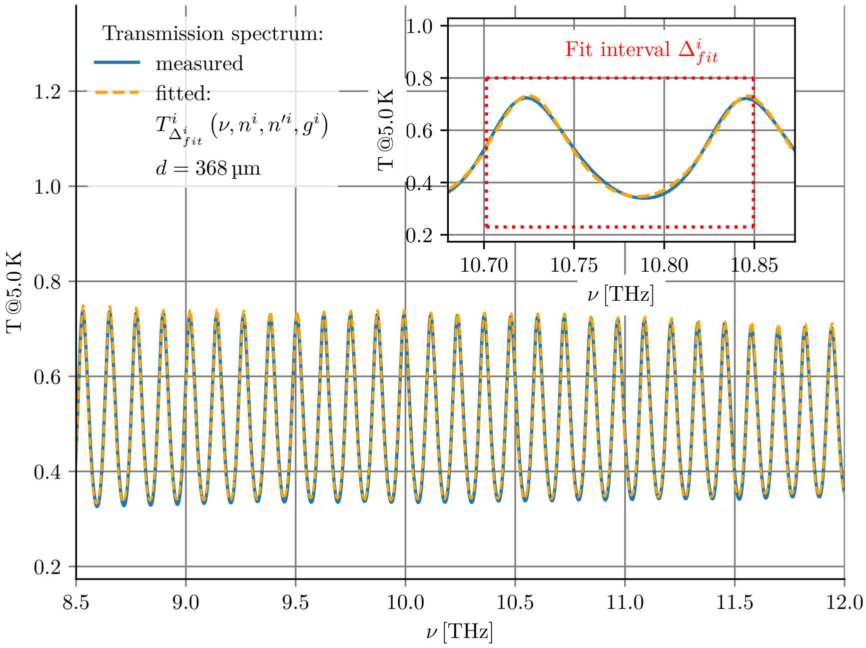

Figure C.9.: Fit of the transmission spectrum of silicon sample no.5 at 5 K assuming a sample thickness of 368 µm. The fit function $T^i_{\Delta^i_{fit}}\left(\nu, n^i, n'^i, g^i\right)$ is given by Eq.(C.38). The fit parameters n^i, n'^i, g^i are considered to be constant within the corresponding fit interval i of width Δ^i_{fit}.

As depicted in Fig.C.9 the absorption and the respective extinction coefficient are extracted by a piecewise, non-linear least-square fit over distinct frequency intervals of the smoothed transmission spectra by the expression given in Eq.(C.38). Within each fit interval i of width Δ^i_{fit} the fit-parameters n^i, n'^i and g^i are considered to be constant. The width of the fit intervals is set to 150 GHz and corresponds to 55 data points.

The extracted coherence factors depicted in Fig. C.10 show a steady, nearly linear decrease with frequency similar to what has been observed in Grossman et al. [73]. A plausible explanation for the dispersive behavior are little thickness fluctuations of the sample. Spatial incoherence produced by thickness variations of the plate would lead to a progressively stronger phase distortion of the multiple reflections the higher the frequency is and results in an increasing loss of coherence with increasing frequency[73].

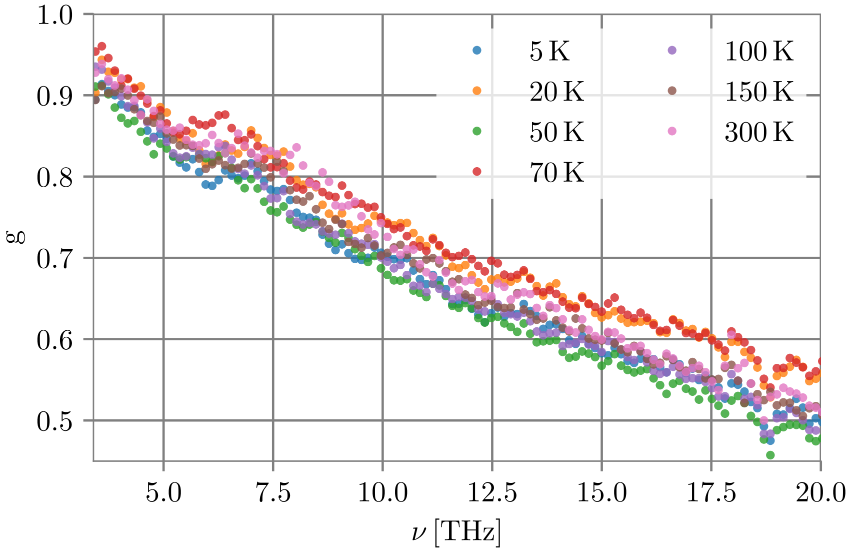

Figure C.10.: Coherence factor g for different temperatures extracted from a piecewise fit of the transmission spectra of sample no.5 with $T^i_{\Delta^i_{fit}}\left(\nu, n^i, n'^i, g^i\right)$ (see Eq.(C.38)). The coherence factor is assumed to be constant within frequency intervals of $\Delta^i_{fit} = 150\,\mathrm{GHz}$ width.

C.5. Thickness variation due to temperature change

When cooled down all silicon samples undergo a temperature-dependent change in thickness [118]. To calculate the expected thickness variation of the sample-plates I used proposed dataset given by [125] to estimate the thermal expansion coefficient α and the according thickness variation related to the thickness measured at room temperature (293 K) via:

$$\frac{\Delta L}{L_{293\,\mathrm{K}}}(T) = \int_{293}^{T} \alpha \mathrm{dT} \tag{C.39}$$

$$\begin{aligned}\alpha(T) = \Bigg[& \left(4.8e - 5 \cdot T^3 + (a \cdot T^5 + b \cdot T^5.5 + c \cdot T^6 + d \cdot T^6.5 + e \cdot T^7) \cdot \frac{1.0 + erf(T-15)}{2}\right) \\ & \cdot \frac{(1.0 - erf(T-52)) \cdot 0.2}{2} \\ & + \left((-47.6 + f \cdot (T-76)^2 + g \cdot (T-76)^3 + h \cdot (T-76)^9) \cdot \left(\frac{(1.0 + erf(T-52)) \cdot 0.2}{2}\right)\right)\end{aligned}$$

	Fitparameter
a	$1.005e-05$
b	$-5.9988e-06$
c	$1.25574e-06$
d	$-1.12086e-07$
e	$3.63225e-09$
f	$2.67708e-02$
g	$-1.22829e-04$
h	$1.62544e-18$
i	$4.72374e+02$
j	$-3.58796e+04$
k	$-1.24191e+07$
l	$1.25972e+09$

Table C.1.: Fit parameter corresponding to Eq.(C.40)

$$\cdot\frac{(1.0-erf(T-200))\cdot 0.1}{2})$$

$$+\left((i+j/T+k/T^2+l/T^3)\cdot\frac{(1.0+erf(T-200))\cdot 0.1}{2}\right)\Bigg]\cdot[10^{-8}\mathrm{K}^{-1}] \tag{C.40}$$

As can be seen from Fig.C.11 silicon contracts when being cooled down until reaching a temperature of about 124 K and extends again for lower temperatures. The variations in the effective thickness of the samples expected due to the temperature changes are taken into account for the calculation of the refractive index based on fringe methods.

C.6. Impact of temperature-related thickness variation: Estimation by tracking of individual local extrema

As can be seen in Fig.C.12 , the spectra of all samples reveal following temperature-dependent behaviour: The local extrema of each sample-spectrum move to higher frequencies when the sample is cooled down and vice versa. As a result of the temperature-dependent change in thickness of the samples this is to be expected. However, also a change in the dielectric constant of the material affects the positions of the extrema. Due to the measurement uncertainties of the sample-thickness at room temperature and the lack of information about the thickness at various temperatures a distinction between both effects purely from measurement data is impossible. However, using eq.(C.40) to approximate the thickness variation of the samples, the data from samples no.2 to no.4[5]

---

[5] For the cooling cycle of sample no.1 the continuous switch between sample and reference measurement yielded variations of the effective sample thickness due to slightly different tilting angles. The resulting

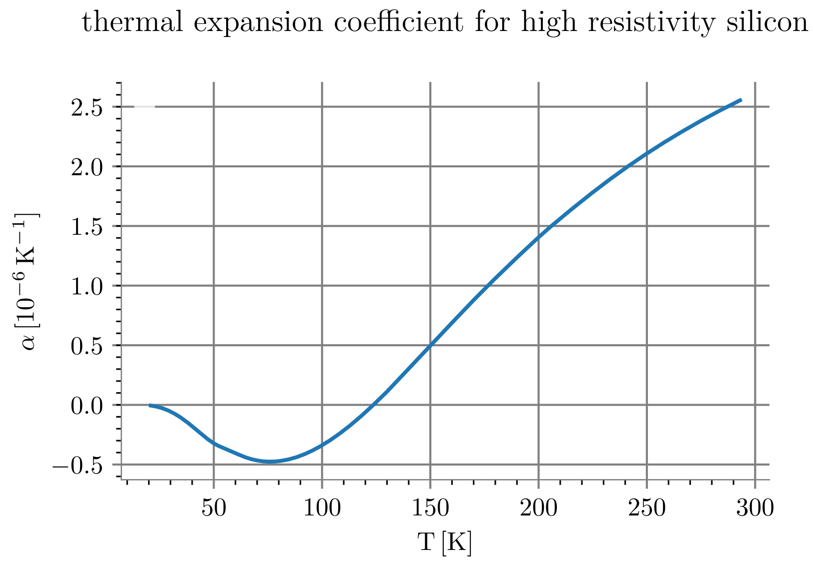

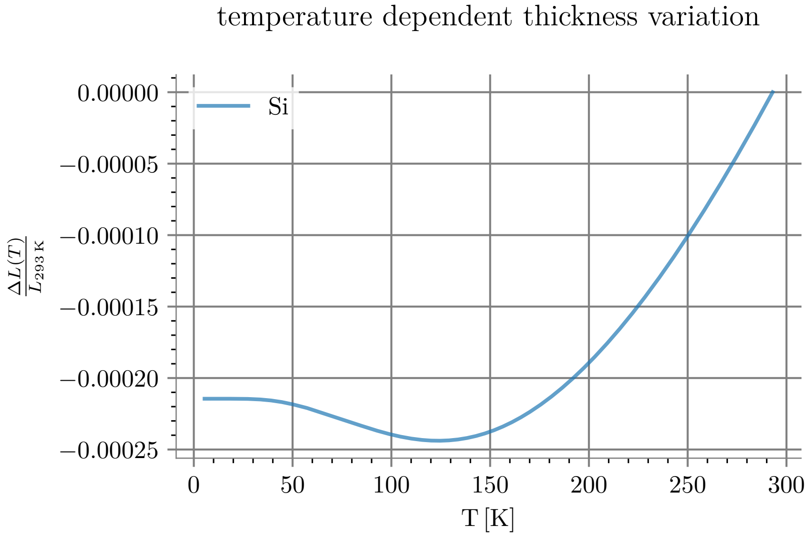

Figure C.11.: The thermal expansion coefficient is calculated on base of the NIST databanc fitparameter (see Eq.(C.40) and Tab.C.1). The temperature-dependent thickness variation refers to the initial thickness at room temperature (293 K).

can be used to estimate which of both effects dominates. Eq.(C.32) relates the frequency positions of a maxima i due to a temperature change from T_1 to T_2 by

$$n_{i,T_1} \cdot \nu_{i,T_1} \cdot d_{i,T_1} = n_{i,T_1} \cdot \nu_{i,T_1} \cdot d_{i,T_1},$$

---

shift of the interference fringe pattern makes this measurements unsuitable for the mentioned analysis.

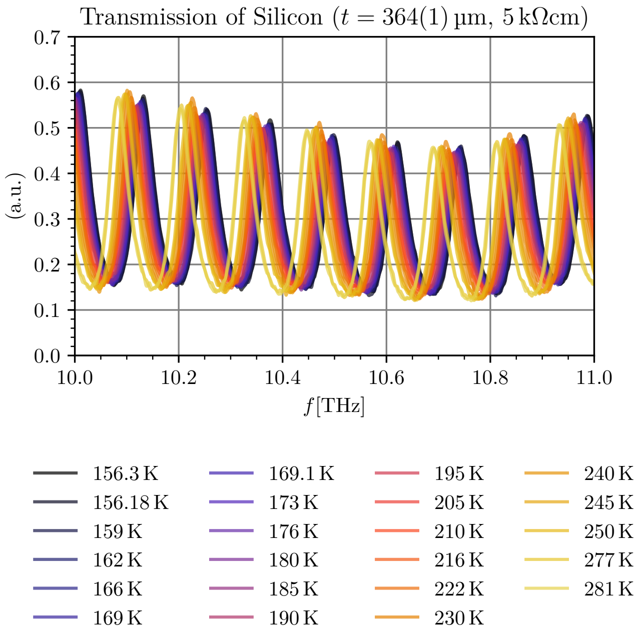

Figure C.12.: Zoom into the transmission spectra of a 364 µm thick, high-resistivity silicon plate for different temperatures. The local extrema arising from interference phenomena of the plane-parallel plate surfaces move to higher frequencies when the sample is cooled down and vice versa.

predicting a relative frequency change about

$$\frac{\nu_{i,T_2} - \nu_{i,T_1}}{\nu_{i,T_1}} = \frac{1}{\Delta L}\frac{n_{i,T_1}}{n_{i,T_2}} - 1, \quad \text{where} \qquad \text{(C.41)}$$

$$\Delta L = \cdot(1 - \int_{T_1}^{T_2} \alpha)$$

The ratio of the refractive index at different temperatures subsequently is given by the product of the inverse ratio of the frequency values of the i^{th} extreme with the relative variation in thickness:

$$\frac{n_{i,T_1}}{n_{i,T_2}} = \frac{\nu_{i,T_2}}{\nu_{i,T_1}} \cdot \Delta L \qquad \text{(C.42)}$$

Based on these equations, an initial estimate of the magnitude in frequency shift due to thickness-variations reveals that the effect is insignificant as long as the change of the refractive index is small. Assuming a change in temperature from 293 K to about 153 K according to eq.(C.40) leads to a relative change in the sample-thickness about approximately $\Delta L = 0.999765$. The corresponding normalized frequency shift is $\frac{\nu_{i,153}-\nu_{i,293}}{\nu_{i,293}} = 1.000235 \cdot (\frac{n_{i,293}-0.999765 n_{i,153}}{n_{i,T_2}})$ and the change in the ratio of the frequency values of the i^{th} extremes is about $\frac{\nu_{i,153}}{\nu_{i,293}} = 1.000235 \frac{n_{i,T_1}}{n_{i,T_2}}$. For a constant refractive index this would result into a frequency shift about $\frac{\nu_{i,153}-\nu_{i,293}}{\nu_{i,293}} = 0.000235$ or a ratio about $\frac{\nu_{i,153}}{\nu_{i,293}} = 1.000235$. The actual measured frequency shift and frequency ratio, however as depicted in Fig. C.13 and C.14, is about one order of magnitude larger proving that the dominant effect on the transmission spectrum is based on a change of the refractive index. A further important observation is that with the exception of two ranges at about 6.8 THz and 17.4 THz, the normalized change in frequency with temperature and thus the ratio of the frequency values of each local extrema is approximately the same over the whole frequency range of the spectra. This suggests a non-dispersive or at least a very slow-dispersive behaviour of the refractive index in the measured frequency-regime except for the two, aforementioned frequency slots. Based on this observation, I applied linear fits for both quantities, each time unveiling slopes of negligible sizes. Thereby, in a good approximation they can be considered as constants for all practical purposes. The constant of each fit is given in the insets of the diagrams (see Fig.C.13 and C.14) in dependence of the corresponding sample-temperatures. At this point it should be noted again that each spectrum depicts the transmission averaged over a certain temperature interval whose size is determined by the duration of each measurement and the velocity of the temperature variation, which itself is a non-linear function of the temperature as can be seen in Fig.5.2. Moreover, the temperature diode is not attached on top of the samples but in close proximity on the same mounting, so that a small difference between the ascertained and the actual temperature value is possible, but if so, it is likely to be very small. The indicated temperature values of all plots represented in this work refer to the initial temperature value recorded at the beginning of each measurement.

no.2: $t = 363(1)\,\mu\text{m}$, $\rho_{Si} \geq 5\,\text{k}\Omega\,\text{cm}$

cooling down cycle

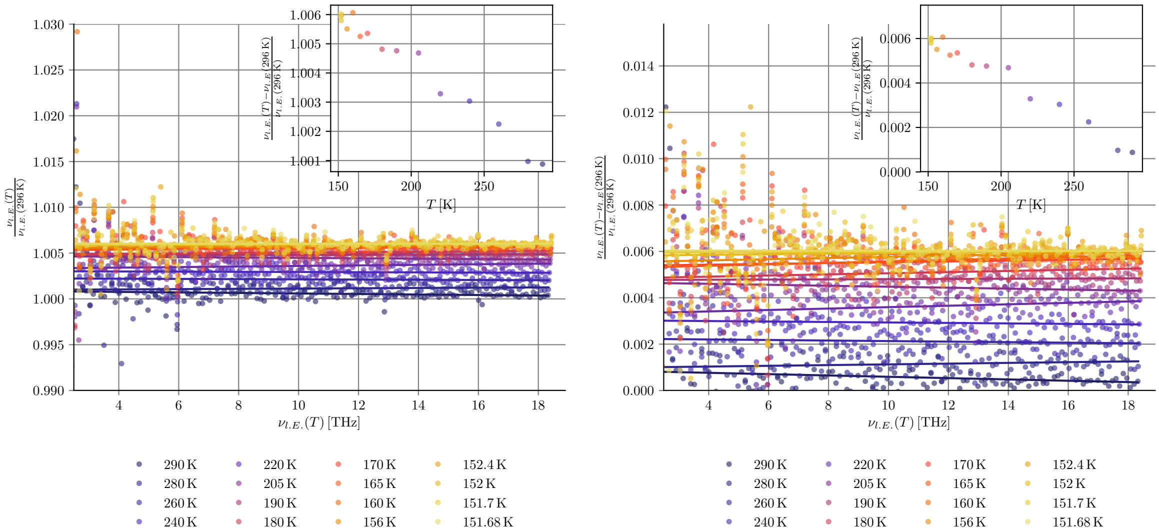

warming up cycle

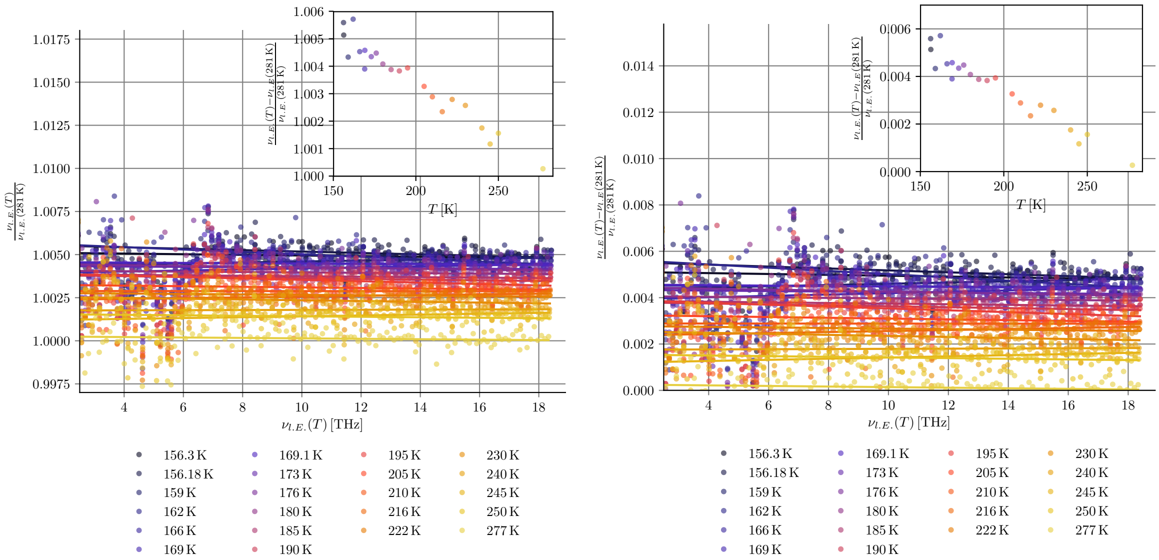

Figure C.13.: Normalized frequency shift and frequency ratio for silicon sample no.2: The frequency position $\nu_{l.E.}$ of each local extrema (l.E.) in the transmission spectrum of the sample was tracked during the cooling-down and warming-up cycle. Applying linear fits over the entire frequency range yields constants which are depicted in the insets, plotted against temperature.

no.3: $t = 535(6)\,\mathrm{\mu m}$, $\rho \geq 3\,\mathrm{k\Omega\,cm}$

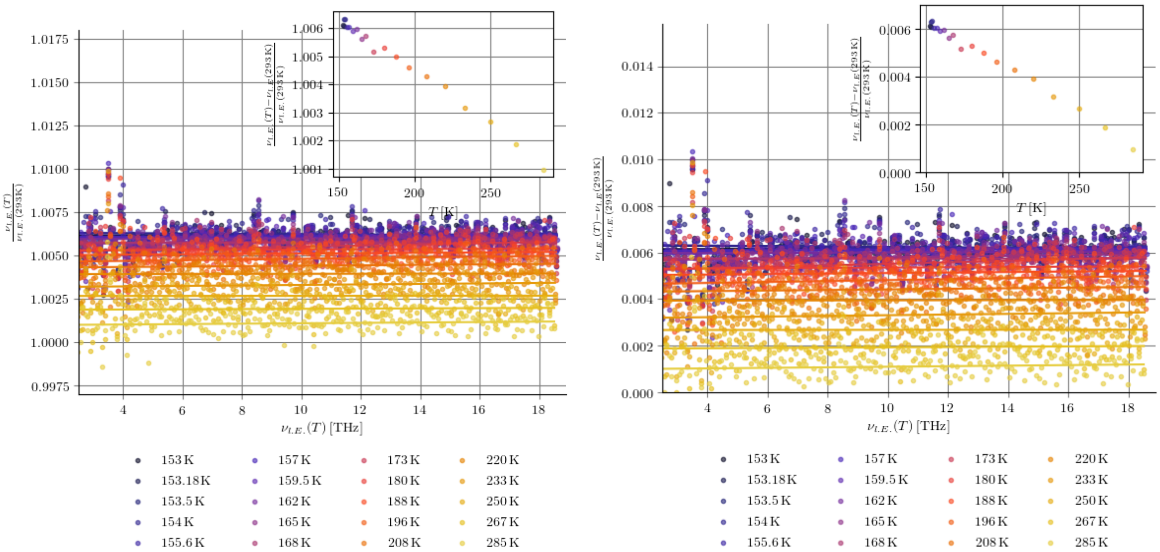

no.4: $t = 533(1)\,\mathrm{\mu m}$, $\rho_{Si} \geq 3\,\mathrm{k\Omega\,cm}$

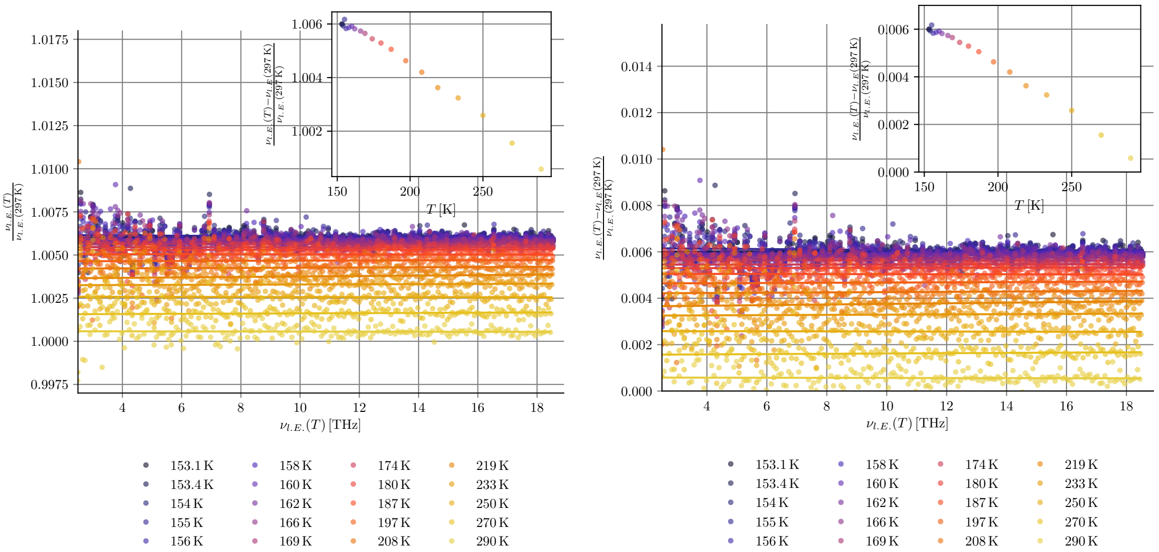

Figure C.14.: Normalized frequency shift and frequency ratio for silicon sample no.3 and no.4: The frequency position $\nu_{l.E.}$ of each local extrema (l.E.) in the transmission spectrum of the sample was tracked during the cooling-down and warming-up cycle. Applying linear fits over the entire frequency range yields constants which are depicted in the insets, plotted against temperature.

Bibliography

Publications

[1] Mohamed Nurul Afsar and Hua Chi. “Millimeter wave complex refractive index, complex dielectric permittivity and loss tangent of extra high purity and compensated silicon.” In: *International Journal of Infrared and Millimeter Waves* 15.7 (1994), pp. 1181–1188.

[2] V Alex, S Finkbeiner, and J Weber. “Temperature dependence of the indirect energy gap in crystalline silicon.” In: *Journal of Applied Physics* 79.9 (1996), pp. 6943–6946.

[4] Constantine A Balanis. *Antenna theory: analysis and design.* John wiley & sons, 1997.

[5] Aurel Bergfalk. *Optical Simulations and Characterisations of Antenna Integrated YBCO THz Detectors.* Sweden, 2014.

[6] Mario Bertolotti et al. “Temperature dependence of the refractive index in semiconductors.” In: *JOSA B* 7.6 (1990), pp. 918–922.

[7] J Böhm, N Honingh, and K Jacobs. “Development of a HEB mixer for the observation of molecular hydrogen on SOFIA.” In: *ISSTT 2019: 30th International Symposium on Space Terahertz Technology.* 2019, p. 104.

[8] J Böhm et al. “10.7 THz HEB heterodyne mixer designs.” In: *ISSTT 2022: 32nd International Symposium on Space Terahertz Technology.* 2022.

[9] J Böhm et al. “Cryogenic temperature-dependence of HRFZ Silicon refractive index from Mid-to Far-IR down to 5 K.” In: *2021 46th International Conference on Infrared, Millimeter and Terahertz Waves (IRMMW-THz).* IEEE, pp. 1–2.

[10] Johanna Böhm, Karl Jacobs, and CE Honingh. “Design of simply structured metamaterial filters at sub-THz frequencies.” In: *ISSTT 2017: 28th International Symposium on Space Terahertz Technology.* 2017.

[11] G. R. Boogaard et al. “Resistance of superconducting nanowires connected to normal-metal leads.” In: *Phys. Rev. B* 69 (22 June 2004), p. 220503.

[12] Max Born et al. *Principles of optics: electromagnetic theory of propagation, interference and diffraction of light.* Vol. 4. Pergamon press Oxford, 1970.

[13] Daniel Bouche, Frédéric Molinet, and Raj Mittra. *Asymptotic methods in electromagnetics.* Springer Science & Business Media, 2012.

[14] Michael Brandt. “Superconducting hot electron bolometers on silicon nitride membranes for terahertz waveguide mixers.” In: (2004).

[16] Denis Büchel et al. “4.7-THz superconducting hot electron bolometer waveguide mixer.” In: *IEEE Transactions on Terahertz Science and Technology* 5.2 (2015), pp. 207–214.

[17] Denis Fabian Büchel. “Hot Electron Bolometer Mixers for THz Arrays.” PhD thesis. Universität zu Köln, 2017.

[18] Eric B Burgh, Kevin France, and Stephan R McCandliss. “Direct measurement of the ratio of carbon monoxide to molecular hydrogen in the diffuse interstellar medium.” In: *The Astrophysical Journal* 658.1 (2007), p. 446.

[19] Michael G Burton, DJ Hollenbach, and AGG Tielens. “Mid-infrared rotational line emission from interstellar molecular hydrogen.” In: *The Astrophysical Journal* 399 (1992), pp. 563–572.

[20] Thomas H Buttgenbach. “An improved solution for integrated array optics in quasi-optical mm and submm receivers: the hybrid antenna.” In: *IEEE transactions on microwave theory and techniques* 41.10 (1993), pp. 1750–1760.

[21] A Carmona et al. “A search for mid-infrared molecular hydrogen emission from protoplanetary disks.” In: *Astronomy & Astrophysics* 477.3 (2008), pp. 839–852.

[22] John Chamberlain, JE Gibbs, and HA Gebbie. “The determination of refractive index spectra by Fourier spectrometry.” In: *Infrared Physics* 9.4 (1969), pp. 185–209.

[23] Deane Chandler-Horowitz and Paul M Amirtharaj. “High-accuracy, midinfrared ($450\,\mathrm{cm}^{-1} \leq \omega \leq 4000\,\mathrm{cm}^{-1}$) refractive index values of silicon.” In: *Journal of Applied physics* 97.12 (2005), p. 123526.

[24] Teng-Kai Chen. *Analysis and design of a multifunctional spiral antenna.* Texas A&M University, 2012.

[25] Teng-Kai Chen and Gregory H Huff. “Modal resistance of spiral antenna.” In: (2013).

[26] Teng-Kai Chen and Gregory H Huff. “On the constant input impedance of the Archimedean spiral antenna in free-space.” In: *IEEE transactions on antennas and propagation* 62.7 (2014), pp. 3869–3872.

[27] SR Chick et al. “Metrology of complex refractive index for solids in the terahertz regime using frequency domain spectroscopy.” In: *Metrologia* 55.6 (2018), p. 771.

[28] Nonchanutt Chudpooti et al. “Wideband dielectric properties of silicon and glass substrates for terahertz integrated circuits and microsystems.” In: *Materials Research Express* 8.5 (2021), p. 056201.

[29] Paul C Clark et al. “How long does it take to form a molecular cloud?” In: *Monthly Notices of the Royal Astronomical Society* 424.4 (2012), pp. 2599–2613.

[30] Phillip Charles Clemmow. *The Plane Wave Spectrum Representation of Electromagnetic Fields: International Series of Monographs in Electromagnetic Waves.* Elsevier, 2013.

[31] RJ Collier. “Coupling between coplanar waveguides and substrate modes.” In: *1999 29th European Microwave Conference.* Vol. 3. IEEE. 1999, pp. 382–385.

[32] RJ Collins and HY Fan. “Infrared lattice absorption bands in germanium, silicon, and diamond.” In: *Physical Review* 93.4 (1954), p. 674.

[33] Françoise Combes, G Pineau des Forets, et al. *Molecular hydrogen in space.* Cambridge University Press, 2000.

[34] Paul D Cunningham et al. “Broadband terahertz characterization of the refractive index and absorption of some important polymeric and organic electro-optic materials.” In: *Journal of Applied Physics* 109.4 (2011), pp. 043505–043505.

[35] Francesco D’Angelo et al. “Ultra-broadband THz time-domain spectroscopy of common polymers using THz air photonics.” In: *Optics express* 22.10 (2014), pp. 12475–12485.

[36] Jianming Dai et al. “Terahertz time-domain spectroscopy characterization of the far-infrared absorption and index of refraction of high-resistivity, float-zone silicon.” In: *JOSA B* 21.7 (2004), pp. 1379–1386.

[37] Nirod K Das. “A new theory of the characteristic impedance of general printed transmission lines applicable when power leakage exists.” In: *IEEE Transactions on Microwave Theory and Techniques* 48.7 (2000), pp. 1108–1117.

[38] R Datta et al. “Large-aperture wide-bandwidth antireflection-coated silicon lenses for millimeter wavelengths.” In: *Applied optics* 52.36 (2013), pp. 8747–8758.

[39] Francesco G Della Corte et al. “Temperature dependence analysis of the thermo-optic effect in silicon by single and double oscillator models.” In: *Journal of Applied Physics* 88.12 (2000), pp. 7115–7119.

[40] Georges A Deschamps. “Ray techniques in electromagnetics.” In: *Proceedings of the IEEE* 60.9 (1972), pp. 1022–1035.

[42] Waveguide Slot Array Design. *by I. Kaminow and R.* Tech. rep. Stegen, Technical Memorandum 348, Hughes Aircraft Company, Microwave Laboratory, Research and Development Laboratories, 1954.

[43] Vincent Dislaire et al. “Nitrogen hydrides and the H2 ortho-to-para ratio in dark clouds.” In: *Astronomy & Astrophysics* 537 (2012), A20.

[44] MS Dresselhaus et al. “Solid state physics part II optical properties of solids.” In: *Lecture Notes (Massachusetts Institute of Technology, Cambridge, MA)* 17 (2001), pp. 15–16.

[45] JD Dyson et al. “A note on the difference between equiangular and Archimedes spiral antennas (correspondence).” In: *IRE Transactions on Microwave theory and techniques* 9.2 (1961), pp. 203–205.

[46] John Dyson. “The equiangular spiral antenna.” In: *IRE Transactions on Antennas and Propagation* 7.2 (1959), pp. 181–187.

[47] David F Edwards. “Silicon (Si).” In: *Handbook of optical constants of solids.* Elsevier, 1997, pp. 547–569.

[48] IA Ehtezazi and C Letrou. “A spectral domain ray tracing method for quasi-optical devices modelling.” In: *Antennas and Propagation Society International Symposium, 1998. IEEE.* Vol. 2. IEEE. 1998, pp. 1086–1089.

[49] Iraj A Ehtezazi, Christine Letrou, and Gerard Beaudin. “Radiation patterns from substrate-lens antennas: A method of analysis for THz application.” In: *Terahertz Electronics Proceedings, 1998. THz Ninety Eight. 1998 IEEE Sixth International Conference on.* IEEE. 1998, pp. 30–33.

[50] Carlos A Fernandes, Eduardo B Lima, and Jorge R Costa. “Dielectric lens antennas.” In: *Handbook of antenna technologies.* Springer, 2016, pp. 1001–1064.

[51] George B Field, WB Somerville, and K Dressler. “Hydrogen molecules in astronomy.” In: *Annual Review of Astronomy and Astrophysics* 4 (1966), p. 207.

[52] Daniel F Filipovic and Gabriel M Rebeiz. “Double-slot antennas on extended hemispherical and elliptical quartz dielectric lenses.” In: *International journal of infrared and millimeter waves* 14.10 (1993), pp. 1905–1924.

[53] Daniel F Filipovic et al. “Double-slot antennas on extended hemispherical dielectric lenses.” In: *The Third International Symposium on Space Terahertz Technology: Symposium Proceedings.* 1992.

[54] MI Finkel et al. “Hot electron bolometer mixer for 20-40 THz frequency range.” In: *Proc. 16th Int.. Space Terahertz Technol. Symp.* Citeseer. 2005, pp. 393–397.

[55] Paolo Focardi, William R McGrath, and Andrea Neto. “Design guidelines for terahertz mixers and detectors.” In: *IEEE Transactions on microwave theory and techniques* 53.5 (2005), pp. 1653–1661.

[56] Paolo Focardi, Andrea Neto, and William R McGrath. “Coplanar-waveguide-based terahertz hot-electron-bolometer mixers mproved embedding circuit description.” In: *IEEE Transactions on Microwave Theory and Techniques* 50.10 (2002), pp. 2374–2383.

[57] Paolo Focardi, Andrea Neto, and William R McGrath. “Electromagnetic model for twin slot terahertz mixers.” In: *17th International Conference on Applied Electromagnetics and Communications, 2003. ICECom 2003.* IEEE. 2003, pp. 316–319.

[59] A Fuente et al. “Infrared Space Observatory observations toward the reflection nebula NGC 7023: A nonequilibrium ortho-to-para-H2 ratio.” In: *The Astrophysical Journal* 518.1 (1999), p. L45.

[60] C Fumeaux et al. “Nanometer thin-film Ni–NiO–Ni diodes for detection and mixing of 30 THz radiation.” In: *Infrared physics & technology* 39.3 (1998), pp. 123–183.

[61] W. F. M. Ganzevles et al. “Direct response of twin-slot antenna-coupled hot-electron bolometer mixers designed for 2.5 THz radiation detection.” In: *Applied Physics Letters* 76.22 (2000), pp. 3304–3306.

[62] JR Gao et al. “Direct comparison of the sensitivity of a spiral and a twin-slot antenna coupled HEB mixer at 1.6 THz.” In: *17th International Symposium on Space Terahertz Technology*. ISSTT. 2007, pp. 59–62.

[63] Steven S Gearhart and Gabiel M Rebeiz. “A monolithic 250 GHz Schottky-diode receiver.” In: *IEEE transactions on microwave theory and techniques* 42.12 (1994), pp. 2504–2511.

[64] EM Gershenzon et al. “Heating of quasiparticles in a superconducting film in the resistive state.” In: *JETP Letters* 34.5 (1981), pp. 268–271.

[65] SCO Glover and M-M Mac Low. “On the relationship between molecular hydrogen and carbon monoxide abundances in molecular clouds.” In: *Monthly Notices of the Royal Astronomical Society* 412.1 (2011), pp. 337–350.

[69] RJ Gould, T Gold, and EE Salpeter. “The Interstellar Abundance of the Hydrogen Molecule. II. Galactic Abundance and Distribution.” In: *The Astrophysical Journal* 138 (1963), p. 408.

[70] Robert J Gould. “The contraction of molecular hydrogen protostars.” In: *The Astrophysical Journal* 140 (1964), p. 638.

[71] Yu P Gousev et al. “Broadband ultrafast superconducting NbN detector for electromagnetic radiation.” In: *Journal of Applied Physics* 75.7 (1994), pp. 3695–3697.

[72] Isabelle A Grenier, Jean-Marc Casandjian, and Régis Terrier. “Unveiling extensive clouds of dark gas in the solar neighborhood.” In: *Science* 307.5713 (2005), pp. 1292–1295.

[73] Erich N Grossman and Donald G McDonald. “Partially coherent transmittance of dielectric lamellae.” In: *Optical Engineering* 34.5 (1995), pp. 1289–1295.

[74] Bruno Guillet et al. “Influence of substrates and buffer layers on the quality of NbN ultra thin film for THz HEB.” In: *proc. 18th Int. Symp. Space THz Technol.* 2007, pp. 153–156.

[75] Emilie Habart et al. “Molecular hydrogen.” In: *ISO Science Legacy*. Springer, 2005, pp. 71–91.

[76] Daniel Hailu. “Hybrid Spectral Ray Tracing Method For Multi-scale Millimeter-wave and Photonic Propagation Problems.” In: (2011).

[77] PY Han and XC Zhang. “Free-space coherent broadband terahertz time-domain spectroscopy.” In: *Measurement Science and Technology* 12.11 (2001), p. 1747.

[78] Rinoud Hanna. “Infrared absorption spectrum of silicon dioxide.” In: *Journal of the American Ceramic Society* 48.11 (1965), pp. 595–599.

[79] Bernd Harbecke. “Coherent and incoherent reflection and transmission of multilayer structures.” In: *Applied Physics B* 39.3 (1986), pp. 165–170.

[80] Parameswaran Hariharan. *Basics of interferometry*. Elsevier, 2010.

[81] NJ Harrick. “Determination of refractive index and film thickness from interference fringes.” In: *Applied optics* 10.10 (1971), pp. 2344–2349.

[82] G Hasnain, A Dienes, and JR Whinnery. “Dispersion of picosecond pulses in coplanar transmission lines.” In: *IEEE Transactions on Microwave Theory and Techniques* 34.6 (1986), pp. 738–741.

[83] Eugene Hecht. “Optics 4th edition.” In: *Optics 4th edition by Eugene Hecht Reading* (2001).

[84] G Hernandez. “Fabry-Perot with an absorbing etalon cavity.” In: *Applied optics* 24.18 (1985), pp. 3062–3067.

[85] Max Herzberger and Calvin D Salzberg. “Refractive indices of infrared optical materials and color correction of infrared lenses.” In: *JOSA* 52.4 (1962), pp. 420–427.

[86] David Hollenbach and EE Salpeter. “Surface recombination of hydrogen molecules.” In: *The Astrophysical Journal* 163 (1971), p. 155.

[87] H-W Hübers et al. “Parylene anti-reflection coating of a quasi-optical hot-electron-bolometric mixer at terahertz frequencies.” In: *Infrared Physics & Technology* 42.1 (2001), pp. 41–47.

[88] Heinz-Wilhelm Hübers et al. “Heterodyne receiver for 3-5 THz with hot-electron bolometer mixer.” In: *Z-Spec: a broadband millimeter-wave grating spectrometer: design, construction, and first cryogenic measurements* 5498 (2004), pp. 579–586.

[90] John David Jackson. *Classical electrodynamics*. John Wiley & Sons, 2007.

[91] M Ji et al. “Study of parylene as anti-reflection coating for silicon optics at THz frequencies.” In: *Eleventh Intern. Symp. Space THz Technology, The University of Michigan, Ann Arbor, MI.* 2000, p. 407.

[92] FA Johnson. “Lattice absorption bands in silicon.” In: *Proceedings of the Physical Society* 73.2 (1959), p. 265.

[93] Julius Kaiser. “The Archimedean two-wire spiral antenna.” In: *IRE Transactions on Antennas and Propagation* 8.3 (1960), pp. 312–323.

[94] BS Karasik and AI Elantiev. “Noise temperature limit of a superconducting hot-electron bolometer mixer.” In: *Applied physics letters* 68.6 (1996), pp. 853–855.

[95] BS Karasik et al. “Low noise in a diffusion-cooled hot-electron mixer at 2.5 THz.” In: *Applied physics letters* 71.11 (1997), pp. 1567–1569.

[96] Akira Kawakami et al. “Broadening the IF band of a THz hot-electron bolometer mixer by using a magnetic thin film.” In: *IEEE Transactions on Terahertz Science and Technology* 8.6 (2018), pp. 647–653.

[97] Sean W King and Milan Milosevic. “A method to extract absorption coefficient of thin films from transmission spectra of the films on thick substrates.” In: *Journal of Applied Physics* 111.7 (2012), p. 073109.

[98] Rei Kitamura, Laurent Pilon, and Miroslaw Jonasz. “Optical constants of silica glass from extreme ultraviolet to far infrared at near room temperature.” In: *Applied optics* 46.33 (2007), pp. 8118–8133.

[99] C Kittel. “Introduction to Solid State Physics, 6th edn., translated by Y.” In: *Uno, N. Tsuya, A. Morita and J. Yamashita,(Maruzen, Tokyo, 1986) pp* (1986), pp. 124–129.

[100] Hermann Kober. *Dictionary of conformal representations.* Vol. 2. Dover New York, 1957.

[101] Sascha Krause et al. “Noise and IF gain bandwidth of a balanced waveguide NbN/GaN hot electron bolometer mixer operating at 1.3 THz.” In: *IEEE Transactions on Terahertz Science and Technology* 8.3 (2018), pp. 365–371.

[102] Sascha Krause et al. “Reduction of phonon escape time for NbN hot electron bolometers by using GaN buffer layers.” In: *IEEE Transactions on Terahertz Science and Technology* 7.1 (2016), pp. 53–59.

[103] Rakesh Kumar. “Advanced parylene technology for sensors, optical windows, and display applications.” In: *Window and Dome Technologies and Materials XI.* Vol. 7302. SPIE. 2009, pp. 362–372.

[104] WD Langer et al. “A Herschel [CII] Galactic plane survey-II. CO-dark H2 in clouds.” In: *Astronomy & Astrophysics* 561 (2014), A122.

[105] J Le Bourlot. “Ammonia formation and the ortho-to-para ratio of H2 in dark clouds.” In: *Astronomy and Astrophysics* 242 (1991), pp. 235–240.

[106] Shung-Wu Lee et al. “Refraction at a curved dielectric interface: geometrical optics solution.” In: *IEEE Transactions on Microwave Theory and Techniques* 30.1 (1982), pp. 12–19.

[107] T-G Lee et al. “Rotational quenching rate coefficients for H2 in collisions with H2 from 2 to 10,000 K.” In: *The Astrophysical Journal* 689.2 (2008), p. 1105.

[108] RA Lewis. “A review of terahertz detectors.” In: *Journal of Physics D: Applied Physics* 52.43 (2019), p. 433001.

[109] HH Li. “Refractive index of silicon and germanium and its wavelength and temperature derivatives.” In: *Journal of Physical and Chemical Reference Data* 9.3 (1980), pp. 561–658.

[110] Yongqian Li et al. “Surface-enhanced molecular spectroscopy (SEMS) based on perfect-absorber metamaterials in the mid-infrared.” In: *Scientific reports* 3.1 (2013), pp. 1–8.

[111] Ernest V Loewenstein, Donald R Smith, and Robert L Morgan. “Optical constants of far infrared materials. 2: Crystalline solids.” In: *Applied optics* 12.2 (1973), pp. 398–406.

[113] Stefano Maci and Andrea Neto. “Green’s function of an infinite slot printed between two homogeneous dielectrics-Part II: Uniform asymptotic solution.” In: *IEEE Transactions on Antennas and Propagation* 52.3 (2004), pp. 666–676.

[114] JC Manifacier, J Gasiot, and JP Fillard. “A simple method for the determination of the optical constants n, k and the thickness of a weakly absorbing thin film.” In: *Journal of Physics E: Scientific Instruments* 9.11 (1976), p. 1002.

[115] C Martin-Zaıdi et al. “Where is the warm H2? A search for H2 emission from disks around Herbig Ae/Be stars.” In: *Astronomy & Astrophysics* 516 (2010), A110.

[116] DC Mattis and John Bardeen. “Theory of the anomalous skin effect in normal and superconducting metals.” In: *Physical Review* 111.2 (1958), p. 412.

[117] William R McGrath. “Novel hot-electron bolometer mixers for submillimeter applications: An overview of recent developments.” In: *Proceedings of ISSE’95-International Symposium on Signals, Systems and Electronics*. IEEE. 1995, pp. 147–152.

[118] Thomas Middelmann et al. “Thermal expansion coefficient of single-crystal silicon from 7 K to 293 K.” In: *Physical Review B* 92.17 (2015), p. 174113.

[119] Carol Gray Montgomery. *Technique of microwave measurements*. Vol. 11. McGraw-Hill Book Co., 1947. Chap. 7.

[120] C Moutou et al. “The rich spectroscopy of reflection nebulae.” In: *The Universe as seen by ISO*. Vol. 427. 1999, p. 727.

[121] Mira Naftaly et al. “Refractive Indices of Ge and Si at Temperatures between 4–296 K in the 4–8 THz Region.” In: *Applied Sciences* 11.2 (2021), p. 487.

[122] Andrea Neto, Peter De Maagt, and Stefano Maci. “Optimized basis functions for slot antennas excited by coplanar waveguides.” In: *IEEE Transactions on Antennas and Propagation* 51.7 (2003), pp. 1638–1646.

[123] Andrea Neto and Stefano Maci. “Green’s function for an infinite slot printed between two homogeneous dielectrics. I. Magnetic currents.” In: *IEEE Transactions on Antennas and Propagation* 51.7 (2003), pp. 1572–1581.

[124] David A Neufeld et al. “Spitzer Observations of HH 54 and HH 7-11: Mapping the H2 Ortho-to-Para Ratio in Shocked Molecular Gas.” In: *The Astrophysical Journal* 649.2 (2006), p. 816.

[126] Evgenii Novoselov and Sergey Cherednichenko. “Low noise terahertz MgB2 hot-electron bolometer mixers with an 11 GHz bandwidth.” In: *Applied Physics Letters* 110.3 (2017), p. 032601.

[127] Tetsuhiko Ohba and Shun-ichi Ikawa. “Far-infrared absorption of silicon crystals.” In: *Journal of applied physics* 64.8 (1988), pp. 4141–4143.

[128] Keita Ohtani et al. “Far-Infrared Quantum Cascade Lasers Operating in the AlAs Phonon Reststrahlen Band.” In: *ACS photonics* 3.12 (2016), pp. 2280–2284.

[129] Krzysztof Pachucki and Jacek Komasa. “Ortho-para transition in molecular hydrogen.” In: *Physical Review A* 77.3 (2008), p. 030501.

[130] D Paradis et al. “Dark gas in the solar neighborhood from extinction data.” In: *Astronomy & Astrophysics* 543 (2012), A103.

[131] N. Perrin and C. Vanneste. “Response of superconducting films to a periodic optical irradiation.” In: *Phys. Rev. B* 28 (9 Nov. 1983), pp. 5150–5159.

[132] AN Pikhtin and AD Yas’kov. “Dispersion of the refractive index in semiconductors with diamond and zinc-blend structures.” In: *Sov. Phys. Semicond.,* 12.6 (1978), pp. 622–626.

[134] David M Pozar. *Microwave engineering.* John wiley & sons, 2011.

[135] William H Press et al. *Numerical recipes 3rd edition: The art of scientific computing.* Cambridge university press, 2007.

[136] Daniel E Prober. “Superconducting terahertz mixer using a transition-edge microbolometer.” In: *Applied Physics Letters* 62.17 (1993), pp. 2119–2121.

[137] Marvin R Querry. *Optical constants of minerals and other materials from the millimeter to the ultraviolet.* Chemical Research, Development & Engineering Center, US Army Armament . . ., 1987.

[138] CM Randall and RD Rawcliffe. “Refractive indices of germanium, silicon, and fused quartz in the far infrared.” In: *Applied Optics* 6.11 (1967), pp. 1889–1895.

[139] Gabriel M Rebeiz. “Millimeter-wave and terahertz integrated circuit antennas.” In: *Proceedings of the IEEE* 80.11 (1992), pp. 1748–1770.

[140] P. L. Richards. “Bolometers for infrared and millimeter waves.” In: *Journal of Applied Physics* 76.1 (1994), pp. 1–24.

[141] Matthew J Richter et al. “Development and future use of the echelon-cross-echelle spectrograph on SOFIA.” In: *Ground-based and Airborne Instrumentation for Astronomy.* Vol. 6269. SPIE. 2006, pp. 503–513.

[142] BK Ridley. “Hot electrons in semiconductors.” In: *Science Progress (1933-)* (1986), pp. 425–459.

[143] A Roederer et al. “IEEE standard for definitions of terms for antennas.” In: *IEEE Std* (2014), pp. 145–2013.

[144] Robert L Rogers and Dean P Neikirk. “Use of broadside twin element antennas to increase efficiency on electrically thick dielectric substrates.” In: *International journal of infrared and millimeter waves* 9.11 (1988), pp. 949–969.

[145] E Roueff et al. “The full infrared spectrum of molecular hydrogen.” In: *Astronomy & Astrophysics* 630 (2019), A58.

[146] Victor Rumsey. “Frequency independent antennas.” In: *1958 IRE International Convention Record.* Vol. 5. IEEE. 1966, pp. 114–118.

[147] David B Rutledge, Dean P Neikirk, and Dayalan P Kasilingam. “Integrated-circuit antennas.” In: *Infrared and millimeter waves* 10.part 2 (1983), pp. 1–90.

[149] AD Semenov et al. “Analysis of the nonequilibrium photoresponse of superconducting films to pulsed radiation by use of a two-temperature model.” In: *Physical Review B* 52.1 (1995), p. 581.

[150] Alexei D Semenov, Gregory N Gol’tsman, and Roman Sobolewski. “Hot-electron effect in superconductors and its applications for radiation sensors.” In: *Superconductor Science and Technology* 15.4 (2002), R1.

[151] Alexei D Semenov et al. “Terahertz performance of integrated lens antennas with a hot-electron bolometer.” In: *IEEE transactions on microwave theory and techniques* 55.2 (2007), pp. 239–247.

[152] Alexey Semenov et al. “Integrated planar antennas at terahertz waves.” In: *Proc. of 16th International Symposium on Space Terahertz Technology, Gothenburg, Sweden.* 2005, pp. 324–328.

[153] M Shcherbatenko et al. “Nonequilibrium interpretation of DC properties of NbN superconducting hot electron bolometers.” In: *Applied Physics Letters* 109.13 (2016), p. 132602.

[154] Shoichi Shiba et al. “3.1-THz heterodyne receiver using an NbTiN hot-electron bolometer mixer and a quantum cascade laser.” In: *IEEE Transactions on Terahertz Science and Technology* 2.1 (2011), pp. 22–28.

[155] Boris I Shklovskii and Alex L Efros. “Variable-range hopping conduction.” In: *Electronic properties of doped semiconductors.* Springer, 1984, pp. 202–227.

[156] E. Shkondin et al. “Large-scale high aspect ratio Al-doped ZnO nanopillars arrays as anisotropic metamaterials.” In: *Opt. Mater. Express* 7.5 (May 2017), pp. 1606–1627.

[157] Mariia Sidorova et al. “Electron energy relaxation in disordered superconducting NbN films.” In: *Physical Review B* 102.5 (2020), p. 054501.

[158] Rowan J Smith et al. “CO-dark gas and molecular filaments in Milky Way-type galaxies.” In: *Monthly Notices of the Royal Astronomical Society* 441.2 (2014), pp. 1628–1645.

[160] J Sophocles. “Orfanidis,‘Electromagnetic waves and antennas.” In: (2003).

[161] Lyman Spitzer Jr. “The Temperature of Interstellar Matter. II.” In: *The Astrophysical Journal* 109 (1949), p. 337.

[162] MA Spivack. “Mechanical properties of very thin polymer films.” In: *Review of Scientific Instruments* 43.7 (1972), pp. 985–990.

[163] MA Spivack. “Parylene thin films for radiation applications.” In: *Review of Scientific Instruments* 41.11 (1970), pp. 1614–1616.

[164] Amiel Sternberg. “The excitation of molecular hydrogen and its significance.” In: *Infrared spectroscopy in astronomy.* Vol. 290. 1989.

[165] Amiel Sternberg and David A Neufeld. “The ratio of ortho-to para-H2 in photodissociation regions.” In: *The Astrophysical Journal* 516.1 (1999), p. 371.

[166] Jörg Stodolka. “Fabrikation und Analyse supraleitender diffusionsgekühlter Hot-Electron-Bolometer als Terahertz-Heterodynmischer.” In: (2003).

[167] R Swanepoel. “Determination of the thickness and optical constants of amorphous silicon.” In: *Journal of Physics E: Scientific Instruments* 16.12 (1983), p. 1214.

[168] J Tennyson and S Wilson. “Handbook of Molecular Physics and Quantum Chemistry.” In: *Wilson, S. ed* (2003).

[169] Wolfgang Theiß. “Optical properties of porous silicon.” In: *Surface Science Reports* 29.3-4 (1997), pp. 91–192.

[170] Chin-Yi Tsai. “Absorption coefficients of silicon: A theoretical treatment.” In: *Journal of Applied Physics* 123.18 (2018), p. 183103.

[171] Edwin M Turner. “Spiral slot antenna.” In: *WADC, Aerial Reconnaissance Laboratory, Project* 4341 (1955), pp. 55–8.

[173] H Van de Stadt et al. “Millimeter and submillimeter studies of planar antennas.” In: *First Int. Symp. on Space Terahertz Technology.* 1990, pp. 235–255.

[174] Martin Van Exter and D Grischkowsky. “Optical and electronic properties of doped silicon from 0.1 to 2 THz.” In: *Applied Physics Letters* 56.17 (1990), pp. 1694–1696.

[175] Yatendra Pal Varshni. “Temperature dependence of the energy gap in semiconductors.” In: *physica* 34.1 (1967), pp. 149–154.

[176] N Vercruyssen et al. “Evanescent states and nonequilibrium in driven superconducting nanowires.” In: *Physical Review B* 85.22 (2012), p. 224503.

[177] Valentine Wakelam et al. “H2 formation on interstellar dust grains: The viewpoints of theory, experiments, models and observations.” In: *Molecular Astrophysics* 9 (2017), pp. 1–36.

[178] Stephen G Warren and Richard E Brandt. “Optical constants of ice from the ultraviolet to the microwave: A revised compilation.” In: *Journal of Geophysical Research: Atmospheres* 113.D14 (2008).

[179] Edward J Wollack et al. “Infrared properties of high-purity silicon.” In: *Optics Letters* 45.17 (2020), pp. 4935–4938.

[180] R Wyss et al. “Submillimeter-wave Spectral Response of Twin Slot Antennas Coupled to Hot Electron Bolometers.” In: (2000).

[181] W Zhang et al. “Noise temperature and beam pattern of an NbN hot electron bolometer mixer at 5.25 THz.” In: *Journal of applied physics* 108.9 (2010), p. 093102.

[182] W Zhang et al. “Temperature dependence of the receiver noise temperature and IF bandwidth of superconducting hot electron bolometer mixers.” In: *Superconductor Science and Technology* 27.8 (2014), p. 085013.

Other Sources

[3] ALTAIR. *Altair Feko*. URL: `https://www.altair.de/feko/` (visited on 01/18/2023).

[15] Bruker. URL: `https://www.bruker.com/de.html`.

[41] Adhirath Deshmuk. *The capabilities of the James Webb Space Telescope*. Advanced Seminar in the I.Physics Institute, University of Cologne. Dec. 2022.

[42] Waveguide Slot Array Design. *by I. Kaminow and R.* Tech. rep. Stegen, Technical Memorandum 348, Hughes Aircraft Company, Microwave Laboratory, Research and Development Laboratories, 1954.

[58] Free Software Foundation. *GNU*. URL: `https://directory.fsf.org/wiki/GNU` (visited on 11/26/2018).

[66] Computer Simulation Technology GmbH. *CST - Computer Simulation Technology*. URL: `https://www.cst.com` (visited on 01/12/2019).

[67] Computer Simulation Technology GmbH. *CST - Computer Simulation Technology*.

[68] Computer Simulation Technology GmbH. *CST Studio Suite 2021 Help*.

[89] Ansys Inc. *ANSYS HFSS*. URL: `https://www.ansys.com/Products/Electronics/ANSYS-HFSS` (visited on 01/12/2019).

[112] Deutsches Zentrum für Luft-und Raumfahrt. *The airborne observatory SOFIA to end its mission after eight years of operations*. URL: `https://www.dlr.de/content/en/articles/news/2022/02/20220428_the-airborne-observatory-sofia-to-end-its-mission.html` (visited on 02/27/2023).

[125] NIST. *Material Properties: Silicon*. data retrieved from `https://trc.nist.gov/cryogenics/materials/Silicon/Silicon.htm`. 2019.

[133] Mikhail Polyanskiy. *refractiveindex.info-scripts*. URL: `https://github.com/polyanskiy/refractiveindex.info-scripts/blob/master/scripts/Kitamura%202007%20-%20Fused%20silica.py` (visited on 12/12/2022).

[148] *Scipy.optimize.curve_fit description*. `https://docs.scipy.org/doc/scipy/reference/generated/scipy.optimize.curve_fit.html`. Accessed: 2022-01-31.

[159] SUMIPRO Optical solutions. URL: `https://www.sumipro.nl`.

[172] TYDEX. *THz_AR_Coatings.pdf*. URL: `http://www.tydexoptics.com/` (visited on 06/28/2019).

Acknowledgment

First of all, I want to thank Professor Dr. Jürgen Stutzki for his support and for the opportunity to gain insights into different interesting topics. Special thanks to Professor Dr. Lucas Labadie for co-reviewing my thesis and many thanks to Professor Dr. Andreas Zilges to chair the board of examiners.

For her continuous guidance during the years of this work I want to especially thank my supervisor Dr. Netty Honingh. Thank you for your assistance and great support over the years. Furthermore, I want to express my deep respect towards Dr. Karl Jacobs who used all his knowledge to fabricate the very tiny HEB-devices for this work and to devote a lot of time and work into complex process development.

Many thanks to Michael Schultz for developing the assembling scheme, the detector block housing and IF-board, and for successfully assembling all parts of the detector module. This work was only possible because of his patience and creative power to put all little parts together.

Moreover, I want to thank Stefan Wulff for his help in the laboratory and for always helping me to get the bond machine run again.

Many thanks to the staff members of the fine mechanic work shop, to fabricate all the components needed for my test setup and a special thank for their creativity to - despite of the lack of a dedicated toolkit - enable the welding of the copper parts that were needed for the cooling chain of the new cooling setup of the FTS. In this context I would also like to thank Henning Adams for his help starting from offering his knowledge, which type of copper is most suited for cryogenic applications.

Many thanks to Philipp Warzanowsky for offering his help and measuring the silicon sample in his FTS setup. Thanks to Wolfram Goerlitz from the company TOPAS Advanced Polymers GmbH for kindly providing and sending us all different TOPAS samples for testing purposes.

Furthermore my thanks go to all (former) colleagues and persons I worked together with over the course of time. My special thanks go to Florian Blauth for general support and stimulating scientific and non-scientific discussions even after having left the university for some years. Thank you for staying in contact. I would further like to thank my office members and colleagues Matthias Justen and Ignacio Barrueto, for the good time together, the pleasant working atmosphere, for their support, and for their reliability which I come to appreciate especially during the period of the Corona epidemic. Many thanks to Ignacio for cheering up over the last years and for lots of tasty cups of coffee.

Last but not least, I want to thank my family for their continuous support on this stage of life and for encouraging me not to give up but to overcome big hurdles. Thank you for your love and for believing in me.

Financial support

This work is carried out within the Collaborative Research Centre 956, sub-project D3, funded by the Deutsche Forschungsgemeinschaft (DFG)- project ID 184018867.

Teilpublikationen:

Konferenzbeiträge:

- Johanna Böhm et al. “Design of simply structured metamaterial filters at sub-THz frequencies.” In: *ISSTT 2017: 28th International Symposium on Space Terahertz Technology.* 2017
- J Böhm et al. “Development of a HEB mixer for the observation of molecular hydrogen on SOFIA.” in: *ISSTT 2019: 30th International Symposium on Space Terahertz Technology.* 2019, p. 104
- J Böhm et al. “Cryogenic temperature-dependence of HRFZ Silicon refractive index from Mid-to Far-IR down to 5 K.” in: *2021 46th International Conference on Infrared, Millimeter and Terahertz Waves (IRMMW-THz).* IEEE, pp. 1–2
- J Böhm et al. “10.7 THz HEB heterodyne mixer designs.” In: *ISSTT 2022: 32nd International Symposium on Space Terahertz Technology.* 2022 (zum Einreichungstermin der Arbeit noch unveröffentlicht)

Eidesamtliche Erklärung zur Disseration:

Hiermit versichere ich an Eides statt, dass ich die vorliegende Dissertation selbstständig und ohne die Benutzung anderer als der angegebenen Hilfsmittel und Literatur angefertigt habe. Alle Stellen, die wörtlich oder sinngemäß aus veröffentlichten und nicht veröffentlichten Werken dem Wortlaut oder dem Sinn nach entnommen wurden, sind als solche kenntlich gemacht. Ich versichere an Eides statt, dass diese Dissertation noch keiner anderen Fakultät oder Universität zur Prüfung vorgelegen hat; dass sie - abgesehen von unten angegebenen Teilpublikationen und eingebundenen Artikeln und Manuskripten - noch nicht veröffentlicht worden ist sowie, dass ich eine Veröffentlichung der Dissertation vor Abschluss der Promotion nicht ohne Genehmigung des Promotionsausschusses vornehmen werde. Die Bestimmungen dieser Ordnung sind mir bekannt. Darüber hinaus erkläre ich hiermit, dass ich die Ordnung zur Sicherung guter wissenschaftlicher Praxis und zum Umgang mit wissenschaftlichem Fehlverhalten der Universität zu Köln gelesen und sie bei der Durchführung der Dissertation zugrundeliegenden Arbeiten und der schriftlich verfassten Dissertation beachtet habe und verpflichte mich hiermit, die dort genannten Vorgaben bei allen wissenschaftlichen Tätigkeiten zu beachten und umzusetzen. Ich versichere, dass die eingereichte elektronische Fassung der eingereichten Druckfassung vollständig entspricht.

Köln, den 20. März 2023